

A framework for joint petrophysically and geologically guided geophysical inversion

by

Thibaut Astic

M.Eng, École Nationale Supérieure des Mines de Nancy, 2011

M.A.Sc, École Polytechnique de Montréal, 2012

A THESIS SUBMITTED IN PARTIAL FULFILLMENT
OF THE REQUIREMENTS FOR THE DEGREE OF

Doctor of Philosophy

in

THE FACULTY OF GRADUATE AND POSTDOCTORAL
STUDIES

(Geophysics)

The University of British Columbia

(Vancouver)

October 2020

© Thibaut Astic, 2020

The following individuals certify that they have read, and recommend to the Faculty of Graduate and Postdoctoral Studies for acceptance, the thesis entitled:

A framework for joint petrophysically and geologically guided geophysical inversion

submitted by **Thibaut Astic** in partial fulfillment of the requirements for the degree of **Doctor of Philosophy in Geophysics**.

Examining Committee:

Douglas W. Oldenburg, Professor, Earth, Ocean and Atmospheric Sciences, The University of British Columbia

Supervisor

Eldad Haber, Professor, Earth, Ocean and Atmospheric Sciences, The University of British Columbia

Supervisory Committee Member

Mark Schmidt, Associate Professor, Computer Sciences, The University of British Columbia

Supervisory Committee Member

Purang Abolmaesumi, Professor, Electrical and Computer Engineering, The University of British Columbia

University Examiner

Michael Bostock, Professor, Earth, Ocean and Atmospheric Sciences, The University of British Columbia

University Examiner

Dario Grana, Associate Professor, Geology and Geophysics, University of Wyoming

External Examiner

Additional Supervisory Committee Members:

Roger Beckie, Professor, Earth, Ocean and Atmospheric Sciences, The University of British Columbia

Supervisory Committee Member

Abstract

Geophysical inversion is a mathematical process from which an image of the underground structures is recovered from geophysical data. Geophysical methods span a wide range of different physical phenomena, from measuring variations of the Earth's magnetic field due to local changes in magnetic characteristics to injecting current in the ground through electrodes to observe electrical conductivity variations. However, this process suffers from two main flaws. First, the problem is highly non-unique as there are usually more unknowns than information in the data. To recover an informative image of the subsurface from geophysical data, *a priori* information about the area is necessary. The widely used minimum-structure approaches usually produce models that are smooth and lack edge resolution while presenting physical properties that are far from their expected values. Second, not all geophysical methods are sensitive to the same features. When multiple surveys with different physics are collected over the same area, combining them in a coherent picture can be complicated by apparent inconsistencies between the inversion results from each method, due to the lack of integration.

To tackle these issues, I first propose a new framework for incorporating petrophysical and geological information into voxel-based geophysical inversion. The inverse problem is developed from a probabilistic perspective and redefined as three interlocked data fitting problems over the geophysical, petrophysical, and geological data, respectively. By quantitatively linking these data into a single framework, I recover a final inverted model that reproduces the observed, or desired, petrophysical and geological features while fitting the geophysical data.

I then expand the framework to multiple physical properties to perform multi-physics joint inversions, using the prior information as a coupling term. By combining the data into a single inversion, I am able to uncover structures that are otherwise indistinguishable using single-physics inversions.

The framework is finally applied to the DO-27 kimberlite pipe case study, in the Tli Kwi Cho (TKC) cluster. I jointly invert airborne and ground-based gravity data, along with airborne magnetic data, to recover a quasi-geology model that can distinguish between the diamondiferous and sterile kimberlite facies.

Lay Summary

Geophysics is an essential tool for imaging the subsurface. Physical property contrasts between subsurface bodies produce physical responses that can be measured remotely by geophysical instruments. Inversion is the process that provides information about those contrasts from the measured responses. However, attempting to extract complex geological information from geophysical inversion is challenging. Large improvements in subsurface imaging can be achieved by incorporating additional information. Direct physical property measurements and geological data provide *a priori* information that can be used to couple multiple geophysical datasets that are otherwise relying on independent physics. By developing the problem from a probabilistic perspective, I quantitatively link these data into a single inversion framework. It allows me to recover a final quasi-geology model that reproduces the desired petrophysical and geological features while fitting the various geophysical datasets. This refines the resolution of the recovered model and improves our understanding of the subsurface structures.

Preface

The research presented in this thesis is original work that I completed at the Geophysical Inversion Facility (GIF), in the Department of Earth, Ocean and Atmospheric Sciences, at the University of British Columbia (UBC), Vancouver, Canada, under the supervision of Professor Douglas W. Oldenburg. Parts of that thesis have been published in peer-reviewed scientific journals and conference proceedings.

The mathematical definition of my framework, presented in chapter 3, was published in December 2019 in *Geophysical Journal International* under the title “*A framework for petrophysically and geologically guided geophysical inversion using a dynamic Gaussian mixture model prior*” (Astic & Oldenburg, 2019). I developed the mathematics of the framework and wrote its implementation in the existing Simulation and Parameter Estimation in Geophysics (SIMPEG) package. The article and scripts to generate examples and figures were written by me. I am the first author and my co-author Dr. Douglas W. Oldenburg provided guidance and feedback. I made all the examples of that paper available online in a cloud environment for reproducibility (Astic, 2019).

An early version of the framework to perform multi-physics inversion (chapter 4) was first published in a peer-reviewed extended abstract in *SEG Technical Program Expanded Abstracts 2018*, for an oral presentation at the Society of Exploration Geophysicist annual meeting in 2018, in Anaheim, California, United-States (Astic & Oldenburg, 2018). It has since been accepted by *Geophysical Journal International* (Astic et al., 2020b) under the title “*Petrophysically and geologically guided multi-physics inversion using a dynamic Gaussian mixture model*”. The implementation of the framework, writing of the article and scripts to generate examples were done by me. I am the first author, and my co-authors are my supervisor Dr. Douglas W. Oldenburg, who provided guidance and feedback, and former colleague Dr. Lindsey J. Heagy, who implemented tools for combining objective functions in SIMPEG and provided guidance and feedback. I made the examples provided in that paper available online for reproducibility (Astic, 2020).

The DO-27 kimberlite pipe case study, presented in chapter 5, was accepted under the title “*Joint inversion of potential fields data over the DO-27 kimberlite pipe using a Gaussian mixture model prior*” for a special issue of *Interpretation* named “*Integrated geophysical imaging*” (Astic et al., 2020a). The article and inversion scripts were written by me. I am the first author and my co-authors are my supervisor Dr. Douglas W. Oldenburg, who provided guidance and feedback, and former colleague Dr. Dominique Fournier, who implemented the potential field operators in SIMPEG and provided guidance and feedback.

Table of Contents

Abstract	iii
Lay Summary	v
Preface	vi
Table of Contents	viii
List of Tables	xvi
List of Figures	xvii
Glossary	xliv
Acknowledgments	xlvi
1 Introduction	1
1.1 Motivation	1
1.1.1 Motivational example: the DO-27 case study	3
1.2 Literature review	7

1.2.1	Inclusion of prior information in inverse problems	7
1.2.2	Coupling terms for multi-physics inversions	10
1.3	Research objectives	13
1.4	Thesis arrangement	15
1.4.1	Background theory	15
1.4.2	Definition of the PGI framework	15
1.4.3	Multi-physics inversions	17
1.4.4	Case study: DO-27	18
1.4.5	Discussions and conclusion	19
2	Key concepts	20
2.1	Notation conventions	21
2.2	Bayesian concepts	23
2.2.1	Bayes' theorem	23
2.2.2	Likelihood and Maximum Likelihood Estimate	24
2.2.3	Prior distribution and Maximum A Posteriori estimate	25
2.3	The univariate Gaussian distribution	26
2.3.1	MLEs of the parameters of the Gaussian distribution	28
2.3.2	MAP estimates of the parameters of the Gaussian distribution	28
2.4	The multivariate Gaussian distribution	35
2.4.1	MLEs for the mean and covariance matrix of the multivariate Gaussian distribution	36

2.4.2	MAP estimates of the parameters of the multivariate Gaussian distribution	37
2.5	Tikhonov inversion and its probabilistic expression	41
2.5.1	The geophysical inverse problem	41
2.5.2	Probabilistic expression of the inverse problem	43
2.5.3	Target value for the data misfit term	48
2.5.4	Solving the geophysical inverse problem	48
3	A framework for petrophysically and geologically guided geophysical inversion using a dynamic Gaussian mixture model prior	54
3.1	Introduction	54
3.2	Univariate Gaussian mixture model representation of petrophysical information	57
3.3	Gaussian mixture model as smallness prior for geophysical inversion	61
3.3.1	Gaussian mixture model prior definition	61
3.3.2	Updating the Gaussian mixture model	67
3.4	Numerical Implementation	74
3.4.1	Petrophysical target misfit and inversion stopping criteria .	75
3.4.2	Pseudocode and weighting strategies	77
3.4.3	Convergence	83
3.5	Examples	84
3.5.1	MT1D, layered and smooth Earth model: demonstration of the framework	85

3.5.2	DC2D, buried cylinders: working with missing petrophysical information and adding geological information	93
3.5.3	Using PGI to reduce ambiguity: a field example	99
3.6	Discussion	109
3.7	Conclusions	113
4	Extension to multi-physics inversions	114
4.1	Introduction	114
4.1.1	Multivariate GMM: modelling multiple physical properties	117
4.1.2	Motivation for simultaneously inverting multiple physical properties	118
4.2	Extension of the PGI framework to multi-physics inversions	120
4.2.1	Definition of the GMM prior	120
4.2.2	The multi-physics PGI geophysical objective function	121
4.2.3	Petrophysical target misfit	123
4.3	Updating the Gaussian mixture model in multi-dimensions	124
4.4	Numerical considerations for reaching multiple target misfits	126
4.4.1	Objective function with multiple geophysical data misfits	127
4.4.2	The regularization scaling parameters	129
4.4.3	Balancing the geophysical data misfits	130
4.4.4	Algorithm	135
4.5	Synthetic example: The DO-27 kimberlite pipe	136
4.5.1	Setup	137

4.5.2	Tikhonov inversions	139
4.5.3	Single-physics PGIs	141
4.5.4	Multi-physics PGI with petrophysical information	145
4.5.5	Multi-physics PGIs with limited information	148
4.5.6	DO-27 example summary	156
4.6	Discussion	157
4.7	Conclusion	159

5 Case study: joint inversion of potential fields data over the DO-27

	kimberlite pipe	160
5.1	Introduction and geological setting	160
5.2	Geophysical datasets	166
5.2.1	Ground gravity	166
5.2.2	Falcon airborne gravity gradiometry	168
5.2.3	VTEM airborne magnetic survey	169
5.3	Tikhonov inversions	169
5.4	Modelling the petrophysical information at DO-27	173
5.4.1	Density information	174
5.4.2	Magnetic susceptibility information	175
5.4.3	Petrophysical characterization summary	179
5.5	Single-physics PGIs	180
5.5.1	Joint PGI of the ground gravity and Falcon airborne grav- ity gradiometry data	182

5.5.2	Magnetic vector inversion of the airborne magnetic data with PGI	183
5.5.3	Post-inversion classification of the individually obtained density and magnetic vector models	184
5.6	Multi-physics PGIs	186
5.6.1	Multi-physics inversion with petrophysical information . .	186
5.6.2	Adding geological information into the multi-physics inversion	190
5.7	Discussion	194
5.8	Conclusion	197
6	Discussions and conclusion	199
6.1	Introduction	199
6.2	Challenges due to consecutive clusters	201
6.2.1	DC example	201
6.2.2	Synthetic DO-27 example: joint inversion with three clusters and no geology or prior petrophysical information . .	204
6.2.3	Summary	207
6.3	Sensitivity analysis	207
6.3.1	Impact of the proportions values set globally	208
6.3.2	Impact of the confidences in the means	210
6.3.3	Impact of the confidences in the variances	214
6.3.4	Impact of varying cluster characteristics	218

6.4	Comparison with existing frameworks	220
6.4.1	Comparison with Sun and Li's FCM guided inversion frame- work	222
6.4.2	Comparison with Giraud et al.'s frameworks	224
6.4.3	Comparison with Grana et al.'s frameworks	226
6.4.4	Comparison with Zhdanov's multinary framework	227
6.5	Future avenues of research: extensions of the framework to in- clude geological rules and modelling	228
6.5.1	Introduction	228
6.5.2	Introduction to Markov random fields	231
6.5.3	Proof of concept with the Ising model	233
6.6	Conclusion	238
	Bibliography	241
	A Working with nonlinear petrophysical relationships	258
	B Numerical implementation	262
	B.1 Integration within SimPEG	262
	B.2 Pseudo-code for the implementation in SimPEG	263
	C Additional models obtained by individual PGIs for the DO-27 syn- thetic case study	270

D	Additional models obtained by multi-physics PGIs with full petro-physical information for the DO-27 synthetic case study with various initializations of the geophysical data misfit scaling parameters .	272
E	Bookpurnong: varying the confidence in the prior variances	275
F	DO-27: Choosing the characteristics of the PK-minor rock unit . . .	278

List of Tables

Table 3.1	Proportions of the GMM $\mathcal{P}(\mathbf{z})$ as a function of depth to include geological information. Legend: bckgrd: background; cond.: conductive unit; res.: resistive unit.	99
Table 5.1	Physical properties and elevation parameters for each rock unit. For the PK/VK-pipe unit, the values are reported without the rotation of the Gaussian distribution caused by the linear trend with depth. Notation and units: \bar{x} : mean of x ; σ_x standard-deviation of x ; ρ : density contrast (g/cm^3); z : elevation (meter); k : effective magnetic susceptibility (log 10 SI); θ : inclination ($^\circ$); ϕ : declination ($^\circ$).	179
Table 6.1	Comparison table with other frameworks	221

List of Figures

Figure 1.1	7 steps procedure for applied geophysics.	2
Figure 1.2	From setup to interpretation.	4
Figure 2.1	Two Gaussian distributions with different means and variances. The histograms represent a set of synthetic realizations sam- pled from the respective distributions.	27

Figure 2.2	A comparison of the MLEs, semi-conjugate prior, and joint conjugate prior MAPS of the mean and variance for a single univariate Gaussian distribution. Observed samples are in blue, along with their estimated MLE Gaussian distribution, and the prior distribution is in grey. Using confidence values of unity in the prior is similar to having an equal number of samples from the prior and the observed data sets. A synthetic prior samples set is represented as the grey histogram. The posterior distribution with a semi-conjugate prior is in black and is seen as an average of the parameters of the observed and prior distributions. The posterior distribution with a joint conjugate prior is in red. The corresponding red histogram is obtained by merging the observed and synthetic prior samples. The variance is larger than for either of the two original distributions; this results because of the difference in the means. Legend: Hist. stands for histogram; Dist. stands for distribution; Obs. stands for observed samples.	34
Figure 2.3	Two-dimensional Gaussian distribution.	35
Figure 2.4	(a) Example of a Gaussian distribution in 1D for one physical property and (b) its quadratic negative-log equivalent.	47

Figure 3.1	A graphical representation of the PGI framework. Each diamond is a MAP estimation which requires data (shown in rectangular boxes) as well as inputs from the other MAP estimates.	55
Figure 3.2	Examples of Gaussian mixture like samples sets. (a) A GMM with two distinct units; the approximation in equation (3.11) is valid. (b) A GMM with overlapping units; the approximation in equation (3.11) is not valid.	59
Figure 3.3	Presentation of two Gaussian distributions with unity standard deviations, and resulting GMMs. Their respective means are separated by various $\Delta\sigma$: (a) $\Delta\sigma = 1$; (b) $\Delta\sigma = 2$; (c) $\Delta\sigma = 3$; (d) $\Delta\sigma = 4$; (e) $\Delta\sigma = 5$	64
Figure 3.4	Illustration of fitting a GMM with parameters Θ through the MAP-EM algorithm, given the geophysical model \mathbf{m} and the prior petrophysical distribution Θ_{prior} with all confidences set to unity.	70
Figure 3.5	A graph illustration of how the various MAP estimate processes are interlocked with each other.	74
Figure 3.6	A visual pseudocode of the iterative cyclic PGI framework to include geological and petrophysical information into geophysical inversion. The numbers correspond to the steps displayed in algorithm 1.	79

Figure 3.7	Setup of the MT1D example: (a) True geophysical model \mathbf{m}_{true} . The dots coincide with the cell centres in the discretized model. (b) True model weighted histogram and prior petrophysical distribution Θ_{prior} ; (c) MT data and uncertainties.	86
Figure 3.8	MT1D example results and comparison. Panels (a), (b) and (c) show the recovered geophysical model, its histogram and the convergence curves respectively for the Tikhonov approach. Panels (d), (e) and (f) shows the same plots for the PGI approach.	89
Figure 3.9	Iterations of the PGI MT1D example. Dist. stands for distribution. Hist. stands for histogram.	91
Figure 3.10	Setup of the DC resistivity example. (a): True conductivity. (b): True petrophysical distribution. (c): DC data to be inverted. (d): Histogram of the measured apparent resistivity. The best fitting half-space (112 Ωm) is indicated by the vertical dashed line. (e): Sensitivity weights \mathbf{w} used for all inversions.	93

Figure 3.11 DC inversion results. The colour scale is the same as for the true model in Figure 3.10a. Panels (a), (b) and (c) present the recovered model, histogram and convergence curves, respectively, for the Tikhonov approach. Panels (d), (e) and (f) show the same plots for PGI when the true petrophysical distribution is provided. Panels (g), (h) and (i) show the results for PGI when no information on the proportions or the physical property means of the units is provided. Panels (j), (k) and (l) show how PGI, with no mean information, can be improved by adding information about the depth and thickness of the cylinders. 96

Figure 3.12 Bookpurnong survey area. The elevation of the survey area is represented as an overlaid colourmap. The white arrows represent the water flow, both from the river and the irrigation zone. Geographic coordinates system: WGS 84 / UTM 54H. Aerial images from Google Earth, ©2019 DigitalGlobe. 101

Figure 3.13 Tikhonov results with two different reference models. All figures share the same colour scale for conductivity. Panels (a), (b) and (c) show the results starting from a conductive half-space. Panels (d), (e) and (f) show the result starting from a resistive half-space. Panels (a) and (d) display the recovered geophysical models on a plan view at a depth of 8.5 m. Panels (b) and (e) display a cross-section of the recovered geophysical models. The Depth Of Investigation (DOI) is evaluated using the method presented in Oldenburg & Li (1999). Panels (c) and (f) display the histogram of the recovered model for each inversion. 103

Figure 3.14 PGI results with two different initial reference models. All figures share the same colour scale for conductivity. Panels (a), (b) and (c) show the results starting from a conductive half-space. Panels (d), (e) and (f) show the results starting from a resistive half-space. Panels (a) and (d) display the recovered geophysical models on a plan view at a depth of 8.5 m. Panels (b) and (e) display a cross-section of the recovered geophysical models. Panels (c) and (f) display the histogram of the recovered model and the learned petrophysical distribution for each inversion. 106

Figure 3.15 Consistency comparison between the two Tikhonov and the two PGI models, starting with conductive and resistive initial and reference models. The first row displays the ratio r of the two PGI conductivity models at different depths. The bottom row displays the same ratio for the two Tikhonov conductivity models. The depth of the plan views increases from left to right. Pale yellow means the two conductivity models differ by less than a factor 2. Orange highlights areas where the recovered conductivities differ by more than a factor 2. Dark purple emphasizes area where the two recovered conductivity models differ by more than a factor 10. 108

Figure 4.1 A graphical representation of the PGI framework. Each diamond is an optimization process that requires data (shown in rectangular boxes) as well as information provided by the other processes (modified from Figure 3.1). 115

- Figure 4.2 Example of a two-dimensional GMM with three rock units. The background is coloured according to the geological classification evaluated by equation (4.2). A thicker contour line indicates a higher iso-probability density level. On the left and bottom panels, I provide the 1D projections of the total and individual probability distributions for each physical property, and the cumulative histograms of the fictitious samples of each rock unit. 119
- Figure 4.3 Evolution curves of the scaling parameters $\{\chi\}$ with the proposed strategy for three multi-physics PGI with full petrophysical information and different initializations for $\{\chi\}$. The colour of each line corresponds to the geophysical misfit: blue for gravity and red with markers for magnetic. The style of the lines corresponds to one of the three inversions ($\chi_{0,\text{grav}} + \chi_{0,\text{mag}} = 1$ in each inversion). 136
- Figure 4.4 Setup: DO-27 synthetic example: (a) Plan map, east-west, and north-south cross-sections through the synthetic geological model. The grid of dots represents the data locations for the gravity and magnetic surveys, and the dotted lines represent the location of each cross-section; (b) Cross-plot and histograms of the physical properties of the synthetic model; (c) Synthetic ground gravity data; (d) Synthetic total amplitude magnetic data. 138

Figure 4.5 DO-27 Tikhonov inversion results. (a) Plan map, east-west, and north-south cross-sections through the recovered density contrast model; (b) Plan map, east-west, and north-south cross-sections through the recovered magnetic susceptibility contrast model; (c) Cross-plot of the density and magnetic susceptibility models; the points are coloured according to both values. The side and bottom panels show the marginal distribution of each physical property, with the best fitting univariate Gaussian (proba. stands for probability, and hist. stands for histogram). Those two univariate Gaussian distributions are used to compute the multivariate Gaussian showed in the background of the cross-plot; (d) Plan map, east-west, and north-south cross-sections coloured based on the combination of density and magnetic susceptibility contrasts. 140

Figure 4.6 Results of the individual PGIs. (a) Plan map, east-west, and north-south cross-sections through the density model recovered using the petrophysical signature of PK/VK; (b) Plan map, east-west, and north-south cross-sections through the magnetic susceptibility model obtained using the petrophysical signature of HK; (c) Cross-plot of the inverted models. The 2D distribution in the background has been determined by combining the two 1D distributions used for density and magnetic susceptibility PGIs, respectively. With only one anomalous unit in each case, there is still four possible combinations; (d) Plan map, east-west, and north-south cross-sections through the quasi-geology model built from the density and magnetic susceptibility models, see cross-plot in (c). 142

Figure 4.7 Results of the multi-physics PGI with petrophysical information. (a) Plan map, east-west, and north-south cross-sections through the recovered density contrast model; (b) Plan map, east-west, and north-south cross-sections through the magnetic susceptibility contrast model; (c) Cross-plot of the inverted models. The colour of the points has been determined by the clustering obtained from this framework joint inversion process. In the background and side panels, I show the prior joint petrophysical distribution with true means used for this PGI; (d) Plan map, east-west, and north-south cross-sections through the resulting quasi-geology model. 146

Figure 4.8 Convergence curves for the three misfits, and evolution curves for the dynamic scaling parameters during the multi-physics PGI with petrophysical information shown in Figure 4.7. (a) Gravity and magnetic geophysical data misfits and their targets (same number of data); (b) Convergence curves of the petrophysical misfit, defined in equation (4.8), and its target value, defined in equation (4.10); (c) Evolution of the $\{\chi\}$ scaling parameters; (d) Evolution of the α_s scaling parameter; (e) Evolution of the trade-off parameter β 147

Figure 4.9 Results of the multi-physics PGI without providing the means of the physical properties for the kimberlite facies; a single kimberlite body is enough to meet the petrophysical requirements (the spread set by the covariances matrices) and reproduce the geophysical datasets; (a) Plan map, east-west, and north-south cross-sections through the recovered density contrast model; (b) Plan map, east-west, and north-south cross-sections through the magnetic susceptibility contrast model; (c) Cross-plot of the inverted models. The colour has been determined by the clustering obtained from this framework joint inversion process. In the background and side panels, I show the learned petrophysical GMM distribution; (d) Plan map, east-west, and north-south cross-sections through the resulting quasi-geology model. 151

Figure 4.10 Results of the multi-physics PGI without providing the means of the physical properties for the kimberlite facies, and assuming a low-density unit and a magnetized unit; (a) Plan map, east-west, and north-south cross-sections through the recovered density contrast model; (b) Plan map, east-west, and north-south cross-sections through the magnetic susceptibility contrast model; (c) Cross-plot of the inverted models. The colour of the points has been determined by the clustering obtained from this framework joint inversion process. In the background and side panels, I show the learned petrophysical distribution; (d) Plan map, east-west, and north-south cross-sections through the resulting quasi-geology model. 154

Figure 4.11 Evolution of the learned means of the GMM throughout the multi-physics PGI with qualitative information for the three assumed rock units (background, low-density kimberlite, and magnetic kimberlite) shown in Figure 4.10. The background mean values, the density of the magnetic rock unit, and the magnetic susceptibility of the low-density rock unit are kept fixed. Initialization has a low impact on the learned mean values, and thus the values at iteration 0 are not shown in the plot. (a) Evolution of the density contrast mean values; (b) Evolution of the magnetic susceptibility mean values. 155

Figure 5.1	Topography map (grey contours and shaded background) and hydrography (blue) at the DO-27 kimberlite pipe in the Northwest Territories, Canada (location in inset). The area of interest is represented as a dashed box. Outline of the PK/VK (dashed) and HK (solid) kimberlite facies present in the pipe, extracted from the geologic model at 285 m of elevation, are overlaid on the map. DO-18 is visible at the northern boundary of the map. Geographic projection: UTM 12N, NAD27.	161
Figure 5.2	(a) Lac De Gras kimberlite pipe conceptual model (modified from Devriese et al. (2017)). HK: Hypabyssal Kimberlite facies; VK: Volcanoclastic Kimberlite facies; PK: Pyroclastic kimberlite facies; (b) Current geological representation of the DO-27 pipe based on drillholes. The same colour convention for the rock units is used for (a) and (b) and throughout the chapter.	163
Figure 5.3	Four potential field datasets, collected over the DO-27 pipe, which are used in this study (after regional removal). (a) Airborne VTEM total field magnetic survey; (b) Ground gravity survey; (c) G_{xy} component of the airborne Falcon gravity gradiometry survey; (d) G_{uv} component of the airborne Falcon gravity gradiometry survey.	167

Figure 5.4 The Octree Mesh used for all of the inversions. The area of interest is outlined in white. The Octree levels represent each increase in cell size (with level 1 being the smallest cells). The volume of interest is discretized with 25 m cubic cells (level 2). The topography is accommodated with a layer of the smallest cells (12.5 m cubic cells, level 1). The other levels (3 and more) serve as padding. 170

Figure 5.5 Results of the smooth gravity inversion and MVI and post-inversion analysis. (a) Plan map, east-west, and north-south cross-sections through the density model obtained by joint smooth inversion of the ground gravity and Falcon data. The dotted lines represent the location of each cross-section; (b) Plan map, east-west, and north-south cross-sections through the magnetic vector model obtained by MVI of the magnetic data. The dark arrows represent the magnetization direction and strength of the magnetic vector projected on the plane; (c) scatter plot of the inverted density contrast and magnetization strength coloured based on both physical properties; (d) coloured model based on the density contrast - magnetization strength couple. 172

Figure 5.6	Design of the PK/VK unit density signature in the GMM. (a) Cross-section of the density contrast estimate for the PK/VK unit from Eggleston et al. (2014); (b) Scatter plot, density contrast versus elevation of the cells, of the cross-section shown in panel (a). I fit a Gaussian on each unit (PK/VK and background); the contour lines represent iso-probability levels from the resulting GMM, and the background colour indicates the geological identification.	176
Figure 5.7	(a) Magnetic measurements in the laboratory; (b) 2D projections of the 3D GMM of the Cartesian components of the magnetic vector resulting from modelling; contour lines represent iso-probability levels of the GMM, and the background colour indicates the geological identification. The background unit is limited to the space defined by the small ellipsoid.	177
Figure 5.8	Highlighting the distinction of rock units in various dimensions: fictitious example of a GMM with two parameters and three rock units, its projections in 1D, and the geological identification prediction in the background (reproduction of Figure 4.2).	181

Figure 5.9	Inversion result with PGI of the ground gravity and Falcon surveys using the density signature of PK/VK; (a) Plan map, east-west, and north-south cross-sections through the recovered density contrast model; (b) Comparison between the petrophysical GMM (contours plot) used to regularize the inversion and the recovered density contrast model (scatter plot).	182
Figure 5.10	Result of the petrophysically guided MVI. (a) Plan map, east-west, and north-south cross-sections through the magnetic vector model; (b) Comparison between the petrophysical GMM (contour plots) used to constrain the magnetic vector model and the recovered magnetic vector model (scatter plots). The background unit appears in the plots as the small ellipsoid. Background cells are all within that small portion of the parameters space. The geological identification is used to colour the background of the plot.	184
Figure 5.11	Plan map, east– west, and north–south cross-sections through the combination of the individual Petrophysically and Geologically guided Inversion (PGI)s. The “UNDEFINED” area corresponds to a volume where both high density and magnetic contrasts were found, corresponding to no known rock units signature.	185

Figure 5.12 Results of the multi-physics PGI with three rock units. (a) Plan map, east-west, and north-south cross-sections through the density contrast model; (b) Magnetic vector model. The grey arrows are the projections of the magnetization directions (unit vector) on the plane for the kimberlite units; (c) Presentation of the 5-dimensional GMM: visualization of all possible 2D projections. Comparison with the recovered model represented as the scatter plots of the four physical properties of the geophysical model and the elevation; (d) Resulting quasi-geology model from the multi-physics PGI with three rock units. 187

Figure 5.13 Results of the multi-physics PGI with an additional rock unit for near-surface PK-minor occurrences, and geological domains. (a) Plan map, east-west, and north-south cross-sections through the density contrast model; (b) Magnetic vector model. The grey arrows are the projections of the magnetization directions (unit vector) on the plane for the kimberlite units; (c) Presentation of the 5-dimensional GMM: visualization of all possible 2D projections. Comparison with the recovered model represented as the scatter plots of the four physical properties of the geophysical model and the elevation; (d) Resulting quasi-geology model from the multi-physics PGI with four rock units. 192

Figure 5.14	Normalized data misfits for all the datasets from the multi-physics PGI with geological domains and four rock units. (a) For the magnetic data; (b) For the gravity data; (c) and (d) For the gravity gradiometry data.	194
Figure 6.1	A graphical representation of the PGI framework. Each diamond is an optimization process that requires data (shown in rectangular boxes) as well as information provided by the other processes (reproduction of Figure 4.1).	200
Figure 6.2	DC 2D survey over 2 buried resistive cylinders. (a) Underground model; (b) Petrophysical characteristics of the model; (c) Simulated DC data; (d) Histogram of the geophysical data.	202
Figure 6.3	Results of the two PGIs for the DC 2D survey over 2 buried resistive cylinders. Panels (a) and (b) show the resulting model, and its distribution, from a PGI with full petrophysical information but no geology information, while panels (c) and (d) show the resulting model, and its distribution, from a PGI with full petrophysical information and geology information.	203
Figure 6.4	Result of the joint inversion of the synthetic data over DO-27 with PGI using the following characteristics: the number of clusters is set to 3, and no petrophysical or geological information is provided. The confidences for the means of the two kimberlite clusters are set to zero.	206

Figure 6.5	Results of the PGIs for the DC 2D survey over 2 buried cylinders for various combinations of proportions for the GMM, with full petrophysical information.	209
Figure 6.6	Results of the PGIs for the DC 2D survey over 2 buried cylinders for various confidences κ values in the prior means, from 0.01 to 0.5, for determining the means of the GMM.	211
Figure 6.7	Results of the PGIs for the DC 2D survey over 2 buried cylinders for various confidences κ values in the prior means, from 0.7 to 100, for determining the means of the GMM.	212
Figure 6.8	Evolution of the MAP estimates of the cluster means by PGI for the DC example with two cylinders, for various values of the confidences κ in the prior means. The prior means are the true means.	213
Figure 6.9	PGIs results on the Bookpurnong case study for various value of the confidence parameter ν in the prior variances. $\nu = 0.3$, $\nu = 0.4$, $\nu = 0.5$	215
Figure 6.10	PGIs results on the Bookpurnong case study for various value of the confidence parameter ν in the prior variances. $\nu = 0.7$, $\nu = 1$, $\nu = 2$	216
Figure 6.11	MAP estimates of the clusters' mean (panel (a)) and variance (panel (b)) from PGIs for the Bookpurnong case study for various values of the confidence parameter ν in the prior variances.	217

Figure 6.12 PGIs of the DO-27 gravity data for various values defining the PK-minor cluster. Panel (a) shows the density contrast model with the characteristics chosen for the multi-physics PGI in section 5.6.2 (see Table 5.1): density contrast of -0.3 g/cm^3 , density standard deviation of 0.1 g/cm^3 , and depth standard deviation of 10 m. Panel (c) represents the GMM corresponding to panel (a). Panel (b) shows another example with different values: density contrast of -0.5 g/cm^3 , density standard deviation of 0.01 g/cm^3 , and depth standard deviation of 10 m. Panel (d) represents the GMM corresponding to panel (b). . 219

Figure 6.13 An example of image segmentation. Panel (a) shows the original image, astronaut and Space Shuttle Commander Eileen Collins (NASA Great Images database, 1998). Panel (b) is the image classified pixel-by-pixel by training a GMM with 24 clusters. Panel (c) is the image classified by a GMMRF with 24 clusters trained using the image segmentation algorithm presented in Nguyen & Wu (2013). Notice the smoothness of this classification compared to the pixel-by-pixel approach shown in panel (b). 231

Figure 6.14 Mesh versus graph representation 232

Figure 6.15 An example of an inversion using structural rules dictated by the c -units Ising model. The following rule is implemented: 'The conductive unit and background cannot touch'. (a) True resistivity model; (b) model recovered with a Tikhonov approach; (c) model recovered with PGI and no structural rule; (d) model recovered with PGI and a GMMRF to implement the structural rule; the plot on the right shows the defined neighbourhood of a cell. 236

Figure A.1 GMM with various polynomial relationships: one linear (no addition required), one quadratic and one cubic. The 1D probability distribution for each physical property, and the respective histogram of each unit, are projected on the left and bottom panels. 259

Figure A.2 Linear joint inversions with various types of physical properties relationships (no trend, quadratic, cubic). Panels (a) to (c) show the inversion result with PGI using the known nonlinear relationships. The first panel (a) shows the result for the first problem, (b) for the second problem. The panel (c) shows the cross-plot of the models over the contour of the GMM with nonlinear relationships. Panels (d) to (f) show the result with PGI without nonlinear relationships. In panel (f), I show the used GMM without nonlinear relationships. Panels (g) to (i) show the Tikhonov inversions results and their cross-plot. . . . 261

Figure C.1 (a) magnetic PGI using the magnetic signature of PK/VK. Note that the recovered volume is much larger than the volume of PK/VK recovered from the gravity inversion with this unit density contrast (Figure 4.6c); (b) gravity PGI using the density contrast signature of HK. Note again the larger volume compared to Figure 4.6d. 271

Figure D.1 Results of the multi-physics PGI with petrophysical information and initialized with $\chi_{0,\text{grav}} = 0.72$ and $\chi_{0,\text{mag}} = 0.28$. (a) Plan map, east-west, and north-south cross-sections through the recovered density contrast model; (b) Plan map, east-west, and north-south cross-sections through the magnetic susceptibility contrast model; (c) Cross-plot of the inverted models. The colour of the points has been determined by the clustering obtained from this framework joint inversion process. In the background the prior joint petrophysical distribution; (d) Plan map, east-west, and north-south cross-sections through the resulting quasi-geology model. 273

Figure D.2 Results of the multi-physics PGI with petrophysical information and initialized with $\chi_{0,\text{grav}} = 0.2$ and $\chi_{0,\text{mag}} = 0.8$. a) Plan map, east-west, and north-south cross-sections through the recovered density contrast model; b) Plan map, east-west, and north-south cross-sections through the magnetic susceptibility contrast model; c) Cross-plot of the inverted models. The colour of the points has been determined by the clustering obtained from this framework joint inversion process. In the background the prior joint petrophysical distribution; d) Plan map, east-west, and north-south cross-sections through the resulting quasi-geology model. 274

Figure E.1	PGIs results for the Bookpurnong case study using various values of the confidence parameter ν in the prior variances. $\nu = 0.01, \nu = 0.1, \nu = 0.2$	276
Figure E.2	PGIs results for the Bookpurnong case study for various values of the confidence parameter ν in the prior variances. $\nu = 5, \nu = 10, \nu = 100$	277
Figure F.1	Density contrast models recovered from PGIs for the DO-27 case study for various values of the mean and variance of the density contrast for the PK-minor unit. The depth variance is equal to 200 m^2	280
Figure F.2	GMMs used to recover the models presented in Figure F.1.	281
Figure F.3	Density contrast models recovered from PGIs for the DO-27 case study for various values of the mean and variance of the density contrast for the PK-minor unit. The depth variance is equal to 100 m^2	282
Figure F.4	GMMs used to recover the models presented in Figure F.3.	283
Figure F.5	Density contrast models recovered from PGIs for the DO-27 case study for various values of the mean and variance of the density contrast for the PK-minor unit. The depth variance is equal to 50 m^2	284
Figure F.6	GMMs used to recover the models presented in Figure F.5.	285

Figure F.7	Density contrast models recovered from PGIs for the DO-27 case study for various values of the mean and variance of the density contrast for the PK-minor unit. The depth variance is equal to 20 m ²	286
Figure F.8	GMMS used to recover the models presented in Figure F.7.	287
Figure F.9	Density contrast models recovered from PGIs for the DO-27 case study for various values of the mean density and variance of the depth for the PK-minor unit. The density variance is equal to 0.01 (g/cm ³) ²	288
Figure F.10	GMMS used to recover the models presented in Figure F.9.	289
Figure F.11	Density contrast models recovered from PGIs for the DO-27 case study for various values of the mean density and variance of the depth for the PK-minor unit. The density variance is equal to 0.001 (g/cm ³) ²	290
Figure F.12	GMMS used to recover the models presented in Figure F.11.	291
Figure F.13	Density contrast models recovered from PGIs for the DO-27 case study for various values of the the mean density and variance of the depth for the PK-minor unit. The density variance is equal to 0.0001 (g/cm ³) ²	292
Figure F.14	GMMS used to recover the models presented in Figure F.13.	293

Figure F.15	Density contrast models recovered from PGIs for the DO-27 case study for various values of the variances of the density and depth for the PK-minor unit. The density mean is equal to -0.2 g/cm^3	294
Figure F.16	GMMS used to recover the models presented in Figure F.15.	295
Figure F.17	Density contrast models recovered from PGIs for the DO-27 case study for various values of the variances of the density and depth for the PK-minor unit. The depth variance is equal to -0.3 g/cm^3	296
Figure F.18	GMMS used to recover the models presented in Figure F.17.	297
Figure F.19	Density contrast models recovered from PGIs for the DO-27 case study for various values of the variances of the density and depth for the PK-minor unit. The depth variance is equal to -0.4 g/cm^3	298
Figure F.20	GMMS used to recover the models presented in Figure F.19.	299
Figure F.21	Density contrast models recovered from PGIs for the DO-27 case study for various values of the variances of the density and depth for the PK-minor unit. The depth variance is equal to -0.5 g/cm^3	300
Figure F.22	GMMS used to recover the models presented in Figure F.21.	301

Glossary

DC	Direct Current
DOI	Depth Of Investigation
EM	Expectation-Maximization
FCM	Fuzzy C-Means
FDEM	Frequency-Domain Electromagnetic
GMM	Gaussian Mixture Model
GMMRF	Gaussian Mixture Markov Random Field
HK	Hypabyssal Kimberlite
HMM	Hidden Markov Model
ICM	Iterative Conditional Modes
IGRF	International Geomagnetic Reference Field
IP	Induced Polarization
MAP	Maximum A Posteriori
MCMC	Markov Chain Monte Carlo

MLE	Maximum Likelihood Estimate
MRF	Markov Random Field
MT	Magnetotelluric
MVI	Magnetic Vector Inversion
PGI	Petrophysically and Geologically guided Inversion
PK	Pyroclastic Kimberlite
SIMPEG	Simulation and Parameter Estimation in Geophysics
TKC	Tli Kwi Cho
VK	Volcanoclastic Kimberlite
VTEM	Versatile Time Domain Electromagnetic

Acknowledgments

First and foremost, I want to thank my supervisor Douglas W. Oldenburg for giving me the opportunity to come back to academia and providing a stimulating and welcoming research environment. You allowed me to pursue a project I am still passionate about.

The UBC-GIF would not be what it is without its sponsors. In particular, I acknowledge Teck resources Ltd., especially Brendan Howe and Chad Hewson, and the CMIC project lead by Robert Lee for the Highland Valley site, which provided data and support that led to the development of this project. I am also grateful to Joel Jansen for his guidance with the Tli Kwi Cho (TKC) datasets, which aided the development and the application of the presented framework.

This study would not have been possible without the work of the SIMPEG community, all friends and colleagues. Especially, I thank Seogi Kang, my office mate, who guided me through the wonders of numerical modelling and encouraged me in my research; Lindsey J. Heagy for introducing me to the open-source initiative and providing feedback on this thesis; Dominique Fournier and Devin Cowan for all the valuable scientific discussions; Rowan Cockett for his inspirational spirit,

and Luz Angelica Caudillo-Mata for her inalterable positiveness.

I was very lucky to meet my friends Michael A. Mitchell, Michael P. Wathen, Anna Grau Galofre, Anna Mittelholtz, Gesa Meyer, and many others, who brought me on so many outdoor adventures and helped me enjoy my time in (and outside) Vancouver.

I am also very fortunate to have always been able to count on the support of my family, my father Pierre Astic, my mother Patricia Astic, my brother Joffrey Astic, his wife Goodness Astic and their child Armand Afumbom Astic, my sister Maëlle Astic, my grand-mothers Jacqueline Astic and Josette Béraldin, and my belated grand-father Albert Astic, who passed away in the last year of that Ph.D. To all of them, thank you so much for your support and for never doubting my choices.

Last but not least, I want to thank the love of my life, Marie-Pier Malouin, for crossing half the globe to move to Vancouver with me, and for her constant support in the highs and lows of graduate life.

And now, without further ado...

Chapter 1

Introduction

1.1 Motivation

Geophysics is an essential tool for imaging the subsurface and, therefore, has the potential to contribute to many practical problems. Whether the objective is to locate future exploration targets or characterize polluted areas of an aquifer (Figure 1.1, step 1), the key step of a geophysical study is first to identify the potential physical property contrasts occurring in the subsurface (Figure 1.1, step 2). Examples of such contrasts can be an increased electrical conductivity in saltwater compared to freshwater, a higher density in rocks rich in heavy minerals compared to their surroundings, etc. Physical property contrasts between subsurface bodies produce a physical response that can be measured remotely by geophysical instruments. Many types of geophysical methods exist, from measuring Earth's gravity field to detect local variations in density to exciting covered electrically conduc-

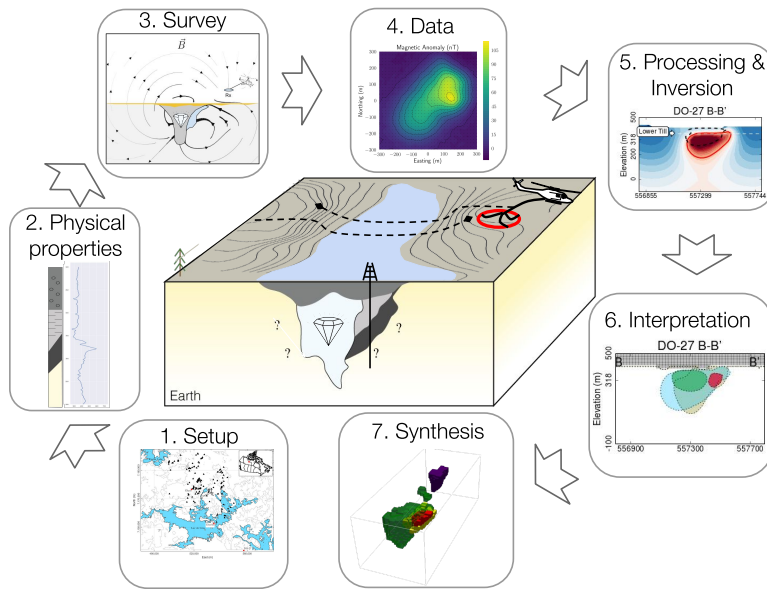


Figure 1.1: 7 steps procedure for applied geophysics.

tive bodies from an inductive loop carried by an aircraft. The type of physical property contrasts that characterizes the problem will determine which geophysical surveys can help resolve the geoscientific questions being asked (Figure 1.1, steps 3). Once the data are acquired (Figure 1.1, steps 4), the role of geophysics is to produce a geologically informative earth model whose spatial distribution of physical properties reproduces the measured signals (Figure 1.1, steps 5). The process of estimating a reasonable physical property model from geophysical data is known as the geophysical inverse problem (see for reference Oldenburg & Li (2005)). This physical property model can then be interpreted by professionals using expert knowledge (Figure 1.1, steps 6) and synthesized with other studies into meaningful information for geoscientists (Figure 1.1, steps 7). The latest steps, from data to synthesis, are the ones of interest in this thesis.

Retrieving an image from the underground is a highly non-unique problem for several reasons. Mainly, there are usually a lot more “pixels” in the image to recover than data. Moreover, the measurements suffer from uncertainties and could have a limited resolution due to either the survey layout or the geological configuration. The addition of *a priori* information in the geophysical inversion is necessary to obtain an informative image. If the subsurface structure is relatively well-known and can be described only by a few parameters (layers thickness, ellipses, etc.), a parametric approach can be taken to reduce the number of unknowns (Bosch & McGaughey, 2001; Fullagar et al., 2008; McMillan et al., 2015). On the other end, voxel-based inversion methods allow for more complexity in the earth model and parry the non-uniqueness by searching for an earth model with minimum structures and minimum deviation from a reference model, according to some metrics (Constable et al., 1987; Fournier & Oldenburg, 2019; Li & Oldenburg, 1994, 1996, 1998; Tarantola, 2005). In the next section, I illustrate the challenges of retrieving geologically meaningful information from voxel inversions through the motivational example of this thesis: the DO-27 diamondiferous kimberlite pipe.

1.1.1 Motivational example: the DO-27 case study

DO-27 is a diamondiferous kimberlite pipe, located in the Northwest Territories, Canada. Discovered thanks to an airborne geophysical survey in the 1992 (Jansen & Witherly, 2004), it has since been extensively studied with various geophysical methods (Devriese et al., 2017; Fournier et al., 2017; Kang et al., 2017a), offering

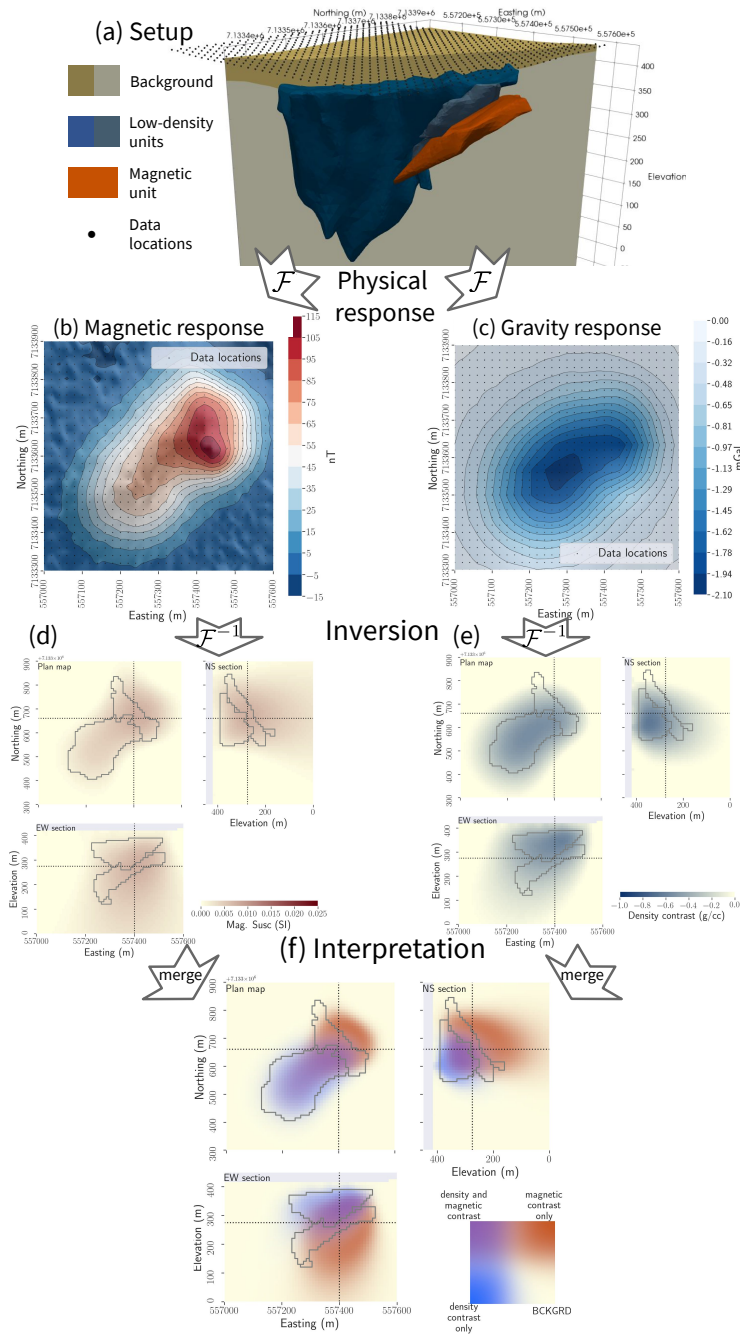


Figure 1.2: From setup to interpretation.

an excellent application case for developing new technology. Two main groups of kimberlite facies are found in the pipe (Figure 1.2a). The first group has low-density, compared to its surrounding, which results locally in a lower intensity of the Earth’s gravity field at the surface (Figure 1.2c); this is the diamondiferous target. The second group has an average density that is similar to that of the background, but is strongly magnetized and is responsible for most of the anomalous magnetic signal measured at the site (Figure 1.2b); it presents no mining potential. The goals of inverting the gravity and magnetic data are to differentiate the kimberlite rock units from the background and to distinguish between the potentially economic kimberlite facies (with a low-density) and the sterile ones (highly magnetized).

Throughout this thesis, I use the DO-27 diamondiferous kimberlite pipe as a motivational example to highlight gains made by the proposed inversion framework compared to the usual Tikhonov (least squares) voxel inversions (Constable et al., 1987; Tikhonov & Arsenin, 1977).

The Tikhonov inversion casts the geophysical inverse problem as an optimization problem in which an objective function Φ is minimized:

$$\underset{\mathbf{m}}{\text{minimize}} \quad \Phi(\mathbf{m}) = \Phi_d(\mathbf{m}) + \beta\Phi_m(\mathbf{m}). \quad (1.1)$$

In equation (1.1), the vector \mathbf{m} is the geophysical model, which represents physical properties on a mesh. A mesh is an ensemble of cells that tiles the volume of the underground that is being investigated; each cell represents a “pixel”

(in 1D, 2D, or 3D) of the discretized image of the subsurface. The term Φ_d is the geophysical data misfit; it measures the difference between the observed data and the signal predicted by the model \mathbf{m} . The term Φ_m , weighted by the trade-off parameter β , is the regularization. It handles the non-uniqueness of the data misfit problem by adding *a priori* information about the geophysical model, such as a reference model (the distance from the model to the reference is called the smallness), and enforcing minimum structures, through terms imposing smoothness. I present more details about the Tikhonov inverse problem in section 2.5.

Tikhonov inversions produce smooth results, which, although they reproduce the data, are often not geologically realistic. Smooth inverted magnetic susceptibility and density contrast models are shown in Figures 1.2d and 1.2e, respectively. Attempting to extract complex geological information from geophysical inversion can thus prove challenging, even with the required expert knowledge. While there is room for practitioners in the choice of the prior model and parameters, it can be difficult to relate the resulting models to some of the complex geological questions that are being asked: what is the depth of a unit? How much is it dipping? I illustrate the difficulty of recovering geological information from Tikhonov inversions in Figure 1.2f. Through the use of a 2D colourscale, I highlight how identifying geologic structures from the combination of the recovered density and magnetic susceptibility models will be highly dependent on the choice of thresholds. Moreover, a substantial volume of the subsurface, covering most of the diamondiferous unit, appears in the inverted models with both a low density and a high magnetic susceptibility (purple area); this is geologically incorrect and hinders the ability to

distinguish the two groups of kimberlite from each other.

A large improvement in the recovery of the subsurface structures, and a significant reduction in the uncertainty of the recovered features, can be achieved by incorporating petrophysical and geological information into the inversion of geophysical data. Prior information is also a key component to design coupling terms that link together various physical property models, which enables joint inversion of multiple geophysical surveys. This thesis contributes to this field of research on both aspects.

1.2 Literature review

1.2.1 Inclusion of prior information in inverse problems

The image of the underground retrieved from an inversion rarely includes petrophysical relationships or expected geologic features because these are not easily incorporated into traditional geophysical inversions. Since the early 2000s, there has been an increasing interest in including these types of information to obtain more realistic geological interpretations. When the geological bodies' geometries are well-known a priori, one can use a parametric formulation of the inverse problem that inverts for a limited set of values defining predetermined shapes of the geological bodies such as ellipses (McMillan et al., 2015) or geologic surfaces (Bosch & McGaughey, 2001; Fullagar et al., 2008). For voxel-based inversions, early works implemented strategies such as setting a reference model and preferential trends representative of the expected geology, or adding bound con-

straints to the geophysical model in the optimization process to narrow the range of possible physical properties in chosen areas (Lelièvre et al., 2009; Li & Oldenburg, 2000; Williams, 2008). Recent works now focus on including more complex non-geophysical datasets as part of the inversion, such as reproducing structural data (Wu, 2017), petrophysical characteristics (Bosch et al., 2009; Grana & Della Rossa, 2010; Sun & Li, 2015; Zhdanov & Lin, 2017) or geological training images (Lochbühler et al., 2015). Linde et al. (2015) and Moorkamp et al. (2016b) provide reviews of the current stage of research.

For the inclusion of petrophysical data as part of a voxel-based inversion, a growing class of frameworks has focused on using clustering techniques such as the Fuzzy C-Means (FCM) clustering algorithm. FCM was first used as part of an inversion in Paasche & Tronicke (2007) and later expanded in Lelièvre et al. (2012). This approach adds a clustering term to the objective function (equation (1.1)) that enforces the geophysical model to take values close to a limited set of expected physical property values. The resulting geophysical model is already classified into distinct geological units, whose properties have been set before the inversion. Further expansion of the method has been carried out by Sun & Li (2015). In addition to the FCM clustering term, they added an iterative update to the cluster centres, a technique they call guided FCM; this starts to introduce the notion of uncertainty for the petrophysical data. Grana & Della Rossa (2010) proposed a Bayesian approach for predicting lithological facies and fluid properties from rock-physics inversions by representing the petrophysical information as a predetermined Gaussian Mixture Model (GMM) prior and combining it with

seismic inversions. For linear 1D problems, Grana et al. (2017) built on this work by adding a first-order Hidden Markov Model (HMM) prior (Cappé et al., 2005) for their lithological classification to model its continuity. They took advantage of the linearity of their problems to sample from the posterior distribution efficiently. Giraud et al. (2017) focused on reducing uncertainties in a geological model obtained by stochastic modelling through a geophysical inversion using a fixed GMM to model the petrophysical information. To this end, they added, to the Tikhonov objective function (equation (1.1)), a sum of least-squares differences between the GMM probability distribution, evaluated at the current model, and reference values representing their prior knowledge. In Giraud et al. (2019b), they modified their formulation to work with a least-squares difference between the log-likelihood of the GMM and their reference values. In both formulations, they required extensive and fixed quantitative petrophysical and geological information. In practice, that information is not often available and might be only qualitative.

In this thesis, I propose a new way to include petrophysical and geological information in the inversion, represented with a GMM, that does not require additional terms in the least-squares formulation, and that can handle missing or qualitative information.

Another major advantage of including petrophysical or geological information in the geophysical inverse problem is to provide an avenue for defining relationships across geophysical models. These relationships constitute a coupling term, which is a necessary part for jointly inverting multiple geophysical datasets that otherwise rely on independent physical phenomena.

1.2.2 Coupling terms for multi-physics inversions

Generally, not all geological features of an area can be characterized through a single geophysical survey and a unique type of physical property contrasts. Building a “quasi-geology model” (Li et al., 2019) from multiple geophysical datasets involves either combining models from single-physics inversions or using a multi-physics inversion framework. The use of post-inversion classification to combine geophysical models and infer geological information has been widely used (Giuseppe et al., 2014; Kang et al., 2017a; Martinez & Li, 2015; Melo et al., 2017; Oldenburg et al., 1997; Paasche, 2016; Paasche et al., 2006). However, there are challenges in using this methodology. Geophysical inversion generally produces a smooth image of the Earth, and the details are dependent upon parameters in the inversion. Apparent inconsistencies between inverted models obtained by single-physics inversions can occur, such as areas with both low density and high magnetic susceptibility in our motivational example in section 1.1.1. Building a geologic model from these inversions also requires specifying thresholds and criteria to discriminate between rock units; these are subjective choices and need expert knowledge that can make post-inversion classification challenging for problems such as resource estimation. Multiple case studies have shown that multi-physics inversions can reveal information that was not accessible through individual geophysical dataset inversions (Doetsch et al., 2010; Jegen et al., 2009; Kamm et al., 2015; Lelièvre & Farquharson, 2016). An extensive compilation of methods and their applications can be found in Moorkamp et al. (2016b). Multi-physics inversions require a coupling term that mathematically describes a relationship be-

tween the different physical property models responsible for the geophysical data. Coupling methods generally use one or a combination of structural or physical property relationships.

The first frameworks for joint inversion focused on linking geophysical models through their structural similarities. Haber & Oldenburg (1997) defined the structure of a model in terms of the absolute value of its spatial curvature and compared different models to see if variations occurred at the same locations. Gallardo & Meju (2003) further developed this idea with the introduction of the concept of cross-gradient between geophysical models. This approach has become commonly used, and both Gallardo & Meju (2011) and Meju & Gallardo (2016) provide in-depth reviews of the method and its application. However, this strategy has several limitations: 1) Meju & Gallardo (2016) points out that “not all physical property distributions in the subsurface will be structurally coincident”; 2) it is unable to reproduce documented or expected petrophysical information (Sun & Li, 2017). These drawbacks can be overcome by other coupling methods.

The second coupling approach uses physical property relationships to link geophysical models. Some of the earliest works used experimental constitutive formulae as their physical properties constraint (Afnimar et al., 2002; Chen et al., 2007; Hoversten et al., 2006). De Stefano et al. (2011) combined this approach with the above mentioned cross-gradient method for sub-salt imaging. Moorkamp et al. (2011) compared the constitutive relationship and the cross-gradient approaches on a 3D synthetic example combining magnetotelluric, gravity and seismic data. They concluded that, overall, a cross-gradient approach was preferable

compared to using constitutive equations because deviations from the constitutive relations resulted in artifacts in the inverted models; in those situations, the cross-gradient method gave consistent satisfactory results. They also pointed out that the cross-gradient method relies on fewer assumptions about the models than the constitutive equations. Some stochastic frameworks have also been proposed that leverage geostatistical tools to define relationships between physical properties. Chen & Hoversten (2012) used a similar coupling approach as in Bosch (2004) (Moorkamp et al., 2016a) by building a rock-physics model from borehole data to jointly invert seismic and controlled-source electromagnetic data. Shamsipour et al. (2012) used the geostatistical techniques of cokriging and conditional simulation to jointly invert gravity and magnetic data assuming that the auto- and cross-covariances of the density and magnetic susceptibility follow a linear model of coregionalization. On the deterministic side, of which the framework I present belongs, recent frameworks use clustering techniques such as the FCM algorithm, which was first used in Paasche & Tronicke (2007) and further expanded in Lelièvre et al. (2012). This approach adds a clustering term to the objective function, which allows more flexible relationships between physical properties. Beyond the addition of the FCM term to the objective function, Sun & Li (2016) generalized their iterative update to the cluster centres, developed in Sun & Li (2015) for a single physical property, to consider multiple physical properties, and further in Sun & Li (2017), they added tools to their approach to consider various types of correlations between physical properties (linear, quadratic, etc.). Giraud et al. (2017, 2019b), mentioned in section 1.2.1, also used their formulation to

perform multi-physics inversions of gravity and magnetic data in their studies.

This thesis develops a framework to use quantitative or qualitative petrophysical and geological information as a coupling term for multi-physics inversions. Numerical strategies are devised for handling multiple geophysical surveys. Capabilities of the framework are demonstrated through the DO-27 case study.

1.3 Research objectives

The challenge of recovering meaningful geological information from multiple geophysical, petrophysical, and geological datasets is the main motivation of this thesis. Integrating various kinds of data into a single inverse problem helps build confidence in the recovered geologic features. Moreover, building a framework that relates the inversion process to geological knowledge (e.g. the number of distinct rock units) is a key step towards combining geophysical and geological modelling. For those purposes, I will focus on the following aspects:

- formulate a geophysical inverse problem that incorporates various petrophysical and geological information without adding extra terms to the objective function,
- design processes that allow the proposed inversion framework to be applied in areas where little to no quantitative *a priori* information about the physical properties is known,
- generalize the proposed approach to link multiple geophysical surveys that do not share the same underlying physics,

- apply the proposed framework to the DO-27 field datasets to improve the understanding of the geologic structures.

This thesis addresses these challenges by developing a new framework, named Petrophysically and Geologically guided Inversion (PGI), that generalizes concepts presented in previously published research. I use a GMM that represents the petrophysical and geological knowledge to regularize the geophysical inversion; this is analogous to the approach used by Grana & Della Rossa (2010). The idea of learning the physical properties mean values described in Sun & Li (2015) is formalized and extended to the covariance matrices and proportions of the GMM. At the same time, I can include the geological information in the GMM in a similar way as did Giraud et al. (2017). The GMM is then used as a coupling term to perform multi-physics inversion; this augments the approach proposed by Sun & Li (2016). I also add capabilities to model various types of physical properties correlations; this expands ideas presented in Sun & Li (2017). The developed tools are applied throughout the thesis to various field and synthetic examples to demonstrate their uses and impacts. Finally, I apply the complete suite of functionalities to the DO-27 kimberlite pipe (Northwest Territories, Canada) to distinguish the various facies present in the area and improve on the geologic models obtained either from drillholes or post-inversion classification.

1.4 Thesis arrangement

This thesis proceeds in the following way:

1.4.1 Background theory

Chapter 2 introduces the key probability concepts and vocabulary that are used throughout the thesis. I first present Bayesian probability concepts such as Bayes' theorem, Maximum Likelihood Estimate (MLE) and Maximum A Posteriori (MAP) estimate. Definitions of the univariate and multivariate Gaussian distributions, and various estimates of their parameters, are given. Finally, I present the geophysical inverse problem formulated as a Tikhonov inversion. I view it through a probabilistic lens to relate it to a MAP estimate of a posterior probability density distribution, before detailing the optimization method used in this thesis to solve the inverse problem.

1.4.2 Definition of the PGI framework

Chapter 3 focuses on the mathematical description of the proposed framework for a single-physics problem depending on a single physical property. I show how geological and petrophysical information can be linked in a voxel-based geophysical inversion through the smallness term of the objective function (equation (1.1)); this is done by replacing the Gaussian prior of the Tikhonov approach with a Gaussian Mixture Model (GMM) representing the petrophysical and geological knowledge. The smallness term can thus be interpreted as a misfit for the petrophysical and geological data. This allows me to define a natural met-

ric for determining an acceptable misfit between the geophysical model and the petrophysical and geological data. This misfit is similar to the geophysical data target misfit. I redesign the objective function and the iteration steps as a suite of cyclic optimization problems in which three separate MAP estimates are obtained using geophysical, petrophysical, and geological data, respectively. After each geophysical model update, the GMM's parameters (means, variances and proportions) are determined by the geophysical model and the expected characteristics of the lithologies through another optimization process using the Expectation-Maximization (EM) algorithm. I then classify the model cells into rock units according to the petrophysical and geological information. These two additional steps over the petrophysical and geological data result in a dynamic update of the reference model and associated weights and guide the inversion towards reproducing the expected petrophysical and geological characteristics. The resulting geophysical objective function does not require extra terms to include the additional petrophysical and geological information; this is an important distinction between my work and previous frameworks that carry out joint geophysical and petrophysical data inversion. I highlight different capabilities of my methodology by inverting Magnetotelluric (MT) and Direct Current (DC) resistivity data in 1D and 2D, respectively. Finally, I apply my framework to inverting airborne frequency domain data, acquired in Australia, for the detection and characterization of saline contamination of freshwater.

1.4.3 Multi-physics inversions

Chapter 4 extends the framework developed in chapter 3 to the case of multi-physics, multi-physical properties problems. This requires advancements in two areas. Firstly, an extension from a univariate to a multivariate analysis of the petrophysical data, and their inclusion within the inverse problem, is necessary. Secondly, the objective function that I define for the inverse problem is comprised of multiple data misfit terms: one for each geophysical survey and one for the petrophysical and geological information. Each of these misfit terms has its target value, which I seek to reach in the inversion. I address the practical issues of simultaneously inverting data from multiple surveys and finding a solution that acceptably reproduces each one, along with the petrophysical and geological information. To illustrate the efficacy of my approach, and the advantages of carrying out multi-physics inversions coupled with petrophysical and geological information, I invert synthetic gravity and magnetic data associated with the DO-27 kimberlite deposit. The kimberlite pipe contains two distinct facies embedded in a host rock. Inverting the datasets individually, even with petrophysical information, leads to a binary geologic model consisting of background or an undetermined kimberlite. A multi-physics inversion, with petrophysical information, differentiates between two main kimberlite facies of the pipe. Through that example, I also highlight the capabilities of the PGI framework to work with minimal quantitative prior information and formulate geologic assumptions. In those cases, the dynamic updates of the GMM allow me to perform multi-physics inversions by learning a suitable coupling term.

1.4.4 Case study: DO-27

In chapter 5, I apply the PGI framework to jointly invert the airborne and ground-based gravity and airborne magnetic field datasets acquired over the DO-27 kimberlite pipe. DO-27 is composed of three main kimberlite rock types in contact with each other and embedded in a granitic host rock covered by a thin layer of glacial till. The Pyroclastic Kimberlite (PK) facies, which is diamondiferous, and the Volcanoclastic Kimberlite (VK) facies have anomalously low density, due to their high porosity, and weak magnetic susceptibility. They are indistinguishable from each other based upon their gravity and magnetic responses. The Hypabyssal Kimberlite (HK) facies, which is not diamondiferous, has been identified as highly magnetic and remanent. Quantitative petrophysical signatures for each rock unit are obtained from sample measurements, such as the increasing density of the PK/VK unit with depth and the remanent magnetization of the HK unit, and represented as a GMM. This GMM guides the PGI towards generating a three dimensional quasi-geology model of the DO-27 kimberlite pipe with physical properties that both satisfies the geophysical datasets and the petrophysical signatures. Density and magnetization models recovered individually yield volumes that have physical properties combinations that do not conform to any known petrophysical characteristics of the rocks in the area. A multi-physics PGI addresses this problem by using the GMM as a coupling term but puts a volume of PK/VK unit at a location that is incompatible with geologic information from drillholes. In order to conform with that geological knowledge, an additional unit is introduced, PK-minor, which is petrophysically and geographically distinct from the main PK/VK

unit. This inversion produces a quasi-geology model that presents good structural locations of the diamondiferous PK unit and can be used to provide a resource estimate or decide the locations of future drillholes.

1.4.5 Discussions and conclusion

In chapter 6, I first develop several discussion topics. I identify cases where the PGI framework can encounter challenges and how they can be handled. I also carry out a sensitivity analysis for the newly introduced inversion parameters, using various examples previously developed throughout the thesis. I then provide a detailed comparison of the PGI formulation with other published frameworks for the inclusion of petrophysical information. Next, I present potential research directions that can build upon the implemented framework. The concept of non-localized petrophysical information is generalized to geological information and included in the current framework. Finally, I conclude with a discussion about the key components of the PGI framework and its implementation.

Chapter 2

Key concepts

This chapter introduces the key concepts and vocabulary specific to a probabilistic formulation of the geophysical inverse problem. I start by defining some of the notation conventions used throughout the thesis. I then present probabilistic estimation concepts for data fitting problems. The univariate and multivariate Gaussian distributions are defined and used to illustrate the previously introduced data fitting concepts. Those distributions are at the heart of this thesis, both to model the geophysical and petrophysical information. Finally, I show how the geophysical inverse problem can be expressed in a probabilistic formulation, under the assumption of Gaussian priors, as a posterior probability density function, and which type of solutions I choose to resolve it.

2.1 Notation conventions

When writing probability density distributions, I adopt the following notation:

- \mathcal{P} denotes any arbitrary probability distribution.
- $\mathcal{P}(A|B)$ denotes the probability distribution of a variable A , knowing or given the parameter B .
- $\mathcal{N}(\cdot|\boldsymbol{\mu}, \boldsymbol{\Sigma})$ denotes a Normal distribution, also named Gaussian, which is defined by its mean $\boldsymbol{\mu}$ and covariance matrix $\boldsymbol{\Sigma}$.

In terms of notation for linear algebra, I use the following conventions:

- Lowercase italic symbols are used for scalar values, such as the trade-off parameter β .
- Bold lowercase symbols designate vectors, such as the geophysical model \mathbf{m} .
- Bold uppercase symbols designate matrices, such as the weighting matrix \mathbf{W} .

For a multi-physics inversion, the geophysical model is likely to contain multiple physical properties. Several surveys might be associated with the same physical property (e.g. gravity and gravity gradiometry are both sensitive to density contrasts) or one survey might depend on several physical properties (e.g. electromagnetic surveys depend on both electrical conductivity and magnetic permeability). I thus adopt the following notations for the geophysical model \mathbf{m} indices:

$$\mathbf{m} = \text{vec}(\mathbf{M}), \quad (2.1)$$

$$\text{with } \mathbf{M} = \begin{pmatrix} m_{1,1} & m_{1,2} & \cdots & m_{1,q} \\ m_{2,1} & m_{2,2} & \cdots & m_{2,q} \\ \vdots & \vdots & \ddots & \vdots \\ m_{n,1} & m_{n,2} & \cdots & m_{n,q} \end{pmatrix}. \quad (2.2)$$

A row of the \mathbf{M} matrix represents all the q physical properties that live in the same location. A column represents a single physical property at all the n cells of the mesh. For clarity, I am consistent throughout this thesis with the index notation. The index i always refers to the cell number, from 1 to n . The vector \mathbf{m}_i then denotes all of the physical properties at the i^{th} cell:

$$\mathbf{m}_i = (m_{i,1}, m_{i,2}, \dots, m_{i,q})^\top. \quad (2.3)$$

Likewise, I denote the vector model for a single physical property on the whole mesh with the index $p \in \{1..q\}$ with a superscript:

$$\mathbf{m}^p = (m_{1,p}, m_{2,p}, \dots, m_{n,p})^\top. \quad (2.4)$$

Lastly, the model at iteration t of an inversion is denoted with parentheses $\mathbf{m}^{(t)}$.

2.2 Bayesian concepts

The mathematical definition of the framework proposed in this thesis relies on a statistical interpretation of the geophysical inverse problem. The probabilistic formulation of the geophysical inversion as a Bayesian problem was popularized by Tarantola in his book “*Inverse Problem Theory and Methods for Model Parameter Estimation*” (first published in 1987). Before I explain this link in section 2.5.2, I present in the current section the necessary Bayesian concepts, from Bayes’ theorem to the deterministic estimates of the solutions.

2.2.1 Bayes’ theorem

The joint probability of two events A and B occurring simultaneously can be determined as follow:

$$\mathcal{P}(A,B) = \mathcal{P}(A|B)\mathcal{P}(B) = \mathcal{P}(B|A)\mathcal{P}(A). \quad (2.5)$$

From the above, the Bayes’ theorem, which is at the foundation of Bayesian statistics, can be deduced (if $\mathcal{P}(B) > 0$):

$$\mathcal{P}(A|B) = \frac{\mathcal{P}(B|A)\mathcal{P}(A)}{\mathcal{P}(B)}. \quad (2.6)$$

In practice, the marginal likelihood $\mathcal{P}(B)$ is often ignored as it generally plays the role of a normalizing constant, leading to the most used form of the theorem:

$$\mathcal{P}(A|B) \propto \mathcal{P}(B|A)\mathcal{P}(A). \quad (2.7)$$

2.2.2 Likelihood and Maximum Likelihood Estimate

Geophysical data acquired during a survey measure a physical response due to physical property contrasts in the subsurface, affected by a certain level of environmental and instrumental random noise:

$$\mathbf{d}_{\text{obs}} = \mathbb{F}[\mathbf{m}_{\text{true}}] + \boldsymbol{\varepsilon}, \quad (2.8)$$

where \mathbf{d}_{obs} is the observed geophysical data, \mathbb{F} is the forward modelling operator of the survey method, \mathbf{m}_{true} is the true distribution of physical properties that produces the dataset, and $\boldsymbol{\varepsilon}$ is the noise affecting the data.

The goal of an inversion is to recover the spatial distribution of physical properties that gave rise to the measured data. How well the signal is reproduced by a model \mathbf{m} is measured by a likelihood function \mathcal{L} , which estimates the probability of the observations given the proposed model:

$$\mathcal{L}_{\mathbf{d}_{\text{obs}}}(\mathbf{m}) = \mathcal{P}(\mathbf{d}_{\text{obs}}|\mathbf{m}). \quad (2.9)$$

Defining the likelihood function directly relates to the assumed distribution of the noise. If the noise $\boldsymbol{\varepsilon}$ is a particular realization of a multivariate probability density distribution \mathcal{E} , then so is $(\mathbf{d}_{\text{obs}} - F[\mathbf{m}])$, thus:

$$\mathcal{L}_{\mathbf{d}_{\text{obs}}}(\mathbf{m}) = \mathcal{E}(\mathbf{d}_{\text{obs}} - F[\mathbf{m}]). \quad (2.10)$$

A first thought for finding a “best” model is to maximize the probability of the

residual ($\mathbf{d}_{\text{obs}} - F[\mathbf{m}]$). This means to maximize the likelihood of the realization \mathbf{d}_{obs} , given a geophysical model \mathbf{m} . This approach is called Maximum Likelihood Estimate (MLE).

$$\mathbf{m}_{\text{MLE}} = \underset{\mathbf{m}}{\operatorname{argmax}} \mathcal{P}(\mathbf{d}_{\text{obs}}|\mathbf{m}). \quad (2.11)$$

2.2.3 Prior distribution and Maximum A Posteriori estimate

The likelihood metric described in section 2.2.2 does not tell anything about the goodness of the model itself. Any model that fits the data is equally good in the above equation (2.11). This is an issue because in many geophysical applications, there is no unique solution. Moreover, not all models are equally useful, because the goal is to inform us about the true geologic structures that produce the signal rather than reproducing the geophysical response itself. While the true subsurface image is obviously unavailable for comparison with the recovered geophysical model, expected characteristics of a useful and informative model can be formulated. For example, one may believe that a spatially coherent model is more informative than one with numerous disconnected structures. Those beliefs need to be brought into a “goodness of a model” metric. The approach is thus not only to maximize the probability of the measured data \mathbf{d}_{obs} , but to also maximize the probability of \mathbf{m} , knowing the observed outcome \mathbf{d}_{obs} . The probability distribution of \mathbf{m} given \mathbf{d}_{obs} , denoted $\mathcal{P}(\mathbf{m}|\mathbf{d}_{\text{obs}})$, is called the Posterior distribution. To quantify this last distribution, *a priori* information on the model is required. This is encoded in a distribution $\mathcal{P}(\mathbf{m})$ that measures how likely is a given model according to expectations; this distribution is called a Prior. Using Bayes’ theorem

(equations (2.6) and (2.7)), the following relationship links Posterior, Likelihood and Prior distributions:

$$\underbrace{\mathcal{P}(\mathbf{m}|\mathbf{d}_{\text{obs}})}_{\text{Posterior}} = \frac{\mathcal{P}(\mathbf{d}_{\text{obs}}|\mathbf{m})\mathcal{P}(\mathbf{m})}{\mathcal{P}(\mathbf{d}_{\text{obs}})} \propto \underbrace{\mathcal{P}(\mathbf{d}_{\text{obs}}|\mathbf{m})}_{\text{Likelihood}} \underbrace{\mathcal{P}(\mathbf{m})}_{\text{Prior}}, \quad (2.12)$$

where $\mathcal{P}(\mathbf{d}_{\text{obs}})$ is the overall probability of the outcome \mathbf{d}_{obs} and serves as a normalizing constant.

The problem is now to maximize the probability of \mathbf{m} given the observed data \mathbf{d}_{obs} ; this is a Maximum A Posteriori (MAP) estimate:

$$\mathbf{m}_{\text{MAP}} = \underset{\mathbf{m}}{\text{argmax}} \mathcal{P}(\mathbf{d}_{\text{obs}}|\mathbf{m})\mathcal{P}(\mathbf{m}). \quad (2.13)$$

This approach implies there is a need to choose a prior for the geophysical model \mathbf{m} . This thesis focuses on defining such informative prior functions.

2.3 The univariate Gaussian distribution

The following derivations are based on Murphy (2012).

The univariate Gaussian distribution, often also called a Normal distribution and denoted \mathcal{N} , is defined as follow:

$$\mathcal{N}(x|\mu, \sigma^2) = \frac{1}{\sigma\sqrt{2\pi}} \exp\left(-\frac{1}{2} \frac{(x-\mu)^2}{\sigma^2}\right), \quad (2.14)$$

with μ the mean of the distribution and σ its standard deviation. The value σ^2 is called the variance of the distribution, and its inverse σ^{-2} is the precision.

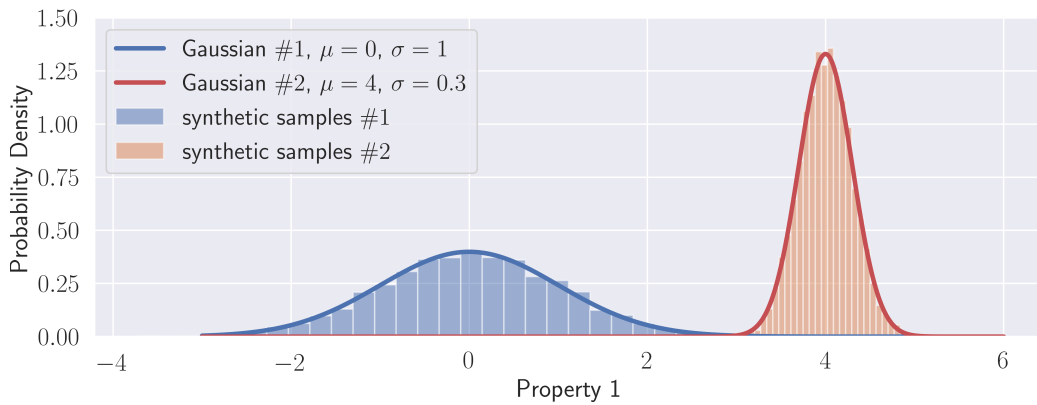


Figure 2.1: Two Gaussian distributions with different means and variances. The histograms represent a set of synthetic realizations sampled from the respective distributions.

The Gaussian distribution is the most widely used probability density distributions in statistics (Jaynes, 2003; Murphy, 2012). I show examples with various parameters in Figure 2.1. Many reasons explain the popularity of the Gaussian distribution. Thanks to the central limit theorem, it has been demonstrated that sums of independent random variables tend to Gaussian distributions as the number of variables increase. This property and its simple mathematical expression make it particularly easy to use and suited to model noise, as that phenomenon encompasses all effects that are not modelled (effect on the instrumentation of temperature or pressure changes, approximations in the positioning, etc.). The Gaussian distribution also has the property of being the distribution with maximum entropy, given a mean and a covariance; it makes the fewest assumptions about the true distribution. It is, thus, for many problems, a suitable prior distribution for continuous variables.

2.3.1 MLEs of the parameters of the Gaussian distribution

Let us consider a given dataset \mathbf{x} with s samples $\{x_i, i = 1..s\}$. To model \mathbf{x} by a Gaussian distribution, it is only necessary to obtain the mean and variance from the samples. The MLEs of these parameters are found by maximizing the likelihood function:

$$\mathcal{L}_{\mathbf{x}}(\mu, \sigma) = \prod_{i=1}^s \mathcal{N}(x_i | \mu, \sigma). \quad (2.15)$$

The resulting MLEs for the best fitting Gaussian distribution have closed-form formulae:

$$\mu_{\text{MLE}} = \bar{x} = \frac{1}{s} \sum_{i=1}^s x_i, \quad (2.16)$$

$$\sigma_{\text{MLE}}^2 = \sigma_{\mathbf{x}}^2 = \frac{1}{s} \sum_{i=1}^s (x_i - \bar{x})^2. \quad (2.17)$$

The MLEs of the Gaussian distribution parameters are thus just the experimental mean and variance of the samples. If prior information is available about the dataset, it is possible to incorporate it to obtain MAP estimates of these parameters.

2.3.2 MAP estimates of the parameters of the Gaussian distribution

To define MAP estimates of the Gaussian distribution parameters, I need to choose the prior distributions for the mean and variance. To this end, I turn to the concept of conjugate prior, which was first introduced in Raïffa & Schlaifer (1961). By definition, a prior is called a conjugate prior of the likelihood function if the posterior belongs to the same family of probability distributions as the prior. For

example, the Gaussian distribution is self-conjugate with regard to the mean. If the likelihood follows a Gaussian distribution, choosing a Gaussian prior for the mean ensures that the posterior distribution for the mean is also Gaussian.

MAP estimate for the mean

Let us define the prior distribution over the mean μ as a Gaussian distribution of mean μ_0 and variance $\kappa_0^{-1}\sigma_x^2$:

$$\mathcal{P}(\mu) = \mathcal{N}(\mu|\mu_0, \kappa_0^{-1}\sigma_x^2). \quad (2.18)$$

Then the posterior distribution over the mean is:

$$\mathcal{P}(\mu|\mathbf{x}, \sigma_x^2) \propto \mathcal{L}_x(\mu, \sigma_x^2) \mathcal{N}(\mu|\mu_0, \kappa_0^{-1}\sigma_x^2), \quad (2.19)$$

which is a univariate Gaussian distribution with mean μ_p and variance σ_p^2 :

$$\mathcal{P}(\mu|\mathbf{x}, \sigma_x^2) = \mathcal{N}(\mu|\mu_p, \sigma_p^2), \quad (2.20)$$

with:

$$\mu_p = \frac{s}{\kappa_0 + s} \bar{x} + \frac{\kappa_0}{\kappa_0 + s} \mu_0, \quad (2.21)$$

$$\sigma_p^2 = \frac{\sigma_x^2}{\kappa_0 + s}. \quad (2.22)$$

The MAP estimate of the mean given the dataset and the prior is thus μ_p . The conjugate prior acts on the estimation of the mean (equation (2.21)) as if there are κ_0 additional synthetic measurements with a mean μ_0 , sampled from the prior.

MAP estimate for the variance

A MAP estimate for the variance σ^2 can similarly be defined. The conjugate prior for the variance follows an Inverse-Gamma distribution \mathcal{G}^{-1} (equation (2.23)). This distribution, defined for positive values, represents the distribution of the reciprocal of a Gamma-distributed variable (the conjugate prior of the precision is thus the Gamma distribution). The Inverse-Gamma distribution takes two arguments, a scale parameter τ_0 that relates to the prior variance as I will show shortly, and a shape parameter ν_0 :

$$\mathcal{P}(\sigma^2) = \mathcal{G}^{-1}\left(\sigma^2 \mid \frac{\nu_0}{2}, \frac{\tau_0}{2}\right). \quad (2.23)$$

The posterior distribution for the variance parameter then follows an Inverse-Gamma distribution:

$$\mathcal{P}(\sigma^2 \mid \mathbf{x}, \bar{x}) = \mathcal{G}^{-1}\left(\sigma^2 \mid \frac{\nu_p}{2}, \frac{\tau_p}{2}\right), \quad (2.24)$$

with:

$$\nu_p = \nu_0 + s, \quad (2.25)$$

$$\tau_p = \tau_0 + s\sigma_{\mathbf{x}}^2. \quad (2.26)$$

The MAP estimate of the variance for the Gaussian distribution model, given the dataset and the prior, is thus the mode of that distribution:

$$\sigma_{\text{MAP}}^2 = \frac{\tau_0 + s\sigma_{\mathbf{x}}^2}{\nu_0 + s + 2} \quad (2.27)$$

The scale value τ_0 is similar to a variance multiplied by the number of observations. the value $s\sigma_x^2$ is the experimental scale. If the prior scale value is defined as $\tau_0 = (v_0 + 2)\sigma_0^2$, the MAP estimate then becomes:

$$\sigma_{\text{MAP}}^2 = \frac{s_0\sigma_0^2 + s\sigma_x^2}{s_0 + s}, \quad (2.28)$$

$$\text{with: } s_0 = v_0 + 2. \quad (2.29)$$

The conjugate prior acts on the estimation of the variance (equation (2.28)) as if there are $v_0 + 2$ new measurements to the dataset, with the same mean \bar{x} but with variance σ_0^2 .

Joint MAP estimate of the mean and covariance matrix

One can also consider using *a priori* information on both the mean and variance simultaneously. In that case, the prior distributions are not anymore independent of each other. Ignoring the dependency of the mean and variance priors by using the previous prior distributions (equations (2.18) and (2.23)) lead to the same MAP estimate as in equations (2.21) and (2.28). This approach is sometimes called a semi-conjugate prior or a conditional conjugate approach since the priors are then the conditional distributions $\mathcal{P}(\mu|\sigma^2)$ and $\mathcal{P}(\sigma^2|\mu)$:

$$\mathcal{P}(\mu|\sigma^2) = \mathcal{N}(\mu|\mu_0, \kappa_0^{-1}\sigma^2), \quad (2.30)$$

and:

$$\mathcal{P}(\sigma^2|\mu) = \mathcal{G}^{-1}\left(\sigma^2\left|\frac{v_0}{2}, \frac{\tau_0}{2}\right.\right). \quad (2.31)$$

The joint conjugate prior distribution for the mean and variance follows what is called a Normal-Inverse-Gamma distribution:

$$\mathcal{P}(\boldsymbol{\mu}, \sigma^2) = \mathcal{N}(\boldsymbol{\mu} | \boldsymbol{\mu}_0, \boldsymbol{\kappa}_0^{-1} \sigma^2, \sigma^2) \mathcal{G}^{-1}\left(\sigma^2 | \frac{v_0}{2}, \frac{\tau_0}{2}, \boldsymbol{\mu}\right). \quad (2.32)$$

The posterior distribution for the mean and variance then follow a Normal-Inverse-Gamma distribution:

$$\mathcal{P}(\boldsymbol{\mu}, \sigma^2 | \mathbf{x}) = \mathcal{N}(\boldsymbol{\mu} | \boldsymbol{\mu}_p, \boldsymbol{\kappa}_p^{-1} \sigma^2, \sigma^2) \mathcal{G}^{-1}\left(\sigma^2 | \frac{v_p}{2}, \frac{\tau_p}{2}, \boldsymbol{\mu}\right), \quad (2.33)$$

with:

$$\boldsymbol{\kappa}_p = \boldsymbol{\kappa}_0 + s, \quad (2.34)$$

$$v_p = v_0 + s, \quad (2.35)$$

$$\boldsymbol{\mu}_p = \frac{s}{s + \boldsymbol{\kappa}_0} \bar{\mathbf{x}} + \frac{\boldsymbol{\kappa}_0}{s + \boldsymbol{\kappa}_0} \boldsymbol{\mu}_0, \quad (2.36)$$

$$\tau_p = \tau_0 + s \boldsymbol{\sigma}_{\mathbf{x}}^2 + \frac{s \boldsymbol{\kappa}_0}{\boldsymbol{\kappa}_n} (\boldsymbol{\mu}_0 - \bar{\mathbf{x}})^2. \quad (2.37)$$

The joint MAP estimates of the variance and mean are thus the joint mode of that distribution. The joint MAP estimate for the mean is $\boldsymbol{\mu}_p$ (equation (2.36)). The joint MAP estimate for the variance is:

$$\sigma_p^2 = \operatorname{argmax}_{\sigma^2} \mathcal{P}(\boldsymbol{\mu}, \sigma^2 | \mathbf{x}) = \frac{\tau_p}{v_0 + s + 3}. \quad (2.38)$$

The values $\boldsymbol{\mu}_p$ and σ_p^2 are the joint MAP estimates of the Gaussian distribution model for fitting \mathbf{x} , given the priors. The conjugate prior acts as if synthetic sam-

ples, with mean μ_0 and variance σ_0^2 (assuming a chosen scale of $\tau_0 = (v_0 + 3)\sigma_0^2$), were added. The number of those synthetic measurements is dependent on both κ_0 and v_0 . The MAP estimate of the mean with the joint conjugate approach is identical to the estimate obtained by using a prior solely on the mean (equation (2.21)). The form of the MAP estimate of the variance is close to the one in equation (2.28). The joint MAP estimate of the variance is a normalized average of the prior τ_0 and observed $s\sigma_x^2$ scale values with an additional term to take into account the difference between the prior mean μ_0 and the observed mean \bar{x} . The estimation of the variance in equation (2.38) differs by one in the denominator compared to equation (2.37). This is because this is the MAP estimate of the joint distribution $\mathcal{P}(\mu, \sigma^2 | \mathbf{x})$ over μ and σ^2 rather than the MAP estimate of the marginal distribution $\mathcal{P}(\sigma^2 | \mathbf{x})$ over σ^2 alone.

I illustrate the concept of semi and joint conjugate priors in Figure 2.2. Let us consider the following setup, where there is a set of observations, represented through their histogram in blue. The Gaussian distribution in blue represents the MLE parameters (estimated without any a priori information). I now add a priori information in the form of a Gaussian distribution, in grey. I set the confidence parameters κ and v so that the prior and the observations have the same importance. The histogram of this prior synthetic samples set is also shown in grey.

The full conjugate prior approach can be understood as fitting a Gaussian distribution on the dataset formed by merging the observed and synthetic observations; this is represented in Figure 2.2 in red. The full conjugate MAP distribution, also in red, is well centred between the two observed and prior distributions as

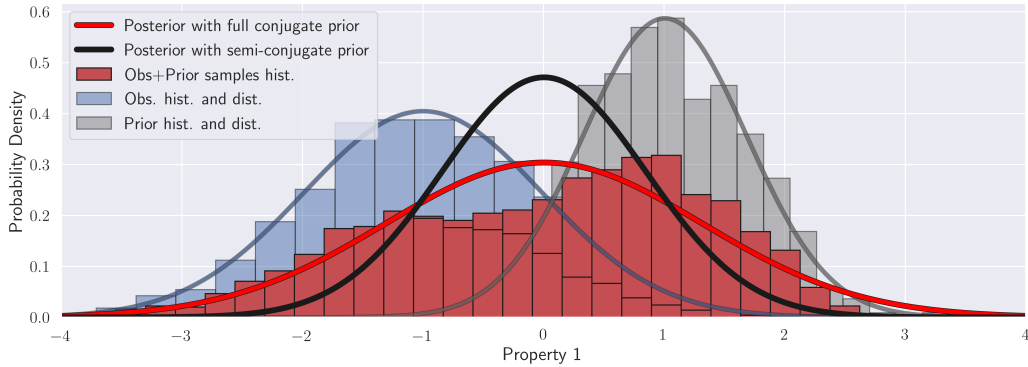


Figure 2.2: A comparison of the MLEs, semi-conjugate prior, and joint conjugate prior MAPs of the mean and variance for a single univariate Gaussian distribution. Observed samples are in blue, along with their estimated MLE Gaussian distribution, and the prior distribution is in grey. Using confidence values of unity in the prior is similar to having an equal number of samples from the prior and the observed data sets. A synthetic prior samples set is represented as the grey histogram. The posterior distribution with a semi-conjugate prior is in black and is seen as an average of the parameters of the observed and prior distributions. The posterior distribution with a joint conjugate prior is in red. The corresponding red histogram is obtained by merging the observed and synthetic prior samples. The variance is larger than for either of the two original distributions; this results because of the difference in the means. Legend: Hist. stands for histogram; Dist. stands for distribution; Obs. stands for observed samples.

expected, and so is the semi-conjugate distribution (in black) as the MAP mean estimates are the same for both priors. However, the variance of the red histogram, and thus of the posterior distribution with full conjugate prior, is higher than the variance of either the observed or prior distributions. This is due to the difference in the means of the two distributions, which the full conjugate prior approach accounts for (equations (2.37) and (2.38)). The semi-conjugate prior approach considers the means and variances independently (equations (2.30) and (2.31)).

2.4 The multivariate Gaussian distribution

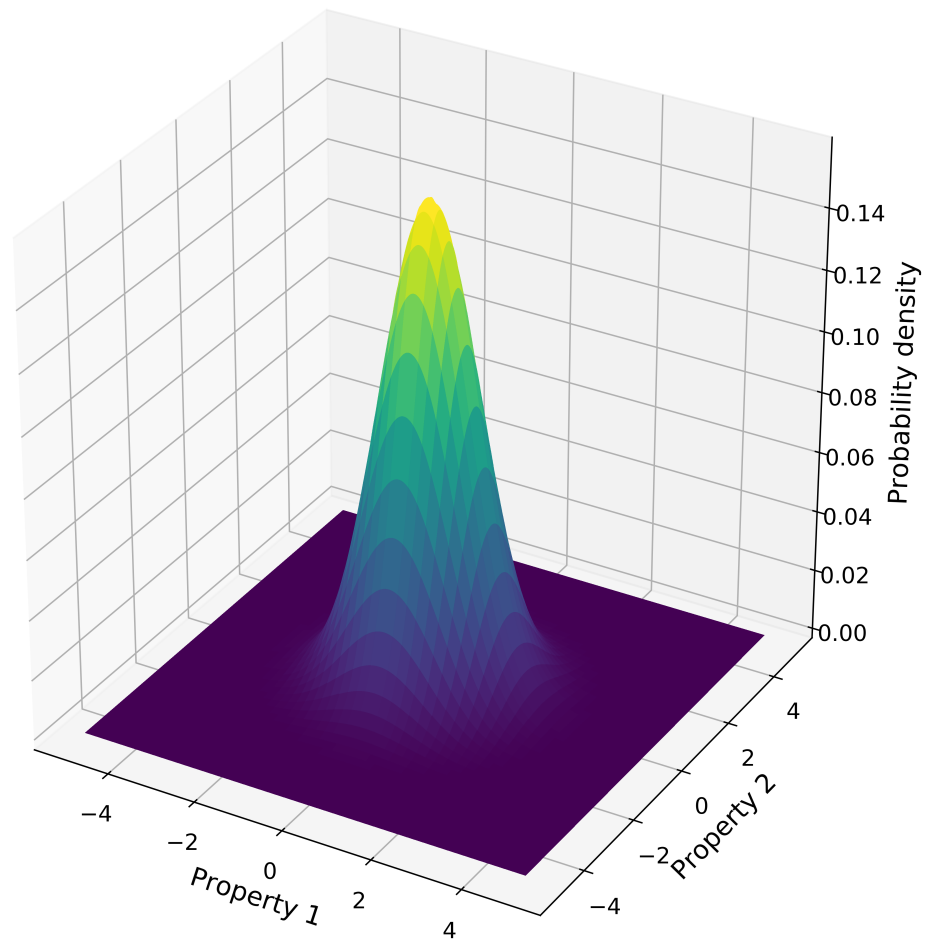


Figure 2.3: Two-dimensional Gaussian distribution.

The multivariate Gaussian distribution, denoted by \mathcal{N} , with mean $\boldsymbol{\mu}$ and covariance matrix $\boldsymbol{\Sigma}$ is defined by (with $\boldsymbol{\Sigma}^{-1/2}$ the upper triangular matrix from the Cholesky decomposition of the precision matrix $\boldsymbol{\Sigma}^{-1}$):

$$\mathcal{N}(\mathbf{x}|\boldsymbol{\mu}, \boldsymbol{\Sigma}) = \frac{\exp(-\frac{1}{2}\|\boldsymbol{\Sigma}^{-\frac{1}{2}}(\mathbf{x} - \boldsymbol{\mu})\|_2^2)}{\sqrt{(2\pi)^k \det(\boldsymbol{\Sigma})}}. \quad (2.39)$$

The multivariate Gaussian distribution generalizes the univariate Gaussian distribution to a multidimensional space. Its formulation can be obtained by applying an affine transformation ($f(\mathbf{x}) = \mathbf{A}\mathbf{x} + \mathbf{b}$) to a set of independent univariate Gaussian distributions. For a space with k dimensions, its mean $\boldsymbol{\mu}$ is a vector of size k , and its covariance matrix $\boldsymbol{\Sigma}$ is a positive-definite matrix of size $k \times k$. An example of a Gaussian distribution in a two-dimensional space is shown in Figure 2.3. Properties presented in section 2.3 are still valid and generalized here to a k -dimensional space. I again rely on derivations gathered in Murphy (2012).

2.4.1 MLEs for the mean and covariance matrix of the multivariate Gaussian distribution

Let us consider a database \mathbf{X} with s samples $\{\mathbf{x}_i, i = 1..s\}$, each with k features. A multivariate Gaussian distribution model can be fitted to represent this dataset.

The MLEs of the parameters for the best fitting multivariate Gaussian distribution are, as the univariate case, the experimental mean and covariance matrix:

$$\boldsymbol{\mu}_{\text{MLE}} = \bar{\mathbf{x}} = \frac{1}{s} \sum_{i=1}^s \mathbf{x}_i, \quad (2.40)$$

$$\boldsymbol{\Sigma}_{\text{MLE}} = \boldsymbol{\Sigma}_{\mathbf{X}} = \frac{1}{s} \sum_{i=1}^s (\mathbf{x}_i - \bar{\mathbf{x}})(\mathbf{x}_i - \bar{\mathbf{x}})^\top. \quad (2.41)$$

2.4.2 MAP estimates of the parameters of the multivariate Gaussian distribution

In this section, I show the generalization from a single dimension (section 2.3.2) to a multidimensional space of the MAP estimates for the mean, covariance and joint parameters, respectively.

MAP estimate of the mean of the multivariate Gaussian distribution

Let us define the prior distribution over the mean $\boldsymbol{\mu}$ as a multivariate Gaussian distribution of mean $\boldsymbol{\mu}_0$ and covariance matrix $\kappa_0^{-1} \boldsymbol{\Sigma}_{\boldsymbol{\mu}}$:

$$\mathcal{P}(\boldsymbol{\mu}) = \mathcal{N}(\boldsymbol{\mu} | \boldsymbol{\mu}_0, \kappa_0^{-1} \boldsymbol{\Sigma}_{\boldsymbol{\mu}}) \quad (2.42)$$

Then the posterior distribution over the mean can be written as a univariate Gaussian distribution with mean $\boldsymbol{\mu}_p$ and variance $\boldsymbol{\Sigma}_p$:

$$\mathcal{P}(\boldsymbol{\mu} | \mathbf{x}, \boldsymbol{\Sigma}_{\mathbf{X}}) = \mathcal{N}(\boldsymbol{\mu} | \boldsymbol{\mu}_p, \boldsymbol{\Sigma}_p), \quad (2.43)$$

with:

$$\boldsymbol{\Sigma}_p = (\kappa_0 \boldsymbol{\Sigma}_{\boldsymbol{\mu}}^{-1} + s \boldsymbol{\Sigma}_{\mathbf{X}}^{-1})^{-1}, \quad (2.44)$$

$$\boldsymbol{\mu}_p = \boldsymbol{\Sigma}_p (s \boldsymbol{\Sigma}_{\mathbf{X}}^{-1} \bar{\mathbf{x}} + \kappa_0 \boldsymbol{\Sigma}_{\boldsymbol{\mu}}^{-1} \boldsymbol{\mu}_0). \quad (2.45)$$

The MAP estimate of the mean given the dataset and the prior is thus $\boldsymbol{\mu}_p$ (equation (2.45)). This is a similar result as for the univariate case (equation (2.21)). The conjugate prior acts on the estimation of the mean (equation (2.45)) as if there are κ_0 additional synthetic measurements with mean $\boldsymbol{\mu}_0$ and covariance $\boldsymbol{\Sigma}_\mu$.

MAP estimate of the covariance matrix of the multivariate Gaussian distribution

The Gamma and Inverse-Gamma distributions are only defined in one dimension. In a multidimensional space, the covariance matrix conjugate prior distribution follows an Inverse-Wishart distribution \mathcal{W}^{-1} , which generalizes the Inverse-Gamma distribution and is defined for positive-definite matrices. In one dimension, the Inverse-Wishart distribution maps onto the Inverse-Gamma distribution:

$$\mathcal{W}^{-1}(\tau_0, \nu_0) = \mathcal{G}^{-1}\left(\frac{\nu_0}{2}, \frac{\tau_0}{2}\right). \quad (2.46)$$

The conjugate prior distribution for the covariance matrix takes two parameters, a prior scale matrix \mathbf{S}_0 and a shape scalar ν_0 :

$$\mathcal{P}(\boldsymbol{\Sigma}|\mathbf{X}, \bar{\mathbf{x}}) = \mathcal{W}^{-1}(\boldsymbol{\Sigma}|\mathbf{S}_0, \nu_0). \quad (2.47)$$

Then the posterior distribution over the covariance matrix can be written as an Inverse-Wishart distribution with parameters \mathbf{S}_p and ν_p :

$$\mathcal{P}(\boldsymbol{\Sigma}|\mathbf{X}, \bar{\mathbf{x}}) = \mathcal{W}^{-1}(\boldsymbol{\Sigma}|\mathbf{S}_p, \nu_p), \quad (2.48)$$

with:

$$\nu_p = \nu_0 + s, \quad (2.49)$$

$$\mathbf{S}_p = \mathbf{S}_0 + s\boldsymbol{\Sigma}_{\mathbf{x}}. \quad (2.50)$$

The MAP estimate of the variance for the Gaussian distribution model, given the dataset and the prior, is thus the mode of that distribution:

$$\boldsymbol{\Sigma}_{\text{MAP}} = \frac{\mathbf{S}_0 + s\boldsymbol{\Sigma}_{\mathbf{x}}}{\nu_0 + s + k + 1}. \quad (2.51)$$

If I define the scale matrix as $\mathbf{S}_0 = (\nu_0 + k + 1)\boldsymbol{\Sigma}_0$, the MAP estimate becomes:

$$\boldsymbol{\Sigma}_{\text{MAP}} = \frac{s_0\boldsymbol{\Sigma}_0 + s\boldsymbol{\Sigma}_{\mathbf{x}}}{s_0 + s}, \quad (2.52)$$

$$\text{with: } s_0 = \nu_0 + k + 1. \quad (2.53)$$

The MAP estimate is again the sum of the scale matrices normalized by the number of observations and the strength of the prior.

Joint MAP estimate of the mean and covariance matrix

The results from section 2.3 are also generalized in k dimensions for the joint MAP estimate of the mean and covariance matrix. I only present here the joint conjugate prior, but the same observations as in one dimension apply for the multivariate

semi-conjugate prior.

The joint conjugate prior distribution follows a Normal-Inverse-Wishart distribution with the following parameters:

$$\mathcal{P}(\boldsymbol{\mu}, \boldsymbol{\Sigma} | \mathbf{x}) = \mathcal{N}(\boldsymbol{\mu} | \boldsymbol{\Sigma}, \boldsymbol{\mu}_0, \kappa_0^{-1} \boldsymbol{\Sigma}) \mathcal{W}^{-1}(\boldsymbol{\Sigma} | \mathbf{S}_0, \nu_0, \boldsymbol{\mu}). \quad (2.54)$$

The Posterior distribution then also follow a Normal-Inverse-Wishart distribution:

$$\mathcal{P}(\boldsymbol{\mu}, \boldsymbol{\Sigma} | \mathbf{X}) = \mathcal{N}(\boldsymbol{\mu} | \boldsymbol{\Sigma}, \boldsymbol{\mu}_p, \kappa_p^{-1} \boldsymbol{\Sigma}) \mathcal{W}^{-1}(\boldsymbol{\Sigma} | \mathbf{S}_p, \nu_p, \boldsymbol{\mu}), \quad (2.55)$$

with:

$$\nu_p = \nu_0 + s, \quad (2.56)$$

$$\kappa_p = \kappa_0 + s, \quad (2.57)$$

$$\boldsymbol{\mu}_p = \frac{s}{\kappa_0 + s} \bar{\mathbf{x}} + \frac{\kappa_0}{\kappa_0 + s} \boldsymbol{\mu}_0, \quad (2.58)$$

$$\mathbf{S}_p = \mathbf{S}_0 + s \boldsymbol{\Sigma}_{\mathbf{x}} + \frac{\kappa_0 s}{\kappa_0 + s} (\bar{\mathbf{x}} - \boldsymbol{\mu}_0)(\bar{\mathbf{x}} - \boldsymbol{\mu}_0)^\top. \quad (2.59)$$

The vector $\boldsymbol{\mu}_p$ is the joint MAP estimate for the mean. The joint MAP estimate of the variance for the Gaussian distribution model, given the dataset and the prior, is the mode of the joint distribution:

$$\boldsymbol{\Sigma}_{\text{MAP}} = \frac{\mathbf{S}_p}{\nu_0 + s + k + 2}. \quad (2.60)$$

2.5 Tikhonov inversion and its probabilistic expression

During a geophysical survey, a physical response due to subsurface physical property contrasts is remotely measured. From the data, the goal of a geophysical inversion is to provide information about the underground structures. In this section, I present a mathematical formulation of the geophysical inversion as a least-squares minimization problem, its links to a MAP estimate of a posterior distribution, and how it can be solved using second-order gradient-based optimization methods.

2.5.1 The geophysical inverse problem

The geophysical inverse problem is posed as an optimization process where the goal is to find a geophysical model \mathbf{m} , which represents physical properties on a mesh, that minimizes an objective function Φ . Using the same formulation as in Oldenburg & Li (2005), the geophysical optimization problem takes the form:

$$\begin{aligned} \underset{\mathbf{m}}{\text{minimize}} \quad & \Phi(\mathbf{m}) = \Phi_d(\mathbf{m}) + \beta\Phi_m(\mathbf{m}), \\ \text{such that} \quad & \Phi_d(\mathbf{m}) \leq \Phi_d^*, \end{aligned} \tag{2.61}$$

where the term Φ_d is the data misfit, Φ_m is the model regularization function, and β is a positive scalar that adjusts the relative weighting between the two terms. A value of β is sought so that the data misfit Φ_d is below an acceptable target misfit Φ_d^* (Parker, 1977).

The geophysical data misfit $\Phi_d(\mathbf{m})$ is defined using a least-squares norm:

$$\Phi_d(\mathbf{m}) = \frac{1}{2} \|\mathbf{W}_d(\mathbb{F}[\mathbf{m}] - \mathbf{d}_{\text{obs}})\|_2^2, \quad (2.62)$$

where the matrix \mathbf{W}_d contains the information about the data uncertainties, assuming an unbiased Gaussian noise, as I show in section 2.5.2. If the noise is considered uncorrelated across data, \mathbf{W}_d then becomes a diagonal matrix with elements ε_p^{-1} where ε_p is the standard deviation for the p^{th} datum.

The regularization term contends with the non-uniqueness of the inverse problem. Here I decompose it as:

$$\Phi_m(\mathbf{m}) = \alpha_s \Phi_s(\mathbf{m}) + \sum_{v \in \{x,y,z\}} \alpha_v \Phi_v(\mathbf{m}), \quad (2.63)$$

where Φ_s is the smallness term; it enforces similarity between the model \mathbf{m} and a reference model \mathbf{m}_{ref} that represents the state of knowledge about the area before inversion (equation (2.64)). The smoothness terms $\{\Phi_v\}$ are designed to penalize roughness of the geophysical model along the $\{x,y,z\}$ directions. The scaling parameters $\{\alpha\}$ weight the different parts of the regularization function. An extensive interpretation and usages of these various parameters can be found in Lelièvre et al. (2009) and Williams (2008).

Both smallness and smoothness are important in my work, but the smallness term will play a dynamic role. My goal is to constrain the value that can be possibly taken by each cell of the model. The smallness term is thus the one

of particular interest here (whereas the smoothness terms constrain the transition from one cell to another). The smallness term is defined as:

$$\Phi_s(\mathbf{m}) = \frac{1}{2} \|\mathbf{W}_s(\mathbf{m} - \mathbf{m}_{\text{ref}})\|_2^2, \quad (2.64)$$

where the matrix \mathbf{W}_s expresses a certain level of confidence in the reference model locally. At locations in the model domain where \mathbf{W}_s is large, the differences between the recovered model and the reference model are highly penalized and vice versa.

2.5.2 Probabilistic expression of the inverse problem

The same objective function as in equation (2.61) can equivalently be expressed as a posterior probability density distribution $\mathcal{P}(\mathbf{m}|\mathbf{d}_{\text{obs}})$ (Tarantola, 2005). This posterior distribution (equation (2.65)), such as defined by the Bayes' theorem (section 2.2.1), is proportional to a likelihood distribution $\mathcal{P}(\mathbf{d}_{\text{obs}}|\mathbf{m})$, representing the data misfit, times a prior distribution $\mathcal{P}(\mathbf{m})$ over the geophysical model (equation (2.66)) that represents the knowledge on the geophysical model such as a reference model, a certain level of smoothness etc.:

$$\mathcal{P}(\mathbf{m}|\mathbf{d}_{\text{obs}}) \propto \mathcal{P}(\mathbf{d}_{\text{obs}}|\mathbf{m}) \mathcal{P}(\mathbf{m}), \quad (2.65)$$

with:

$$\mathcal{P}(\mathbf{m}) = \mathcal{P}_s(\mathbf{m}) \mathcal{P}_{\{x,y,z\}}(\mathbf{m}). \quad (2.66)$$

Going from a posterior distribution to an objective function is done by taking the negative natural logarithm of the posterior. Maximizing the posterior distribution is then equivalent to minimizing its negative logarithm. Thus, the geophysical model \mathbf{m} that maximizes the posterior distribution (the MAP estimate) also minimizes the objective function.

In a Tikhonov inversion, the data misfit and regularizer are generally expressed as least-squares (equations (2.62) and (2.64)). This translates into multivariate Gaussian distributions for the terms of the posterior distribution (see Figure 2.4a for a unidimensional example of a Gaussian distribution with its quadratic counterpart). Indeed, taking the negative logarithm of a multivariate Gaussian distribution (equation (2.39)) gives:

$$-\log(\mathcal{N}(\mathbf{m}|\boldsymbol{\mu}, \boldsymbol{\Sigma})) = \frac{1}{2}\|\boldsymbol{\Sigma}^{-\frac{1}{2}}(\mathbf{m} - \boldsymbol{\mu})\|_2^2 + \log\left(\sqrt{(2\pi)^k \det(\boldsymbol{\Sigma})}\right). \quad (2.67)$$

The first term obtained in equation (2.67) is recognizable as a least-squares misfit. The second term is a constant independent of \mathbf{m} . As constants do not play any role in the minimization of the objective function, it is discarded.

In this context, likelihood and data misfit are equivalent. The least-squares data misfit term in equation (2.62) can thus be expressed as a multivariate Gaussian distributions of mean $\mathbf{0}$ and covariance matrix $(\mathbf{W}_d^\top \mathbf{W}_d)^{-1}$ that characterize the noise (unbiased Gaussian noise, see equation (2.10)):

$$\mathcal{P}(\mathbf{d}_{\text{obs}}|\mathbf{m}) = \mathcal{E}(F[\mathbf{m}] - \mathbf{d}_{\text{obs}}) = \mathcal{N}([\mathbb{F}[\mathbf{m}] - \mathbf{d}_{\text{obs}}]|\mathbf{0}, (\mathbf{W}_d^\top \mathbf{W}_d)^{-1}). \quad (2.68)$$

Similarly, the prior distribution and the regularizer are equivalent. The smallness term in equation (2.64) can be obtained from a prior multivariate Gaussian distribution \mathcal{P}_s . Its mean is the reference model \mathbf{m}_{ref} and its covariance matrix is the weighting matrix $(\beta \alpha_s \mathbf{W}_s^\top \mathbf{W}_s)^{-1}$:

$$\mathcal{P}_s(\mathbf{m}) = \mathcal{N}(\mathbf{m} | \mathbf{m}_{\text{ref}}, (\beta \alpha_s \mathbf{W}_s^\top \mathbf{W}_s)^{-1}). \quad (2.69)$$

Finally, the smoothness terms can be expressed as multivariate Gaussian distribution over the derivatives of the geophysical model:

$$\mathcal{P}_v(\mathbf{m}) = \mathcal{N}(\mathbf{L}_v \mathbf{m} | \mathbf{L}_v \mathbf{m}_{\text{ref}}, (\beta \alpha_v \mathbf{W}_v^\top \mathbf{W}_v)^{-1}), \text{ for } v \in \{x, y, z\}, \quad (2.70)$$

where the finite difference operator \mathbf{L}_v represents the first or second derivatives in the v -direction, and the matrices $\{\mathbf{W}_v\}$ contain the weights applied to the respective derivatives. Including the reference model in the smoothness terms to favour interfaces in the recovered model is often optional, and the choice depends on the situation and the state of *a priori* knowledge. If a reference model is not included in the smoothness terms, the mean of the multivariate Gaussian distribution is simply $\mathbf{0}$. By default, in this thesis, the smoothness terms do not include a reference model, unless stated otherwise.

The Tikhonov objective function in equation (2.61) is obtained by applying the negative natural logarithm to the posterior distribution in equation (2.65), with the likelihood defined in equation (2.68) and priors given in equations (2.69) and (2.70). The summation form is simply a consequence of the fundamental prop-

erty of the logarithm function, the multiplication becomes an addition in this new space. It follows:

$$\Phi(\mathbf{m}) = -\log(\mathcal{P}(\mathbf{m}|\mathbf{d}_{\text{obs}})) \quad (2.71)$$

$$\begin{aligned} \Phi(\mathbf{m}) = & \frac{1}{2} \|\mathbf{W}_d(\mathbb{F}[\mathbf{m}] - \mathbf{d}_{\text{obs}})\|_2^2 + \frac{\beta\alpha_s}{2} \|\mathbf{W}_s(\mathbf{m} - \mathbf{m}_{\text{ref}})\|_2^2 + \\ & \sum_{v \in \{x,y,z\}} \frac{\beta\alpha_v}{2} \|\mathbf{W}_v \mathbf{L}_v(\mathbf{m} - \mathbf{m}_{\text{ref}})\|_2^2 + \text{Constant}, \end{aligned} \quad (2.72)$$

where the constant term in equation (2.72) contains the constant terms for each Gaussian distribution and the constant term $\log(\mathcal{P}(\mathbf{d}_{\text{obs}}))$.

This completes the operations to go from a posterior distribution to an objective function formulation of the Tikhonov inverse problem.

The factor $\{\beta\alpha\}$ expresses the confidences in the various priors (equations (2.69) and (2.70)). Increasing the value of $\{\beta\alpha\}$ is equivalent to reducing the variance around the reference model (or its derivatives). This is illustrated in Figure 2.5. For example, for the smallness, raising the value of $\beta\alpha_s$ forces the solution to become closer to the reference model by increasing the strength of the prior:

$$\mathcal{P}_s(\mathbf{m}) = \mathcal{N}(\mathbf{m}|\mathbf{m}_{\text{ref}}, (\beta\alpha_s \mathbf{W}_s^T \mathbf{W}_s)^{-1}), \quad (2.73)$$

or equivalently:

$$\mathcal{P}_s(\mathbf{m}) \propto \mathcal{N}(\mathbf{m}|\mathbf{m}_{\text{ref}}, (\mathbf{W}_s^T \mathbf{W}_s)^{-1})^{\beta\alpha_s}. \quad (2.74)$$

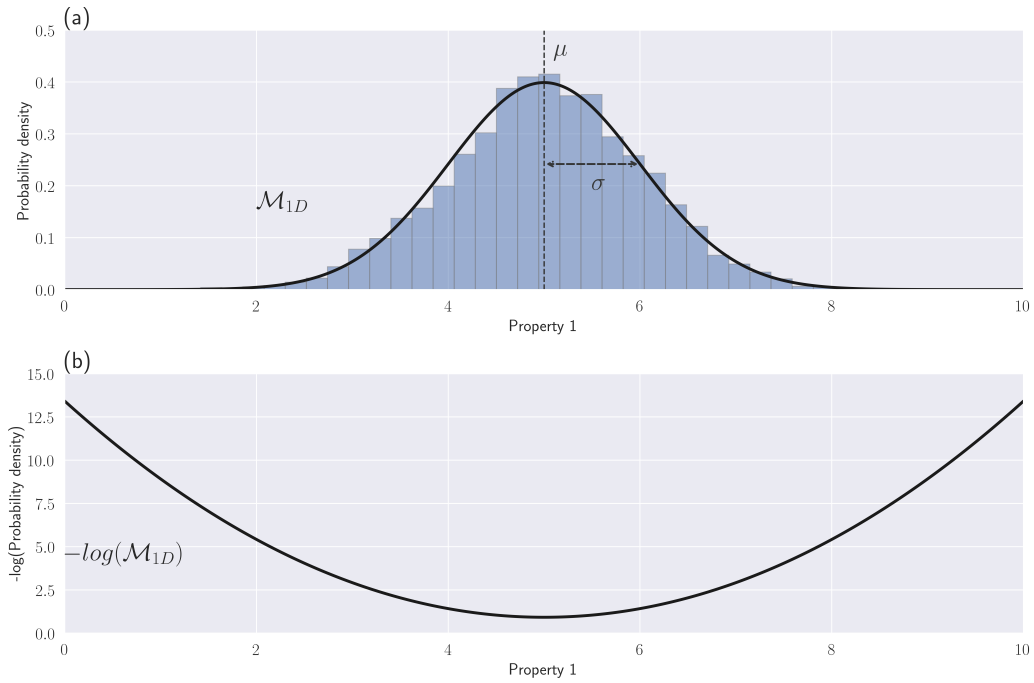


Figure 2.4: (a) Example of a Gaussian distribution in 1D for one physical property and (b) its quadratic negative-log equivalent.

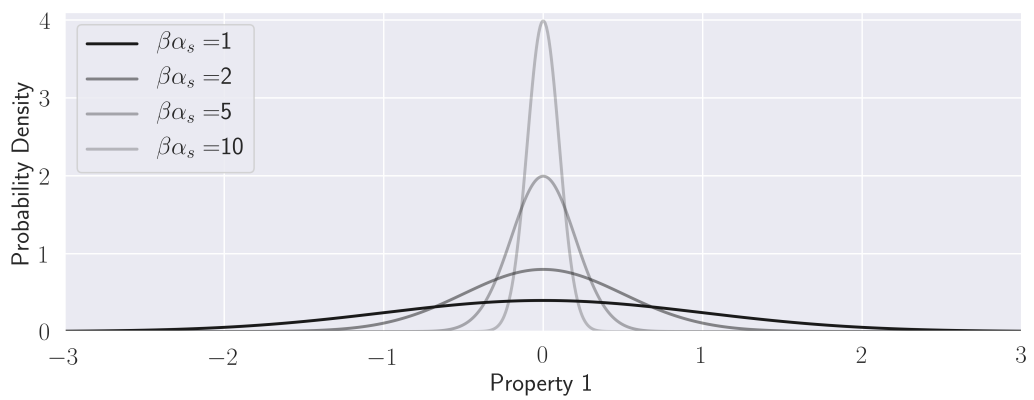


Figure 2.5: Gaussian distributions for various $\beta\alpha_s$ values.

2.5.3 Target value for the data misfit term

I stated in equation (2.61) that a geophysical model reasonably fits the data once its data misfit term (equation (2.62)) is below a target value Φ_d^* . In section 2.5.2, I showed that, in the data misfit term, $(\mathbb{F}[\mathbf{m}] - \mathbf{d}_{\text{obs}})$ follows a multivariate Gaussian distribution of mean $\mathbf{0}$ and covariance matrix $(\mathbf{W}_d^\top \mathbf{W}_d)^{-1}$ (equation (2.68)). Thus, each element in $\{[\mathbf{W}_d(\mathbb{F}[\mathbf{m}] - \mathbf{d}_{\text{obs}})]_l, l = 1..d\}$, with d the number of data, follows a univariate Gaussian distribution of mean 0 and variance 1, and their sum of squares follow a Chi-square distribution. Applying Pearson's chi-square test (Pearson, 1900), I define the target as the expected value of the data misfit, for a geophysical model whose residuals fit the distribution of the noise (Parker, 1977):

$$\Phi_d^* = \mathbb{E}[\Phi_d] = \frac{d}{2}, \quad (2.75)$$

2.5.4 Solving the geophysical inverse problem

The goal is to find a geophysical model \mathbf{m} that minimizes the objective function Φ (equation (2.61)). For conciseness, I only show the case where the reference model is in the smoothness terms; the derivation can be easily repeated without it.

At its minimum, the gradients \mathbf{g} of the function Φ with respect to \mathbf{m} are null:

$$\mathbf{g}(\mathbf{m}_{\text{MAP}}) = \nabla \Phi(\mathbf{m}_{\text{MAP}}) = \frac{\partial \Phi}{\partial \mathbf{m}}(\mathbf{m}_{\text{MAP}}) = \mathbf{0}. \quad (2.76)$$

The problem to be solved is thus:

$$\mathbf{J}_m^\top \mathbf{W}_d^\top \mathbf{W}_d (\mathbb{F}[\mathbf{m}] - \mathbf{d}_{\text{obs}}) + \beta \mathbf{W}_m^\top \mathbf{W}_m (\mathbf{m} - \mathbf{m}_{\text{ref}}) = \mathbf{0}, \quad (2.77)$$

with:

$$\mathbf{J}_m = \frac{\partial \mathbb{F}[\mathbf{m}]}{\partial \mathbf{m}}, \quad (2.78)$$

$$\mathbf{W}_m^\top \mathbf{W}_m = \alpha_s \mathbf{W}_s^\top \mathbf{W}_s + \sum_{v \in \{x,y,z\}} \alpha_v \mathbf{L}_v^\top \mathbf{W}_v^\top \mathbf{W}_v \mathbf{L}_v. \quad (2.79)$$

\mathbf{J}_m is called the Jacobian, or sensitivity, matrix (McGillivray & Oldenburg, 1990).

The problem presented in equation (2.77) can be solved iteratively using second-order methods. Those methods compute successive $\delta \mathbf{m}$ perturbations of an initial model that get closer to a local minimum. Such methods rely on the Hessian matrix (second-order partial derivatives) of the objective function:

$$\mathbf{H}_m = \nabla^2 \Phi(\mathbf{m}) = \mathbf{J}_m^\top \mathbf{W}_d^\top \mathbf{W}_d \mathbf{J}_m + \mathbf{A}(\mathbf{m}) + \beta \mathbf{W}_m^\top \mathbf{W}_m, \quad (2.80)$$

with:

$$A_{i,j} = \sum_{l=1}^d r_l \frac{\partial^2 r_l}{\partial m_i \partial m_j}, \quad (2.81)$$

and:

$$\mathbf{r} = \mathbf{W}_d (\mathbb{F}[\mathbf{m}] - \mathbf{d}_{\text{obs}}). \quad (2.82)$$

The term \mathbf{A} is often hard to compute, but it is null for linear forward operators \mathbb{F} . The Gauss-Newton optimization method uses an approximation of the Hessian matrix that ignores that term; it assumes the problem is only “mildly nonlinear”

(see Ascher & Greif (2011) and Haber (2014) for discussions on the subject):

$$\left(\mathbf{J}_m^\top \mathbf{W}_d^\top \mathbf{W}_d \mathbf{J}_m + \beta \mathbf{W}_m^\top \mathbf{W}_m \right)_{i,j} \gg A_{i,j}, \quad \forall \{i, j\}, \quad (2.83)$$

thus:

$$\mathbf{H} \approx \tilde{\mathbf{H}} = \mathbf{J}_m^\top \mathbf{W}_d^\top \mathbf{W}_d \mathbf{J}_m + \beta \mathbf{W}_m^\top \mathbf{W}_m, \quad (2.84)$$

which allows me to consider the linearized problem at \mathbf{m} to find $\delta \mathbf{m}$:

$$\underset{\delta \mathbf{m}}{\text{minimize}} \Phi(\mathbf{m} + \delta \mathbf{m}), \quad (2.85)$$

with:

$$\mathbb{F}[\mathbf{m} + \delta \mathbf{m}] \approx \mathbb{F}[\mathbf{m}] + \mathbf{J}_m \delta \mathbf{m}, \quad (2.86)$$

$$\text{and } \mathbf{J}_m \approx \mathbf{J}_{m+\delta m}. \quad (2.87)$$

This results in the following system to find a descent direction $\delta \mathbf{m}$ for $\Phi(\mathbf{m})$:

$$\frac{\partial \Phi(\mathbf{m} + \delta \mathbf{m})}{\partial \delta \mathbf{m}} = \mathbf{0}, \quad (2.88)$$

$$\underbrace{(\mathbf{J}_m^\top \mathbf{W}_d^\top \mathbf{W}_d \mathbf{J}_m + \beta \mathbf{W}_m^\top \mathbf{W}_m)}_{\tilde{\mathbf{H}}} \delta \mathbf{m} + \quad (2.89)$$

$$\underbrace{\mathbf{J}_m^\top \mathbf{W}_d^\top \mathbf{W}_d (\mathbb{F}[\mathbf{m}] - \mathbf{d}_{\text{obs}}) + \beta \mathbf{W}_m^\top \mathbf{W}_m (\mathbf{m} - \mathbf{m}_{\text{ref}})}_{\mathbf{g}(\mathbf{m})} = \mathbf{0},$$

which can be rewritten simply as:

$$\delta \mathbf{m} = -\tilde{\mathbf{H}}^{-1} \mathbf{g}(\mathbf{m}). \quad (2.90)$$

The system in equation (2.90) can be solved approximately using a Conjugate-Gradient method (Hestenes & Stiefel, 1952) since the approximation of the Hessian $\tilde{\mathbf{H}}$ is symmetric and assumed to be positive definite. The optimization procedure is then referred to as an Inexact Gauss-Newton method.

At each iteration t of the geophysical inverse problem, the model is updated using the obtained perturbation $\delta\mathbf{m}$:

$$\mathbf{m}^{(t+1)} = \mathbf{m}^{(t)} + \eta\delta\mathbf{m}^{(t)}, \quad (2.91)$$

where η is a step-size that scales the perturbation.

For problems with a linear forward operator \mathbb{F} (gravity or magnetic surveys for examples), the Hessian is precisely what is written in equation (2.84) and the MAP geophysical model, for a given value of β , is found in a single model update with η equal to unity. The problem then is to find a value of β such that the data misfit is approximately equal to its target value (see equation (2.75) and Parker (1977)). When the noise level is unknown, other criteria are possible such as the value of β that minimize the generalized cross-validation function (Wahba, 1990), or the value with maximum curvature on a Φ_d versus Φ_m curve for all possible values of β ; this is the L-curve criteria (Hansen, 1998, 2000; Hansen & O’Leary, 1993; Santos & Bassrei, 2007).

However, when the forward operator \mathbb{F} is nonlinear, several successive model updates might be necessary to reach a minimum. In addition, a proper step-size η needs to be found at each iteration t to guarantee a satisfactory decrease of the

objective function. For that purpose, I use a backtracking approach, in which the η value is reduced as long as the following Armijo's condition (Armijo, 1966) is not met:

$$\Phi(\mathbf{m}^{(t+1)}) \leq \Phi(\mathbf{m}^{(t)}) + \gamma\eta\mathbf{g}(\mathbf{m}^{(t)})^\top \delta\mathbf{m}, \quad (2.92)$$

where γ is usually chosen quite small; Nocedal & Wright (2006) recommends a value of $\gamma = 10^{-4}$. I choose to divide η by 2 any time the condition is not met, up to ten times. This is similar to strategies used in examples in Ascher & Greif (2011).

As in the case of a linear problem, a suitable value for β needs to be found to ensure the data are fitted reasonably well. General practice is to start from a relatively high value of β and then decrease it throughout the inverse iterative process. The idea is to start with a well-regularized problem when the model is far from a minimum, and then decrease the importance of the regularization in favour of the data misfit. Many strategies have been proposed for the iterative alterations of this trade-off parameter β , such as through an imposed schedule (Farquharson & Oldenburg, 1993), by making it part of the inverted parameters with a generalized cross-validation method (Haber & Oldenburg, 2000), or with an L-curve criterion adapted to nonlinear problems (Li & Oldenburg, 1999). A comparison of the different approaches has been done in Farquharson & Oldenburg (2004).

To complete this review, I want to mention the possibility of using stochastic sampling optimization approaches. One of their advantages, over the deterministic approach I just presented, is to characterize the posterior distribution over a range

of possible and acceptable models, rather than finding a single MAP estimate. This enables the uncertainty analysis of the model. One of the most popular families of methods is the Markov Chain Monte Carlo (MCMC) approach (for reference, see Andrieu et al. (2003)). MCMC methods have been applied in several geophysical applications (Mosegaard & Tarantola, 1995; Sambridge & Mosegaard, 2002). The use of MCMC approaches has also been recently extended by de Figueiredo et al. (2019a,b) to posterior distributions with Gaussian Mixture Model (GMM) priors, similar to the one used in the framework developed in chapter 3. However, those methods present the drawback to be computationally expensive, which often limits them to small-scale problems.

Chapter 3

A framework for petrophysically and geologically guided geophysical inversion using a dynamic Gaussian mixture model prior

3.1 Introduction

I have shown in section 2.5 that, in a Tikhonov inversion (equation (2.61)), defining the smallness term as a least-squares term such as in equation (2.64) assumes a Gaussian distribution of the model \mathbf{m} values around the reference model. This is unlikely to correspond to the true physical property distribution, especially when the reference model is a half-space as commonly used. With the Tikhonov ap-

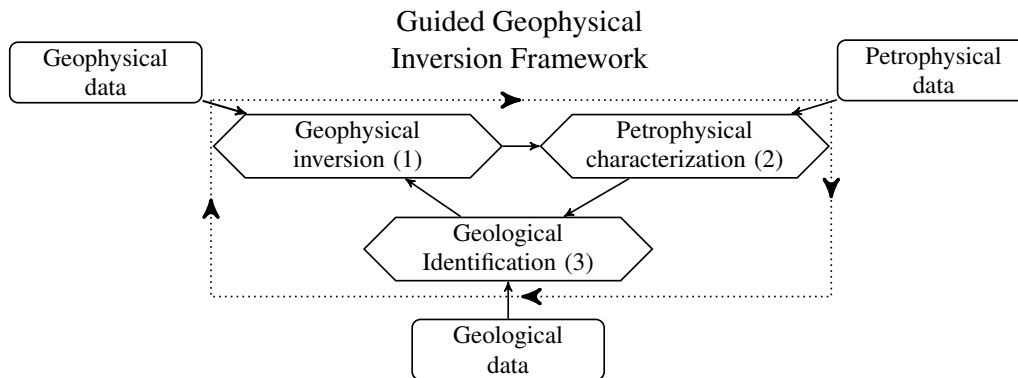


Figure 3.1: A graphical representation of the PGI framework. Each diamond is a MAP estimation which requires data (shown in rectangular boxes) as well as inputs from the other MAP estimates.

proach, the incorporation of knowledge about the physical properties can only be done locally at fixed locations defined by the users (Lelièvre et al., 2009). A more versatile method is required.

My focus in this chapter is on designing a more meaningful and dynamically updatable prior for the smallness term $\mathcal{P}_s(\mathbf{m})$ when non-geophysical data are available but not necessarily well located. This will allow me to guide the model \mathbf{m} towards producing an expected petrophysical distribution as well as capturing geological features. To perform inversions that include all three types of information, my framework involves three optimization problems (Figure 3.1, diamond-shape nodes) over the geophysical, petrophysical, and geological knowledge. The goal of this chapter is thus to define each optimization process in Figure 3.1 as a MAP estimation over a posterior distribution to be able to include various types of *a priori* information about the expected subsurface structures and contrasts. I have already introduced the geophysical inverse problem (Figure 3.1, Process 1) in sec-

tion 2.5. I now focus on the petrophysical characterization and geological identification and their integration with the geophysical inversion. I define the geological identification (Figure 3.1, Process 3) as the process that builds the “quasi-geology model” from the geophysical model (Li et al., 2019). The framework definition is completed by presenting the approach to the dynamic petrophysical characterization (Figure 3.1, Process 2). This step allows dealing, in certain cases, with limited prior information by mitigating it with the knowledge gained during the inversion process.

The Gaussian Mixture Model (GMM) is introduced as a way to represent geological and petrophysical information in section 3.2. I show in section 3.3 how petrophysical and geological information, represented as a GMM, can be integrated into the smallness term of a conventional regularization operator in the geophysical inversion. Consequently, I can achieve my objectives by carrying out a conventional deterministic geophysical inversion without adding extra terms in the regularization term. This is an important simplification since it eliminates the need for extra weighting parameters; it also allows previously developed Tikhonov-style inversion codes to be used. The framework is iterative, and the geophysical model, petrophysical distribution, and quasi-geology model are updated through successive cycles. Petrophysical information is brought at the same level as the geophysical information, which allows me to generalize the concepts of uncertainties for the petrophysical data and define a formal target misfit for the petrophysical and geological information that is similar to the geophysical data target misfit; this concept has been missing from previous frameworks.

Numerical implementation and solutions such as weighting strategy, convergence and pseudocode are presented in section 3.4. In section 3.5, synthetic and field examples are used to illustrate some essential aspects of the algorithm. A 1D Magnetotelluric (MT) example with both sharp and smooth features is used to illustrate the gain made in the recovery of a geophysical model when petrophysical information is available. I also use this example to step through the various stages of the algorithm. A 2D Direct Current (DC) resistivity example is used to demonstrate the capabilities of the proposed framework when petrophysical information is minimal; for instance, when only a specific number of distinct units is expected. This example is also used to emphasize the gain made by the inclusion of prior geological information. Finally, I highlight how this framework can be used to incorporate constraints regarding the number of geological units and narrow down the domain of possible geophysical models. I use an airborne Frequency-Domain Electromagnetic (FDEM) field example, with data acquired in the Bookpurnong area in Australia, to invoke a geologic assumption about the number of units needed to characterize saltwater contamination.

3.2 Univariate Gaussian mixture model representation of petrophysical information

To include physical property information into the inversion, I first need to define a way to model the physical property distributions. Gaussian distributions are well adapted to represent unimodal distributions. However, different rock units can have widely different petrophysical characteristics. These distinct characteristics

can be represented in a discrete latent variable model. A discrete latent variable is a categorical value, that might be known or not, that determines the characteristics of a distribution. A popular model to represent distributions with a discrete latent variable is the Gaussian Mixture Model (GMM), where each geological unit's physical property is represented by a Gaussian distribution.

Let us consider a given petrophysical dataset with n samples, denoted $\{s_i, i = 1..n\}$, which represents the measured physical property of each sample. The current geological classification of each sample is known. This is denoted by $j = \{1..c\}$ where c is the number of distinct geological units. The geological classification is used as a categorical variable. The n_j physical property measurements of each geological unit j are denoted $s_{i \in j}$.

For each geological unit j , a Gaussian probability density distribution can be fit on its samples (see also section 2.3). If the physical property distribution of the unit does not follow a Gaussian distribution, the physical property can often be projected into a transformed space where it appears approximately Gaussian, such as a log-space for electrical conductivity or magnetic susceptibility (see the notion of mapping in Kang et al. (2015)). With known labels, the MLEs of the Gaussian distribution parameters for each unit $j = \{1..c\}$, its mean μ_j and its variance σ_j^2 (or standard deviation σ_j), plus its proportion π_j among the dataset, are given in equations (3.1) to (3.3):

$$\pi_j = \frac{n_j}{n}, \quad (3.1)$$

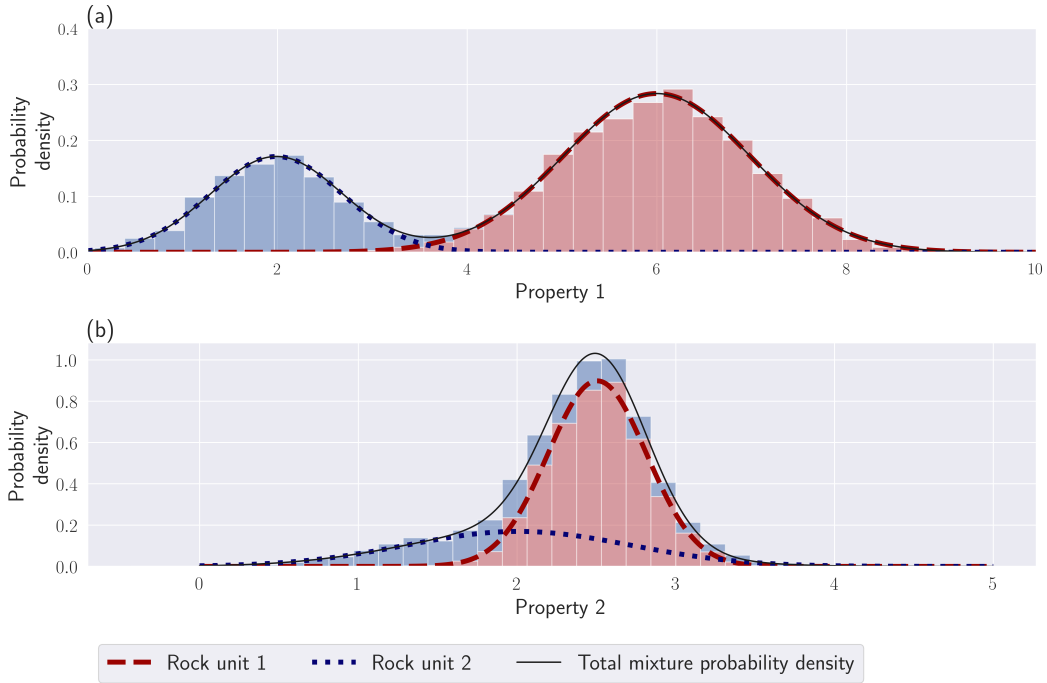


Figure 3.2: Examples of Gaussian mixture like samples sets. (a) A GMM with two distinct units; the approximation in equation (3.11) is valid. (b) A GMM with overlapping units; the approximation in equation (3.11) is not valid.

$$\mu_j = \frac{1}{n_j} \sum_{i=1}^{s_j} s_{i \in j}, \quad (3.2)$$

$$\sigma_j^2 = \frac{1}{n_j} \sum_{i=1}^{s_j} (s_{i \in j} - \mu_j)^2. \quad (3.3)$$

The full probability function to observe an unlabeled physical property data point s can be written as a GMM (see also Figure 3.2):

$$\mathcal{P}(s|\Theta) = \sum_{j=1}^c \pi_j \mathcal{N}(s|\mu_j, \sigma_j^2). \quad (3.4)$$

The variable Θ holds the GMM global variables $\Theta = \left\{ \pi_j, \mu_j, \sigma_j^2 \right\}_{j=1..c}$. A GMM is a parametric probability density distribution that can fit any continuous probability density distribution, when its number of clusters tends to infinity (Murphy, 2012). It has gained popularity in recent years for representing geological and petrophysical information (Giraud et al., 2017, 2019b; Grana & Della Rossa, 2010; Grana et al., 2017; Granek, 2011).

I denote \mathbf{z} as the categorical variable for the labels, i.e. the geological classification. I call this variable the membership. Given an unlabeled data point s , its membership z takes the value of the geological unit with the highest probability:

$$z = \operatorname{argmax}_{z \in \{1..j\}} \mathcal{P}(s|z) \mathcal{P}(z), \quad (3.5)$$

with:

$$\mathcal{P}(z) = \pi_z, \quad (3.6)$$

$$\mathcal{P}(s|z) = \mathcal{N}(s|\mu_z, \sigma_z^2). \quad (3.7)$$

Note that equation (3.5) defines a MAP estimate of the geological identifier \mathbf{z} . The parameters $\left\{ \pi_j \right\}_{j=1..c}$ represent the prior expectation of observing a certain unit before observing s (equation (3.6)). This MAP estimate will be the template for designing the geological identification process in the framework (Figure 3.1, Process 3).

The only posterior distribution left to define is for the petrophysical characterization process, to determine MAP estimates of the GMM's parameters when

labels are unknown (Figure 3.1, Process 2). This is done in section 3.3.2. However, before developing this point, I first present how to link the petrophysical and geological knowledge, represented as a GMM, and the geophysical inversion.

3.3 Gaussian mixture model as smallness prior for geophysical inversion

3.3.1 Gaussian mixture model prior definition

Let us assume there is given petrophysical and geological information about the geophysical model. Petrophysical information can include mean or variance values of physical properties for different geological units. Geological information can consist of an expected number of distinct units or anticipation of encountering certain rock units in particular locations. I need to design a prior that offers the maximum flexibility for representing that petrophysical and geological prior knowledge.

In equation (3.8), I propose a GMM that is designed to serve as a prior distribution for the values of the geophysical model \mathbf{m} . This prior's parameters are both spatially (index i) and lithologically (index j) dependent. The probability function is defined as:

$$\mathcal{M}(\mathbf{m}|\Theta) = \prod_{i=1}^n \sum_{j=1}^c \mathcal{P}(z_i = j) \mathcal{N}(m_i | \mu_j, w_i^{-2} \sigma_j^2), \quad (3.8)$$

where:

- c is the number of distinct rock units, or clusters.
- n is the number of active cells in the mesh.
- m_i represents the physical property value at the i^{th} cell.
- \mathbf{z} describes the membership to a certain rock unit.
- $\mathcal{P}(z_i = j)$ represents the geological information. It is the prior probability of observing rock unit j at location i (vector notation: $\mathcal{P}(\mathbf{z})$). It can be either constant over the whole area, then representing an expected relative volume of each unit denoted by the global proportion π_j , or locally set if the information is available (e.g borehole logs, outcrops or geological modelling; see Giraud et al. (2017)).
- μ_j is the mean physical property of rock unit j .
- $w_i^{-2}\sigma_j^2$ is the variance of the rock unit j at the i^{th} cell. It includes both the expected physical property variance σ_j^2 of the rock unit j globally and a local prior confidence w_i^2 that, at a certain cell i , the model value m_i should belong closer or farther away from the mean μ_j of the rock unit j . Those \mathbf{w} weights can be used to include depth or sensitivity weighting.
- Θ holds the GMM global variables $\Theta = \left\{ \pi_j, \mu_j, \sigma_j^2 \right\}_{j=1..c}$.

Instead of adding an extra term in the objective function, I use the previously defined GMM probability distribution (equation (3.8)), representing the current geological and petrophysical knowledge, as the smallness prior. To have consistency with the Tikhonov framework, such as defined in equation (2.74), I write:

$$\mathcal{P}_s(\mathbf{m}) \propto \mathcal{M}(\mathbf{m}|\Theta)^{\beta\alpha_s}. \quad (3.9)$$

To formulate the objective function (see section 2.5.2), a negative logarithm is applied to the new posterior distribution, which uses the GMM the smallness prior defined in equation (3.9). The resulting smallness term is then:

$$\Phi_s(\mathbf{m}) = - \sum_{i=1}^n \log \left(\sum_{j=1}^c \mathcal{P}(z_i = j) \mathcal{N}(m_i | \mu_j, w_i^{-2} \sigma_j^2) \right). \quad (3.10)$$

Although I have had positive results with using the above *LogSumExp* function (the exponential function being in the Gaussian distribution \mathcal{N}) as the smallness regularizer, there are benefits of using the following approximation. Gaussian distributions decay exponentially. If the units have distinguishable enough contrasts, it is reasonable to approximate the *LogSumExp* function in equation (3.10) by its locally dominant quadratic term. This means considering only the most probable rock unit for each cell given the current model \mathbf{m} . The other terms of the summation are deemed negligible. For example, consider the 1D physical property distributions in Figure 3.2. For the physical property distribution in Figure 3.2a, the individual Gaussian functions representing each rock unit can locally approximate the GMM extremely well. On the other hand, for the physical prop-

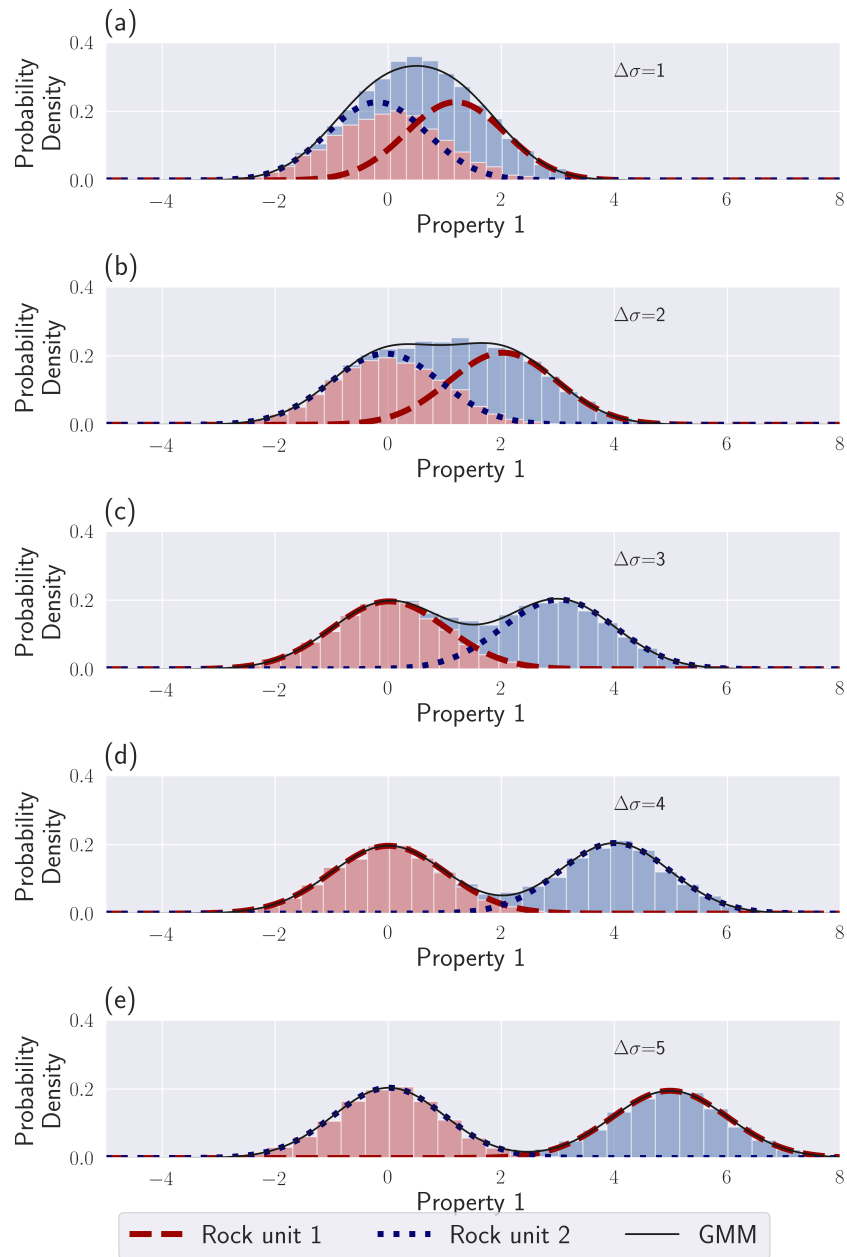


Figure 3.3: Presentation of two Gaussian distributions with unity standard deviations, and resulting GMMs. Their respective means are separated by various $\Delta\sigma$: (a) $\Delta\sigma = 1$; (b) $\Delta\sigma = 2$; (c) $\Delta\sigma = 3$; (d) $\Delta\sigma = 4$; (e) $\Delta\sigma = 5$.

erty distribution displayed in Figure 3.2b, there is too much overlap between the two individual Gaussian components. Individually they are not a good approximation to the full GMM distribution and the above assumption is incorrect. In that case, one can either work with the full expression shown in equation (3.10), or potentially re-evaluate whether the individual distributions are distinct enough to be considered as separate units. As a rule of thumb, contrasts are deemed distinguishable enough to apply this approximation if the centres of two clusters are separated by at least three times the largest standard deviation (see Figure 3.3). By using the parameters of the most likely cluster at each active cell, $\Phi_s(\mathbf{m})$ can be approximated as:

$$\Phi_s(\mathbf{m}) = \frac{1}{2} \|\mathbf{W}_s(\Theta, \mathbf{z})(\mathbf{m} - \mathbf{m}_{\text{ref}}(\Theta, \mathbf{z}))\|_2^2, \quad (3.11)$$

with:

$$\mathbf{z} = \underset{\tilde{\mathbf{z}}}{\text{argmax}} \mathcal{P}(\mathbf{m}|\tilde{\mathbf{z}}) \mathcal{P}(\tilde{\mathbf{z}}), \quad (3.12)$$

$$\mathbf{m}_{\text{ref}}(\Theta, \mathbf{z}) = \mu_{\mathbf{z}}, \quad (3.13)$$

$$\mathbf{W}_s(\Theta, \mathbf{z}) = \text{diag}(\mathbf{w} \circ \sigma_{\mathbf{z}}^{-1}). \quad (3.14)$$

Note the similarity of the smallness term in equation (3.11) with the Tikhonov formulation (equation (2.64)). This allows me to generate a Petrophysically and Geologically guided Inversion (PGI) that uses traditional algorithms and thus can rely on the research literature on the Tikhonov approach.

My approach, regarding the regularized geophysical problem, can be summa-

rized as follows: At each iteration, I first identify the most probable unit for each cell; I call it its membership, and store it in the categorical vector \mathbf{z} (equation (3.12)). The reference model \mathbf{m}_{ref} and smallness weights \mathbf{W}_s are then updated according to the membership \mathbf{z} . The reference model at each cell takes the physical property mean value of the most likely unit z_i (equation (3.13)). The smallness weights depend on the value of the corresponding variances and on the local weights (e.g. depth or sensitivity weighting; see equation (3.14)). These updates represent the newly acquired knowledge on \mathbf{m} according to the petrophysical information Θ and geological prior $\mathcal{P}(\mathbf{z})$. I refer to the updated reference model as the learned reference model. The next inversion step then pushes each cell of the mesh towards the mean of its most probable rock unit. The strength of the push is proportional to the variance of the physical property for that unit (the higher the variance, the smaller the push), and the weights \mathbf{w} .

Equations (3.12) defined the MAP estimate for the geological identification (Figure 3.1, Process 3). Equations (3.13) and (3.14) linked the petrophysical and geological information with the geophysical inversion. With these definitions, one can proceed to perform PGI by using the means and variances fit on the petrophysical data, as well as the proportions from the geological data, to compute \mathbf{z} , \mathbf{m}_{ref} and \mathbf{W}_s at each iteration (equation (3.12), (3.13) and (3.14)). However, when the petrophysical knowledge is incomplete or uncertain, the estimated GMM may not be accurate. Carter-McAuslan et al. (2015) have investigated that issue and shown that inaccurate petrophysical information can significantly affect the recovered model. Sun & Li (2015) partially overcome this by updating the cluster

centres through the iteration process; they average the observed means in the geophysical model with the means from the petrophysical measurements through a separate clustering optimization problem. I generalize this approach to all of the parameters of the GMM. In the next section 3.3.2, I formulate the petrophysical characterization step of my framework (Figure 3.1, Process 2) as a MAP estimation process.

3.3.2 Updating the Gaussian mixture model

One can either consider that the GMM's parameters derived from petrophysical and geological data give the best estimation of the true distribution, or that it is only an approximation, and additional information can be obtained from the geophysical model during the inversion (Sun & Li, 2015). I prefer this latter approach. Since the prior knowledge might be incomplete or only known qualitatively, it is important to mitigate possible biases that can affect the final recovered model (Carter-McAuslan et al., 2015). For that purpose, Sun & Li updated each cluster centre, during their Fuzzy C-Means (FCM) clustering step, through a weighted average of the expected centre from the petrophysical data with the observed centre in the geophysical model. From a statistical viewpoint, this resembles the use of a MAP estimator to find the cluster means applied to the geophysical model itself, with the addition of a conjugate prior (Raïffa & Schlaifer (1961), see section 2.3.2) based on the petrophysical data. The conjugate prior approach is used to formalize the update of the means done in Sun & Li (2015) and generalize it to the other GMM's parameters.

Obtaining the GMM’s parameters Θ is thus made part of the iterative inversion process. I define the petrophysical characterization process (Figure 3.1, Process 2) as a MAP estimator for Θ . This MAP estimate benefits both from the petrophysical and geological data known before the inversion and the current geophysical model. After each geophysical inversion iteration, and before updating the membership \mathbf{z} , the mixture parameters Θ are learned using the current geophysical model \mathbf{m} and the confidence in the prior knowledge Θ_{prior} . The posterior distribution on Θ , given the geophysical model \mathbf{m} and prior knowledge, is defined as:

$$\mathcal{P}(\Theta|\mathbf{m}) \propto \mathcal{M}(\mathbf{m}|\Theta)\mathcal{P}(\Theta). \quad (3.15)$$

In section 3.2, the problem of fitting a single Gaussian distribution to each unit, and thus defining its petrophysical mean and variance, was made easy by knowing the geological unit of each sample. A much harder problem is to recover the full multimodal probability function described in equation (3.4) when there are missing labels. For example, in an inverted geophysical model \mathbf{m} , most locations for the geological units are unknown except where there are drillholes and outcrops. In fact, this is usually the information that is to be determined. The categorical variable \mathbf{z} that represents the geological classification is now a hidden variable to recover along with the GMM’s parameters. Clustering algorithms are specially designed for this sort of task. The Expectation-Maximization (EM) algorithm (Dempster et al., 1977) is one of the most widely used for semi-supervised and unsupervised learning in mixture modelling. It allows me to fit the parame-

ters $\Theta = \left\{ \pi_j, \mu_j, \sigma_j^2 \right\}_{j=1..c}$ of a mixture model to a multimodal distribution with partial or no labelling. The EM algorithm is often presented in its MLE form; thus, no prior information is involved. To include prior information in the algorithm, and thus find a MAP estimate for the posterior distribution on Θ shown in equation (3.15), I use a MAP variation of the EM algorithm (also introduced in Dempster et al. (1977)); I refer to this algorithm as the MAP-EM algorithm.

For the MAP-EM algorithm, I need to choose how to model the prior $\mathcal{P}(\Theta)$ for each type of parameter. I can follow either a conjugate prior or semi-conjugate prior approach as described in section 2.3. Each step of the MAP-EM algorithm applied to a GMM with a conjugate or semi-conjugate prior can be understood as a weighted average of the observed parameters with their priors. Figure 3.4 shows an example of such a MAP estimate of the GMM's parameters. I define the importance of each prior function so that an importance input value of unity denotes an equal weighting of the observed and prior distributions. I refer to those importance values as the confidences in the GMM's prior parameters. Confidences of zero in the prior generate a MLE estimator; the prior parameters are not taken into account, and the algorithm reverts to the MLE EM algorithm. Infinite confidences in the prior fix the GMM's parameters equal to the value of their prior.

The MAP-EM algorithm is an iterative process. I initialize by starting with the parameters determined at the previous cycle. The usual stopping criteria in the literature for the MAP-EM algorithm is to define a minimum increase of the posterior probability density value. At each MAP-EM iteration (k), the responsibility $\{n_{ij}\}_{j=1..c, i=1..n}$ of each cluster j for each point m_i are first computed. This is re-

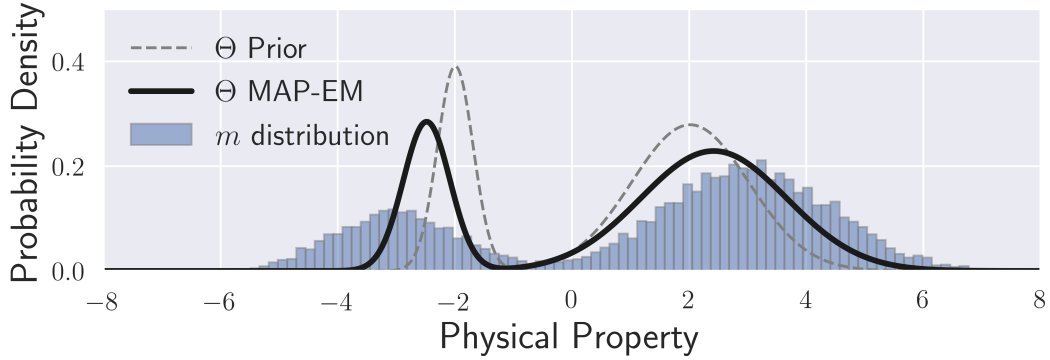


Figure 3.4: Illustration of fitting a GMM with parameters Θ through the MAP-EM algorithm, given the geophysical model \mathbf{m} and the prior petrophysical distribution Θ_{prior} with all confidences set to unity.

ferred to as the E-step in the EM algorithm and it stays unchanged in its MAP-EM variation:

$$n_{ij}^{(k)} = \frac{\mathcal{P}(z_i = j)^{(k-1)} \mathcal{N}(m_i | \mu_j^{(k-1)}, (\sigma_j^2)^{(k-1)})}{\sum_{t=1}^c \mathcal{P}(z_i = t)^{(k-1)} \mathcal{N}(m_i | \mu_t^{(k-1)}, (\sigma_t^2)^{(k-1)})}. \quad (3.16)$$

The MAP-EM steps at iteration (k) , with respect to the global proportion weights $\{\pi_j\}_{j=1..c}$, means $\{\mu_j\}_{j=1..c}$, and variances $\{\sigma_j^2\}_{j=1..c}$ of the GMM, are then computed. These steps are referred to as the M-step in the EM-algorithm. The MAP-EM variation of the M-step includes *a priori* information as part of the iterative update.

The global proportion parameters of the GMM follow a categorical distribution whose conjugate prior is the Dirichlet distribution:

$$\mathcal{P}(\boldsymbol{\pi}) = \text{Dir}(\zeta \boldsymbol{\pi}_{\text{prior}} V - 1). \quad (3.17)$$

At iteration (k), the resulting posterior estimate of the proportions $\{\pi_j\}_{j=1..c}$, given the prior proportions $\{\pi_{j\text{prior}}\}_{j=1..c}$ and with confidence $\{\zeta_j\}_{j=1..c}$, is:

$$\pi_j^{(k)} = \frac{V_j^{(k)} + \zeta_j \pi_{j\text{prior}} V}{V(1 + \sum_{t=1}^c \zeta_t \pi_{t\text{prior}})}, \quad (3.18)$$

with:

$$V_j^{(k)} = \sum_{i=1}^n v_i n_{ij}^{(k)}, \quad (3.19)$$

$$\text{and } V = \sum_{i=1}^n v_i, \quad (3.20)$$

where v_i is the volume of the i^{th} cell, and V is the volume of the active mesh. The addition of these volume weights is necessary because the cells of the mesh can have different sizes. I want to use prior information that is mesh-independent. That is why I use volumetric proportions instead of cell counts, which is the way the EM algorithm is usually implemented.

The full conjugate priors of the likelihood function in equation (3.15) for the means and for the variances are not independent of each other, as they follow a joint Normal-Inverse-Gamma distribution (see section 2.3.2). However, using the full conjugate prior approach can be harmful to the variances in the first few iterations. Mean values from models at early iterations may be far from their final target values; that would drive the GMM estimated by MAP-EM to have very high variances to compensate for the difference between the observed and prior means and thus compromise the clustering (see equation (2.38)).

To avoid this issue, a semi-conjugate prior approach is possible where the

dependency of the means and variances is avoided by using the conditional distributions as priors. In this case, the semi-conjugate prior for the means follows a Gaussian distribution (equation (3.21)) while the semi-conjugate prior for the variances follows an Inverse-Gamma distribution (equation (3.22)). The semi-conjugate priors for the means and variances, with their respective confidences $\{\kappa\}$ and $\{v\}$, are:

$$\mathcal{P}(\boldsymbol{\mu}|\boldsymbol{\sigma}^2) = \mathcal{N}(\boldsymbol{\mu}|\boldsymbol{\mu}_{prior}, (\boldsymbol{\kappa}\boldsymbol{\pi}_{prior}V)^{-1}\boldsymbol{\sigma}^2), \quad (3.21)$$

and:

$$\mathcal{P}(\boldsymbol{\sigma}^2|\boldsymbol{\mu}) = \mathcal{G}^{-1}\left(\boldsymbol{\sigma}^2\left|\frac{v\boldsymbol{\pi}_{prior}V - 2}{2}, \frac{v\boldsymbol{\pi}_{prior}V\boldsymbol{\sigma}_{prior}^2}{2}\right.\right). \quad (3.22)$$

Note that if prior information is put only on the means, or only on the variances, then this is a full conjugate prior. The semi-conjugate prior approach arises only when prior information on both means and variances are set (meaning that $\{\kappa\}$ and $\{v\}$ are both non zero).

The update of the means is the same for both the full conjugate and semi-conjugate prior approaches. The current (k) posterior estimate of the means $\{\boldsymbol{\mu}_j\}_{j=1..c}$ is a weighted average of the MLEs $\{\bar{\mathbf{m}}_j\}_{j=1..c}$ from equation (2.16), using the geophysical model as the samples, with the prior means $\{\boldsymbol{\mu}_{j\text{prior}}\}_{j=1..c}$ and with confidences $\{\kappa_j\}_{j=1..c}$:

$$\mu_j^{(k)} = \frac{V_j^{(k)} \bar{m}_j^{(k)} + \kappa_j \pi_{j \text{ prior}} V \mu_{j \text{ prior}}}{V_j^{(k)} + \kappa_j \pi_{j \text{ prior}} V}, \quad (3.23)$$

with:

$$\bar{m}_j^{(k)} = \frac{\sum_{i=1}^n v_i n_{ij}^{(k)} m_i}{V_j^{(k)}}. \quad (3.24)$$

For the semi-conjugate prior, the current (k) posterior estimate of the variances $\{\sigma_j^2\}_{j=1..c}$ is a weighted average, with confidences $\{v_j\}_{j=1..c}$, of the MLEs of the variances $\{\sigma_{\bar{\mathbf{m}}_j}^2\}_{j=1..c}$ from equation (2.17) with their priors $\{\sigma_{j \text{ prior}}^2\}_{j=1..c}$:

$$\sigma_j^{2(k)} = \frac{V_j^{(k)} \sigma_{\bar{\mathbf{m}}_j}^{2(k)} + v_j \pi_{j \text{ prior}} V \sigma_{j \text{ prior}}^2}{V_j^{(k)} + v_j \pi_{j \text{ prior}} V}, \quad (3.25)$$

with:

$$\sigma_{\bar{\mathbf{m}}_j}^{2(k)} = \frac{1}{V_j^{(k)}} \sum_{i=1}^n v_i n_{ij}^{(k)} (m_i - \bar{m}_j^{(k)})^2. \quad (3.26)$$

I run fully the MAP-EM algorithm to learn a new petrophysical distribution with parameters $\Theta = \{\pi_j, \mu_j, \sigma_j^2\}_{j=1..c}$ after each iteration (t) of the geophysical inversion process, using the current geophysical model $\mathbf{m}^{(t)}$ and the prior petrophysical distribution Θ_{prior} .

This completes the derivation. Equation (3.15), in particular, describes the MAP estimator for the petrophysical characterization. The three MAP estimates are interconnected through the sharing of the geophysical model, petrophysical

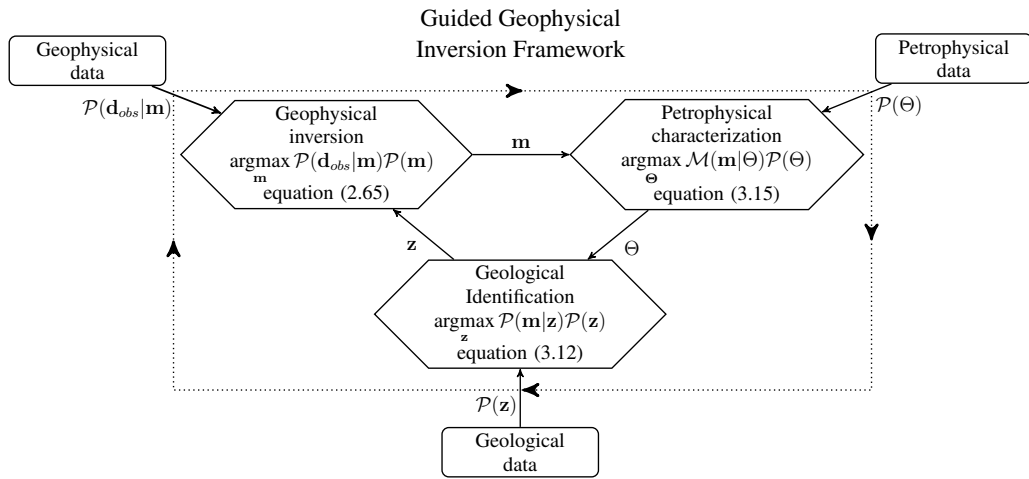


Figure 3.5: A graph illustration of how the various MAP estimate processes are interlocked with each other.

distribution and geological classification. The final PGI framework is summarized in Figure 3.5, which is the completed version of the previous diagram (Figure 3.1). The next step is to implement this procedure numerically. That is done in the following section.

3.4 Numerical Implementation

The PGI framework defines three interconnected inverse problems, and special care is required to ensure that each is reasonably well-solved. In this section, I look at some of the essential implementation elements of this framework. A comprehensive algorithm and a flowchart can be found in section 3.4.2. Before going into the details of the pseudocode, I first formalize the concept of fitting the petrophysical and geological data and define stopping criteria for the numerical solution.

3.4.1 Petrophysical target misfit and inversion stopping criteria

The smallness term, such as defined in equation (3.11), measures how well the geophysical model fits the petrophysical and geological data through the GMM. I need to define a target for this misfit term.

For the definition and evaluation of the petrophysical target misfit, I focus on the petrophysical and geological information contained in the smallness term; that is to say I omit the survey-related weights \mathbf{w} . I identify this quantity as Φ_{petro} :

$$\Phi_{\text{petro}}(\mathbf{m}) = \frac{1}{2} \|\tilde{\mathbf{W}}_s(\Theta, \mathbf{z})(\mathbf{m} - \mathbf{m}_{\text{ref}}(\Theta, \mathbf{z}))\|_2^2, \quad (3.27)$$

with:

$$\tilde{\mathbf{W}}_s(\Theta, \mathbf{z}) = \text{diag}(\sigma_{\mathbf{z}}^{-1}), \quad (3.28)$$

where \mathbf{z} and \mathbf{m}_{ref} are the same as in equations (3.12) and (3.13).

At each iteration, the i^{th} element ($m_i - m_{\text{ref}i}$) is a Gaussian random variable of mean zero and variance σ_i^2 . Consequently, elements in $\tilde{\mathbf{W}}_s(\mathbf{m} - \mathbf{m}_{\text{ref}})$ are Gaussians with zero mean and unit standard deviation. Thus, Φ_{petro} is a chi-squared statistical parameter with expectation:

$$E[\Phi_{\text{petro}}] = \Phi_{\text{petro}}^* = \frac{n}{2}. \quad (3.29)$$

This defines the petrophysical target misfit value Φ_{petro}^* for Φ_{petro} as being half the number of active cells n in the geophysical model. This is one condition for

stopping the algorithm, I want to find a geophysical model \mathbf{m} for which Φ_{petro} is less than or equal to Φ_{petro}^* .

The equation (3.27) for evaluating the petrophysical stopping criterion omits the weights \mathbf{w} (equation (3.11)). The additional weights \mathbf{w} are used to include depth or sensitivity weighting, which is more related to the physics of the survey rather than to the desired properties of the geophysical model. I have taken two approaches; the first is to minimize Φ_s but keep the stopping criterion attached to Φ_{petro} . The second is to minimize and measure the stopping criterion using Φ_s after adjusting the target misfit value to be $\|\mathbf{w}\|_2^2/2$. Thus far, I prefer the former approach because the second has lead me in certain cases to underfit the petrophysical distribution. The examples, developed in sections 3.5, all use various weighting strategies and the Φ_{petro} stopping criterion approach.

This stopping criterion for the petrophysical data is analogous to the geophysical data misfit criterion. The geophysical data misfit term Φ_d , such as defined in equation (2.62), is also a sum of Gaussian variables with zero mean and unit standard deviation. Thus, a reasonable target misfit Φ_d^* for Φ_d is (Parker, 1977):

$$\Phi_d^* = \frac{d}{2}, \quad (3.30)$$

where d is the number of geophysical data.

The algorithm stops when it finds a model that simultaneously has both Φ_d and Φ_{petro} equal or below their respective target value Φ_d^* and Φ_{petro}^* . Reaching multiple target misfits adds a new challenge to solving the inverse problem. I

address this in the following section as I work through the important components of the pseudocode.

3.4.2 Pseudocode and weighting strategies

At each iteration of the PGI algorithm, three inverse problems need to be solved. I discuss the important elements that assist in understanding the details of the algorithm. To accompany this discussion, the algorithm is provided in two forms. The first is a pseudo-algorithm (algorithm 1) that details my implementation of this framework. The optimization notions of inexact Gauss-Newton and backtracking line search are detailed in section 2.5.4. The second is a flowchart (Figure 3.6) that summarizes how my framework loops over the various datasets to produce a final geophysical model with the desired petrophysical distribution and geological features.

Step 1: Initialization

I am solving three MAP problems. Each needs to be initialized with an initial geophysical model $\mathbf{m}^{(0)}$, petrophysical distribution $\Theta^{(0)}$ and membership $\mathbf{z}^{(0)}$, respectively. I usually have these elements consistent with each other. For example, the initial reference model is usually the starting model; I can start from a background half-space $\mathbf{m}^{(0)}$, whose value is the same as in $\Theta^{(0)}$, and set $\mathbf{z}^{(0)}$ at the background unit everywhere.

Algorithm 1: This algorithm finds a geophysical model reproducing the geophysical, petrophysical, and geological data.

1 Initialization:

- Input:
 - Initial geophysical model $\mathbf{m}^{(0)}$, petrophysical distributions $\Theta^{(0)}$ and geological model $\mathbf{z}^{(0)}$.
- Parameters:
 - *Objective function:* data's noise matrix \mathbf{W}_d , trade-off parameter $\beta^{(0)}$, prior matrices and weights $\{\alpha\}, \{W\}$.
 - *Localized prior:* specific $\mathcal{P}(z_i)$ for available locations $i \in \{1..n\}$, local weights $\{\mathbf{w}_i\}_{i=1..n}$.
 - *Confidences in the petrophysical prior:* $\{\kappa_j, v_j, \zeta_j\}_{j=1..c}$ for the means, variances and global proportions.
 - *Optimization:* β -cooling factor $\gamma (> 1)$, sufficient decrease rate $\tau (\leq 1)$.
- Output:
 - $\mathbf{m}, \Theta, \mathbf{z}$.

2 while $\Phi_d > \Phi_d^*$ **and** $\Phi_s > \Phi_s^*$ **do**

3 Objective-Function Descent Step:

- Compute a model perturbation $\delta\mathbf{m}$ for (2.61) with the smallness defined in (3.11) using an inexact Gauss-Newton approach.
- Backtracking line search with a Armijo's condition to find a step-size η that satisfy a sufficient decrease of the objective function.
- Return $\mathbf{m}^{(t)} = \mathbf{m}^{(t-1)} + \eta\delta\mathbf{m}$.

4 Update Petrophysical Distribution

- Fit a new GMM $\Theta^{(t)}$ on $\mathbf{m}^{(t)}$ with a confidence in the prior determined by the hyper-parameters $\{\zeta\}, \{\kappa\}, \{v\}$ such as in equations (3.18), (3.23) and (3.25) until no sufficient increase of (3.15) is observed.

5 Classification:

- Compute the membership $\mathbf{z}^{(t)}$ of the current model $\mathbf{m}^{(t)}$ as in equation (3.12) using $\Theta^{(t)}$ as the classifier.
- Update \mathbf{m}_{ref} and \mathbf{W}_s according to (3.13) and (3.14) respectively using $\mathbf{z}^{(t)}$.

6 Update weights:

if $\Phi_d^{(t)} > \Phi_d^*$ **and** $\Phi_d^{(t)} > \tau\Phi_d^{(t)}$ **then**

- Decrease β : $\beta^{(t)} = \frac{\beta^{(t-1)}}{\gamma}$

else if $\Phi_d^{(t)} \leq \Phi_d^*$ **and** $\Phi_s > \Phi_s^*$ **then**

- Increase α_s : $\alpha_s^{(t)} = \alpha_s^{(t-1)} \times \frac{\Phi_d^*}{\Phi_d^{(t)}}$

if (optional) $\Phi_d^{(t)} \leq \Phi_d^*$ **and** $\Phi_s > \Phi_s^*$ **and** $\mathbf{z}^{(t)} == \mathbf{z}^{(t-1)}$ **then**

- Include \mathbf{m}_{ref} in Smoothness

7 end

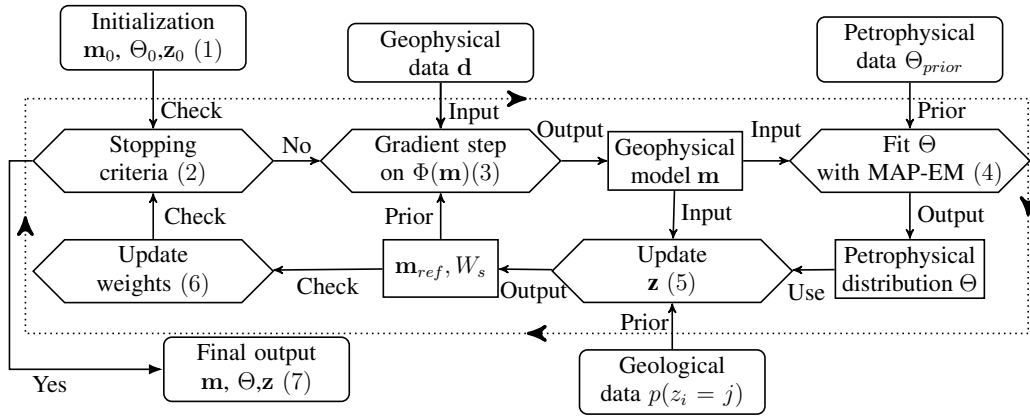


Figure 3.6: A visual pseudocode of the iterative cyclic PGI framework to include geological and petrophysical information into geophysical inversion. The numbers correspond to the steps displayed in algorithm 1.

For the success of geophysical inversions, the choice of the various weighting parameters can be critical. My framework still uses a conventional geophysical inversion objective function, and hence previous studies and good practices are still applicable. I need to provide uncertainties \mathbf{W}_d for the geophysical data least-squares misfit term (equation (2.62)). The objective function (equation (2.61)) requires a reference model and initial weighting parameters. A common practice is to start with a large β and then decrease its value during the inversion iterative process (Farquharson & Oldenburg, 2004). For the smallness and derivative weights $\{\alpha\}$, the similarity of my formulation with the Tikhonov approach allows me to rely on the existing literature (e.g Lelièvre et al. (2009); Oldenburg & Li (2005); Williams (2008)).

For the petrophysical inverse problem, I initialize the petrophysical distribution by setting $\Theta^{(0)} = \Theta_{\text{prior}}$. I thus need to design Θ_{prior} . For each unit, when

petrophysical measurements or *a priori* estimates are available, both the means and variances of the GMM clusters can be set. When no information is available, it is still required to provide some estimates for the variances. These prior variances can be thought of as petrophysical noise levels, analogous to the geophysical noise levels. They play an essential role in determining the petrophysical target misfit and regulate the clustering of each unit around its, to be determined, mean value. The proportions represent geological knowledge. When they are set globally, they represent the expected relative volume of each unit. The choice of confidences in the prior parameters is still a challenging question (see section 3.3.2 for definitions, and section 6.3 for a sensitivity analysis). When the petrophysical information is well-known, values of unity, or higher, have worked well. When no petrophysical information is known *a priori*, values of unity or above for the confidences in the prior variances are used, while confidences in the means and proportions are set to zero. In section 3.5, I show examples for both the known and unknown petrophysical information cases.

The starting geological model can be determined by the starting geophysical model and petrophysical distribution. Additional local knowledge about the geology can be added through the choice of local proportion values for the GMM. I show a simple demonstration through the 2D DC resistivity example (section 3.5.2). For example, knowing that a rock unit appears at a certain location can be added to the inversion. For that purpose, I can locally set the proportion for this rock unit to unity, consequently giving a probability of zero for the other rock units at that same location.

This completes the initialization (step 1 in algorithm 1 and flowchart Figure 3.6). The next step is to evaluate the stopping criteria and update the models.

Step 2 - 5: Check convergence and update the model

At step 2, I check if the convergence criteria $\Phi_d \leq \Phi_d^*$, and $\Phi_{\text{petro}} \leq \Phi_{\text{petro}}^*$ have been met. If these are not satisfied, then a model update is required. I start by taking a single Gauss-Newton step on the geophysical objective function (equation (2.91); step 3). Step 4 consists in running the MAP-EM algorithm described in section 3.3.2 to learn a new petrophysical distribution parameters $\Theta^{(t)}$, using the updated geophysical model $\mathbf{m}^{(t)}$. Finally, at step 5, I update the membership $\mathbf{z}^{(t)}$, using $\mathbf{m}^{(t)}$ and $\Theta^{(t)}$ according to equation (3.12). This updates the smallness weights and reference model for the next iteration, such as described in equation (3.13) and (3.14).

Step 6: Updating β and α_s

In this step, the weights are adjusted so that the inversion arrives at a solution that acceptably fits both the geophysical data and the GMM containing the geological and petrophysical data. Two adjustable parameters are available: β and α_s . The parameter β balances the data misfit with the total regularization function, while α_s allows me to adjust the importance of the smallness term.

The current procedure uses a computationally inexpensive heuristic approach to find suitable β and α_s parameters such that both geophysical and petrophysical misfits are equal or below their respective target value. I initially set β and $\{\alpha\}$ to values I would use for a standard inversion. I first invoke a β -cooling to get

towards a solution that fits the geophysical data. Once reached, I focus more on fitting the petrophysical data by warming α_s .

If the geophysical data misfit term reaches a plateau before attaining its target, I decrease β by a predetermined factor (step 6, first case scenario). The parameter β is considered as an outer-control parameter since it is a weighing for the entire regularization function, which includes smallness and gradient terms.

I also want to find a solution that fits the petrophysical and geological data. For this, I fine-tune the inner-control parameter α_s . If the geophysical data misfit target Φ_d^* has been reached, but not the petrophysical data misfit Φ_{petro}^* , I put more emphasis on the smallness model term. α_s is increased by a factor $\Phi_d^*/\Phi_d^{(t)}$ (step 6, second case scenario). This is similar to the β -warming strategy described in Fournier (2015). Generally, this allows me to focus the algorithm on reaching the petrophysical data misfit target without significantly altering the geophysical data misfit. If the geophysical data misfit is increased too much, then β is reduced. In summary, I use α_s as a fine-tuning parameter as it is not adjusted until the late stages of the inversion when the major structures have already been identified.

Step 7: Final output

The algorithm stops when both the geophysical and petrophysical misfits are below or equal to their respective targets. The PGI framework outputs three quantities: the recovered geophysical model, the learned petrophysical distribution and the membership. The geophysical model fits both the geophysical data and the learned petrophysical distribution. The membership attributes a rock unit to each

cell; I refer to this final categorized model as a quasi-geology model, as proposed by Li et al. (2019).

Options

It is possible to include, or not, the learned reference model inside the smoothness components of the objective function. My preferred strategy is to leave it out until the geophysical data misfit target is reached, and when only a small fraction of the membership \mathbf{z} is changing. This avoids the creation of interfaces at locations that are likely to change later in the inversion. Once the learned reference model has stabilized, the reference model is incorporated into the smoothness term. It promotes the creation of interfaces, which also help to reach the smallness target misfit if it has not yet happened. This strategy and its effects are illustrated in the DC example (section 3.5.2).

3.4.3 Convergence

At each iteration, the gradient-step for the geophysical objective function is similar to that in the Tikhonov formulation. This step is guaranteed to be a descent direction for the objective function. The objective function to be minimized, however, changes because the solution of the MAP-EM problem changes the reference model and smallness weights. Fortunately, the MAP-EM algorithm guarantees a decrease of the smallness term at each iteration. In other words, the updated petrophysical distribution is guaranteed to be closer to the current geophysical model than the previous distribution.

Thanks to these properties, the algorithm usually reaches the geophysical target misfit at a rate comparable to the Tikhonov approach and then requires only a few additional iterations to reach the petrophysical target misfit. Each PGI example presented in the next section 3.5 runs in a number of iterations comparable to the Tikhonov inversion while reaching both of the stopping criteria. This is a significant result as this means that applying this framework does not necessarily end in a massive loss of efficiency.

3.5 Examples

In this section, I present two synthetic examples and a field example that illuminate important aspects of my framework. The Python scripts to reproduce these examples are available as part of the Simulation and Parameter Estimation in Geophysics (SIMPEG) package on GitHub at <https://github.com/simpeg-research/Astic-2019-PGI> (Astic, 2019). These scripts are presented in the form of Jupyter Notebooks (Perez et al., 2015). For convenience, a cloud computing environment to run the notebooks is provided, and readers are invited to reproduce the results.

The first synthetic example is a nonlinear inverse problem in electromagnetics. Magnetotelluric (MT) data (Ward & Hohmann, 1988) are generated over a layered-earth that has sharp and smooth features. The true petrophysical distribution is provided, and the goal is to use it, along with the MT data, to find a solution that has the desired features. I present the results at the various steps of the algorithm and display the updates done to the initial petrophysical and geological models that are used to guide the geophysical inversion.

In the second synthetic example, a DC resistivity profile (Ward & Hohmann, 1988) is acquired over two cylinders. I demonstrate how the PGI framework performs when the GMM is not known *a priori*. I also use this example to show how prior geological information can be included in the inversion.

The third example is a real Frequency-Domain Electromagnetic (FDEM) field survey (Ward & Hohmann, 1988) over a floodplain in Australia potentially contaminated by saline water. I highlight the influence of the choice of a reference model on the Tikhonov models. I then illustrate how the PGI approach can reduce ambiguity in the recovered features by constructing models in which the Earth is assumed to have a certain number of distinct units. These sorts of questions (what if there are c units?), crucial for interpretation, are otherwise difficult to ask in a traditional Tikhonov setting.

3.5.1 MT1D, layered and smooth Earth model: demonstration of the framework

In this example, I demonstrate how to use the PGI framework to include petrophysical information in geophysical inversion. I first highlight the gains made in the recovered geophysical model. I then provide details about how the PGI iterations proceed.

Setup

For this example, inspired by Kang et al. (2017b), I want to recover a 1D earth model that is made up of a resistive layer and a smoothly varying conductor embedded in a uniform background. The conductivity model, which is discretized

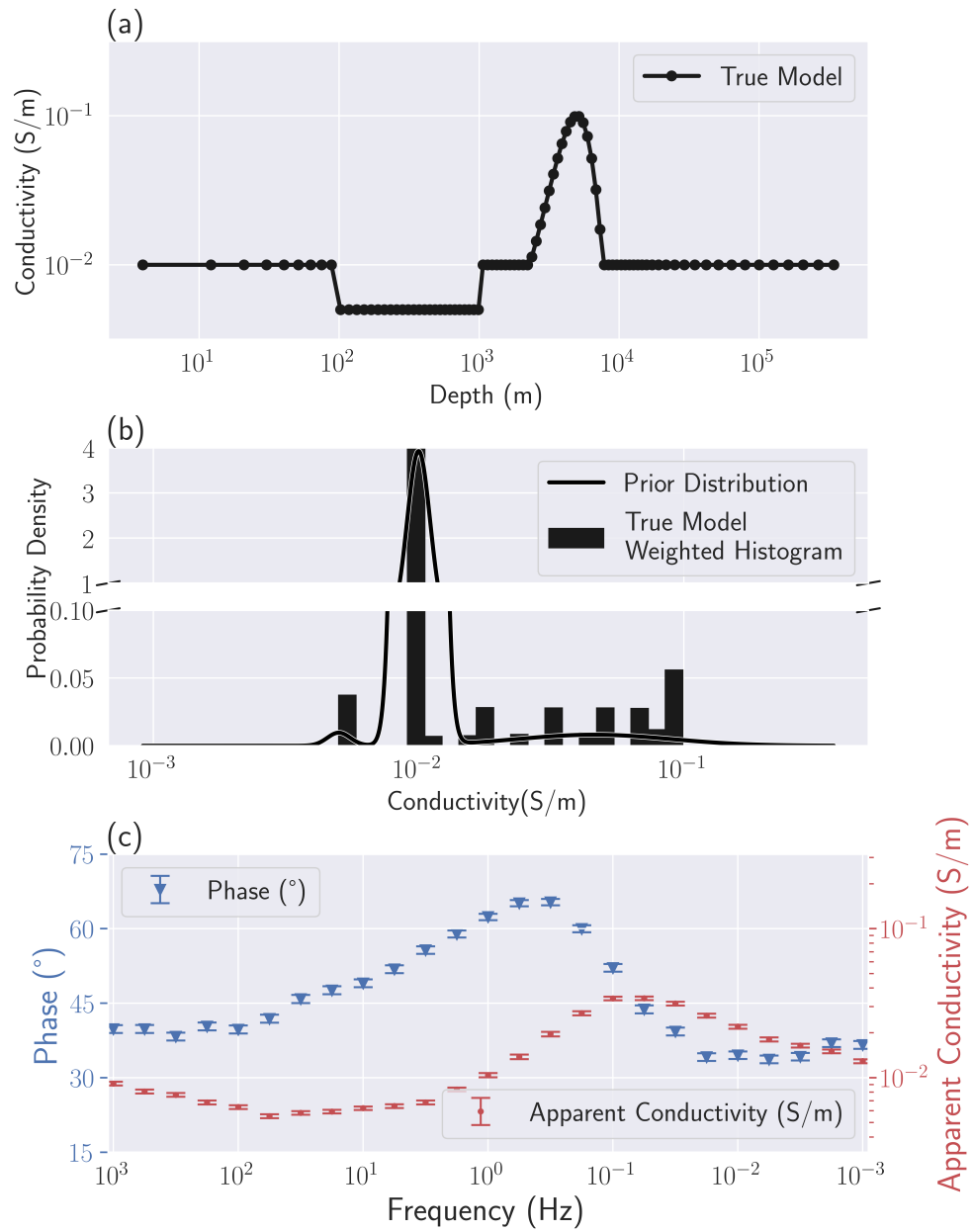


Figure 3.7: Setup of the MT1D example: (a) True geophysical model \mathbf{m}_{true} . The dots coincide with the cell centres in the discretized model. (b) True model weighted histogram and prior petrophysical distribution Θ_{prior} ; (c) MT data and uncertainties.

onto a mesh with 89 cells, is shown in Figure 3.7a. The background unit has a conductivity of 0.01 S/m (100 Ωm). The resistive unit ($5 \cdot 10^{-3}$ S/m or 200 Ωm) is 900 m thick and starts at a depth of 100 m. The smooth conductor, with a maximum conductivity of 0.1 S/m (10 Ωm), is located between 2,300 m and 7,560 m depth. A log-scale, which is traditional for MT, is used.

In the MT experiment, the electric and magnetic fields recorded at the Earth's surface are combined to generate impedances. In this example, data are collected at 25 logarithmically spaced frequencies between 10^{-3} and 10^3 Hz. This generates 50 data points composed of the real and imaginary components of the impedance for each frequency. Unbiased Gaussian noise with a standard deviation of 2% of the data value is added. These observed data and their uncertainties are represented in the form of apparent conductivity and phase in Figure 3.7c.

Initialization

I first describe the initialization for both the Tikhonov and PGI algorithms. For the initial geophysical model $\mathbf{m}^{(0)}$, I choose a uniform half-space with the same conductivity as the background unit. For the PGI approach, the starting membership $\mathbf{z}^{(0)}$ is set to the background unit everywhere. Both the Tikhonov and PGI approaches start with the same objective function; the models after the first iteration are thus identical. This helps in comparing results between the two approaches.

For the PGI approach, it is also needed to provide a GMM to describe the prior petrophysical and geological information Θ_{prior} . I use the exact information from the true earth model for the means and global proportions. For the variances, I

use the true variance for the smooth unit. This unit is characterized by a wide distribution, and thus it has a large variance. The background and the resistive unit are characterized by single values, so their true variances are zero (Dirac distribution). I assign a standard deviation of $0.1 \ln(\text{S/m})$ (or variance of $0.01 [\ln(\text{S/m})]^2$) as an acceptable level of petrophysical noise for those two units. This prior petrophysical distribution can be visualized in Figure 3.7b. All the parameters were estimated by taking into account the “volume” of the cells. This is necessary to make the GMM’s parameters independent of the discretization. The histogram in Figure 3.7b and all subsequent take into account the cell volumes and are thus referred to as weighted histograms.

I set all confidences in the prior petrophysical distribution $\{\boldsymbol{\zeta}, \boldsymbol{\kappa}, \boldsymbol{\nu}\}$ to unity. Unity confidence parameters mean an equal trust in the geophysical model and the prior information when computing the new GMM’s parameters at each iteration of the petrophysical characterization. Each new estimate of the parameters, at each iteration of the MAP-EM algorithm (equations (3.18), (3.23) and (3.25)), is thus a simple unweighted average of the observed and priors. This allows me to see how well each parameter of the GMM is recovered without forcing or fixing its value in the inversion.

Comparison of the Tikhonov and PGI results

The results of the Tikhonov and PGI algorithms are shown in Figure 3.8. The Tikhonov model is presented in Figure 3.8a and the PGI model is shown in Figure 3.8d. The Tikhonov inversion is smooth everywhere, while the unit’s blockiness or

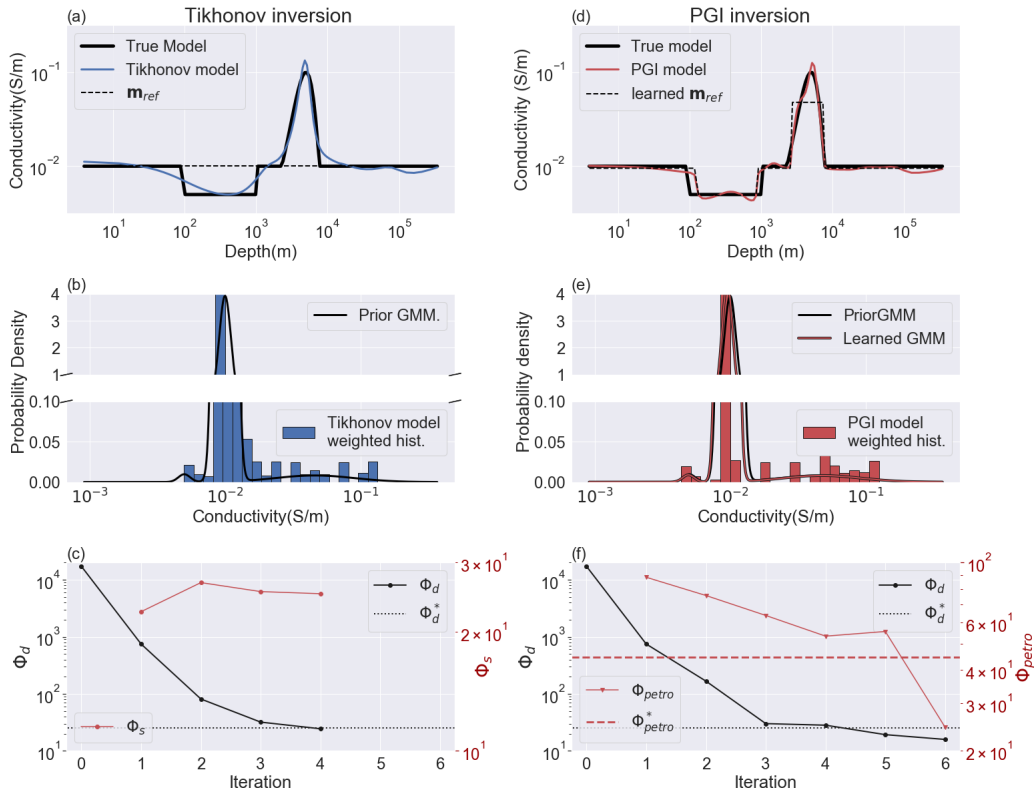


Figure 3.8: MT1D example results and comparison. Panels (a), (b) and (c) show the recovered geophysical model, its histogram and the convergence curves respectively for the Tikhonov approach. Panels (d), (e) and (f) shows the same plots for the PGI approach.

smoothness is much better recovered in the PGI model. Note that both algorithms started from the same reference model. This reference model is kept constant in the Tikhonov approach, whereas the PGI algorithm updates it, along with the smallness weights, at each iteration.

The petrophysical distribution recovered by the PGI (Figure 3.8e) is also much closer to the prior and true distributions, compared to the Tikhonov result (Figure 3.8b). The means, variances and proportions of each unit are well recovered.

Even though I used only confidences of unity in the prior GMM's parameters, the algorithm was able to recover a learned petrophysical distribution that was close to the true distribution. The recovered variance of the background is $7.2 \cdot 10^{-3} [\ln(S/m)]^2$. This is less than the prior value of $0.01 [\ln(S/m)]^2$. This means that the algorithm recovered a background conductivity with a smaller variance than the one prescribed by the prior.

In addition to being closer to the ground truth, the inversion procedure converges similarly as the Tikhonov approach (Figures 3.8c and 3.8f). The PGI method took only two additional iterations, compared to the Tikhonov approach, to reach the geophysical and petrophysical target misfits (shown respectively in black and red in Figure 3.8f). They are reached respectively at the fifth and sixth iterations. These two Figures 3.8c and 3.8f also highlight that the smallness is now a term to be minimized in the PGI. A Tikhonov inversion is unconcerned about the value of Φ_s , and it usually increases when β decreases. In PGI, Φ_s measures how well the petrophysical and geological information is recovered.

Step-by-step of the PGI iterations

The iterations of the PGI are shown in Figure 3.9. Figures 3.9a and 3.9b show the initialization. The initial and reference model is a half-space with a conductivity equal to the background conductivity. The prior and initial petrophysical distribution Θ_{prior} was described in the initialization section for this example. The first iteration (Figures 3.9c and 3.9d) is the same as the first Tikhonov iteration, and the current recovered geophysical model is fairly smooth. In the Tikhonov

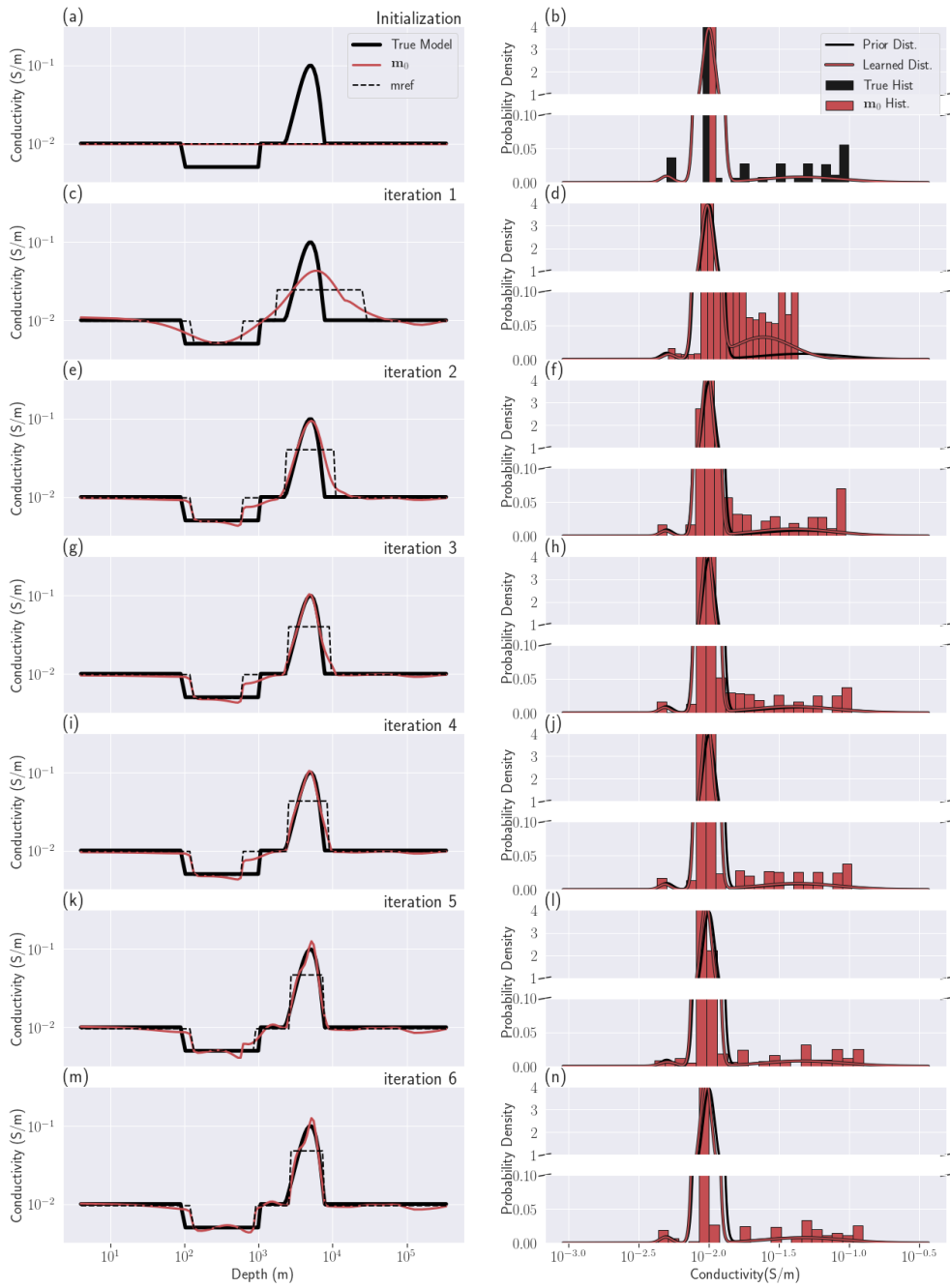


Figure 3.9: Iterations of the PGI MT1D example. Dist. stands for distribution. Hist. stands for histogram.

inversion, the reference model remains the same throughout the inversion. However, in the PGI, the reference model and smallness weights are updated at the end of each iteration. The updated reference model is determined from the learned petrophysical distribution applied to the current geophysical model, as described in equations (3.12) to (3.14). The recovered petrophysical distribution at this first iteration already distinguishes three units but displays higher variances than the prior. The conductivity contrasts are underestimated, but the overall geological classification is correct. The recovered geophysical model after the second step (Figures 3.9e and 3.9f), with the updated reference model and smallness weights from the previous step, starts to display the desired features both spatially and in its physical property distribution; a sharper resistive unit and smoother conductive unit are seen. The geophysical target misfit is reached at iteration 5 (Figure 3.9k and 3.9l), and the parameter α_s is increased. In one further step (Figures 3.9m and n), both the geophysical and petrophysical target misfits are reached. The last iteration successfully clustered the model values while conserving $\Phi_d \leq \Phi_d^*$. The sharp contrast of the resistive unit is well recovered as well as the smoothness of the conductive unit. The learned petrophysical distribution is very close to the prior distribution. It also has a lower variance for the background unit compared to its prior value, and thus is closer to the truth.

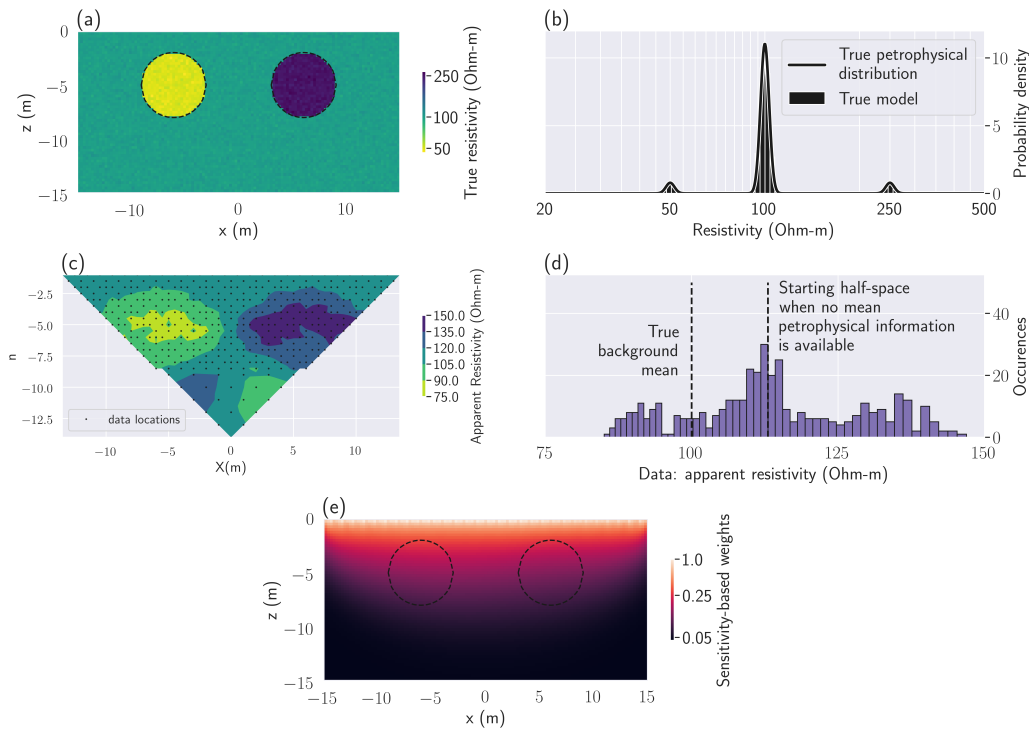


Figure 3.10: Setup of the DC resistivity example. (a): True conductivity. (b): True petrophysical distribution. (c): DC data to be inverted. (d): Histogram of the measured apparent resistivity. The best fitting half-space ($112 \Omega\text{m}$) is indicated by the vertical dashed line. (e): Sensitivity weights \mathbf{w} used for all inversions.

3.5.2 DC2D, buried cylinders: working with missing petrophysical information and adding geological information

In this example, I illustrate the performance of the PGI framework when no physical property mean values are available and compare it to the result when full petrophysical information is available. I then show how geological information, such as depth and thickness or rock units, can be incorporated.

Setup

I apply the procedure to a 2.5D DC resistivity problem (2D geology but 3D sources) to recover two cylindrical units, one conductive (with a mean resistivity of $50 \Omega\text{m}$), one resistive (with a mean resistivity of $250 \Omega\text{m}$), embedded in a background unit with a mean resistivity of $100 \Omega\text{m}$ (see Figure 3.10a). To make the model slightly more geologically realistic, I added Gaussian noise to the log-conductivity model. The noise had zero mean and a variance of $1 \cdot 10^{-3} [\ln(\text{S/m})]^2$ (see Figure 3.10b).

The survey is a dipole-dipole with electrode separation of 1 m and 2 m (Figure 3.10c). The maximum dipole separation is set to $n = 16$. A total of 419 resistance measurements are simulated. Unbiased Gaussian noise, with a standard deviation of 2% of the original value, is added to the forwarded geophysical data. A histogram of the apparent resistivity data is shown in Figure 3.10d.

For the inversion, I limit the active cells to the region covered by the survey, omitting the padding cells, as shown in Figure 3.10a. The active mesh is composed of 7021 cells. For the geophysical data misfit uncertainties, I used a floor value of $10^{-4} V/I$ in addition to the 2% noise standard-deviation.

For all of the inversions, I used a sensitivity weighting that is similar to that developed in Mehanee et al. (2005). This is used in place of the usual smoothing weights at the surface to compensate for the high sensitivities near electrodes. Those weights are shown in Figure 3.10e. Both Φ_d and Φ_{petro} are used as stopping criteria. To illustrate the functionality, I also incorporated the learned reference model in the smoothness term of the geophysical objective function. This was done towards the end of the inversion after the reference model was stabilized,

and Φ_d^* was reached (see algorithm 1, step 6).

To set benchmarks for the inversion results, I first carry out a Tikhonov inversion and a PGI with full petrophysical information. I then run a PGI without providing any information about the physical property mean values or the proportions. I finally run another PGI, still without means information, but with added geological information included through the use of local proportion weights in the GMM. All inversions start with the same geophysical objective function.

Tikhonov inversion

The Tikhonov inversion starts from the best fitting half-space of 112 Ωm , instead of the true background value of 100 Ωm (see Figure 3.10d). The inversion produces the result presented in Figure 3.11a. The two bodies are detected, but their edges are smoothed. This smoothness is also visible in the histogram of the model that is characterized by continuous values centred on the starting half-space value (Figure 3.11b). The conductivity values do not attain the true electrical conductivity of the anomalies. The geophysical target misfit is reached in six iterations (Figure 3.11c). The parameter β was cooled at each iteration, and the smallness term kept increasing; this is expected in the Tikhonov approach.

PGI with full petrophysical information

In this example, I first want to establish a benchmark result by using the true petrophysical distribution with global proportions. I fix the petrophysical distribution at the true one (Figure 3.10b) by setting all the confidences in the petrophysical prior to infinity. Thus, $\Theta = \Theta_{\text{prior}} = \Theta_{\text{true}}$ is fixed for all iterations. I start from a

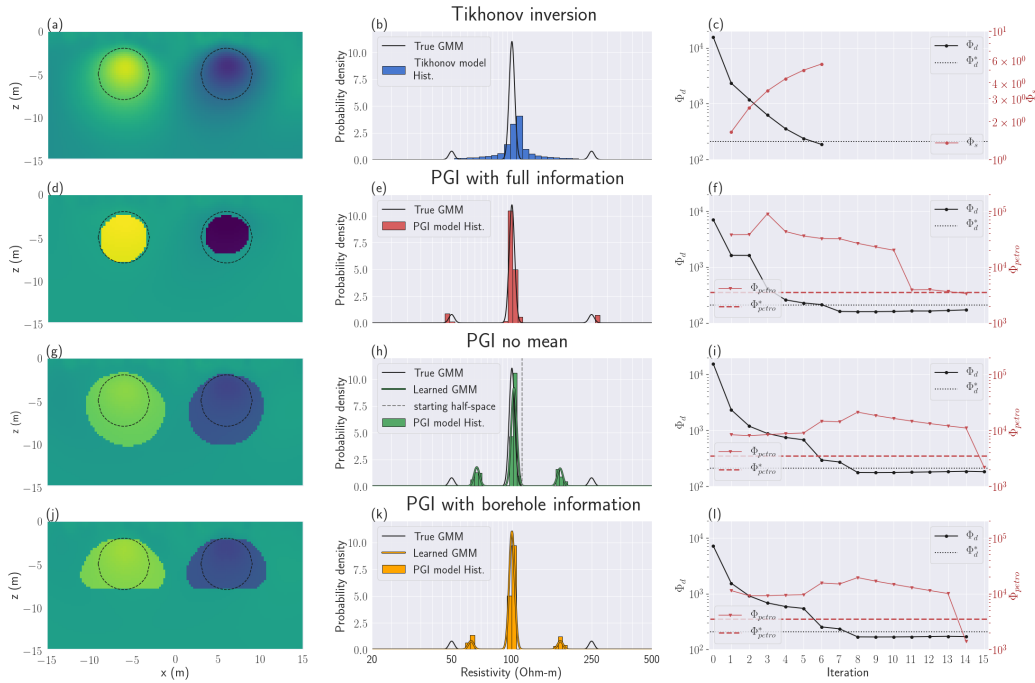


Figure 3.11: DC inversion results. The colour scale is the same as for the true model in Figure 3.10a. Panels (a), (b) and (c) present the recovered model, histogram and convergence curves, respectively, for the Tikhonov approach. Panels (d), (e) and (f) show the same plots for PGI when the true petrophysical distribution is provided. Panels (g), (h) and (i) show the results for PGI when no information on the proportions or the physical property means of the units is provided. Panels (j), (k) and (l) show how PGI, with no mean information, can be improved by adding information about the depth and thickness of the cylinders.

half-space with the true mean background value.

This benchmark inversion recovers the two cylinders (Figure 3.11d) quite well. The locations of the cylinders, their outer boundaries and their conductivities are in reasonable agreement with the true model. The geophysical model also satisfactorily fits the true petrophysical distribution being imposed (Figure 3.11e). The

geophysical target misfit is reached after seven iterations (Figure 3.11f). Seven more iterations are needed to reach the petrophysical target misfit while keeping $\Phi_d \leq \Phi_d^*$. The two increases of Φ_{petro} seen at iteration 3 and 7 correspond to β -coolings. This was necessary since the geophysical misfit was not decreasing enough (see algorithm 1, step 6). The important decrease seen at iteration 11 corresponds to the inclusion of the learned reference model in the smoothness. This helps me reach the petrophysical target misfit. This highlights the importance of incorporating a discontinuous reference model into the smoothness terms so that large gradients in the model are not penalized. This allowed the final model to have sharp boundaries, which is consistent with the true model.

PGI with no physical property means information

I now consider the situation where no prior information is known, except the expected number of units (three in this example). The framework can still be used, but the prior on the means and proportions are turned off. The confidences $\{\zeta, \kappa\}$ are thus set to zero (no prior information on the means or proportions). I used the true variances with infinite confidences \mathbf{v} in them. I thus have specified the petrophysical noise levels, which regulate how much each unit has to cluster around its unknown mean. This is analogous to choosing an appropriate geophysical data noise level. The inversion starts from the best fitting half-space, as in the Tikhonov inversion, since the true background value is now considered to be unknown.

The recovered geophysical model still displays a clustered aspect with structures close to the ground truth (Figure 3.11g). The volumes of the two cylindrical

units are overestimated. The histogram and model show three distinct units. Without the true means information, the recovered means of the cylinders are slightly shifted towards the background value (Figure 3.11h). Interestingly, the recovered mean of the background is closer to the true mean than the initial half-space model. The number of iterations to reach both target misfits is comparable to the PGI example that used full petrophysical information.

PGI with geological information

My next goal with this example is to illustrate how geological information might be included. It is motivated by the fact that, in the two previous PGI results (using full and no petrophysical information), the cylindrical units display various anomaly sizes, compared to the ground-truth, and extend to different depths. Suppose information about the anomalous zone's depth and thickness are provided. This additional information can be added to the inversion through local proportion parameters $\mathcal{P}(\mathbf{z})$, by making them vary with depth. At depths where the anomalous bodies are expected, prior expectations of encountering any of the three units are set equal (so here $\pi = 1/3$ for all three units for locations at depths between 2 m and 8 m). At depths where only the background is expected, the following values are set: $\mathcal{P}(\mathbf{z} = \text{background}) = 1$ and $\mathcal{P}(\mathbf{z} = \text{cylinders}) = 0$. Those proportions are summarized in table 3.1. I used these proportions, the means recovered from the PGI with no mean information, and the true variances, as Θ_{prior} in a new PGI. Proportions and variances are kept fixed, while means are still learned (confidences κ of zero).

Table 3.1: Proportions of the GMM $\mathcal{P}(\mathbf{z})$ as a function of depth to include geological information. Legend: bckgrd: background; cond.: conductive unit; res.: resistive unit.

Depth range (m)	$\mathcal{P}(\mathbf{z} = \text{bckgrd})$	$\mathcal{P}(\mathbf{z} = \text{cond.})$	$\mathcal{P}(\mathbf{z} = \text{res.})$
≤ 2	1	0	0
2 – 8	1/3	1/3	1/3
≥ 8	1	0	0

The recovered model (Figure 3.11j) is similar to the PGI result with no petrophysical information, except the anomalies are now restricted to the right depths. Comparing the two learned distributions, with and without depth information, the recovered conductivity values from the PGI model with geological information are closer to the ground-truth than the conductivities recovered from the PGI with no petrophysical or geological information (Figure 3.11k). The convergence of the algorithm is similar to the previous PGIs (Figure 3.11l).

3.5.3 Using PGI to reduce ambiguity: a field example

Any inversion result is affected by many terms and parameters in the objective function, but of particular interest here is the choice of a reference model. In a Tikhonov inversion, starting from different half-space reference models can lead to different solutions, and this complicates the interpretation. Some of the ambiguity might be reduced if more information is incorporated. The PGI approach allows me to add information, such as the desired number of geological units, that are otherwise difficult to use in a Tikhonov setting. Adding a constraint on the number of units to recover, without incorporating other extensive geological or petrophysical information, can be enough to reduce the realm of possible models.

I illustrate this on a field FDEM dataset (Ward & Hohmann, 1988) for saline water delineation. I begin by emphasizing the discrepancies seen in Tikhonov models using different half-space reference models. I then show that, by using PGI and assuming an expected number of distinct units, starting from different reference models leads to similar inversion results that have consistent petrophysical distributions and simplified structures. The lack of dependence upon the initial and initial reference models helps to build confidence in the final images.

Setup

The Bookpurnong irrigation District is part of the Riverland region of South Australia along the Murray River. The irrigation on the highland river bank has led to the salinization of the floodplain soil and threatens to make the area inhospitable for vegetation (Figure 3.12). The key issue is to determine if (and where) the freshwater river is charging the aquifer (this is the healthy scenario, called “losing stream”), or if the saline aquifer is charging the river, and thus contaminating the floodplain soil (“gaining stream” scenario). To help the work of hydrogeologists, various frequency and time-domain electromagnetic surveys have been conducted to characterize saline zones, which are diagnosed by an increase in electrical conductivity. High conductivities close to the surface will indicate a “gaining stream” scenario, while low conductivities will be a sign of a “losing stream”.

The Bookpurnong case study has been studied in previous publications (Viezoli et al., 2009, 2010; Yang, 2017). Here, I focus on the RESOLVE FDEM dataset, flown in 2008, which covers an area of approximately 6,650 m by 2,400 m.

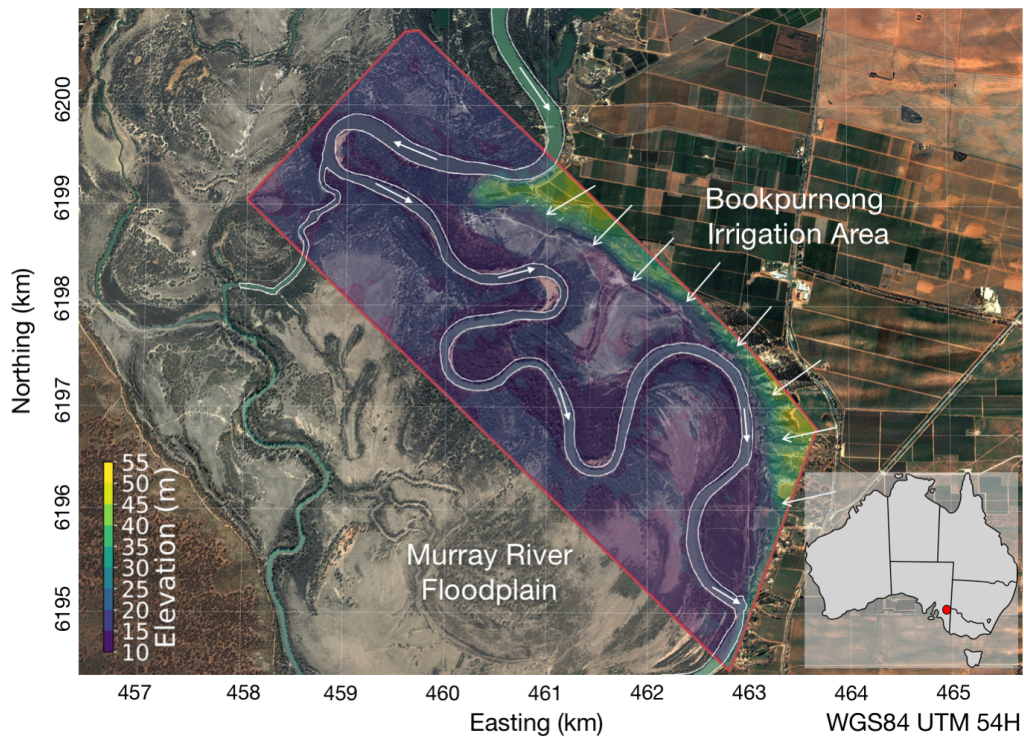


Figure 3.12: Bookpurnong survey area. The elevation of the survey area is represented as an overlaid colourmap. The white arrows represent the water flow, both from the river and the irrigation zone. Geographic coordinates system: WGS 84 / UTM 54H. Aerial images from Google Earth, ©2019 DigitalGlobe.

At each sounding, the RESOLVE system measures the real and imaginary parts of the induced magnetic field for 5 frequencies ranging from 382 Hz to 130.1 kHz. The survey consists of 1022 soundings, resulting in a total number of data of 10,220. For the geophysical noise levels, I use a standard deviation of 10% of the absolute value of the datum and add a 20 ppm floor value; this is consistent with previous studies.

Inversion setup

To invert the RESOLVE dataset, I choose a laterally-constrained 1D approach, similar to Viezzoli et al. (2008), using the EM1D module of the SIMPEG package (Heagy et al., 2017; Kang et al., 2018). Each sounding is inverted in 1D using a mesh, with 19 layers, which extends to a depth of 187 m. The cells increase in size from 2.5 m at the surface to 25 m for the last layer. Their thicknesses are used as weights in the regularization, which relates to an integral formulation of the regularizer (Oldenburg & Li, 2005).

For each Tikhonov and PGI approach, I run two separate inversions using 0.01 S/m (100 Ω m) and 1 S/m (1 Ω m) models, respectively, as reference models (thus four inversions are carried out). The reference models are also used as initial models $\mathbf{m}^{(0)}$. The reference model stays the same throughout the Tikhonov inversions while the PGI algorithm updates it.

Tikhonov inversions

The results of the Tikhonov inversions using two different reference models are summarized in Figure 3.13. Both Tikhonov models (Figures 3.13a and 3.13d) detect the river at the surface as a resistive feature; it is also visible where the cross-section crosses the river near 459 ,459.8 , 460.5, 461, 461.8 and 462.5 km on Figures 3.13b and 3.13e. Both models also pick up highly conductive features at depth, and the laterally-constrained regularization helps ensure horizontal continuity. The ranges of conductivity are similar to those observed in boreholes (Holland et al., 2008).

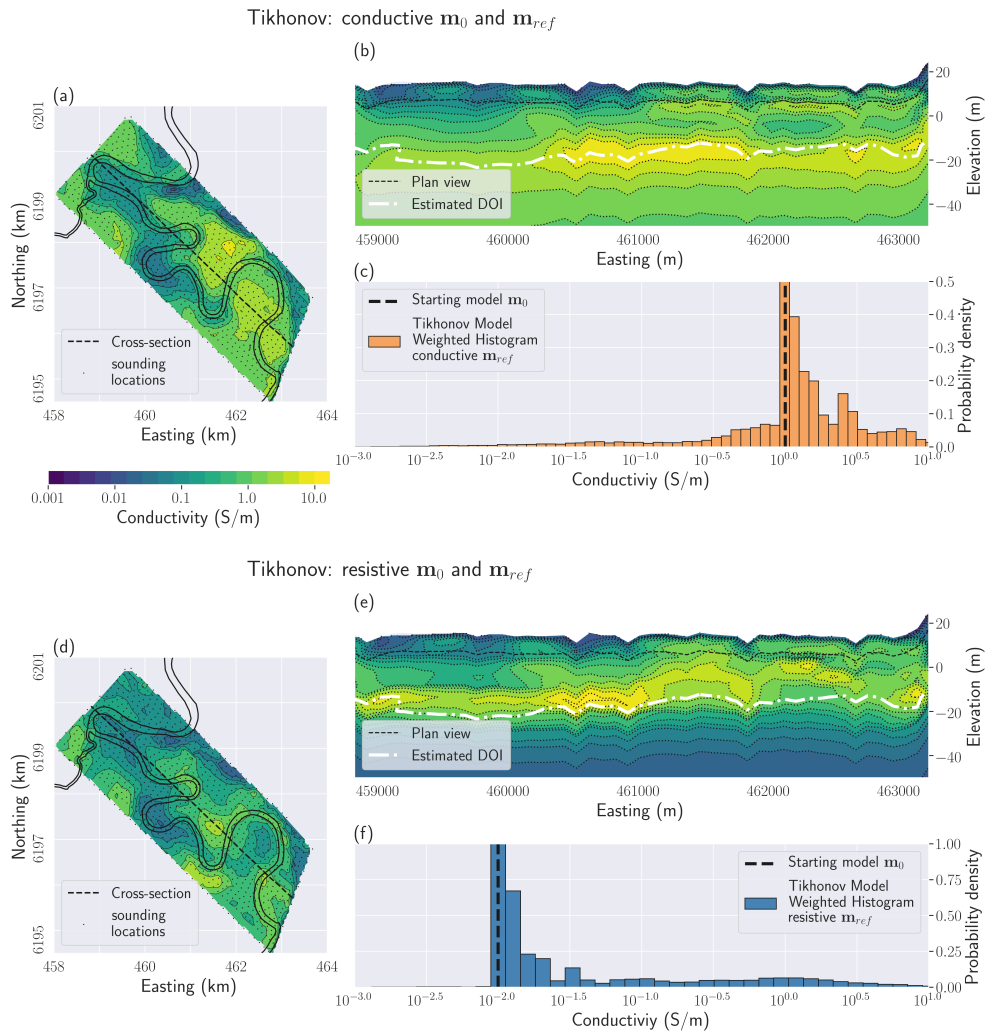


Figure 3.13: Tikhonov results with two different reference models. All figures share the same colour scale for conductivity. Panels (a), (b) and (c) show the results starting from a conductive half-space. Panels (d), (e) and (f) show the result starting from a resistive half-space. Panels (a) and (d) display the recovered geophysical models on a plan view at a depth of 8.5 m. Panels (b) and (e) display a cross-section of the recovered geophysical models. The Depth Of Investigation (DOI) is evaluated using the method presented in Oldenburg & Li (1999). Panels (c) and (f) display the histogram of the recovered model for each inversion.

In the north-west part of the area, the recovered conductivity models are consistent and transition smoothly from resistive at the surface to conductive at depth. In the south-east part of the area, more discrepancies in the two models are visible (see section 3.5.3 for quantification of the discrepancies). On the plan views (Figures 3.13a and 3.13d), the overall recovered conductivities in the biggest river bend differ by an order of magnitude between the two inversions. Inconsistent pocket-like structures are seen in both inversions in the cross-sections (Figures 3.13b and 3.13e). Both cross-sections, however, show that the conductive layer is closer to the surface in the South-East than in the North-West.

PGI

I now apply the PGI approach without providing specific petrophysical information; only the number of units is specified. I show that similar geophysical models and petrophysical distributions are obtained even though the inversions are carried out with different initial reference models.

As I did for the Tikhonov inversions, I now run two inversions starting from uniform 0.01 S/m (100 Ω m) and 1 S/m (1 Ω m) models, respectively, used as initial and initial reference models. For the conductive and resistive reference model cases, respectively, both the Tikhonov and PGI approaches start with the same objective function; the models after the first iteration are thus identical.

For the prior petrophysical distribution, I do not specify any prior value for the mean conductivity values nor the proportions; their respective confidence parameters are thus set to zero. I choose variances of $0.1[\ln(\text{S/m})]^2$. I set the confidences

in the prior variances to unity. My goal with this choice is to recover a model with distinct units but still reasonably smooth.

A critical point here is to choose the number of distinct units to recover. I assume that there are three units, as this matches the interpretation goal of distinguishing freshwater from salinized water, with an additional transition zone. This adds constraint on the models to recover.

The PGI results are compiled in Figure 3.14. All PGI have reached their geophysical and petrophysical misfits. The recovered models (Figures 3.14a and 3.14d) are more consistent with each other than those in the Tikhonov case; I will discuss this later in section 3.5.3.

Counterintuitively, by clustering the histograms, the resulting model appears smoother by forcing more homogeneity inside each distinct unit. Neither cross-section (Figures 3.14b and 3.14e) shows the pocket-like structure in the south-east end of the profile that was observed in the Tikhonov inversions; it indicates that those features were not robust. The high conductivity layer is closer to the surface in the South-East than in the North-West in both models.

The histograms and recovered petrophysical distributions (Figures 3.14c and 3.14f) display several interesting characteristics. First, three distinct units are recovered that can be interpreted as fresh, transition and saline zones. The learned means of the clusters are very similar between the two inversions. In the case of the resistive initial model, the resistive unit conductivity has been corrected to about 0.017 S/m (60 Ω m). The same phenomenon happens in the case with a conductive initial model, with a corrected conductive unit conductivity value

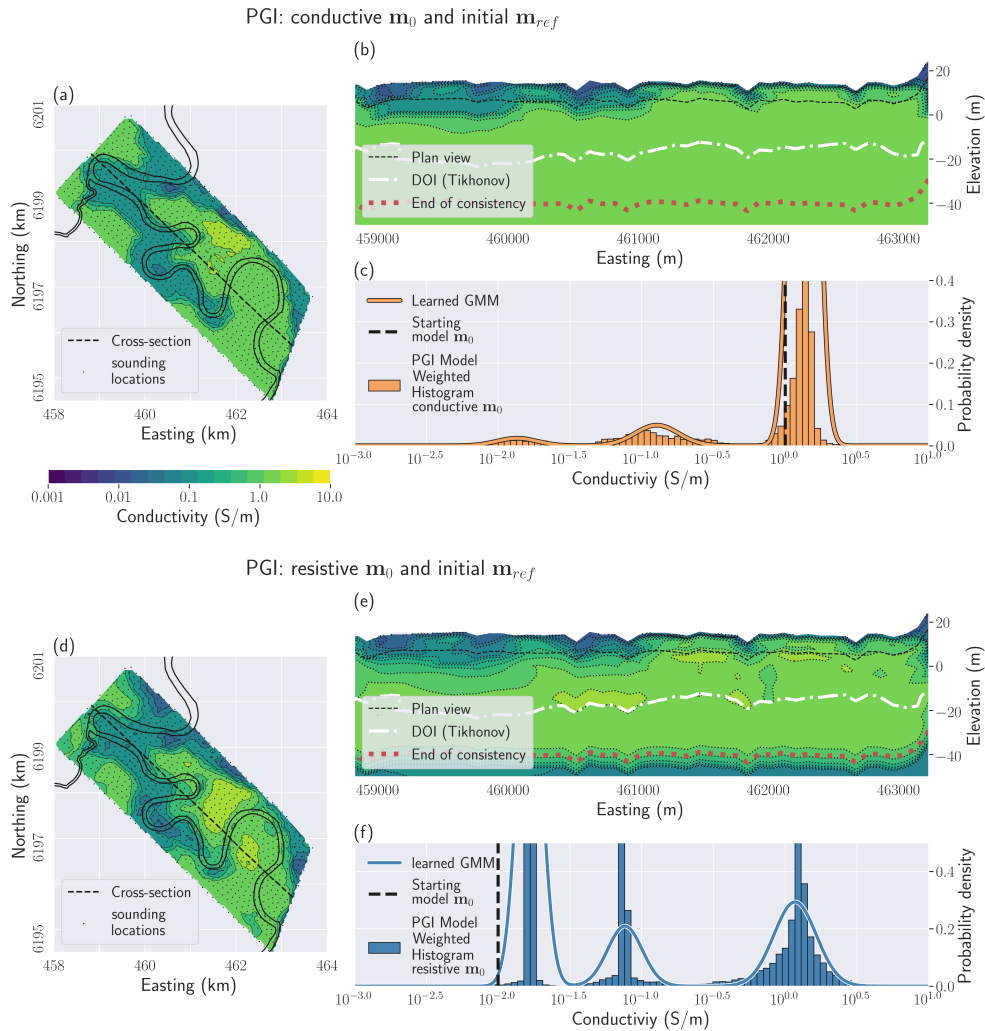


Figure 3.14: PGI results with two different initial reference models. All figures share the same colour scale for conductivity. Panels (a), (b) and (c) show the results starting from a conductive half-space. Panels (d), (e) and (f) show the results starting from a resistive half-space. Panels (a) and (d) display the recovered geophysical models on a plan view at a depth of 8.5 m. Panels (b) and (e) display a cross-section of the recovered geophysical models. Panels (c) and (f) display the histogram of the recovered model and the learned petrophysical distribution for each inversion.

of 1.35 S/m (0.74 Ω m). This behaviour was noticed in the DC example (section 3.5.2) when starting from a biased background value. The major difference between the GMM for the two models is the variance and proportion of the most resistive and most conductive units. This is due to the volume of the region in the padding zones that are outside the region of influence of the data. The values of conductivity in those regions stay close to the cluster mean which is closest to the conductivity of the initial reference model.

PGI - Tikhonov comparison

In addition to the removal of the unnecessary structure mentioned earlier, the models recovered with the PGI approach display more consistent subsurface features than do the Tikhonov models. To quantify the similarities between models within the same methodology but with different initial and reference models, I adopt an approach analogous to the Depth Of Investigation (DOI) estimation presented in Oldenburg & Li (1999). For the two Tikhonov and the two PGI conductivity models respectively, which for clarity in the notation are referred to in the following equation as electrical resistivity ρ_1 and ρ_2 , I compute their maximum ratio r everywhere:

$$\mathbf{r} = \max\left(\frac{\rho_1}{\rho_2}, \frac{\rho_2}{\rho_1}\right) (1 \leq r \leq \infty). \quad (3.31)$$

A ratio r of unity indicates similar values of conductivity. The higher the value of r , the more the two models differ. Figure 3.15 shows the result of this two-by-two comparison. The two PGI models are quite consistent, with ratio r values close to unity almost everywhere, except in a small area in the North-West. On the

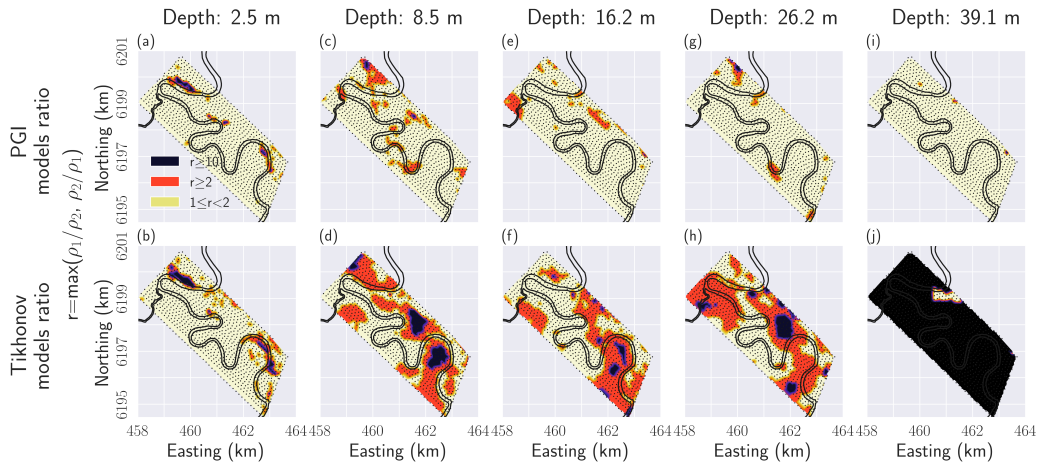


Figure 3.15: Consistency comparison between the two Tikhonov and the two PGI models, starting with conductive and resistive initial and reference models. The first row displays the ratio r of the two PGI conductivity models at different depths. The bottom row displays the same ratio for the two Tikhonov conductivity models. The depth of the plan views increases from left to right. Pale yellow means the two conductivity models differ by less than a factor 2. Orange highlights areas where the recovered conductivities differ by more than a factor 2. Dark purple emphasizes area where the two recovered conductivity models differ by more than a factor 10.

contrary, the Tikhonov inversions show significant discrepancies, even in the near-surface, with r values greater than 2 in most of the survey area. This is especially visible near the important bend in the river in the South-East where discrepancies of more than an order of magnitude ($r \geq 10$) are observed (dark areas in Figure 3.15). Figure 3.15j highlights when the Tikhonov inversions reached their DOI and where the final model is controlled mostly by the regularization. It is worth noticing that the PGI models are still consistent past the DOI estimated from the Tikhonov inversions (Figures 3.14b and 3.14e).

Field example summary

I demonstrated that, even in the near-surface above the Depth Of Investigation (DOI), the Tikhonov inversions had different structures when different initial and reference models were used. On the contrary, the two PGI lead to similar near-surface models with consistent petrophysical distributions. The removal of structures, evidently not required by the data, and the simplification of the geology provide a result that is more appealing to interpret geologically. Making a reasonable guess about the variances and the number of units was the crucial additional information required to achieve this. All four models point to a “losing stream” scenario in the North-West while three (both PGI models and the Tikhonov inversion with a conductive reference model) indicate a “gaining stream” in the South-East. This is coherent with the conclusions given in Viezzoli et al. (2009, 2010) and Yang (2017). To further extend the analysis, ground-truthing the depth of the saturation salinization zone and adding it into the PGI as geological information, or adding petrophysical measurements, would be required.

3.6 Discussion

I have presented a framework for carrying out a Petrophysically and Geologically guided Inversion (PGI), which allows the user to recover a quasi-geology model (Li et al., 2019) and a petrophysical distribution in addition to the geophysical model. The framework has three main modules, each of which is formulated as a MAP estimate. The framework is flexible, and goals, achieved by others and using different approaches, can be incorporated while the reverse is not true.

Carrying out an inversion that includes three separate sub-problems that communicate with each other, and for which two target misfits are to be achieved, is challenging. To address this, I have provided a pseudocode as well as a flowchart in section 3.4.2. The important part of the procedure is the initialization step, where the user must specify what is known, how to incorporate it, and what they want as an end product. The examples explore those various aspects as well as the convergence of the PGI approach.

The crucial component of my framework is to provide a different role for the smallness component of the regularization term in the geophysical objective function. An evolving reference model, tied to different units in a GMM, ultimately allows this term to be viewed as a quantitative metric for determining how well the petrophysical and geological data are fit. This has many advantages. The inverse problem is now solved by finding a model \mathbf{m} and a reference model \mathbf{m}_{ref} , along with the smallness weights, such that the geophysical, petrophysical, and geological data are fit. This complicates the inversion, but the procedure is greatly simplified compared to adding additional terms, along with their adjustable hyperparameters, in the regularization. This also allows this research to be incorporated with other developments done using the Tikhonov approach. For example, when sharp contrasts are expected, such as in the DC example developed in section 3.5.2, the effects of using sparse norms for the model gradients in the smoothness terms (Fournier & Oldenburg, 2019) are worth exploring. This would allow the combined use of petrophysical and structural data to guide the inversion.

A solution is achieved by first focusing on the geophysical data misfit and solv-

ing the optimization problem at successively smaller values of the global trade-off parameter β . In some cases, finding an acceptable model to the geophysical data also makes the petrophysical misfit sufficiently small. If it doesn't, then α_s is adjusted to control the relative weight between the smallness and the other components of the objective function. So far, my heuristic approach has worked satisfactorily but searching simultaneously for optimal β and α_s values such that both $\Phi_d(\mathbf{m}) \simeq \Phi_d^*$ and $\Phi_{\text{petro}}(\mathbf{m}) \simeq \Phi_{\text{petro}}^*$ is a more advanced optimization process and deserves further research. For example, Sun & Li (2018) is entirely dedicated to the problem of refining the values of β and α_s within the guided FCM inversion approach (Sun & Li, 2015), and only for magnetic linear problems.

The use of weights \mathbf{w} based on the physics of the survey, in the regularizer, is a common practice in geophysical inversion, either through depth, distance or sensitivity-based weights (Fournier et al., 2020; Li & Oldenburg, 1996, 1998; Mehanee et al., 2005). There are often necessary in practice to obtain a reasonable result from an inverse problem with greatly varying sensitivities (e.g. potential fields or near electrodes for DC). It could be considered a theoretical issue, as the prior is no longer independent from the likelihood function. However, this is a consideration that is outside the scope of the current thesis. It concerns the field of geophysical inversion as a whole and, as such, is not specific to the PGI framework being developed here.

Further work is also required for the best way to evaluate the petrophysical target misfit. In my framework, Φ_s is a weighted petrophysical misfit. Since the weights \mathbf{w} are known, $\mathbb{E}[\Phi_s]$ can be evaluated and used as a fitting criterion. An-

other option is to evaluate Φ_{petro} ; this amounts to evaluating Φ_y without weights. Both have worked for me, but working with Φ_{petro} has constantly produced good results, and it is appealing to have a stopping criterion tied only to the petrophysical and geological characteristics of the model.

Another key component of my framework is the possibility for the algorithm to learn all the parameters of a suitable GMM distribution when little to no information is known *a priori*. The MAP-EM algorithm has been an essential element in achieving this goal. The minimum requirement is to provide an expected number of distinct units and a prior petrophysical noise level for each unit.

The MAP-EM algorithm with semi-conjugate priors formalizes the update of the means done in Sun & Li (2015) and generalizes it to the other GMM's parameters. An important aspect of the formulation of the MAP-EM algorithm is the incorporation of the volume elements into the evaluation of the GMM's parameters, rather than just working with cell-counts. Working with volumetric values ensures that the recovered GMM's parameters are independent of the discretization. The estimation of the GMM's parameters includes a prior value weighted by the confidences in this prior, in a similar sense that there is a confidence β in the geophysical model prior during the geophysical inversion. So far, values of unity or above for the confidences in the variances have worked well whether or not I knew the true petrophysical distribution. Confidences in the means and proportions appear dependent on the quality of the prior knowledge. Their effects are to be further investigated (see section 6.3), and if cooling or warming those parameters, similar to what is done with β , can impact the recovery or convergence.

3.7 Conclusions

I have developed a framework for carrying out Petrophysically and Geologically guided Inversion (PGI) using a dynamic Gaussian Mixture Model (GMM) prior. Importantly I achieve my goal of incorporating both geological and petrophysical information in geophysical inversions without including an additional term in the objective function. Rather, I update the reference model and the smallness weighting matrix at each iteration of the geophysical model through the optimization of posterior probability distributions. This allows my work to be compatible with previous Tikhonov approaches and readily adapted to existing inversion codes. The flexible prior formulation allows me to refine the petrophysical model as part of the iterative process. The inversion continues until the geophysical, geological and petrophysical data are fit. For that purpose, I have defined a target misfit to measure how well the recovered geophysical model fits the petrophysical and geological distribution. I have presented a suite of synthetic and field examples to illustrate important aspects of my framework, especially in demonstrating how prior petrophysical and geological information is incorporated. I have also shown that detailed knowledge of the petrophysical or geological properties is not required to make significant gains in the recovered geophysical models. The examples deal with a single physical property, but my framework has been designed to carry out joint inversion of different types of geophysical data; this topic is addressed in the next chapter.

Chapter 4

Extension to multi-physics inversions

4.1 Introduction

Chapter 3 presented a petrophysically and geologically guided inversion (PGI) framework that generalized concepts presented in Giraud et al. (2017, 2019b); Grana & Della Rossa (2010) and Sun & Li (2015). I showed how geological and petrophysical knowledge represented as a univariate Gaussian Mixture Model (GMM) could be incorporated in a voxel-based geophysical inversion through a single smallness term. Each contrasting geological unit was represented by a univariate Gaussian distribution, which summarized its physical property signature. Geological information was included in the GMM through its proportions in a manner similar to that of Giraud et al. (2017, 2019b). The log-likelihood of the GMM

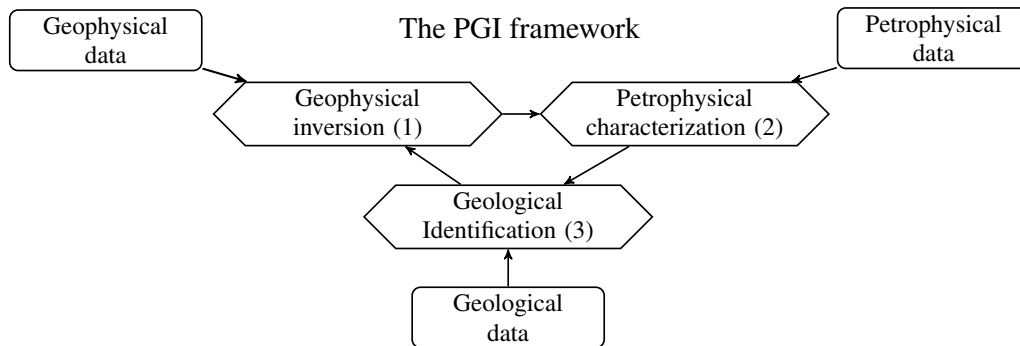


Figure 4.1: A graphical representation of the PGI framework. Each diamond is an optimization process that requires data (shown in rectangular boxes) as well as information provided by the other processes (modified from Figure 3.1).

was then used to regularize the geophysical inversion; this is analogous to the approach taken by Grana & Della Rossa (2010). Incorporating both petrophysical and geological information into a single smallness term in the regularization has several advantages. First, it does not require adding a term in the classic Tikhonov formulation. Second, this approach brings the petrophysical data to the same level as the geophysical data, which allows me to define a misfit, with a target value, between the geophysical model and the petrophysical and geological data. The iteration steps were decomposed into a suite of cyclic optimization problems across the geophysical, petrophysical, and geological data. The petrophysical step formalized the idea of learning the physical property mean values described in Sun & Li (2015) and generalized it to enable the variances and proportions of the GMM to be learned as well during the inversion. These updates to the GMM parameters allowed me to work with partial petrophysical information. The geological step built at each iteration a “quasi-geology model” (Li et al., 2019), based on the

current geophysical and petrophysical models. In chapter 3, I applied the PGI approach on synthetic and field data, but the analysis was restricted to single datasets and a single physical property.

This chapter extends the PGI framework to perform multi-physics inversions, involving several physical properties. I show how geological and petrophysical information represented as a multivariate GMM can be used to couple multiple voxel-based geophysical inversions through a single smallness term in the regularization. The updates to the means, covariances and proportions of the GMM are extended to inversions with multiple physical properties, which expands the work of Sun & Li (2016). Tools for handling various types of relationships between physical properties are designed, which further develop ideas presented in Sun & Li (2017). These capabilities, and the gains that they generate, are demonstrated on inversions of synthetic gravity and magnetic data.

I start by generalizing the PGI approach to the case of multiple physical properties and governing equations for performing multi-physics inversions. I then delineate my strategy to address the numerical challenges of finding a solution to the inverse problem that fits each geophysical dataset and, at the same time, adequately fits the petrophysical and geological data. Finally, I demonstrate the advantages of performing joint inversions, with various levels of prior knowledge, by using a synthetic model of the DO-27 kimberlite pipe, in the Tli Kwi Cho (TKC) cluster, Northwest Territories, Canada (Jansen & Witherly, 2004).

4.1.1 Multivariate GMM: modelling multiple physical properties

To extend the approach presented in chapter 3, I represent the petrophysical signature of each geological unit j ($j = 1..c$) as a multivariate Gaussian probability distribution, denoted by \mathcal{N} . The Gaussian distribution representing the q physical properties of interest for each unit is defined by its mean $\boldsymbol{\mu}_j$ (vector of size q), and its covariance matrix $\boldsymbol{\Sigma}_j$ (matrix of size $q \times q$), plus its proportion π_j .

The multivariate GMM simply sums the Gaussian probability distributions representing each known rock unit, weighted by their proportion:

$$\mathcal{P}(\mathbf{x}|\Theta) = \sum_{j=1}^c \pi_j \mathcal{N}(\mathbf{x}|\boldsymbol{\mu}_j, \boldsymbol{\Sigma}_j). \quad (4.1)$$

The variable Θ holds the GMM global variables $\Theta = \{\pi_j, \boldsymbol{\mu}_j, \boldsymbol{\Sigma}_j\}_{j=1..c}$. With some modifications, the GMM can also represent nonlinear relationships between physical properties, such as polynomial as presented in Onizawa et al. (2002). I present those modifications in Appendix A, along with an example of an inversion with various nonlinear relationships between two physical properties.

The geological classification (or membership) is denoted \mathbf{z} . It is defined as the most probable geological unit, given a set of values \mathbf{x} for the q physical properties:

$$z = \operatorname{argmax}_{j \in \{1..c\}} \pi_j \mathcal{N}(\mathbf{x}|\boldsymbol{\mu}_j, \boldsymbol{\Sigma}_j). \quad (4.2)$$

The categorical variable is key for building a “quasi-geology model” (Li et al., 2019) from the physical properties model obtained by inversion. This corresponds to Process 3 in the PGI framework (Figure 4.1).

4.1.2 Motivation for simultaneously inverting multiple physical properties

In Figure 4.2, I present an example of a GMM with three distinct rock units characterized by two physical properties (two-dimensional space). The background is coloured according to the geological identification that would be made at each location using equation (4.2). The bottom and left panels represent the marginal GMM probability distribution for each physical property individually. While all three units are distinct in the two-dimensional space, they overlap significantly when only considering one physical property at the time. For physical property 1, rock units 1 and 2 are distinct while rock unit 3 is indistinguishable from rock unit 1. For physical property 2, rock units 1 and 3 are now distinct while unit 2 is indistinguishable from either rock units 1 or 3. This highlights that it is only by jointly inverting for several physical properties that one might be able to uniquely identify three rock units. Units that might not be distinguishable in one survey may be in another one, and by simultaneously working with both physical properties in an inversion, I am able to explore the multidimensional physical property space in the centre panel of Figure 4.2. In the following section, I show how to use this probability distribution that links the various physical properties as *a priori* information to regularize the multi-physics inverse problem.

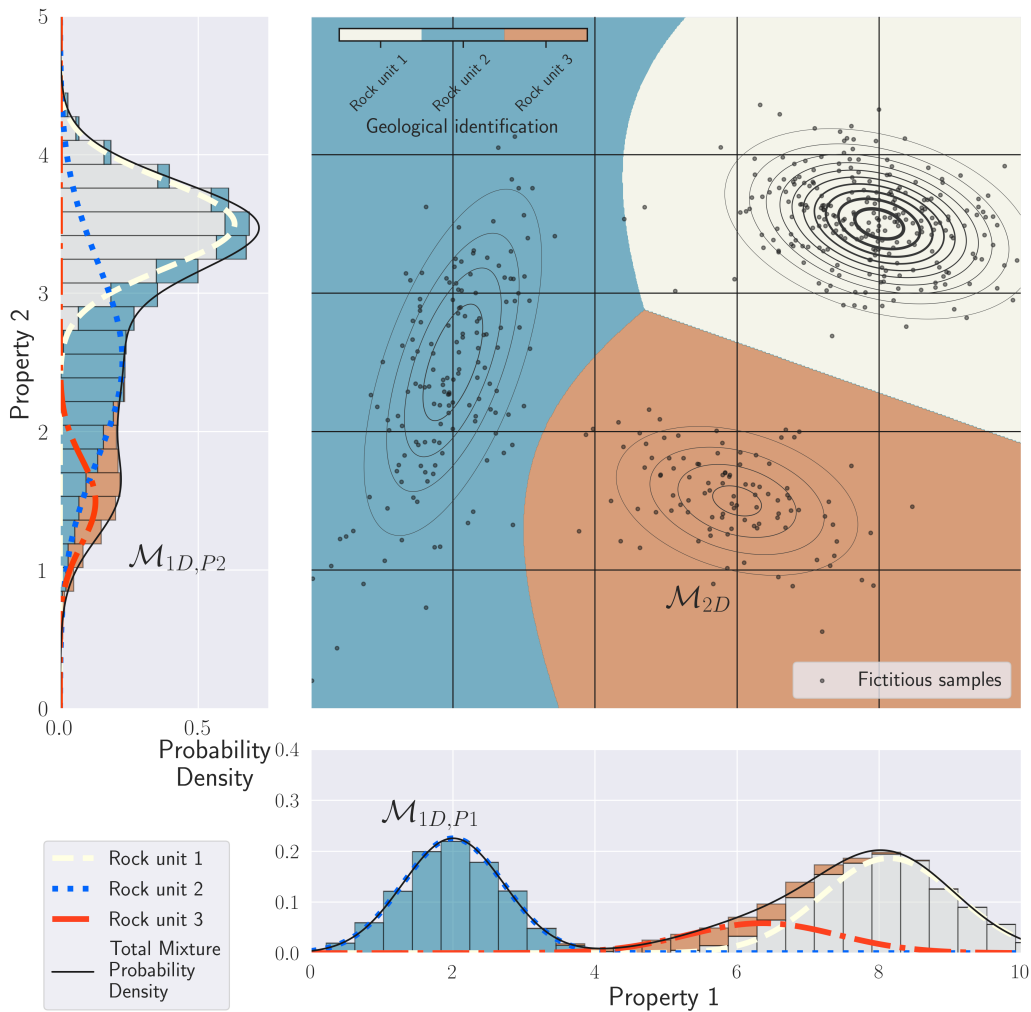


Figure 4.2: Example of a two-dimensional GMM with three rock units. The background is coloured according to the geological classification evaluated by equation (4.2). A thicker contour line indicates a higher iso-probability density level. On the left and bottom panels, I provide the 1D projections of the total and individual probability distributions for each physical property, and the cumulative histograms of the fictitious samples of each rock unit.

4.2 Extension of the PGI framework to multi-physics inversions

4.2.1 Definition of the GMM prior

In chapter 3, I developed a GMM smallness prior to include petrophysical and geological information in inversions involving only one type of geophysical survey with only one physical property to recover. In equation (4.3), I propose a generalized version of this GMM smallness prior that is designed to couple multiple physical properties and incorporate geological information. Note that the means are now vectors that are the size of the number of different physical properties, and the scalar variance becomes a full positive-definite matrix of the same size. The parameters are both spatially (index i) and lithologically (index j) dependent.

$$\mathcal{M}(\mathbf{m}|\Theta) = \prod_{i=1}^n \sum_{j=1}^c \mathcal{P}(z_i = j) \mathcal{N}(\mathbf{m}_i | \boldsymbol{\mu}_j, \mathbf{W}_i^{-\top} \boldsymbol{\Sigma}_j \mathbf{W}_i^{-1}), \quad (4.3)$$

where:

- c is the number of distinct rock units.
- n is the number of active cells in the mesh.
- \mathbf{m}_i represents the q physical property values at location i .
- $\mathcal{P}(z_i = j)$ is the *a priori* probability of observing rock unit j at location i .

It can be either constant over the whole area, then denoted by π_j , or locally determined by *a priori* geological knowledge.

- $\boldsymbol{\mu}_j$ contains the means of the physical properties of rock unit j .
- $\boldsymbol{\Sigma}_j$ is the covariance matrix of the physical properties of rock unit j .
- \mathbf{W}_i^{-1} is a weighting term at location i , used for example to include depth or sensitivity weighting. I define it from weights $\{w_{i,p}, i = 1..n, p = 1..q\}$; this is a scalar value for each cell i and physical property p . \mathbf{W}_i is defined as a diagonal matrix made of the combination of all the weights at the specific location i : $\mathbf{W}_i = \text{diag}(\mathbf{w}_i)$, with the same notation convention as for the model \mathbf{m} . This allows the weighting to be different for each physical property. I can thus weight each physical property according to the survey on which it depends.
- Θ holds the GMM global variables $\Theta = \left\{ \pi_j, \boldsymbol{\mu}_j, \boldsymbol{\Sigma}_j \right\}_{j=1..c}$.

This GMM probability distribution (equation (4.3)), representing the current geological and petrophysical knowledge, is used to define the smallness term in the regularization. In the next subsection, I use this multivariate GMM prior to develop a modified objective function for the inverse problem.

4.2.2 The multi-physics PGI geophysical objective function

Chapter 3 demonstrated how to use the negative log-likelihood of a univariate GMM as the smallness term in the Tikhonov inverse problem. The resulting smallness term could be approximated by a least-squares misfit between the current model and a reference model \mathbf{m}_{ref} , which was updated at each iteration, as was the smallness matrix \mathbf{W}_s . Those dynamic reference model and smallness matrix

updates were determined based on the current geophysical model and the geological and petrophysical prior information. The least-squares approximation enabled the use of the PGI framework with compiled codes working with the Tikhonov formulation.

Generalizing the result obtained in chapter 3 to multiple physical properties, I use the negative log-likelihood of the GMM defined in equation (4.3) to obtain a single smallness term that couples all of the model parameters. That smallness term can be approximated by the following least-squares misfit:

$$\Phi_s(\mathbf{m}) = \frac{1}{2} \sum_{i=1}^n \|\mathbf{W}_s(\Theta, z_i)(\mathbf{m}_i - \mathbf{m}_{\text{ref}}(\Theta, z_i))\|_2^2, \quad (4.4)$$

with:

$$z_i = \underset{\tilde{z}_i}{\operatorname{argmax}} \mathcal{P}(\mathbf{m}|\tilde{z}_i) \mathcal{P}(\tilde{z}_i), \quad (4.5)$$

$$\mathbf{m}_{\text{ref}}(\Theta, z_i) = \boldsymbol{\mu}_{z_i}, \quad (4.6)$$

$$\mathbf{W}_s(\Theta, z_i) = \boldsymbol{\Sigma}_{z_i}^{-1/2} \mathbf{W}_i, \quad (4.7)$$

where $\boldsymbol{\Sigma}^{-1/2}$ is the upper triangular matrix from the Cholesky decomposition of the precision matrix $\boldsymbol{\Sigma}^{-1}$.

My implementation can handle either the log-likelihood of the GMM or its least-squares approximation. When the petrophysical signature of the rock units are not known, I also showed that it is possible to learn the parameters of the GMM (section 3.3.2, Figure 4.1, Process 2). The extension of that learning process to multiple physical properties is developed in section 4.3.

4.2.3 Petrophysical target misfit

The PGI smallness expresses a misfit between the petrophysical and geological information and the geophysical model. To measure the goodness of fit and define a stopping criterion for the petrophysical misfit, I defined in section 3.4.1 a measure Φ_{petro} and its target value Φ_{petro}^* . This measure is similar to the PGI smallness term but without the weights \mathbf{W}_i in equation (4.7). The same approach can be taken here to define the value Φ_{petro} for the multivariate case:

$$\Phi_{\text{petro}}(\mathbf{m}) = \frac{1}{2} \sum_{i=1}^n \|\tilde{\mathbf{W}}_s(\Theta, z_i)(\mathbf{m}_i - \mathbf{m}_{\text{ref}}(\Theta, z_i))\|_2^2, \quad (4.8)$$

with:

$$\tilde{\mathbf{W}}_s(\Theta, z_i) = \boldsymbol{\Sigma}_{z_i}^{-1/2}, \quad (4.9)$$

where z_i and \mathbf{m}_{ref} are the same as in equations (4.5) and (4.6).

Looking at the term Φ_{petro} (equation (4.8)) from a probabilistic point of view (Tarantola, 2005), each variable \mathbf{m}_i follows a multivariate Gaussian of dimension q , with mean $\mathbf{m}_{\text{ref}}(\Theta, z_i)$, and covariance matrix $(\tilde{\mathbf{W}}_s(\Theta, z_i)^\top \tilde{\mathbf{W}}_s(\Theta, z_i))^{-1}$. Thus, the variable $\tilde{\mathbf{W}}_s(\Theta, z_i)(\mathbf{m}_i - \mathbf{m}_{\text{ref}}(\Theta, z_i))$ follows a multivariate Gaussian variable with mean $\mathbf{0}$ and an identity covariance matrix. Thus, the sum in Φ_{petro} follows a chi-squared distribution and I can apply Pearson's chi-squared test (Pearson, 1900). The target misfit value Φ_{petro}^* is defined as the expectation of Φ_{petro} :

$$\Phi_{\text{petro}}^* = E[\Phi_{\text{petro}}] = \frac{n \cdot q}{2}, \quad (4.10)$$

with n being the number of active cells in the mesh and q being the number of physical properties. This generalizes the result obtained in chapter 3 ($q = 1$). This is a similar approach to the definition of a target misfit for the geophysical data as given in section 2.5.3.

The algorithm stops when all of the target misfits, geophysical and petrophysical, are achieved. Next, I generalize the petrophysical characterization step (Figure 4.1, Process 2), introduced in section 3.3.2, to the multivariate case.

4.3 Updating the Gaussian mixture model in multi-dimensions

In this section, I generalize the learning of the GMM parameters, presented in section 3.3.2, to multivariate Gaussian distributions, representing multiple physical properties. The main difference comes from the fact that the means are now vectors (they are scalars in 1D) and that the scalar variances in 1D become covariance matrices. The confidences in the means $\{\boldsymbol{\kappa}\}$ are also defined as vectors. Following section 2.4, I define the problem as a MAP estimate of the GMM's means, proportions and covariance matrices. I again choose to follow a conjugate prior approach for the choice of the prior distributions $\mathcal{P}(\Theta)$ (equation (3.15)). I use the MAP-EM) algorithm to estimate the parameters (Dempster et al., 1977).

The computation of the responsibilities for the E-step of the MAP-EM algorithm stay the same as in chapter 3, except for the dimension of the parameters:

$$n_{ij}^{(k)} = \frac{\mathcal{P}(z_i = j)^{(k-1)} \mathcal{N}(\mathbf{m}_i | \boldsymbol{\mu}_j^{(k-1)}, \boldsymbol{\Sigma}_j^{(k-1)})}{\sum_{t=1}^c \mathcal{P}(z_i = t)^{(k-1)} \mathcal{N}(\mathbf{m}_i | \boldsymbol{\mu}_t^{(k-1)}, \boldsymbol{\Sigma}_t^{(k-1)})}. \quad (4.11)$$

The update to the proportions is similar to the univariate case (equation (3.18)):

$$\pi_j^{(k)} = \frac{V_j^{(k)} + \zeta_j \pi_{j \text{ prior}} V}{V(1 + \sum_{t=1}^c \zeta_t \pi_{t \text{ prior}})}, \quad (4.12)$$

with:

$$V_j^{(k)} = \sum_{i=1}^n v_i n_{ij}^{(k)}, \quad (4.13)$$

$$\text{and } V = \sum_{i=1}^n v_i, \quad (4.14)$$

where ζ_j is the confidence in the prior proportion $\pi_{j \text{ prior}}$ of the rock unit j , v_i is the volume of the i^{th} cell and V is the volume of the active mesh, allowing the estimates to be mesh-independent by using volumetric proportions.

I generalize the update to the means (equation (3.23)) for each physical property p as:

$$\mu_j^{p(k)} = \frac{V_j^{(k)} \bar{m}_j^{p(k)} + \kappa_j^p \pi_{j \text{ prior}} V \mu_{j \text{ prior}}^p}{V_j^{(k)} + \kappa_j^p \pi_{j \text{ prior}} V}, \quad (4.15)$$

with:

$$\bar{\mathbf{m}}_j^{(k)} = \frac{\sum_{i=1}^n v_i n_{ij}^{(k)} \mathbf{m}_i}{V_j^{(k)}}, \quad (4.16)$$

where κ_j^p is the confidence in $\mu_{j \text{ prior}}^p$, which is the prior mean of the physical property p of the rock unit j . The confidences $\{\boldsymbol{\kappa}\}$ are thus consider as vectors now. This is an important tool that I use in section 4.5.5 to formulate a geologic assumption about the model.

Finally, the covariance matrices update has a similar form as in equation (3.25):

$$\boldsymbol{\Sigma}_j^{(k)} = \frac{V_j^{(k)} \boldsymbol{\Sigma}_{\bar{\mathbf{m}}_j}^{(k)} + v_j \pi_{j \text{ prior}} V \boldsymbol{\Sigma}_{j \text{ prior}}}{V_j^{(k)} + v_j \pi_{j \text{ prior}} V}, \quad (4.17)$$

with:

$$\boldsymbol{\Sigma}_{\bar{\mathbf{m}}_j}^{(k)} = \frac{1}{V_j^{(k)}} \sum_{i=1}^n v_i n_{ij}^{(k)} (\mathbf{m}_i - \bar{\mathbf{m}}_j^{(k)}) (\mathbf{m}_i - \bar{\mathbf{m}}_j^{(k)})^\top, \quad (4.18)$$

where v_j is the confidence in the prior covariance matrix $\boldsymbol{\Sigma}_{j \text{ prior}}$ of the rock unit j .

I have now generalized all three processes of the PGI framework (Figure 4.1) to the multiple physical properties case. The next goal is to define an approach for fitting multiple geophysical datasets at once while using the PGI framework. In the next section, I present my strategies for handling multiple geophysical data misfits as well as an additional petrophysical misfit, each with its target value I seek to reach.

4.4 Numerical considerations for reaching multiple target misfits

I have multiple geophysical data misfits that I wish to fit. The inclusion of petrophysical and geological data with PGI adds another data misfit term that also needs to reach its target misfit (section 4.2.3). In this section, I provide my strategies for choosing and dynamically adjusting the various parameters of the objective function to find a solution that fits all the data. An algorithm that summarizes the whole framework is provided in section 4.4.4.

4.4.1 Objective function with multiple geophysical data misfits

The objective function I seek to minimize for the multi-physics inversion process (Figure 4.1, Process 1) takes the form:

$$\Phi(\mathbf{m}) = \Phi_d(\mathbf{m}) + \beta \left(\alpha_s \Phi_s(\mathbf{m}) + \sum_{v \in \{x,y,z\}} \sum_{p=1}^q \alpha_{v,p} \Phi_{v,p}(\mathbf{m}) \right), \quad (4.19)$$

with:

$$\Phi_d(\mathbf{m}) = \sum_{k=1}^r \chi_k \Phi_d^k(\mathbf{m}) = \frac{1}{2} \sum_{k=1}^r \chi_k \|\mathbf{W}_d^k (\mathbb{F}^k[\mathbf{m}^{\{k\}}] - \mathbf{d}_{\text{obs}}^k)\|_2^2, \quad (4.20)$$

$$\Phi_{v,p}(\mathbf{m}) = \frac{1}{2} \|\mathbf{W}_{v,p} \mathbf{L}_v(\mathbf{m}^p - \mathbf{m}_{\text{ref}}^p)\|_2^2. \quad (4.21)$$

The data misfit term $\Phi_d(\mathbf{m})$ now contains multiple geophysical data misfits, each defined as a weighted least-squares norm. Φ_d^k is the data misfit of the k^{th} survey, where the forward operator \mathbb{F}^k generates the predicted data for that survey from $\mathbf{m}^{\{k\}}$. The notation $\mathbf{m}^{\{k\}}$ denotes the subset of model parameters associated with the k^{th} survey. Note that multiple surveys can be associated with the same physical property, for example, gravity and gravity gradiometry both depend on density contrasts. Similarly, one survey can be sensitive to several physical properties; for example, electromagnetic surveys are sensitive to electrical conductivity and magnetic susceptibility. The data measured by the k^{th} survey is symbolized by $\mathbf{d}_{\text{obs}}^k$ and the uncertainty on those measurements by the matrix \mathbf{W}_d^k . Each data misfit Φ_d^k is weighted by a scaling parameter χ_k . Those $\{\chi\}$ scaling parameters are important for balancing the various geophysical data misfits and finding a solution that fits all of them. My strategy for updating these parameters is developed

later in this section.

The regularization is still composed of the smallness and smoothness terms. The smallness term Φ_s is the coupling term, which is defined in equation (4.4). The smoothness terms, one for each direction and physical property, are represented by $\Phi_{v,p}$. In the smoothness terms (equation (4.21)), the smoothness operators (usually first or second-order difference) are represented by the matrix \mathbf{L}_v , and weights (sensitivity or depth) are represented by the matrix $\mathbf{W}_{v,p}$.

Equation (4.19) is an intricate objective function that is the sum of many quadratic regularization terms, each of which is multiplied by an adjustable constant. Finding values for these constants and carrying out a nonlinear inversion to produce a model that acceptably fits the data, and is a good candidate for representing information from the true geologic model, is numerically challenging.

In the following sections, I present my approach for estimating and updating these parameters throughout the inversion. The smoothness scaling parameters $\{\alpha_{v,p}\}$ are the only values that are kept constant. The scaling parameter α_s weights the importance of the petrophysical misfit term, and the trade-off parameter β influences the importance of the regularization (which contains the petrophysical misfit) relative to the geophysical data misfits. The geophysical data misfit scaling parameters $\{\chi\}$ are used to adjust the relative importance of each geophysical dataset. Values of β , α_s , and $\{\chi\}$ are sought so that each geophysical data misfit Φ_d^k is below or equal to its target misfit Φ_d^{k*} , along with a value of the petrophysical data misfit Φ_{petro} that is less or equal to its target misfit Φ_{petro}^* .

4.4.2 The regularization scaling parameters

Two types of scaling parameters act on the regularization terms; they are the trade-off parameter β and the $\{\alpha\}$ parameters. The $\{\alpha_{v,p}\}$ parameters acting on the smoothness terms are kept constant while β and α_s are updated to reach a suitable solution to the PGI problem. Next, I outline my strategies for each of these parameters.

Fixed parameters: the smoothness scaling parameters

In the smoothness terms, the scaling parameters $\{\alpha_{v,p}\}$ control the relative importance of spatial derivative terms in the regularization. Each set of assigned values will yield different outcomes. This is often a way in which model space can be explored (e.g. preferential smoothness in some directions, see Lelièvre et al. (2009); Williams (2008)). They are generally specified *a priori*, and I keep them fixed in the objective function throughout the inversion process. In addition to the common practical considerations for choosing the smoothness parameters (Oldenburg & Li, 2005; Williams, 2006), I use the $\{\alpha_{v,p}\}$ to weight each physical property representation, by dividing it by the square of its expected maximum amplitude (available through the GMM means if provided). This helps equalize the contribution of the smoothness terms to the objective function value when parameters have widely different scales (like density, log- electrical conductivity and magnetic susceptibility contrasts). The scaling of the physical properties in my extended smallness term (equation (4.4)) is taken care of by the covariance matrices of the GMM.

Varying parameters: the trade-off and the smallness scaling parameters

In the case of a single geophysical data misfit with a petrophysical misfit, I developed in section 3.4.2 a strategy for cooling β and warming α_s to find a solution to the inverse problem that reaches the target values of both misfits. This approach is still appropriate in the multi-physics inversion framework and is what I use in this study (step 6 in algorithm 2). I alter it for the multi-physics case in the following way: when all geophysical data misfits are equal or below their target value, the strategy for warming the scaling parameter α_s on the coupling term is:

$$\alpha_s^{(t+1)} = \alpha_s^{(t)} \cdot \operatorname{median}_{k=1..r} \left(\frac{\Phi_d^{k*}}{\Phi_d^{k(t)}} \right). \quad (4.22)$$

4.4.3 Balancing the geophysical data misfits

My goal is to develop a strategy for scaling multiple geophysical data misfits so that each geophysical dataset is adequately fit. I propose a strategy where the scaling parameters $\{\chi_k\}_{(k=1..r)}$ in equation (4.20) are successively updated. My approach has a heuristic foundation and does not incur the significant computational cost often associated with optimization-based approaches, and generalize to any number of geophysical data misfits. Before presenting its details, I first outline some strategies that others have taken in addressing this problem.

Review of previous strategies for balancing various geophysical data misfits and coupling terms

Several approaches for weighting multiple geophysical data misfits have been proposed in the recent literature. Some frameworks do not follow any prescribed strategy for updating the scaling parameters of the geophysical data misfits. This is the case for the approaches proposed by Sun & Li (2016, 2017) and Sosa et al. (2013); both keep those scaling parameters constant. Sun & Li use values of unity, while Sosa et al. normalize each geophysical data misfit by its number of data. In my experience, keeping the weights constant has led me to overfit some surveys while underfitting others. Other frameworks have adopted the approach of running their joint inversions for multiple combinations of parameters. For three geophysical data misfits, Moorkamp et al. (2011) adopted a manual check-and-guess approach to adjust the parameters. For two geophysical data misfits, Giraud et al. (2019b) ran a subset of their inversions hundreds of times for various combinations of scaling parameters before choosing values based on the L-curve principle (Hansen, 2000; Hansen & O’Leary, 1993; Santos & Bassrei, 2007). They then manually “fine-tuned” those values using the full joint inversion problem. To avoid the issue of having to choose multiple appropriate scaling parameters, Bijani et al. (2017) developed a compromise between deterministic and stochastic optimizations for joint inversions. They adopted a “Pareto Multi-Objective Global Optimization” strategy with genetic algorithms that generate populations of candidate models that “simultaneously minimize multiple objectives in a Pareto-optimal sense”, rather than working with a fully aggregated ob-

jective function. This approach was still computationally expensive and limited to small 2D studies in the paper.

To limit the number of multiple runs of the same inversion, Lelièvre et al. (2012) devised a rigorously defined, but computationally expensive, strategy for dynamically balancing two geophysical data misfits. Their approach relies on adjusting the trade-off parameter until the two data misfits are Pareto-optimal. Next, they adjust the relative weights of the two surveys to fit both geophysical surveys. They then reinforce the importance of the coupling term before going into another round of adjustments of the trade-off and surveys weights parameters. The approach developed in section 3.4.2 for a single geophysical data misfit, but with a petrophysical data misfit, is related to the work of Lelièvre et al. (2012). Both focus first on fitting the geophysical data misfit terms and then adjusting the coupling term. On the contrary, the strategy presented in Gallardo & Meju (2004) favoured the cross-gradient coupling over the geophysical misfits.

Here I define a practical, computationally inexpensive, heuristic strategy for balancing the geophysical data misfits as well as the coupling term. I design this strategy to work for any number of surveys, and thereby generalize the work of Lelièvre et al. (2012). For the full algorithm, the reader can refer to algorithm 2.

Updating the geophysical data misfit scaling parameters

I now define my strategy for weighting the multiple geophysical data misfits to reach all the target values. I use the scaling parameters $\{\chi_k\}_{(k=1..r)}$ defined in equation (4.20). I dynamically update each geophysical misfit scaling parameter

based on its current misfit and target values, compared to the other surveys.

I start with a set of initial scaling parameters $\{\chi\}$ that sums to unity. To ensure the progress of all data misfits, while limiting the possibilities of overfitting any given term, I update the scaling parameters $\{\chi\}$ during the inversion. My approach is philosophically similar to what I proposed in chapter 3 for β and α_s in order to balance the geophysical data misfit and the petrophysical misfit at each iteration in the inversion, and generalizes ideas proposed in Lelièvre et al. (2012) to more than two geophysical data misfits. If one geophysical data misfit reaches its target value before the others, I use the ratio of its current value with its target to warm the scaling parameters of the other geophysical data misfit terms. I then normalize the sum of the scaling parameters to be equal to unity again. This is to keep the importance of the total Φ_d term relatively similar before and after adjusting the scaling parameters $\{\chi\}$. If several surveys are below their respective targets, I simply use the median of the ratios to warm the scaling parameters of the still unfit surveys. Thus, at any iteration (t) of the geophysical inverse problem, if an ensemble of $\{k_f\}$ surveys has reached their respective targets, I warm the scaling parameters of the remaining $\{k_u\}$ surveys that are not yet fit as (step 7 in algorithm 1):

$$\tilde{\chi}_{k_u}^{(t+1)} = \chi_{k_u}^{(t)} \cdot \text{median}_{\{k_f\}} \left(\frac{\Phi_d^{k_f(t)}}{\Phi_d^{k_f^*}} \right), \quad (4.23)$$

$$\tilde{\chi}_{k_f}^{(t+1)} = \chi_{k_f}^{(t)}, \quad (4.24)$$

then I normalize the sum:

$$\chi_k^{(t+1)} = \frac{\tilde{\chi}_k^{t+1}}{\sum_{k=1}^r \tilde{\chi}_k^{(t+1)}}. \quad (4.25)$$

An example of convergence curves for the data misfits and evolution of the dynamic scaling parameters is proposed in Fig. 4.8 for a multi-physics PGI with full petrophysical information.

My strategy has proven to be insensitive to the initialization of the scaling parameters $\{\chi\}$ for linear problems. To demonstrate this point, I show in Figure 4.3 the evolution of the scaling parameters $\{\chi\}$ for three multi-physics PGI with full petrophysical information. The synthetic example presented in section 4.5.4 is run with various initializations $\{\chi^{(0)}\}$. The outcomes of all these three PGI were similar to the result I show in Fig. 4.7 and are provided in Appendix D. The scaling parameters χ associated with the magnetic and gravity misfits, respectively, all finish at approximately the same value even though the initializations are very different: The final χ scaling values are about 0.8 for the gravity data misfit and around 0.2 for the magnetic data misfit. This is an appealing property as it reduces the need to fine-tune the initialization of the scaling parameters $\{\chi\}$, which can be costly for large-scale inversions.

4.4.4 Algorithm

Algorithm 2: PGI extended from chapter 3 for multi-physics inversions

2 Initialization:

- Input:
 - Initial geophysical model $\mathbf{m}^{(0)}$, GMM parameters $\Theta^{(0)}$ and geological model $\mathbf{z}^{(0)}$.
- Parameters:
 - *Objective function:* data's noise $\{\mathbf{W}_{dp}\}_{p=1..d}$, $\beta^{(0)}$ and $\{\alpha\}$ parameters.
 - *Localized prior:* specific $\mathcal{P}(z_i)$ for available locations $i \in \{1..n\}$, weights $\{\mathbf{w}\}$.
 - *GMM prior weights:* $\{\boldsymbol{\kappa}_j, v_j, \zeta_j\}_{j=1..c}$ for the means, variances and proportions.
 - *Optimization:* β -cooling factor $\gamma (> 1)$, sufficient decrease rate $\tau (\leq 1)$, tolerance on target misfit ϵ .
- Output:
 - $\mathbf{m}, \Theta, \mathbf{z}$.

3 while any($\Phi_d^k > \Phi_d^{k*}, k = 1..r$) and $\Phi_{petro} > \Phi_{petro}^*$ **do**

4 Objective Function Descent Step:

- Compute a model perturbation $\delta\mathbf{m}$ using an inexact Gauss-Newton.
- Line search with Wolfe condition to find an η that satisfy a sufficient decrease of Φ .
- Return $\mathbf{m}^{(t)} = \mathbf{m}^{(t-1)} + \eta\delta\mathbf{m}$.

5 Update Petrophysical Distribution

- Fit a new GMM $\Theta^{(t)}$ on $\mathbf{m}^{(t)}$ such as in equations (4.12), (4.15) and (4.17) until no sufficient increase of the posterior is observed.

6 Classification:

- Compute the membership $\mathbf{z}^{(t)}$ of the current model $\mathbf{m}^{(t)}$ as in equation (4.5) using $\Theta^{(t)}$.
- Update \mathbf{m}_{ref} and \mathbf{W}_s according to equations (4.6) and (4.7) respectively using $\mathbf{z}^{(t)}$.

7 Update regularization weights:

if all($\Phi_d^{k(t)} \geq \max((1 + \epsilon)\Phi_d^{k*}, \tau\Phi_d^{k(t-1)}), k = 1..r$) **then**

| Decrease β : $\beta^{(t)} = \frac{\beta^{(t-1)}}{\gamma}$.

else if all($\Phi_d^{k(t)} \leq \Phi_d^{k*}, k = 1..r$) and $\Phi_{petro} > \Phi_{petro}^*$ **then**

| Increase α_s : $\alpha_s^{(t)} = \alpha_s^{(t-1)} \times \text{median}\left(\frac{\Phi_d^{k*}}{\Phi_d^{k(t)}}, k = 1..r\right)$ (equation (4.22)).

if (optional) all($\Phi_d^{k(t)} \leq \Phi_d^{k*}$) and $\Phi_{petro} > \Phi_{petro}^*$ and $\mathbf{z}^{(t)} == \mathbf{z}^{(t-1)}$ **then**

| Include \mathbf{m}_{ref} in Smoothness.

8 Update geophysical data misfit weights:

if any($\Phi_d^{k(t)} \leq \Phi_d^{k*}, k = 1..r$) **then**

| update $\{\chi\}$ according to equations (4.23) to (4.25).

9 end

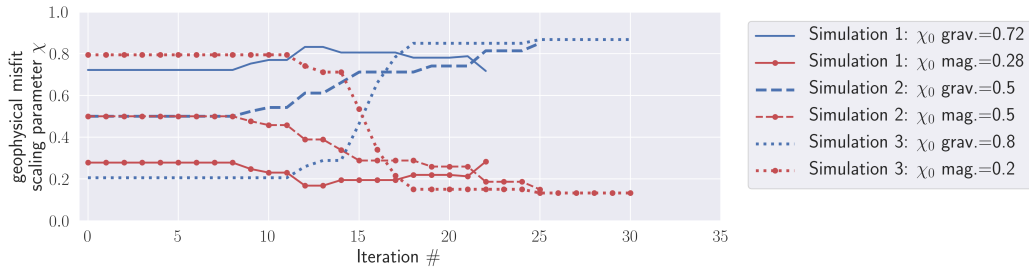


Figure 4.3: Evolution curves of the scaling parameters $\{\chi\}$ with the proposed strategy for three multi-physics PGI with full petrophysical information and different initializations for $\{\chi\}$. The colour of each line corresponds to the geophysical misfit: blue for gravity and red with markers for magnetic. The style of the lines corresponds to one of the three inversions ($\chi_{0,\text{grav}} + \chi_{0,\text{mag}} = 1$ in each inversion).

4.5 Synthetic example: The DO-27 kimberlite pipe

In this section, I illustrate the joint PGI approach on synthetic gravity and magnetic data based on the DO-27 kimberlite pipe (Jansen & Witherly, 2004), which is composed of two different kimberlite facies. I compare standard Tikhonov inversions of the individual geophysical datasets and independent PGIs of the gravity and magnetic data with the multi-physics PGI approach. Both the Tikhonov inversions and single-physics PGIs produce models that enable only a binary distinction: kimberlite or host rock. Only the multi-physics PGI allows me to identify the two kimberlite facies as distinct from the background host rock.

I implemented my framework as part of the open-source SIMPEG (Simulation and Parameter Estimation in Geophysics) project (Cockett et al., 2015; Heagy et al., 2017). As such, I am able to share both the software environment and the scripts to reproduce the examples shown in this chapter through `GitHub` at

<https://github.com/simpeg-research/Astic-2020-JointInversion> (Astic, 2020). To encourage the use of this work and future collaborations, I highlight some key points of my implementation in Appendix B.

4.5.1 Setup

The DO-27 Kimberlite pipe (Northwest Territories, Canada) is part of a complex, also known as the Tli Kwi Cho (TKC) kimberlite cluster (Jansen & Witherly, 2004) (Figure 4.4). The pipe has two distinctive kimberlite units that are embedded in a background consisting of a granitic basement covered by a thin layer of till (Figure 4.4a). The first pipe unit is a pyroclastic and volcanoclastic kimberlite (called PK/VK), which has a weak magnetic susceptibility and a very high density contrast. The second unit is a Hypabyssal Kimberlite (HK), which has a strong magnetic susceptibility and a weak density contrast. The Tikhonov inversions of the field gravity and magnetic datasets have been documented in Devriese et al. (2017).

For this example, I use simulated surface gravity and airborne magnetic data modelled from a synthetic model of the DO-27 pipe. The forward and inversion mesh is a tensor mesh with 375 442 active cells; each has a pair of density-magnetic susceptibility values. The smallest cells are cubes with a 10 m edge length. All chosen values for the surveys and geological units are consistent with observations documented in Devriese et al. (2017). For the PK/VK unit, I assume a magnetic susceptibility of $5 \cdot 10^{-3}$ SI and a density contrast with the background of -0.8 g/cm^3 . For the HK unit, the magnetic susceptibility is set to $2 \cdot 10^{-2}$ SI

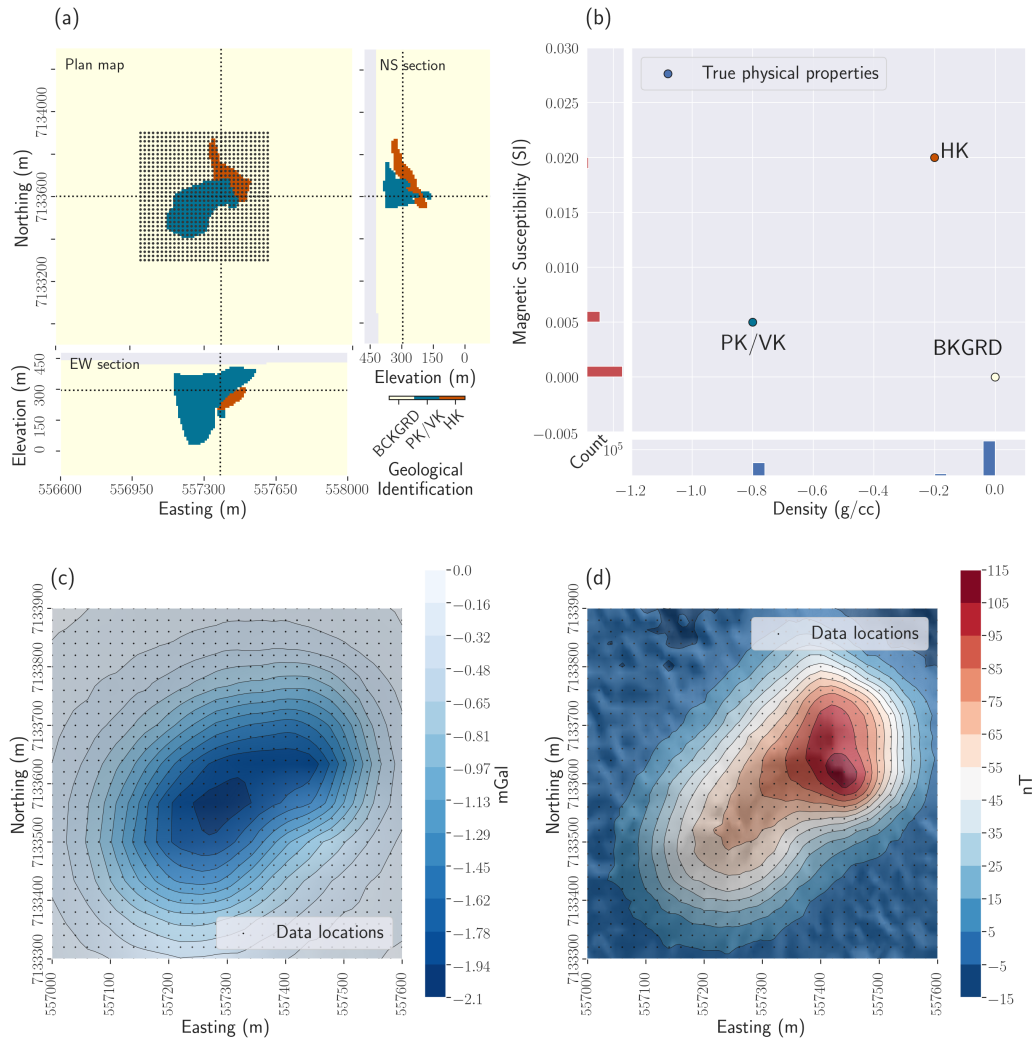


Figure 4.4: Setup: DO-27 synthetic example: (a) Plan map, east-west, and north-south cross-sections through the synthetic geological model. The grid of dots represents the data locations for the gravity and magnetic surveys, and the dotted lines represent the location of each cross-section; (b) Cross-plot and histograms of the physical properties of the synthetic model; (c) Synthetic ground gravity data; (d) Synthetic total amplitude magnetic data.

and the density contrast to -0.2 g/cm^3 (Figure 4.4b). I forward modelled the data over a grid of 961 receivers, at the surface for the gravity survey, and at the height of 20 m above the ground for the airborne magnetic survey (Figure 4.4c and 4.4d). I added unbiased Gaussian noise to the gravity and magnetic data with standard deviations of 0.01 mGal and 1 nT, respectively. These standard deviations are input into the data weighting matrices $\{\mathbf{W}_d^k, k = 1, 2\}$.

For each inversion, I added bound constraints so that the sought density contrast values are null or negative, and the magnetic susceptibility contrast values are null or positive. I used the sensitivity of each survey to define the $\{\mathbf{w}_{ip}, i = 1..n, p = 1..q\}$ weights. Each physical property is weighted by the sensitivity of its associated survey. Sensitivity-based weighting is a common practice for potential fields inversions (Fournier et al., 2020; Li & Oldenburg, 1996, 1998; Portniaguine & Zhdanov, 2002). The initial model is the background half-space for all inversions.

4.5.2 Tikhonov inversions

I first run the individual inversions of the gravity and magnetic data using the well-established Tikhonov approach described in section 2.5. The results, shown in Figure 4.5, are relatively smooth. The gravity inversion (Figure 4.5a) provides an approximate outline of the pipe. The magnetic inversion (Figure 4.5b) shows a body centred on HK, but it is too diffuse to delineate a shape. Figure 4.5c shows the cross-plot of the recovered density and magnetic susceptibility models. Each point is coloured based on both its density and magnetic susceptibility values:

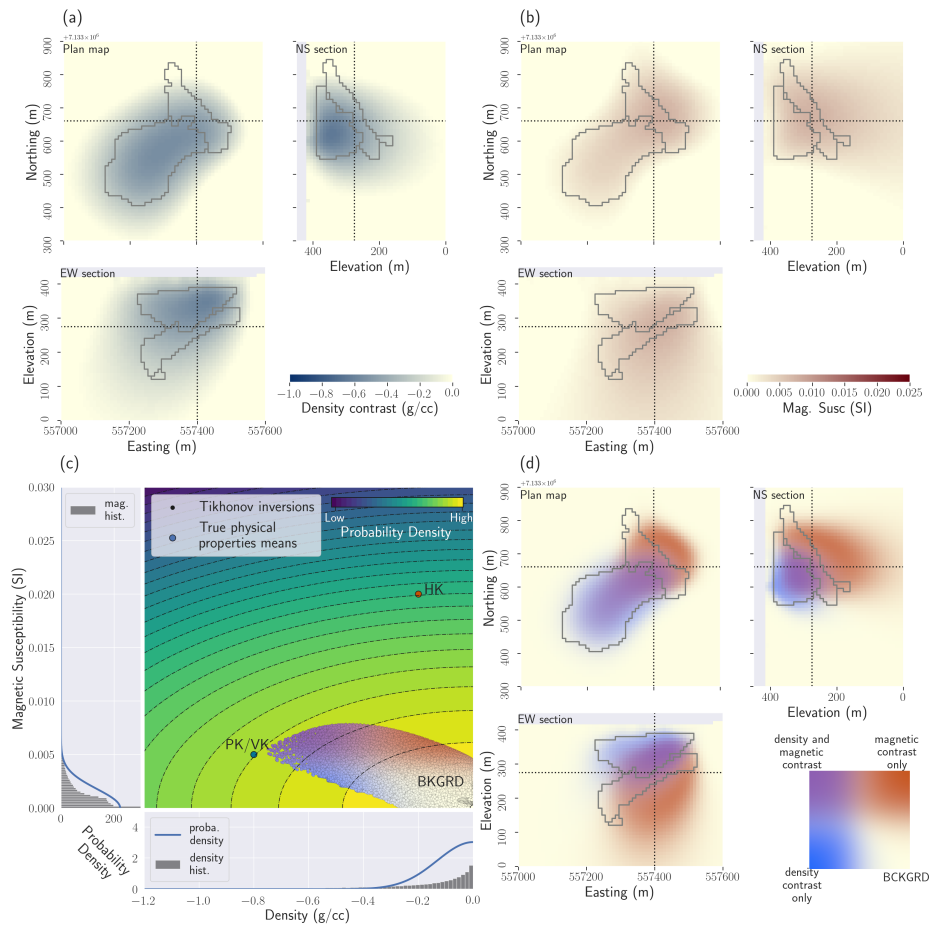


Figure 4.5: DO-27 Tikhonov inversion results. (a) Plan map, east-west, and north-south cross-sections through the recovered density contrast model; (b) Plan map, east-west, and north-south cross-sections through the recovered magnetic susceptibility contrast model; (c) Cross-plot of the density and magnetic susceptibility models; the points are coloured according to both values. The side and bottom panels show the marginal distribution of each physical property, with the best fitting univariate Gaussian (proba. stands for probability, and hist. stands for histogram). Those two univariate Gaussian distributions are used to compute the multivariate Gaussian showed in the background of the cross-plot; (d) Plan map, east-west, and north-south cross-sections coloured based on the combination of density and magnetic susceptibility contrasts.

white when both contrasts are low, with a blue-scale for a significant density contrast only, with a red-scale for only a significant magnetic susceptibility, and with a purple-scale when both contrasts are significant. I observe the expected continuous Gaussian-like distribution of the model parameters (in the region allowed by the bound constraints). Petrophysical signatures are not reproduced, with notably the strongest density contrasts being co-located with the highest magnetic susceptibility values (mesh cells coloured in purple in Figure 4.5c and d); this is in contradiction with the setup where PK/VK, the unit with a low density, is distinct from HK, the unit with high magnetic susceptibility. In both gravity and magnetic inversions, the two anomalous units are indistinguishable from each other. To highlight this, I show an overlap of the two inversions in Figure 4.5d. I coloured each point relative to its density and magnetic susceptibility values, as in Figure 4.5c. This juxtaposition highlights that combining both models does not show structures that seem closer to the ground truth. Post-inversions classification would give highly variable results, depending on the thresholds chosen to delineate units.

I next move to a PGI approach and include petrophysical information. I start by inverting each geophysical dataset individually, and I assess what gains are made before moving to a multi-physics PGI.

4.5.3 Single-physics PGIs

I apply the PGI framework developed in chapter 3 to invert each geophysical dataset individually. Results are shown in Figure 4.6. For the prior petrophysical distribution, I use the true value for the means of each unit. For the petrophysi-

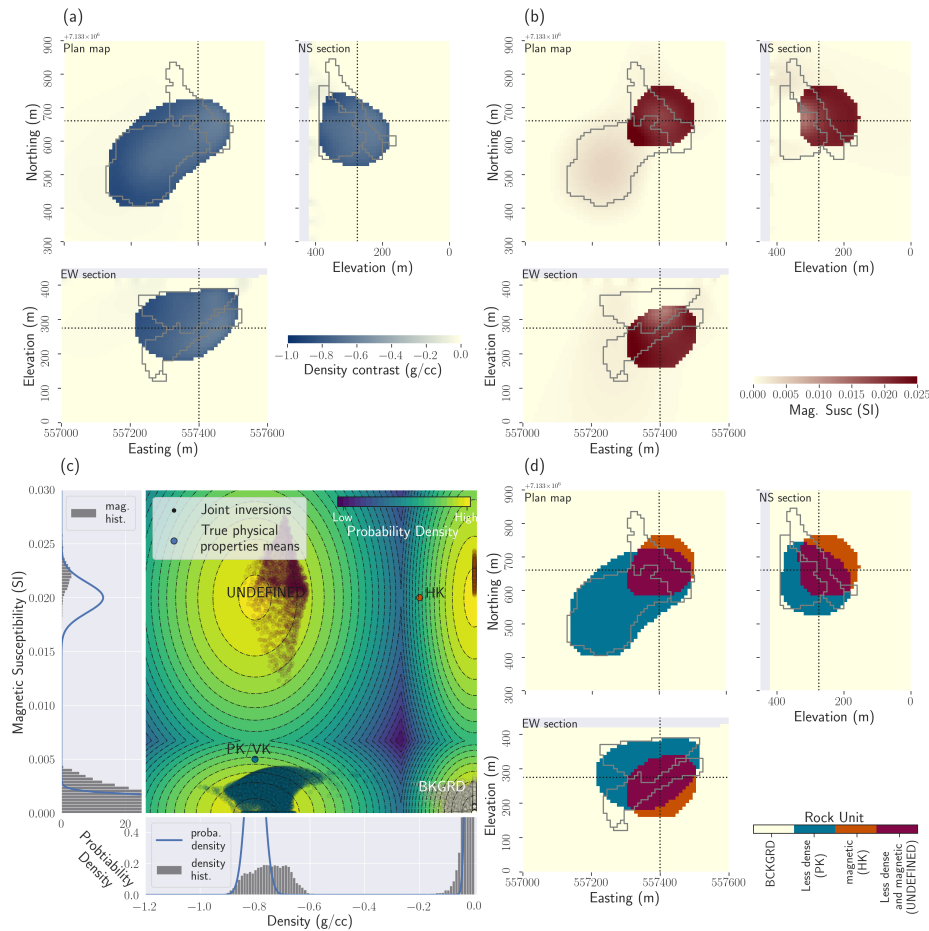


Figure 4.6: Results of the individual PGIs. (a) Plan map, east-west, and north-south cross-sections through the density model recovered using the petrophysical signature of PK/VK; (b) Plan map, east-west, and north-south cross-sections through the magnetic susceptibility model obtained using the petrophysical signature of HK; (c) Cross-plot of the inverted models. The 2D distribution in the background has been determined by combining the two 1D distributions used for density and magnetic susceptibility PGIs, respectively. With only one anomalous unit in each case, there is still four possible combinations; (d) Plan map, east-west, and north-south cross-sections through the quasi-geology model built from the density and magnetic susceptibility models, see cross-plot in (c).

cal noise levels, I assign standard deviations of 3.5% of the highest known mean value for each physical property except for the background for which I assign 1.75% (see the 1D left and bottom panels for the distribution of each physical property, respectively, in Figure 4.6c). For the proportions, I also used the true values. I acknowledge that proportion values could be difficult to estimate in practice. However, in my experiments, the values of the global proportions have not had a significant impact on the inversion result. The use of locally varying proportions can, however, guide the reproduction of particular features (see section 3.5.2 or Giraud et al. (2017)). All the GMM parameters are held fixed in those single-physics inversions.

In carrying out the inversions, I found that both magnetic and gravity data can be explained individually by assuming a single unit, either PK/VK or HK. Each dataset, gravity or magnetic, can be fit by either reproducing the signature of PK/VK or HK, or any value in between. The difference in physical property contrast is compensated for by a difference in the volume of the recovered body. The two kimberlite facies are thus indistinguishable when I consider one geophysical survey at the time. Adding a third cluster in either inversion to represent the second kimberlite facies does not help, as it only gives the algorithm more “choices” that are not supported by the data. For conciseness, I choose to show here the gravity result recovered using only the petrophysical signature of the PK/VK unit (Figure 4.6a), which is the most responsible for the gravity anomaly; for the magnetic inversion, I show the model obtained by only using the petrophysical signature of HK, which is the unit that is the most responsible for the magnetic response (Figure

4.6b). The additional models (gravity inversion with HK's density signature and magnetic inversion with PK/VK's magnetic signature) are shown in Appendix C; these demonstrate the discrepancy in the recovered volumes of each unit between the magnetic and gravity inversions. For example, explaining the gravity anomaly with only a body with the same density as HK leads to a very large body, bigger than the volume of that same unit recovered through the magnetic inversion. The same reasoning applies to the PK/VK body.

The gravity PGI using the PK/VK unit petrophysical signature (Figure 4.6a) gives useful information about the depth and delineation of the pipe that was not available from the Tikhonov inversion. The magnetic PGI using the HK petrophysical signature (Figure 4.6b) places a body around the HK unit location but misses its elongated shape. From the petrophysical perspective, both the gravity signature of PK/VK and the magnetic signature of HK are individually well reproduced. However, the combination of the density and magnetic susceptibility contrasts recovered by the individual PGIs (cross-plot in Figure 4.6c) is very far from the desired multidimensional petrophysical distributions. Even assuming just two units for each inversion (background and kimberlite) as I did, there are still four different combinations of density and magnetic susceptibility values. In this specific case, looking at Figures 4.6c and 4.6d, there is: 1) a cluster representing the background with both weak density and magnetic susceptibility contrasts (coloured in white); 2) a cluster with a large density contrast and a low susceptibility (coloured in blue); this is close to the petrophysical signature of the PK/VK unit; 3) a cluster with high magnetic susceptibility and very small density contrasts (coloured

in orange); This would be the HK unit; 4) a cluster that has both high magnetic susceptibility and high-density contrasts, that I identify as 'undefined' in the figures. This last cluster does not correspond to any unit signature and occupies a large volume. This hinders the ability to resolve two clear kimberlite facies from the inversions. Therefore, this motivates me to move to a multi-physics inversion approach to take advantage of the density-magnetic susceptibility relationships in the inversion and finally delineate two distinct kimberlite facies.

4.5.4 Multi-physics PGI with petrophysical information

I now apply the multi-physics PGI framework to jointly invert the gravity and magnetic data with petrophysical information (means, covariances, proportions for each unit, background, PK/VK, HK, of the GMM). The parameters $\{\mathbf{w}_{ij}\}_{i=1..n, j=1..c}$ are again used to include the appropriate sensitivity weighting for each method and physical property. I use the same uncertainties that I used for the individual PGIs. The off-diagonal elements of the covariance matrices are set to null, which just means I assume no correlations between the density and magnetic susceptibility variations within a single rock unit. The GMM parameters are still held fixed. The results are shown in Figure 4.7.

The improvement is significant. The joint inversion succeeds in recovering two distinct kimberlite facies that reproduce the provided petrophysical signatures. The quasi-geology model (Figure 4.7d) is geologically consistent and does not introduce erroneous structures. The surface outline of the pipe is well recovered. The vertical extension is similar to that of the true model. I also now

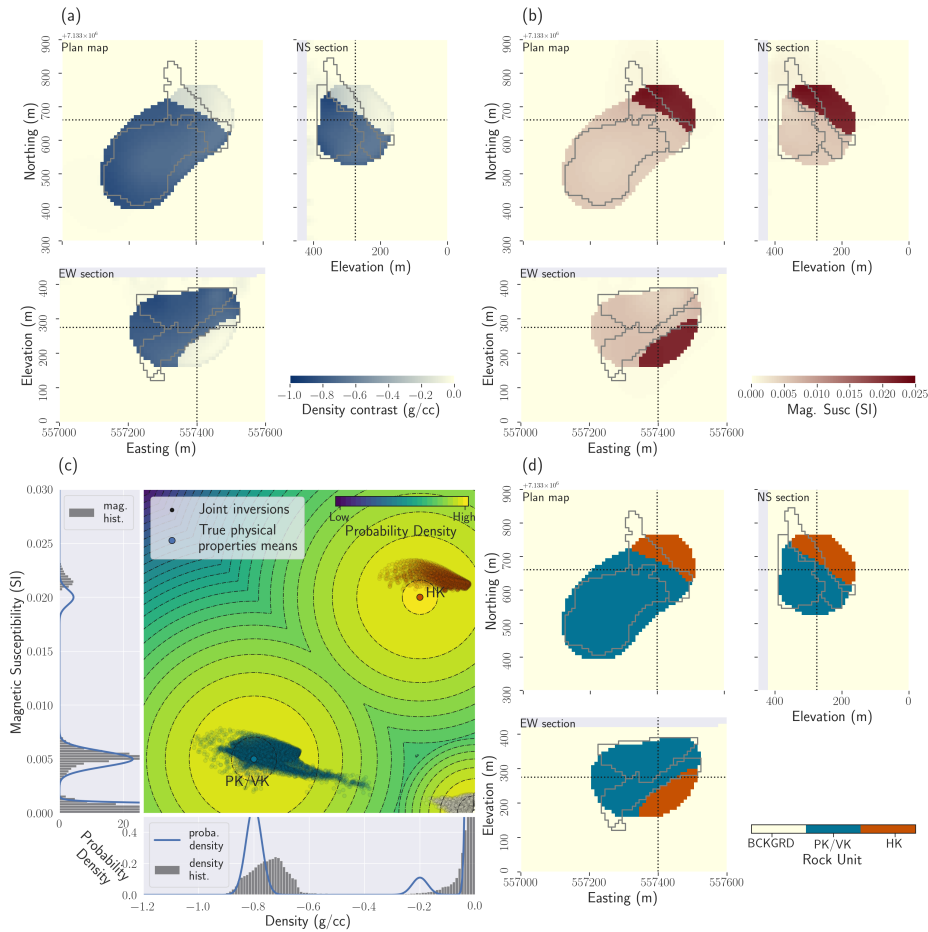


Figure 4.7: Results of the multi-physics PGI with petrophysical information. (a) Plan map, east-west, and north-south cross-sections through the recovered density contrast model; (b) Plan map, east-west, and north-south cross-sections through the magnetic susceptibility contrast model; (c) Cross-plot of the inverted models. The colour of the points has been determined by the clustering obtained from this framework joint inversion process. In the background and side panels, I show the prior joint petrophysical distribution with true means used for this PGI; (d) Plan map, east-west, and north-south cross-sections through the resulting quasi-geology model.

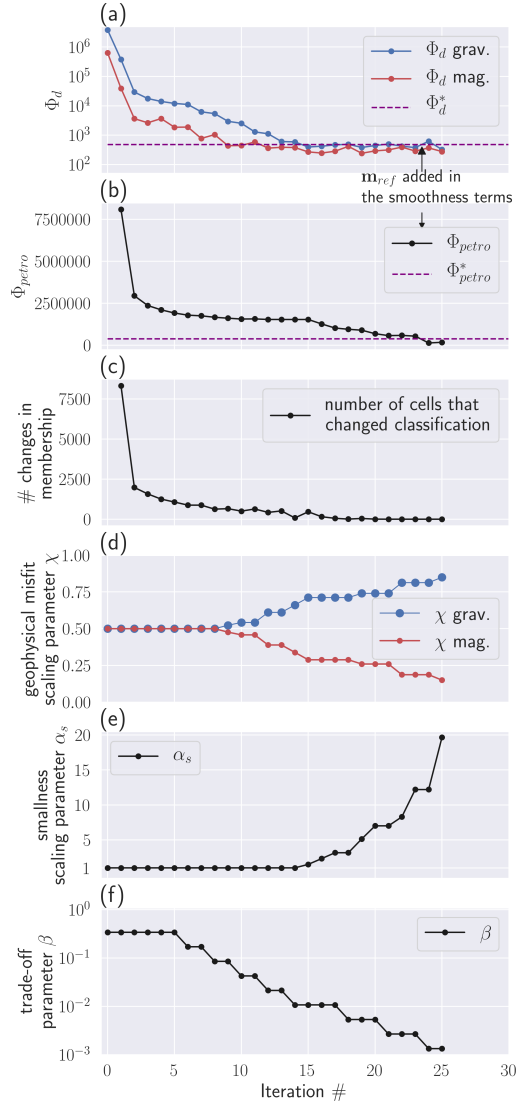


Figure 4.8: Convergence curves for the three misfits, and evolution curves for the dynamic scaling parameters during the multi-physics PGI with petrophysical information shown in Figure 4.7. (a) Gravity and magnetic geophysical data misfits and their targets (same number of data); (b) Convergence curves of the petrophysical misfit, defined in equation (4.8), and its target value, defined in equation (4.10); (c) Evolution of the $\{\chi\}$ scaling parameters; (d) Evolution of the α_s scaling parameter; (e) Evolution of the trade-off parameter β .

have indications of the elongated shape and tilt of the HK unit. The magnetic susceptibility of HK is slightly overestimated but still within the acceptable margins defined by the petrophysical noise levels I assigned (Figure 4.7c).

To illustrate the behaviour of the heuristic strategy for the update of the objective function scaling parameters, I provide in Figure 4.8 the convergence curves of the three data misfits (gravity, magnetic, and petrophysical), and the evolution of the dynamic scaling parameters, for the multi-physics PGI with full petrophysical information. All target values are reached after 25 iterations, and the PGI stops.

This result was obtained by providing the petrophysical means of the rock units in the GMM. In the next inversion, I devise my approach to using the multi-physics PGI framework when quantitative information is not available.

4.5.5 Multi-physics PGIs with limited information

I have illustrated the gains made by the multi-physics PGI framework when extensive and quantitative *a priori* information is provided. I now investigate how to perform multi-physics inversions when *a priori* information to design the coupling term is not available. Chapter 3 emphasized the benefits of learning a GMM during the inversion process to compensate for uncertain, or unknown, petrophysical information. At each iteration, the GMM parameters are determined by running a Maximum A Posteriori Expectation-Maximization (MAP-EM) clustering algorithm (Dempster et al., 1977). The MAP-EM algorithm estimates compromise values for the GMM parameters based on the prior GMM parameters, weighted by confidence parameters in this prior knowledge, and the current geophysical model.

I generalized the learning process of the GMM parameters to a multidimensional case in section 4.3.

In the next two multi-physics PGI inversions, I demonstrate how learning the means of the kimberlite units iteratively through the inversion allows me to still perform multi-physics inversions without providing physical property mean values. This is done by acting on the $\{\kappa\}$ confidence parameters in the means. Confidence κ values of zero indicate that the mean is fully learned from the inversions, while infinite confidences fix the mean to its prior value. In all the inversions with limited information, I fix the means of the background for both physical properties to their true values (zero); this is a usual assumption in Tikhonov inversions of potential fields that the background has a zero contrast. I keep the covariances of the GMM fixed and similar to what I used previously. The covariance matrices define the petrophysical noise levels and how spread each petrophysical signature can be.

In the first example, I show that geophysical datasets alone do not require two distinct kimberlite facies. In the absence of petrophysical information and qualitative geologic assumption, both magnetic and gravity datasets can be reproduced by a single unidentified kimberlite unit with low density and high magnetic susceptibility.

In the second example, I demonstrate that employing qualitative information about the geologic setup can help recover valuable information about the two kimberlite facies, even without quantitative information about their physical property contrasts.

Multi-physics PGI with no petrophysical information and only one kimberlite facies

Here, I present a multi-physics PGI with no petrophysical information about the mean values of the kimberlite units. I only set two clusters in the GMM, one for the background and one for a general kimberlite unit. The confidences in the mean κ are all zeros for the kimberlite unit; the PGI algorithm is tasked with determining the mean of that unit at each iteration of the inversion. The mean of the background unit is kept fixed at zero contrast for both physical properties. The result, shown in 4.9, highlights that a single anomalous kimberlite body is able to fit both gravity and magnetic datasets, with a learned mean and an acceptable spread according to the set covariance matrices.

Distinguishing two kimberlite facies is thus not automatically required from the geophysical datasets themselves. Same as for the single-physics inversions, adding a third cluster without additional information would not help, as the data do not support this third cluster. I show that case in the next chapter, in section 6.2.2, when discussing how to identify and address challenging cases.

However, it is possible to add qualitative information about the expected physical properties of the kimberlite facies to recover geologically insightful information about the two kimberlite facies from the geophysical datasets. This is demonstrated in the next example.

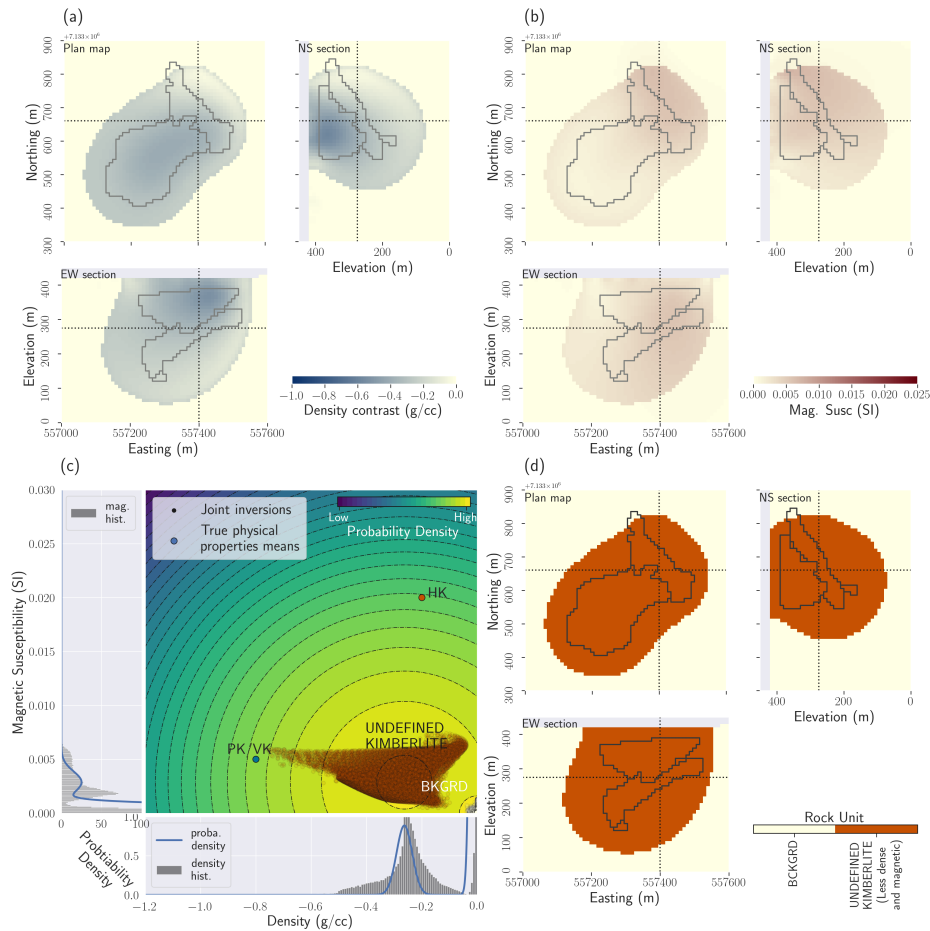


Figure 4.9: Results of the multi-physics PGI without providing the means of the physical properties for the kimberlite facies; a single kimberlite body is enough to meet the petrophysical requirements (the spread set by the covariances matrices) and reproduce the geophysical datasets; (a) Plan map, east-west, and north-south cross-sections through the recovered density contrast model; (b) Plan map, east-west, and north-south cross-sections through the magnetic susceptibility contrast model; (c) Cross-plot of the inverted models. The colour has been determined by the clustering obtained from this framework joint inversion process. In the background and side panels, I show the learned petrophysical GMM distribution; (d) Plan map, east-west, and north-south cross-sections through the resulting quasi-geology model.

Employing qualitative information with PGI

Once the Tikhonov inversions have been run (see Figure 4.5), it already appears likely that the gravity and magnetic anomalies are mostly generated by two distinct bodies, as the centres of the two recovered anomalous bodies (density and magnetic susceptibility) are at different locations. In order to deal with the lack of quantitative petrophysical information, the multi-physics PGI framework allows me to formulate the following “interpreter’s assumption”: one kimberlite unit is responsible for the gravity anomaly, while a second one is responsible for the magnetic response. Employing this assumption is made possible in my framework by defining the confidences in the means of each unit $\{\kappa\}$ as vectors (equation (4.15)). This allows me to act on each individual physical property mean value of each unit. For example, for the kimberlite unit that is assumed to be responsible for the magnetic response, I set the confidence κ in its magnetic susceptibility to zero; the MAP-EM algorithm decides its value at each iteration based solely on the current geophysical model. On the contrary, its mean density contrast is kept fixed at zero by setting the confidence κ in this mean value to infinity. The same procedure is applied for the kimberlite unit that is assumed to be responsible for the gravity response. The initialization of the density contrast and magnetic susceptibility mean values, for the kimberlite units responsible for the gravity and magnetic responses respectively, has little impact on the inversion result, so long as the initial guess is reasonable. It is also common practice, in general, to run clustering algorithms multiple times from various initializations before choosing a specific outcome (Dempster et al., 1977; Murphy, 2012). In the specific result

shown in Figure 4.10, the density contrast and magnetic susceptibility mean values for the respective kimberlite rock units were initialized at -1 g/cm^3 and 0.1 SI . Similar results were obtained with other initializations (-0.4 g/cm^3 and 0.01 SI etc., but not 0 g/cm^3 and 0 SI for all units). Because of the weak dependency of the result with regard to the initialization, I choose not to show the initial value in Figure 4.11, which presents the evolution of the means throughout the multi-physics PGI with qualitative information.

The result of the multi-physics PGI, with no petrophysical information but with the assumption of distinct low-density and magnetized units, is shown in Figure 4.10. Three distinct clusters (background, low-density unit, magnetized unit) are well recovered. The final learned means are respectively -0.33 g/cm^3 for the low-density unit and $1.1 \cdot 10^{-2} \text{ SI}$ for the magnetized unit.

This multi-physics inversion has several advantages over any of the single-physics inversions. First, by bringing in a qualitative, geologic assumption, I am able to delineate two units by avoiding the overlap of low density and high susceptibility anomalies. Second, I get a sense of the dip of the HK unit. None of those two achievements was reached by the Tikhonov inversions or the single-physics PGIs, even with petrophysical information.

The means of the GMM are learned iteratively following the constraints defined by my assumptions: the background has a fixed contrast of zero in both physical properties, one rock unit is responsible for the gravity response with a null magnetic contrast, and one rock unit is responsible for the magnetic response with a null density contrast. The evolution of the estimations of the means throughout the

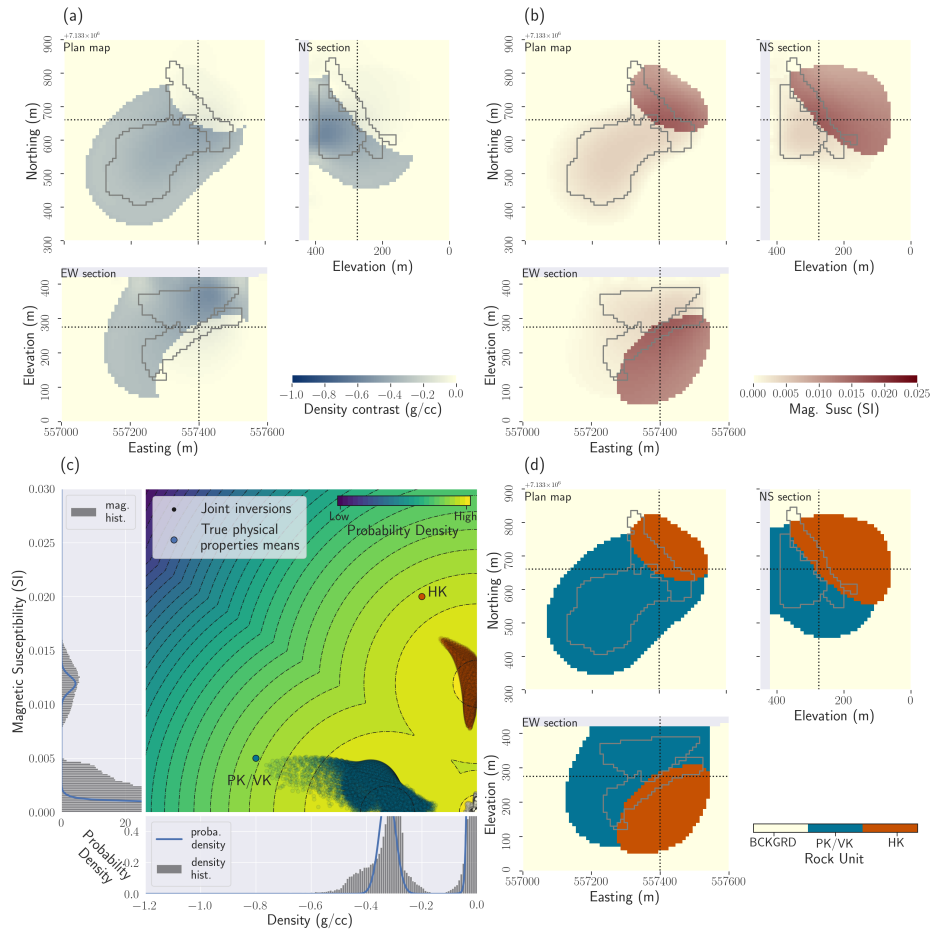


Figure 4.10: Results of the multi-physics PGI without providing the means of the physical properties for the kimberlite facies, and assuming a low-density unit and a magnetized unit; (a) Plan map, east-west, and north-south cross-sections through the recovered density contrast model; (b) Plan map, east-west, and north-south cross-sections through the magnetic susceptibility contrast model; (c) Cross-plot of the inverted models. The colour of the points has been determined by the clustering obtained from this framework joint inversion process. In the background and side panels, I show the learned petrophysical distribution; (d) Plan map, east-west, and north-south cross-sections through the resulting quasi-geology model.

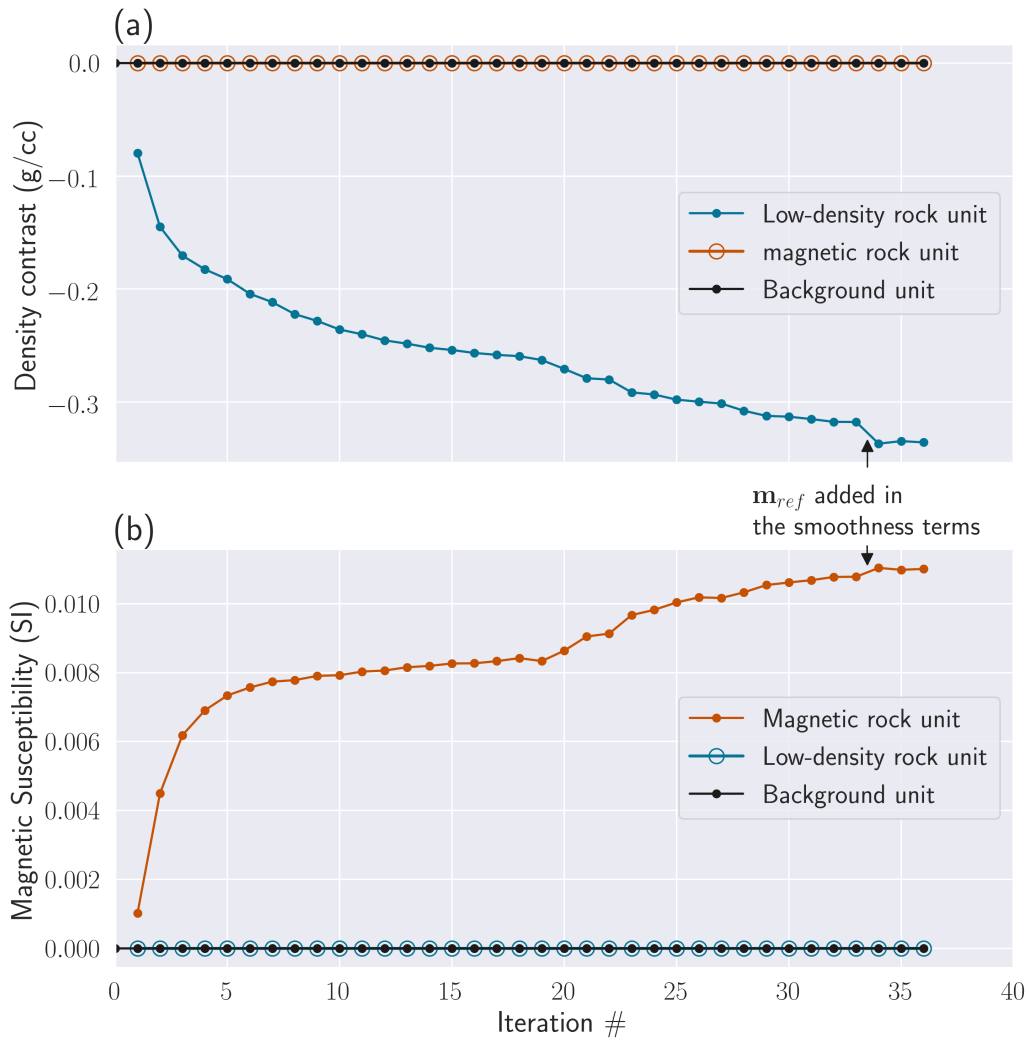


Figure 4.11: Evolution of the learned means of the GMM throughout the multi-physics PGI with qualitative information for the three assumed rock units (background, low-density kimberlite, and magnetic kimberlite) shown in Figure 4.10. The background mean values, the density of the magnetic rock unit, and the magnetic susceptibility of the low-density rock unit are kept fixed. Initialization has a low impact on the learned mean values, and thus the values at iteration 0 are not shown in the plot. (a) Evolution of the density contrast mean values; (b) Evolution of the magnetic susceptibility mean values.

inversion is shown in Figure 4.11. All target values are reached after 36 iterations, and the PGI stops.

4.5.6 DO-27 example summary

From the petrophysical perspective, the density-magnetic susceptibility cross-plots for the standard Tikhonov inversions are very different from the expected distributions (Fig. 4.7c). The smoothness of the recovered models and physical property distributions does not allow me to clearly delineate and distinguish between the two kimberlite facies. Using PGI, individual datasets can both be reproduced using a single kimberlite facies. The individual gravity PGI yields more information about the depth and delineation of the main PK/VK body. The individual magnetic PGI gives a reasonable estimate for the depth of the HK unit but misses its elongated shape. The two individually recovered geologic models are, however, incompatible when they are combined because of the significant overlap of the PK/VK and HK unit. The multi-physics PGI without petrophysical information produces a geological model that distinguishes between the two kimberlite facies. It also begins to give me information about the elongated shape and dip of the HK unit; this result was not achieved by any of the single-physics inversions, not even by the ones that included petrophysical information. However, the accuracy of the boundaries of the bodies is affected by the lack of petrophysical information. The result is improved by providing petrophysical information to the multi-physics PGI, which yields my best recovered model.

4.6 Discussion

I have expanded the PGI framework developed in chapter 3 to carry out joint inversions, and I have proposed a strategy to balance any number of geophysical data misfits along with a coupling term. In my experiments, this strategy appeared to be critical to fitting data from multiple surveys as well as petrophysical data. Finally, I have used a synthetic example to demonstrate the capabilities of the multi-physics PGI framework.

With regards to the iterative learning of GMM means when limited information is available, considering the confidences $\{\kappa\}$ as vectors is an important contribution of my framework, and it advances the approach of Sun & Li (2016) for updating the means. In their approach, the updates to the means are controlled per unit only, without differentiating the physical properties that are well-known from the undocumented ones. They can either learn the means of a unit or keep it fixed, whereas the framework I present is capable of learning specific components of the GMM means for each unit, as demonstrated in this example.

I demonstrated examples of multi-physics inversions with linear problems. In chapter 3, the PGI approach was applied to nonlinear electromagnetic problems (MT, DC resistivity, and a field FDEM dataset), but it considered only individual surveys depending on a single physical property. I plan to implement this approach for performing multi-physics inversions with electromagnetic methods. This will also be an opportunity to test the robustness of my reweighting strategies for multi-physics inversions with nonlinear geophysical problems. Areas such as

the DO-27 kimberlite pipe (Devriese et al., 2017; Fournier et al., 2017; Kang et al., 2017a), with many different types of geophysical surveys available, are prime candidates for the application of the PGI approach to refine the image of the subsurface structures by integrating more datasets and physical properties in a single inversion.

As I apply the PGI framework to more complex problems, the handling of various types of relationships between physical properties is required. Linear relationships are straight-forward to implement with Gaussian distributions through the covariance matrix, which can define tilted, elongated probability distributions. In Appendix A, I discuss how to account for nonlinear relationships. Such nonlinear relationships are found, for example, between density and seismic velocities (Onizawa et al., 2002). My framework is flexible enough that different relationships can be included for each rock unit. While modest, my example shown in Figure A.2 is, to my best knowledge, the first one in the literature with such diverse relationships in a single inversion. For the moment, my framework assumes that those nonlinear relationships are given. An interesting avenue of research would be to develop the mathematics for the learning of those nonlinear relationships, along with the other GMM parameters, such as defined in section 4.3.

4.7 Conclusion

I have expanded the Petrophysically and Geologically guided Inversion (PGI) framework to use petrophysical and geological information, represented as a multivariate Gaussian Mixture Model (GMM), as a coupling term to perform multi-physics joint inversions. I described my strategies for handling multiple geophysical target misfits as well as a petrophysical target misfit. Finally, I demonstrated, through the DO-27 kimberlite pipe synthetic example, the gains that can be made by including various types of information into a single inversion. Only a joint approach for inverting the potential field datasets allows me to delineate two kimberlite facies and to reproduce their petrophysical signature.

Chapter 5

Case study: joint inversion of potential fields data over the DO-27 kimberlite pipe

5.1 Introduction and geological setting

The DO-27 kimberlite pipe is located in the kimberlite-rich Lac De Gras region, Northwest Territories, Canada (Figure 5.1). It was first discovered in 1992, following the discovery of the Ekati kimberlite field in September 1991 (Kjarsgaard & Levinson, 2002), thanks to an airborne DIGHEM Frequency-Domain Electromagnetic (FDEM) survey. Two distinct anomalies were identified, which were initially thought to be part of a single large complex. After multiple revisions of the conceptual geologic model (Harder et al., 2009), it is now believed that there

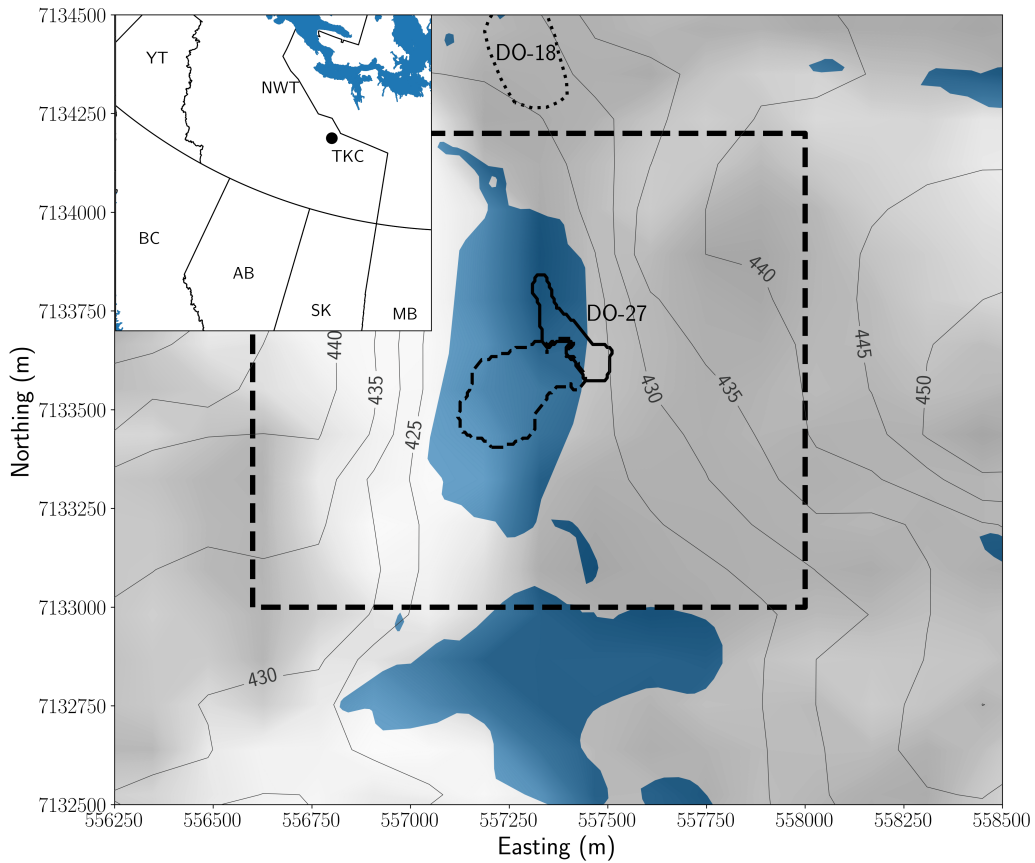


Figure 5.1: Topography map (grey contours and shaded background) and hydrography (blue) at the DO-27 kimberlite pipe in the Northwest Territories, Canada (location in inset). The area of interest is represented as a dashed box. Outline of the PK/VK (dashed) and HK (solid) kimberlite facies present in the pipe, extracted from the geologic model at 285 m of elevation, are overlaid on the map. DO-18 is visible at the northern boundary of the map. Geographic projection: UTM 12N, NAD27.

are two main pipes, designated DO-18 and DO-27, with distinct rock types. Kimberlite pipes are potentially diamondiferous, and the assessment of their economic potential requires an understanding of their geologic structures.

Several types of kimberlite facies can reside inside the same pipe. A schematic representation of the architecture of a typical Lac de Gras pipe is shown in Figure 5.2a. The various kimberlite facies are classified based on their genesis (Field & Smith, 1998; Kjarsgaard, 2007). At DO-27, there are three main facies, embedded in a granitic host rock, that play a role in the potential field responses. The first is a hypabyssal kimberlite (HK), which is an intrusive igneous rock often found at the base of the pipe (Figure 5.2a). The second is a volcanoclastic kimberlite (VK), which is an extrusive igneous rock with high porosity, that is typically found above the HK unit. The last facies is a pyroclastic kimberlite (PK), which is the diamondiferous unit at DO-27. It shares many characteristics with VK because both formed during extrusion events accompanied by an explosion. Glaciers eroded the top of the pipes, allowing the formation of lakes, and deposited a thin layer of till (Doyle et al., 1998; Dyke & Prest, 1987).

The geologic model of the DO-27 pipe, built from several drilling campaigns, is presented in Figure 5.2b. The geometry of DO-27 diverges significantly from the standard kimberlite model with a sheet-like hypabyssal unit present near the surface. Harder et al. (2009) concluded that DO-27 was formed in several successive volcanic phases with the HK unit pre-dating the VK intrusion (Doyle et al., 1998). This VK intrusion was later disturbed by another volcanic event, with the PK unit infilling the pipe. Several minor occurrences of kimberlite units, that have

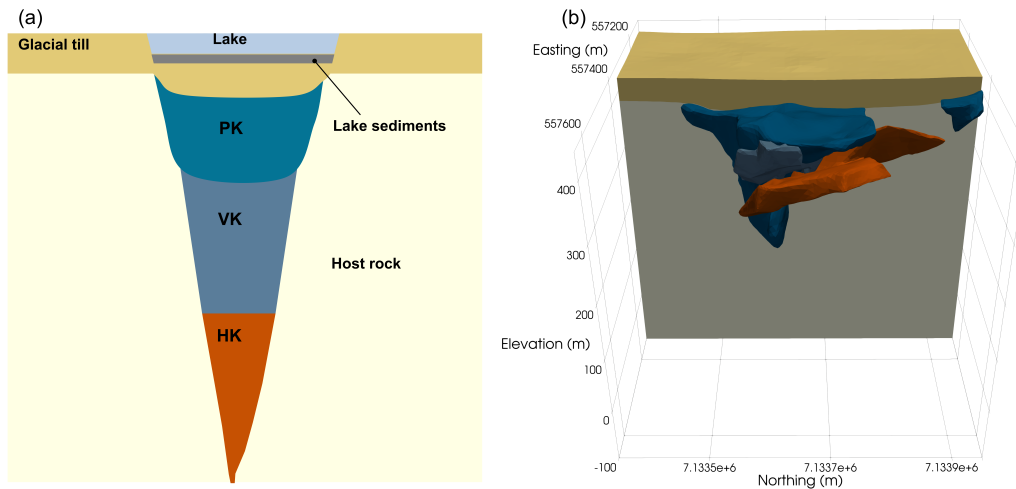


Figure 5.2: (a) Lac De Gras kimberlite pipe conceptual model (modified from Devriese et al. (2017)). HK: Hypabyssal Kimberlite facies; VK: Volcanoclastic Kimberlite facies; PK: Pyroclastic kimberlite facies; (b) Current geological representation of the DO-27 pipe based on drill-holes. The same colour convention for the rock units is used for (a) and (b) and throughout the chapter.

been identified as PK facies, have been observed close to the surface. As discussed in Devriese et al. (2017), the density and magnetic characteristics of the different units are as follows: 1) the PK and VK units have low density and are weakly magnetic susceptible. They are indistinguishable from each other in potential field surveys, and they are thus referred to as a PK/VK unit; 2) the HK unit has a density that is close to the granitic host rock, but it has a high magnetic susceptibility and is remanently magnetized; 3) the thin horizontal layer of glacial till, that only plays a minor role from a potential field standpoint, and granitic host rock are regrouped under the term “background”.

Geophysics plays an important role in kimberlite exploration, such as illus-

trated in Keating & Sailhac (2004); Macnae (1995) and Power & Hildes. (2007), and much work has been done over the DO-27 and DO-18 kimberlite pipes. Jansen & Witherly (2004) presented an overview of the exploration geophysical surveys acquired before 2000. Devriese et al. (2017) performed smooth inversions of individual potential field datasets. Their interpretation of the physical property models defined the overall shape of the DO-27 and DO-18 pipes. Their analysis provided a valuable start in distinguishing between the PK/VK and the HK units. Fournier et al. (2017) focused on the inversion and interpretation of the electromagnetic surveys. They were able to distinguish the top of the pipe from the lake-bottom sediments and till layer. Finally, Kang et al. (2017a) extracted Induced Polarization (IP) information from airborne electromagnetic surveys to distinguish between adjacent kimberlites based on their clay mineral content. They subsequently built a geologic model using a post-inversion classification. The inputs to their classification were density, magnetic susceptibility, electrical conductivity, and chargeability obtained from the individual smooth inversions.

Rather than generate a quasi-geology model from a post-inversion classification (Li et al., 2019), my goal is to carry out a single inversion that integrates potential fields data with petrophysical and geological information. I use my joint inversion framework, defined in chapters 3 and 4 for Petrophysically and Geologically guided Inversion (PGI). In this study, I jointly invert potential fields data from a ground gravity survey, an airborne gravity gradiometry (Falcon) survey (Lee, 2001), and an airborne magnetic survey (acquired during a Versatile Time Domain Electromagnetic (VTEM) survey (Witherly, 2005)). I use the petrophys-

ical signatures of the background, PK/VK, and HK rock units as a coupling term. This coupling term links density, the three components of the magnetization of the rocks, and the elevation to account for variations of the density signature of the PK/VK unit with depth. The petrophysical data are represented as a Gaussian Mixture Model (GMM) (Dempster et al., 1977; Murphy, 2012). This GMM is used to generate a misfit function that quantifies how well the inversion fits the petrophysical signatures. A successful inversion simultaneously achieves acceptable fits of the geophysical and petrophysical data.

This case study is segmented into four parts. First, I introduce the geophysical datasets and the data processing steps. Next, I design the GMM from the available petrophysical data by identifying the physical properties characteristics of each rock unit. The first inversion with the PGI approach focuses on recovering density from the two gravity surveys. I jointly invert ground gravity and Falcon data to recover a density model that is consistent with the PK/VK density increase with depth. I then invert the airborne magnetic data. To recover a magnetization model consistent with the high remanence of the HK unit, I use a Magnetic Vector Inversion (MVI). I show that combining these density and magnetic vector models yields volumes with erroneous combinations of physical properties and uncertainties about the extent of the HK and PK/VK units. I follow up with a fully integrated multi-physics inversion of the potential field datasets by inverting all three geophysical surveys together with the signature of all three rock units (background, PK/VK, and HK). This model is a significant improvement over what is obtained from post-inversion classifications. The delineation of the diamondif-

erous PK/VK unit over the central part of the DO-27 pipe is in good agreement with the outline drawn from drillholes. The model, however, disagrees with drill-hole information north of the DO-27 pipe. To address this, I add to the inversion geological information in the form of an extra rock unit to represent minor near-surface occurrences of PK facies. The final quasi-geology model obtained with the PGI approach resolves the geologic conflicts and allows me to estimate the volume of the PK/VK unit, which is the potential diamondiferous resource at DO-27.

5.2 Geophysical datasets

5.2.1 Ground gravity

Ground gravity data were acquired, on the ice, over DO-27 in the spring of 1994. The survey is composed of 441 stations with a 25 m spacing along east-west lines 100 m apart. Gravity data were processed by the contractor and provided as the complete Bouguer anomaly.

In preparation for the inversion, I upward continued the data by 6.25 m so that they are half a cell-width above the surface. This is done to minimize the effects of potential small-scale heterogeneities inside a subsurface cell that is mathematically modelled as a volume with homogeneous density (Li & Oldenburg, 1996). A low-frequency signal was seen in my early inversions that manifested as density contrasts in the padding cells. While this low-frequency signal can be absorbed this way, I chose to remove a linear trend from the data to focus the inversion on the local anomalies. I used a robust Cauchy loss function for the linear regres-

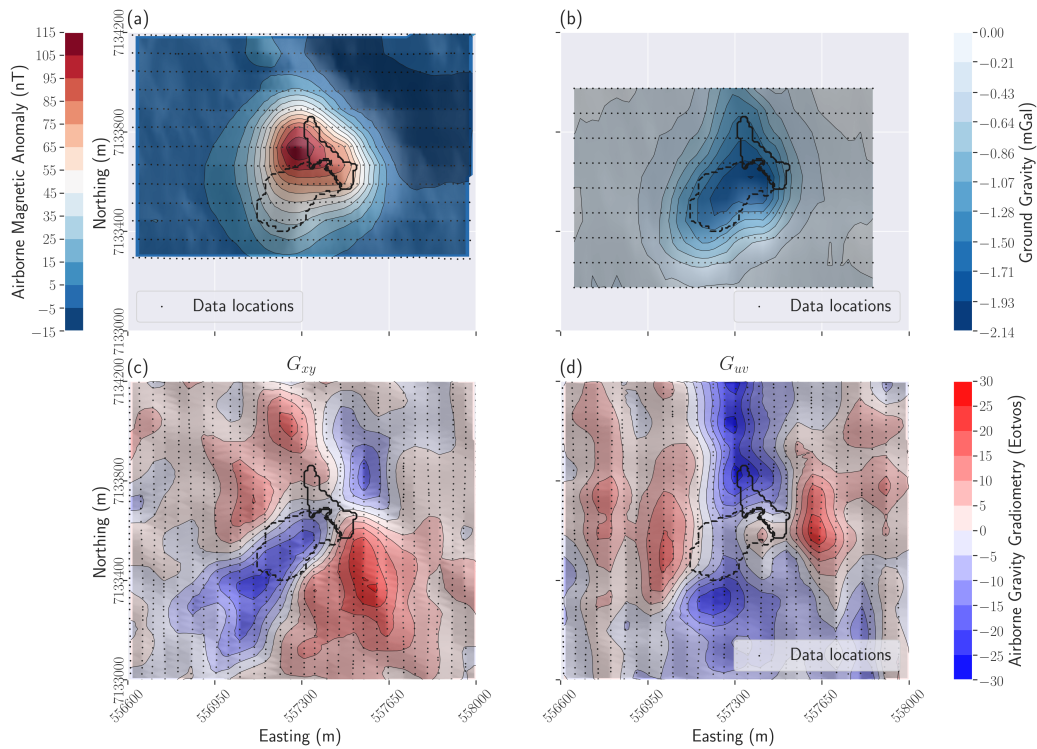


Figure 5.3: Four potential field datasets, collected over the DO-27 pipe, which are used in this study (after regional removal). (a) Airborne VTEM total field magnetic survey; (b) Ground gravity survey; (c) G_{xy} component of the airborne Falcon gravity gradiometry survey; (d) G_{uv} component of the airborne Falcon gravity gradiometry survey.

sion, which is less affected by outliers than a least-squares estimation (Kadiyala & Murthy, 1977). The processed dataset is shown in Figure 5.3b.

A clear negative anomaly of -2.14 mGal, associated with the DO-27 kimberlite pipe, is visible. A northern extension was first interpreted as a connection between the DO-18 and the DO-27 kimberlite pipes. The current understanding is that it is due to several minor near-surface kimberlite dikes and sills (Doyle et al., 1998).

In the inversion, I assign a uniform unbiased Gaussian noise level with a standard deviation of 0.045 mGal; this is identical to what is used in Devriese et al. (2017).

5.2.2 Falcon airborne gravity gradiometry

An airborne Falcon gravity gradiometry survey was flown in 2001 over the property. Over the area of interest, the survey flew 29 north-south flight lines spaced 50 m apart with an average 53 m ground clearance. I down-sampled the data along the lines to one measurement every 25 m to yield approximately one data point per surface cell in my mesh. This ensures that there is no signal in the data with a smaller wavelength than can be modelled by the mesh (Figure 5.3c and 5.3d).

At each station, two combinations of the gravity gradiometry tensor (Pawlowski, 1998) are measured by the Falcon system (Lee, 2001). The first component is simply G_{xy} . The second measurement is a linear combination of two components of the tensor: $G_{uv} = (G_{yy} - G_{xx})/2$. I invert directly for those two measurements. The data were processed by the contractor with an equivalent source transformation using a 2.67 g/cm³ background density.

In the inversion, I assign a uniform unbiased Gaussian noise level with a standard deviation of 5 eotvos for both G_{xy} and G_{uv} components; this is identical to the one used in Devriese et al. (2017).

5.2.3 VTEM airborne magnetic survey

Total field magnetic data were recorded during a VTEM survey flown in 2004 over the property, using a cesium vapour magnetometer towed 15 m below the aircraft. The survey over the area of interest is composed of 13 east-west flight lines 75 m apart with an average 72 m ground clearance.

Before the inversion, I removed a linear trend from the data using a Cauchy norm. I down-sampled the lines to one data point every 25 m. The processed dataset is shown in Figure 5.3a.

A strong positive anomaly of 115 nT is visible north of the complex. It is associated with a negative signal of -15 nT on the North-East; this is relatively strong for that latitude. It suggests that the data are affected by a strong remanent magnetization (Devriese et al., 2017).

To handle the different types of magnetization (induced and remanent) and the uncertainties about the remanent field direction (see Devriese et al. (2017) and section 5.4.2), I use a full Magnetic Vector Inversion (MVI) with a Cartesian formulation (Lelièvre & Oldenburg, 2009b) to invert the magnetic data.

In the inversion, I assign a uniform unbiased Gaussian noise level with a standard deviation of 1 nT; this is identical to the noise level used in Devriese et al. (2017).

5.3 Tikhonov inversions

All the inversions presented here are carried out with the open-source SIMPEG package (Cockett et al., 2015). In addition, they all share the same Octree mesh

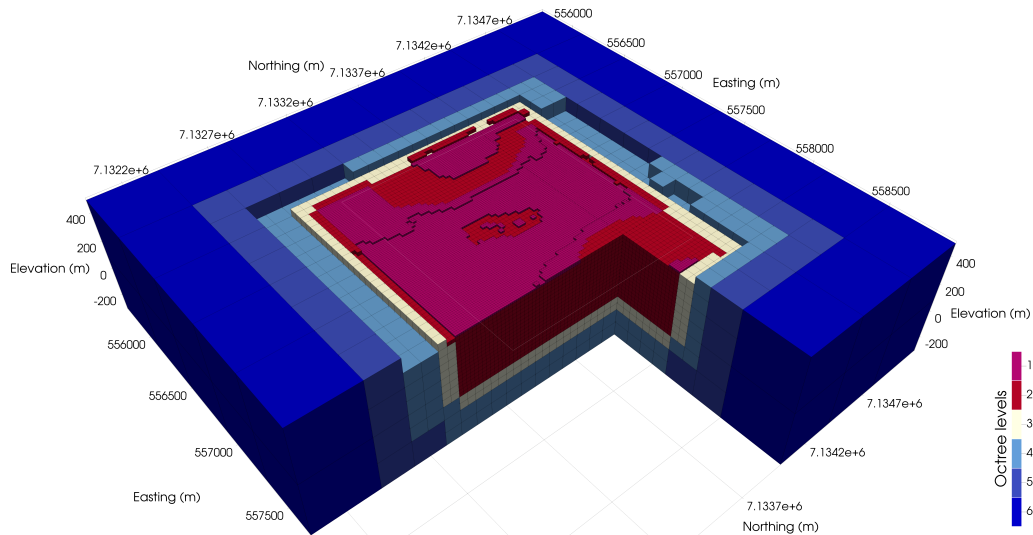


Figure 5.4: The Octree Mesh used for all of the inversions. The area of interest is outlined in white. The Octree levels represent each increase in cell size (with level 1 being the smallest cells). The volume of interest is discretized with 25 m cubic cells (level 2). The topography is accommodated with a layer of the smallest cells (12.5 m cubic cells, level 1). The other levels (3 and more) serve as padding.

(Figure 5.4). The use of an Octree mesh significantly speeds up the inversions while maintaining high resolution in the area of interest. All the inversions start from null half-spaces initial and reference models. For all the joint inversions, I use the strategy outline in section 4.4 to handle multiple geophysical surveys, where the weights of the components of the total data misfit term are adjusted during the inversion until each geophysical misfit is equal or below its target value (Parker, 1977).

Smooth inversions of all the individual potential field surveys can be found in Devriese et al. (2017). To extend that work, and to highlight the gains obtained using a PGI approach, I show two additional smooth inversion results: a smooth

inversion combining the gravity and gravity gradiometry data, and a smooth MVI of the magnetic data. A post-inversion combination of the physical property models is then conducted (Figure 5.5).

I first perform the smooth joint inversion of the ground gravity and Falcon gravity gradiometry surveys. This is possible because both surveys are sensitive to the same physical property. Plan view and cross-sections of the recovered density model are shown in Figure 5.5a. The model is relatively smooth, as it is expected, and the low-density material extends well beyond the boundaries of the outline of the kimberlite units.

I then carry out the unconstrained smooth MVI to recover the magnetization vector for each cell. The MVI problem is more challenging than gravity inversions because three components need to be recovered. I use the Cartesian approach outlined in Lelièvre & Oldenburg (2009b) and find a smooth solution for each component. Plan view and cross-sections of the recovered model are shown in Figure 5.5b. Each magnetization vector is projected onto the plotting plane. The recovered vector magnetizations smoothly vary in amplitude and orientation, as it is expected. Only the large-scale region of high magnetization is predominantly visible. The cross-sections chosen for magnetization are not in the same location as those used for density because high magnetizations occur at a different location than the high-density contrast values. It is reflective of the different rock units that are generating the two responses. Close to the location of the HK unit, the vectors are oriented in a direction close to the remanent field direction estimated in Devriese et al. (2017) (inclination: 53° , declination: 22°).

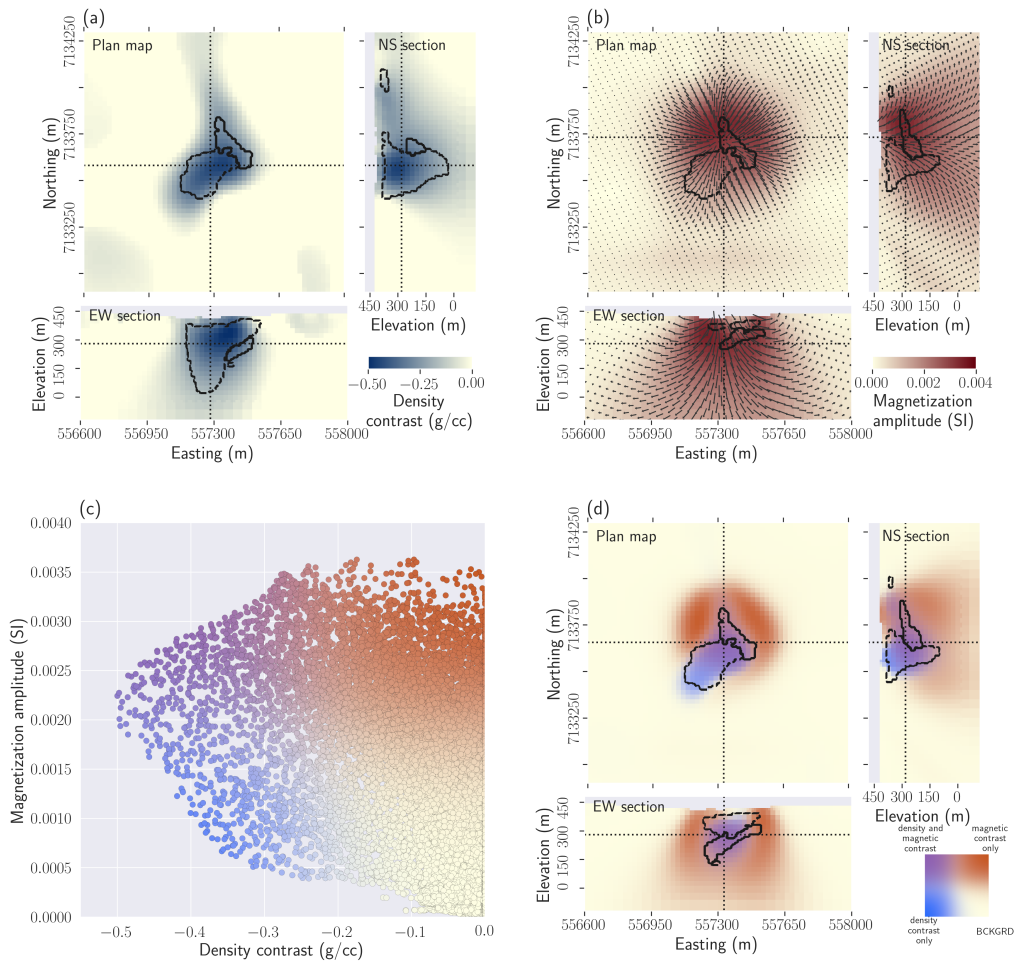


Figure 5.5: Results of the smooth gravity inversion and MVI and post-inversion analysis. (a) Plan map, east-west, and north-south cross-sections through the density model obtained by joint smooth inversion of the ground gravity and Falcon data. The dotted lines represent the location of each cross-section; (b) Plan map, east-west, and north-south cross-sections through the magnetic vector model obtained by MVI of the magnetic data. The dark arrows represent the magnetization direction and strength of the magnetic vector projected on the plane; (c) scatter plot of the inverted density contrast and magnetization strength coloured based on both physical properties; (d) coloured model based on the density contrast - magnetization strength couple.

To evaluate the interpretation achievable by combining the smooth inversions, I take the magnitude of the magnetization, convert it to an effective susceptibility, and then plot the scatter plot of magnetization versus density (Figure 5.5c). The points are coloured based on both the density contrast and magnetization strength (shades of blue for significant density contrast only, red for magnetic contrast and purple when both contrasts occur). The scale is provided in Figure 5.5d. No distinct clustering of rocks is observed. In Figure 5.5d, each cell in the model is assigned a colour that conveys the relative values of the physical properties in that cell. For instance, a white cell denotes a background rock while a blue cell indicates a rock that has low density. Figure 5.5c and 5.5d highlight that trying to evaluate a specific volume for the PK/VK unit from these inversions would be highly dependent on the threshold value one would choose to delineate the body. Estimates obtained with clustering algorithms would have the same issues. Those limitations motivate the search for an improved solution that reproduces the petro-physical characteristics of each rock.

5.4 Modelling the petrophysical information at DO-27

Qualitative information about the physical properties of the various rock types found at DO-27 was used during previous studies relying on Tikhonov inversions (Devriese et al., 2017; Fournier et al., 2017; Kang et al., 2017a). For my work, I need more quantitative information from field samples. I obtained 20 samples of the various kimberlite facies from Peregrine Diamonds Ltd. 11 samples of PK, 4

of VK, and 5 of HK were sent to the Geological Survey of Canada Paleomagnetism and Petrophysics Laboratory, Victoria, BC, for characterizing the physical properties of each unit. In the following material, I discuss those measurements and how I compiled the information into a form that allows me to generate a GMM. Means and standard deviations summarizing the petrophysical characteristics of each rock unit are provided in Table 5.1.

5.4.1 Density information

The HK samples were mechanically competent, and 5 densities were obtained: 2.764, 2.867, 2.435, 2.632 and 2.677 g/cm³. These samples yield an average density of 2.675 g/cm³, which is similar to the estimated background density of 2.67 g/cm³ (Devriese et al., 2017). The HK unit is deemed indistinguishable from the background from the density standpoint. The mean density contrast of both rock units is thus set to 0 g/cm³. The density of the background unit is, however, assigned a smaller standard deviation.

The PK and VK units are highly porous and mechanically weak. Unfortunately, this prevented density information from being obtained from several samples. Those that were successfully analyzed are believed to be associated with more competent and denser samples. Those samples are thus deemed unrepresentative of the kimberlite unit in general and were not used. Instead, I rely on density measurements taken by Peregrine Diamonds Ltd during the drilling programs. A block model of the density of PK was built based on those measurements (Eggleston et al., 2014). To include this information in the inversion, I used the published

cross-section through this block model (Figure 5.6a). Assuming a background density of 2.67 g/cm^3 , the density contrast is $\sim -1.1 \text{ g/cm}^3$ at 400 m elevation and changes linearly to achieve a value of $\sim -0.5 \text{ g/cm}^3$ at 200 m elevation. This cross-section provides enough information for me to characterize the density signature of the PK/VK unit and build a GMM. To include the linear trend of density contrast with depth, I add the elevation as a fixed parameter in the coupling term. I generate a two-dimensional GMM (density contrast and elevation) that is consistent with the observations (shown in Figure 5.6b along with the scatter plot of the cross-section). The elongated and tilted shape of the Gaussian distribution representing the PK/VK unit accounts for the correlation of density contrast with depth. On the contrary, the background (and HK) density values are assumed to be independent of the depth. This is modelled by assigning a high standard deviation for the elevation of those units; their assigned mean elevation is then of no consequence in the inversion. The long vertically elongated shape of the Gaussian distribution for the background unit manifests the independence of the density contrast with respect to the elevation for that unit. Means and standard-deviations characterizing the density contrast of each rock unit are provided in Table 5.1.

5.4.2 Magnetic susceptibility information

Both the induced magnetization and the strength of the remanent field of the samples were measured (Figure 5.7a). The strength of the remanent field was given in the form of a Koenigsberger ratio (Koenigsberger, 1938). The magnetic susceptibility of the samples spans a wide range of values, which is consistent with the

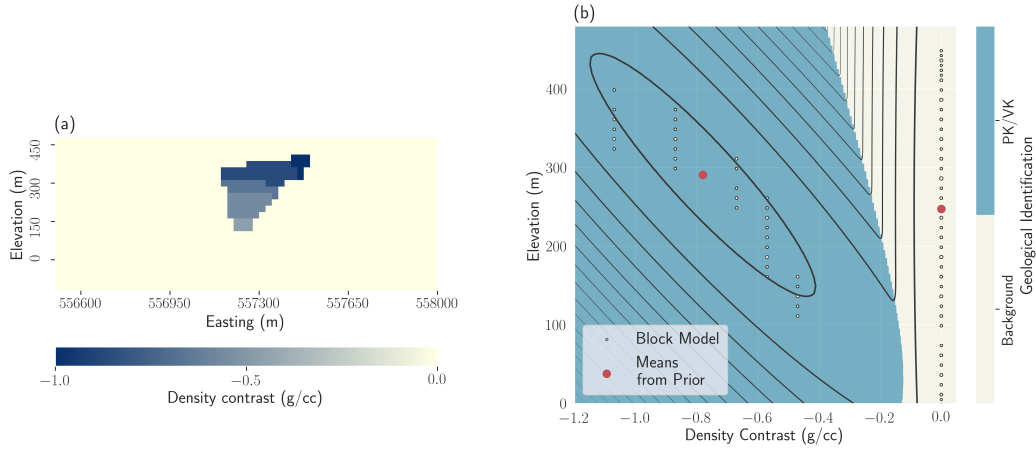


Figure 5.6: Design of the PK/VK unit density signature in the GMM. (a) Cross-section of the density contrast estimate for the PK/VK unit from Eggleston et al. (2014); (b) Scatter plot, density contrast versus elevation of the cells, of the cross-section shown in panel (a). I fit a Gaussian on each unit (PK/VK and background); the contour lines represent isoprobability levels from the resulting GMM, and the background colour indicates the geological identification.

fact that magnetic susceptibility generally has a logarithmic distribution (Enkin et al., 2020; Latham et al., 1989; Rauen et al., 2000).

If the remanent magnetization direction is known, it is possible to estimate an effective susceptibility k_{eff} for the magnetic vector of each unit:

$$k_{\text{eff}} = k \left\| \hat{u}_{\text{earth}} + Q \frac{B_{\text{lab}}}{B_{\text{earth}}} \hat{u}_{\text{rem}} \right\|_2, \quad (5.1)$$

where k is the measured magnetic susceptibility (purely inductive magnetic response), \hat{u}_{earth} is the unit vector of the Earth's magnetic field direction at DO-27, Q is the Koenigsberger ratio, B_{earth} is the International Geomagnetic Reference Field (IGRF) at DO-27, B_{lab} is the amplitude of the magnetic field used in the

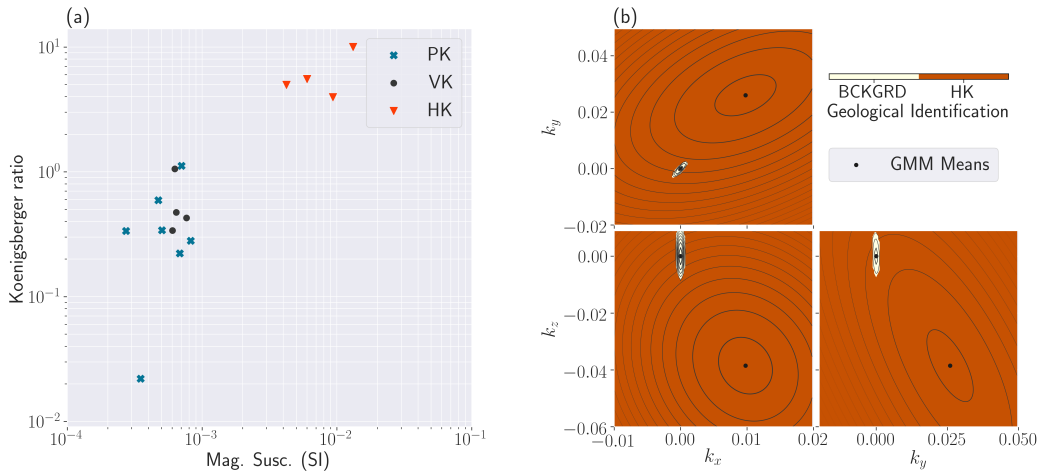


Figure 5.7: (a) Magnetic measurements in the laboratory; (b) 2D projections of the 3D GMM of the Cartesian components of the magnetic vector resulting from modelling; contour lines represent iso-probability levels of the GMM, and the background colour indicates the geological identification. The background unit is limited to the space defined by the small ellipsoid.

laboratory for the measurements (59000 nT) and \hat{u}_{rem} is the unit vector of the remanent magnetization direction.

The PK and VK units have a small magnetic susceptibility and are weakly remanent. Their effective susceptibility, assuming that the remanent field is aligned with the current Earth's magnetic field, is estimated at $8 \cdot 10^{-4}$ SI.

Only 4 samples of HK were measured for their magnetic response. Their Koenigsberger ratios are close to 10. Hence the magnetic response of the HK unit is essentially due to remanent magnetism. However, I need an estimation of the remanent magnetization orientation of the HK unit to obtain an effective susceptibility. Devriese et al. (2017) obtained an estimation of a 53° inclination and 22° declination, with uncertainties of about 10° for each angle, by cross-correlation of

the vertical and total gradients of the reduced to pole data. Using these estimated angles, I obtain a mean effective susceptibility of $5 \cdot 10^{-2}$ SI for the HK unit.

The mean and standard deviation values of the log-effective magnetic susceptibility, inclination, and declination for each rock unit are provided in Table 5.1. Those values define Gaussian distributions of the magnetization parameters in a spherical coordinates system with a logarithmic distribution for magnetization amplitudes. Ideally, I would like to invert for a log-susceptibility model, but that poses challenges because the very low susceptibilities do not generate a substantial signal in the magnetic field data. Therefore, I revert to the usual practice of inverting for magnetic susceptibility on a linear scale. The MVI algorithm inverts for each Cartesian component of magnetization $\{k_x, k_y, k_z\}$. For PGI, I need to represent the magnetization in a GMM. I thus need to obtain means and covariance matrices for $\{k_x, k_y, k_z\}$. To this end, I appeal to random numerical sampling methods. For each rock unit, I randomly sample, from their Gaussian distributions in spherical coordinates, log-effective susceptibility and angles triplets. I convert those synthetic samples to Cartesian values and use them to estimate the desired means and covariances (equations (2.40) and (2.41)).

The resultant GMM for the magnetic parameters can be visualized in Figure 5.7b. The distributions appear elongated and tilted, indicating correlations between the Cartesian magnetization components. Given the measured magnetization and uncertainties, the weakly magnetic PK/VK is difficult to distinguish from a non-susceptible background due to the nearby highly magnetic HK unit. PK/VK and the background have thus been grouped under “background” in Figure 5.7b.

Table 5.1: Physical properties and elevation parameters for each rock unit. For the PK/VK-pipe unit, the values are reported without the rotation of the Gaussian distribution caused by the linear trend with depth. Notation and units: \bar{x} : mean of x ; σ_x standard-deviation of x ; ρ : density contrast (g/cm^3); z : elevation (meter); k : effective magnetic susceptibility (\log_{10} SI); θ : inclination ($^\circ$); ϕ : declination ($^\circ$).

Rock unit	$\bar{\rho}$	σ_ρ	\bar{z}	σ_z	\bar{k}	σ_k	$\bar{\theta}$	$\bar{\phi}$	$\sigma_{\theta,\phi}$
Background	0	0.03	290	180	-6	0.24	83.8	19.5	10
PK/VK	-0.78	0.07	290	75	-3.1	0.24	83.8	19.5	10
HK	0	0.1	290	180	-1.3	0.33	53	22	10
PK-minor	-0.3	0.1	360	10	-3.1	0.24	83.8	19.5	10

5.4.3 Petrophysical characterization summary

I have defined, in terms of density and magnetization, the characteristics of the background and main kimberlite units identified in the DO-27 pipe. Table 5.1 summarizes the quantitative values used to define the GMMs for the various inversions I conduct. Information about a new unit, PK-minor, is also reported. This unit is used in my final inversion, and more details are given in section 5.6.

Regarding density, the background and HK units are both assigned a 0 g/cm^3 mean density contrast, while the PK/VK unit presents a mean density that varies with depth. The background and HK units are indistinguishable, and the gravity anomaly is primarily due to the PK/VK unit. Thus, carrying out an inversion just for a density contrast model with PGI only requires a petrophysical GMM consisting of two rock units (background and PK/VK).

A similar situation occurs for magnetic properties. The HK unit is dominant, and its magnetization is nearly two orders of magnitude larger than the PK/VK

unit. Any inversion that focuses purely on magnetic data would have challenges delineating the PK/VK unit from the background in the presence of the HK unit. Thus carrying out a PGI solely for a magnetic vector model only necessitates a petrophysical GMM with two rock units (background and HK).

Although only two rock units are justified when inverting for a single type of physical property, the situation changes when density and magnetic characteristics are considered together. This is illustrated in Figure 5.8 (reproduction of Figure 4.2) with a fictitious GMM with two physical properties (the axes) and three rock units (the Gaussian distributions). Pairs of units appear indistinguishable in one physical property or the other (1D spaces), but they are all distinct when considering a higher-dimensional petrophysical space (the 2D space). In the DO-27 real case scenario, the background, PK/VK, and HK units are distinct in the 5D space composed of density, elevation, and the three magnetic vector components. The multi-physics inversions take advantage of that higher dimensionality of the GMM to recover all three rock units at once (see section 5.6). I now carry out the single-physics and multi-physics PGI to illustrate these ideas.

5.5 Single-physics PGIs

I now invert, with the PGI approach, datasets that are connected by a single physics. A density model is recovered from gravity and gravity gradiometry data using the information that the density of the PK/VK unit increases with depth. From the magnetic data, I recover a magnetic vector model that is compatible with the knowledge about the magnetization of the HK unit. The density and magnetiza-

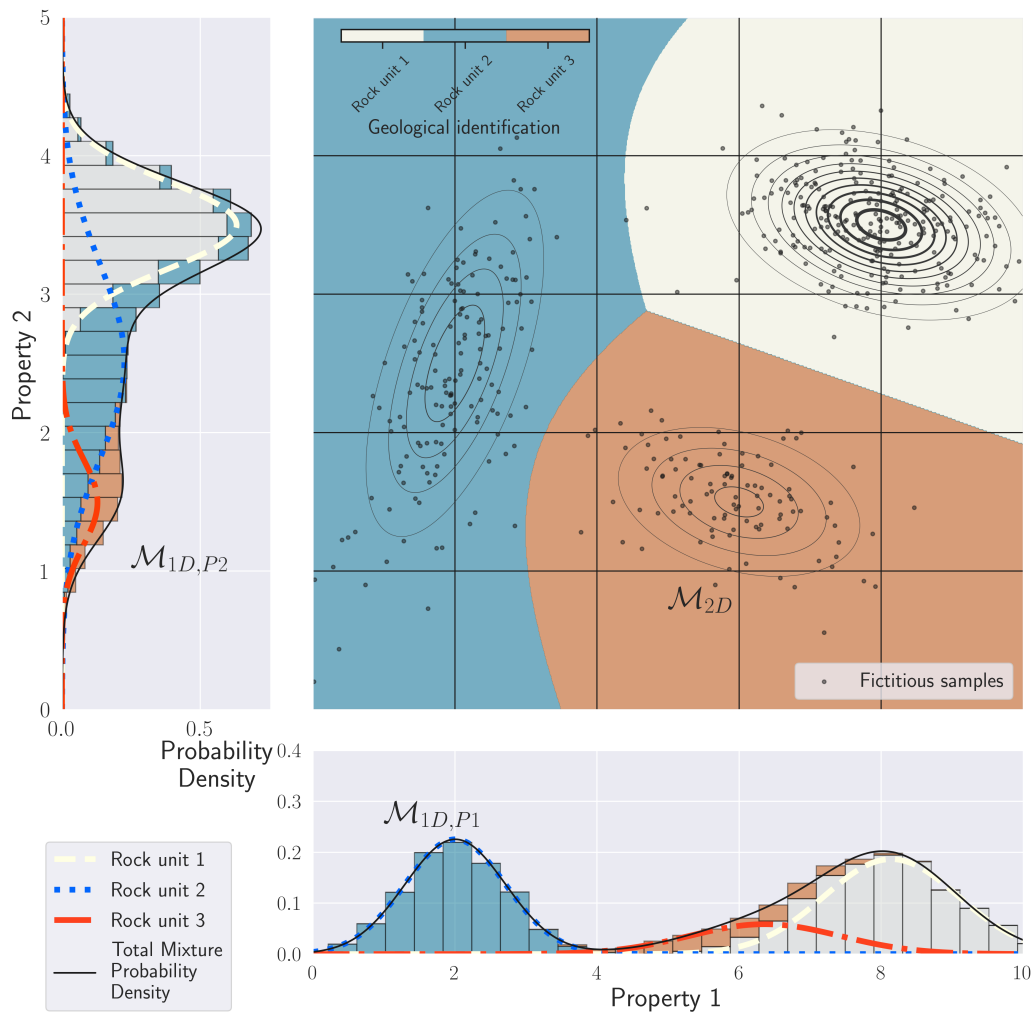


Figure 5.8: Highlighting the distinction of rock units in various dimensions: fictitious example of a GMM with two parameters and three rock units, its projections in 1D, and the geological identification prediction in the background (reproduction of Figure 4.2).

tion models then are combined to highlight the limitation of single-physics and post-inversion classification approaches in delineating the two kimberlite units.

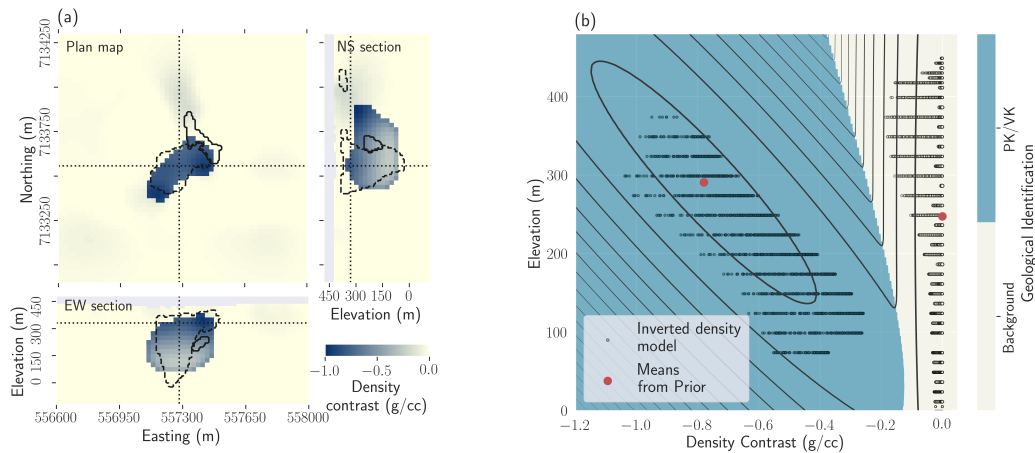


Figure 5.9: Inversion result with PGI of the ground gravity and Falcon surveys using the density signature of PK/VK; (a) Plan map, east-west, and north-south cross-sections through the recovered density contrast model; (b) Comparison between the petrophysical GMM (contours plot) used to regularize the inversion and the recovered density contrast model (scatter plot).

5.5.1 Joint PGI of the ground gravity and Falcon airborne gravity gradiometry data

I first jointly invert the ground gravity and airborne gravity gradiometry data with the addition of the petrophysical model to include the knowledge about the expected density contrasts and their variations with depth. The obtained density model is shown in Figure 5.9a, and it can be compared with the result obtained by jointly inverting the two datasets but without a petrophysical constraint (Figure 5.5). The trend with depth can be seen in the scatter plot in Figure 5.9b. Each survey has reached its target misfit.

A single body, reproducing the PK/VK petrophysical signature, is sufficient to fit the gravity data. The horizontal outline of this PK/VK body is in reasonable

agreement with the geologic model, except for a region north of the pipe. The bottom of the PK/VK body is relatively well constrained. On the north-south cross-section, low-density material can be distinguished in the upper surface (approximately -0.1 g/cm^3 , at elevation greater than 300 m) that lies above the northern extension of the identified PK/VK volume. That anomaly may be related to other minor kimberlite occurrences and is still identified as background in the quasi-geology model (Figure 5.9b).

5.5.2 Magnetic vector inversion of the airborne magnetic data with PGI

Here, I invert the magnetic data using a MVI to recover each component $\{k_x, k_y, k_z\}$ of a magnetic vector. The inclusion of petrophysical information, through the GMM, ensures the algorithm is reproducing the signature of the HK unit.

The result of the inversion with petrophysical knowledge is shown in Figure 5.10a. The algorithm recovers a well-defined, compact magnetic body with consistent magnetic orientation reproducing the modelled petrophysical signature of HK (Figure 5.10b). The location of the HK unit coincides well with that obtained from drillholes, except that the eastern side of the mapped HK unit is not recovered, and no dip is visible. No anomaly related to PK/VK is visible in the magnetic vector model.

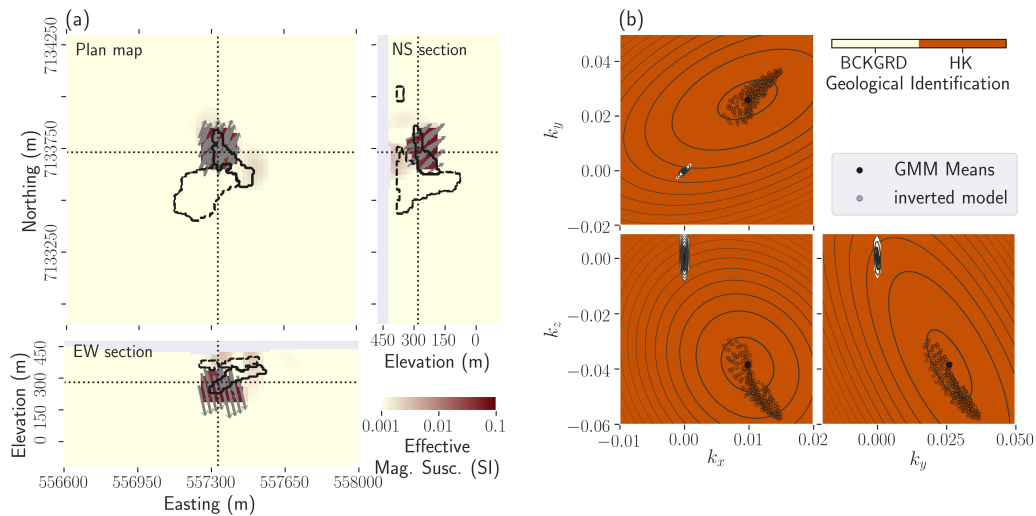


Figure 5.10: Result of the petrophysically guided MVI. (a) Plan map, east-west, and north-south cross-sections through the magnetic vector model; (b) Comparison between the petrophysical GMM (contour plots) used to constrain the magnetic vector model and the recovered magnetic vector model (scatter plots). The background unit appears in the plots as the small ellipsoid. Background cells are all within that small portion of the parameters space. The geological identification is used to colour the background of the plot.

5.5.3 Post-inversion classification of the individually obtained density and magnetic vector models

At this stage, I have obtained two physical property models. One is a density model that reproduces both gravity datasets and the PK/VK density signature. The HK unit is not necessary to explain the gravity data and is considered to be indistinguishable from the background regarding its density. The second is a magnetic vector model that globally reproduces the magnetic data and HK magnetic signature. In this inversion, the PK/VK unit is deemed to be indistinguishable from the background regarding its magnetic susceptibility.

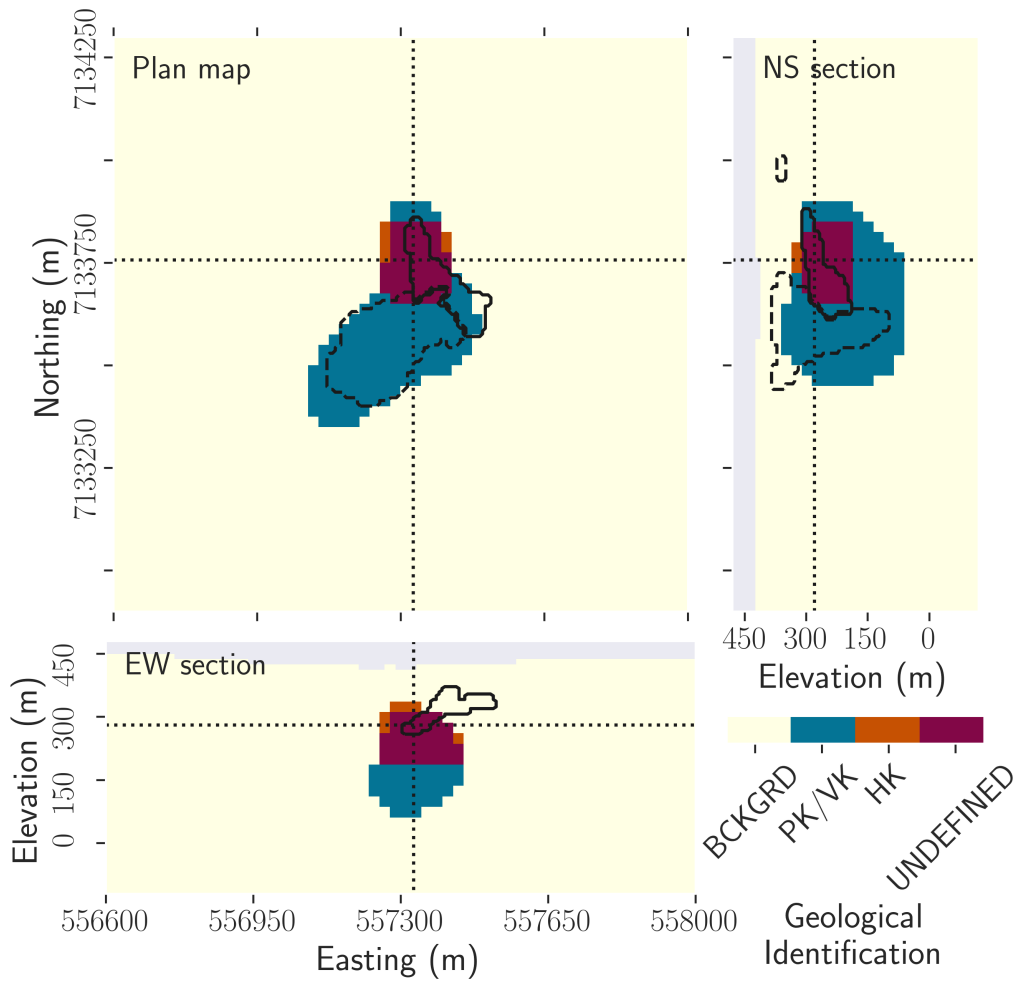


Figure 5.11: Plan map, east– west, and north–south cross-sections through the combination of the individual PGIs. The “UNDEFINED” area corresponds to a volume where both high density and magnetic contrasts were found, corresponding to no known rock units signature.

Combining the two models (Figure 5.11) highlights the limits of post-inversion classification with single-physics inversions of geophysical datasets. Even with the addition of petrophysical information and the dominance of each unit in each inversion, the combination of the two models shows an important overlap between the recovered PK/VK and HK units (marked as the “UNDEFINED” area). This volume, actually covering most of the recovered HK unit, is found to have both strong density and magnetic contrasts. This signature disagrees with the petrophysical knowledge of the area.

To overcome this, I propose to invert all three surveys (ground gravity, airborne gravity gradiometry, and airborne magnetic) together with all five coupling parameters (density contrast, elevation, and the three components of the magnetic vector).

5.6 Multi-physics PGIs

In this section, the PGI approach is used to invert all three datasets along with the petrophysical information about the rock units. I first consider three rock units (the background, PK/VK, and HK) to form the GMM. I then further refine the quasi-geology model by adding a fourth unit and geological *a priori* information, based on drillholes, into a subsequent inversion to recover desired geological features.

5.6.1 Multi-physics inversion with petrophysical information

The multi-physics PGI result is presented in Figure 5.12. The improvement over the single-physics inversions, both smooth and petrophysically guided, is quite

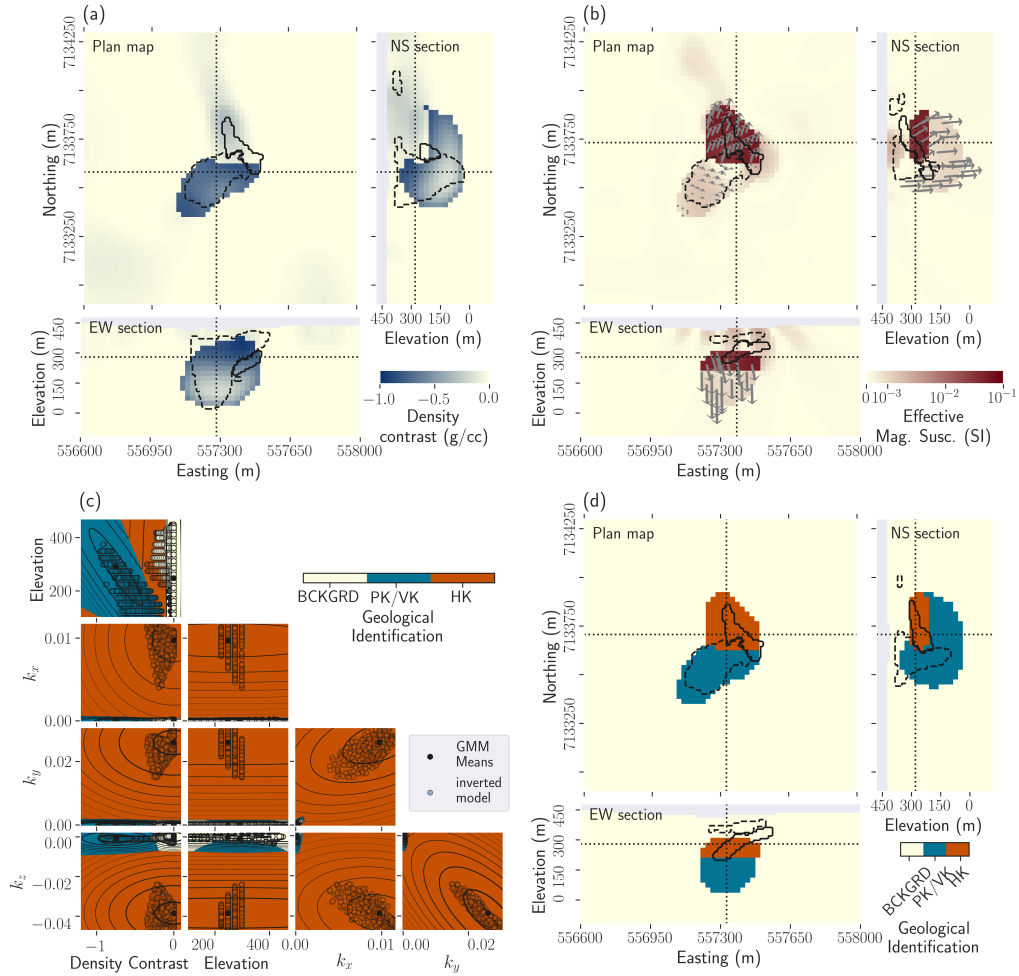


Figure 5.12: Results of the multi-physics PGI with three rock units. (a) Plan map, east-west, and north-south cross-sections through the density contrast model; (b) Magnetic vector model. The grey arrows are the projections of the magnetization directions (unit vector) on the plane for the kimberlite units; (c) Presentation of the 5-dimensional GMM: visualization of all possible 2D projections. Comparison with the recovered model represented as the scatter plots of the four physical properties of the geophysical model and the elevation; (d) Resulting quasi-geology model from the multi-physics PGI with three rock units.

pronounced. The overlapping of the units observed by combining single-physics inversions has been resolved by the multi-physics inversion, which reproduces the full five-dimensional petrophysical distribution.

Figure 5.12c presents the 5D GMM by showing all possible 2D projections. The values of the physical properties model are well clustered around the prescribed means and along determined trends. The dimensionality increase of the GMM allows me to define three distinct units (the background, PK/VK and HK), with their specific signature for all physical properties. The multi-physics inversion recovers an HK unit with a mean density contrast of approximately -0.12 g/cm^3 . Similarly, the magnetic signature of the recovered PK/VK unit now is distinguishable from the background; it has a mean effective susceptibility of $1.06 \cdot 10^{-3}$ SI, which is close to the expected value of $8 \cdot 10^{-4}$ SI. The PK/VK magnetization is oriented along the Earth's magnetic field, as required. This orientation differs from the remanent magnetization given to the HK unit. This difference in orientation can be seen in Figure 5.12b. It is only with the multi-physics inversion approach that I can define two clear kimberlite facies (Figure 5.12d).

Comparison with a geologic model from drilling

Now that I have obtained a quasi-geology model containing all three major units that reproduce the geophysical datasets and petrophysical information, I can compare it to the geologic model built from drillholes (Figure 5.12d).

The HK unit is reasonably well localized, but not all of the details are reproduced by the inversion. In reality, the HK unit is a thin, dipping body that is imaged

here as a horizontal body. I miss a portion of the unit that is mapped on the East, and the unit continues further West than that in the geologic model. However, I note that few drillholes have been logged in the western area, so there might be some uncertainty in the geologic model.

The PK/VK unit, which is diamondiferous, is in good agreement with the geologic model over the region of the pipe. Importantly, the bottom extension of that unit seems to have been well-constrained by incorporating the petrophysical data. The major discrepancy between my model and the geologic model is in the northern region, where some PK/VK material has been placed beneath the HK unit. This result contradicts drillhole observations that show no PK/VK occurrence beneath the HK unit. To understand how this happened, I need to re-examine the gravity inversion results and the information that is input into the PGI. In the inversion of the gravity data alone, low-density material is required in the region north of the pipe. However, in the magnetic inversion, that region is occupied by the HK unit, which is assumed to have no density contrast with the background. In the multi-physics inversion, any low-density material required to fit the gravity data must, therefore, be put either at depth or in a near-surface layer. However, because of the assumed dependence of density and elevation, the density of a near-surface layer must be very low. The inability to fit the gravity data with that very low-density shallow layer provides no alternative for the inversion except to put anomalous density material at depth. To resolve this inconsistency with geology, I introduce another geologic unit and carry out a new multi-physics inversion that includes expanded *a priori* information.

5.6.2 Adding geological information into the multi-physics inversion

The previously obtained model from a multi-physics inversion with petrophysical information allows me to recover distinct units with the required petrophysical signature. However, several features of the quasi-geology model are in disagreement with the geological knowledge from drillholes, namely the northern extension of the PK/VK-pipe below the HK unit and the lack of dip for the HK unit.

To overcome those issues, I revise my assumptions of what to add as *a priori* information into the inversion. I have assumed so far that near-surface occurrences of PK facies had similar density characteristics as the PK/VK unit found in the DO-27 pipe. Those near-surface occurrences, which showed up in the inversion results as smooth density contrast features, still were categorized as background (Figures 5.9 and 5.12). It is an indication that those minor occurrences potentially have a different petrophysical signature than the main pipe, which displays extreme density contrasts near the surface (up to -1 g/cm^3). To accommodate the need to have a mass deficiency in the near-surface region north of the pipe, I introduce an additional rock unit. This new unit represents near-surface occurrences of PK-like rocks outside of the main pipe. Henceforth, I call this unit PK-minor and distinguish it from PK/VK-pipe, which has been focused on thus far, through a different density signature. I lack representative samples for PK-minor to define its petrophysical characteristics. To select its GMM parameters for the density and elevation, I ran several gravity PGIs with three rock units (the background, PK/VK-pipe, and PK-minor) for a range of values for the means and standard deviations. I

chose a mean density of -0.3 g/cm^3 , in line with observations in the area, with a standard deviation of 0.1 g/cm^3 , which is close to the standard-deviation observed for the HK unit. The mean elevation for PK-minor is set at 360 m with a standard deviation of 10 m; those values effectively limit the occurrence of the PK-minor unit to the near-surface at elevations greater than 300 m. For its magnetic properties, I chose to assign it the same as for the main PK/VK-pipe unit. The properties of the PK-minor unit are summarized in Table 5.1.

In the above, I have separated the original PK/VK unit into a PK/VK-pipe and a PK-minor through distinct petrophysical signatures. These two units also are separated geographically. I include this information into the PGI by using local proportions (equation (4.3)). I implement a simple constraint: the PK/VK-pipe unit can occur only at locations south of 7,133,685 m, which is the northern limit of the mapped pipe, as seen in the geological data and the geophysical inversions I ran so far. In other words, I set $\pi_{\text{PK/VK}} = 0$ at locations north of 7,133,685 m. Similarly, I set the proportions of the new PK-minor rock unit so that it occurs only north of that bound and does not overprint the surface of the pipe. It effectively decomposes the area of interest into two domains that see different GMMs.

The result of the multi-physics inversion with an additional rock unit for near-surface kimberlites and geological domains is shown in Figure 5.13. This model is geologically appealing. It reproduces known geological features better than in the previous multi-physics inversion. The northern extension of the PK/VK-pipe unit is now gone, and the general outline of the pipe is thus much better recovered. Most of the northern tip gravity anomaly is explained by a near-surface sheet of

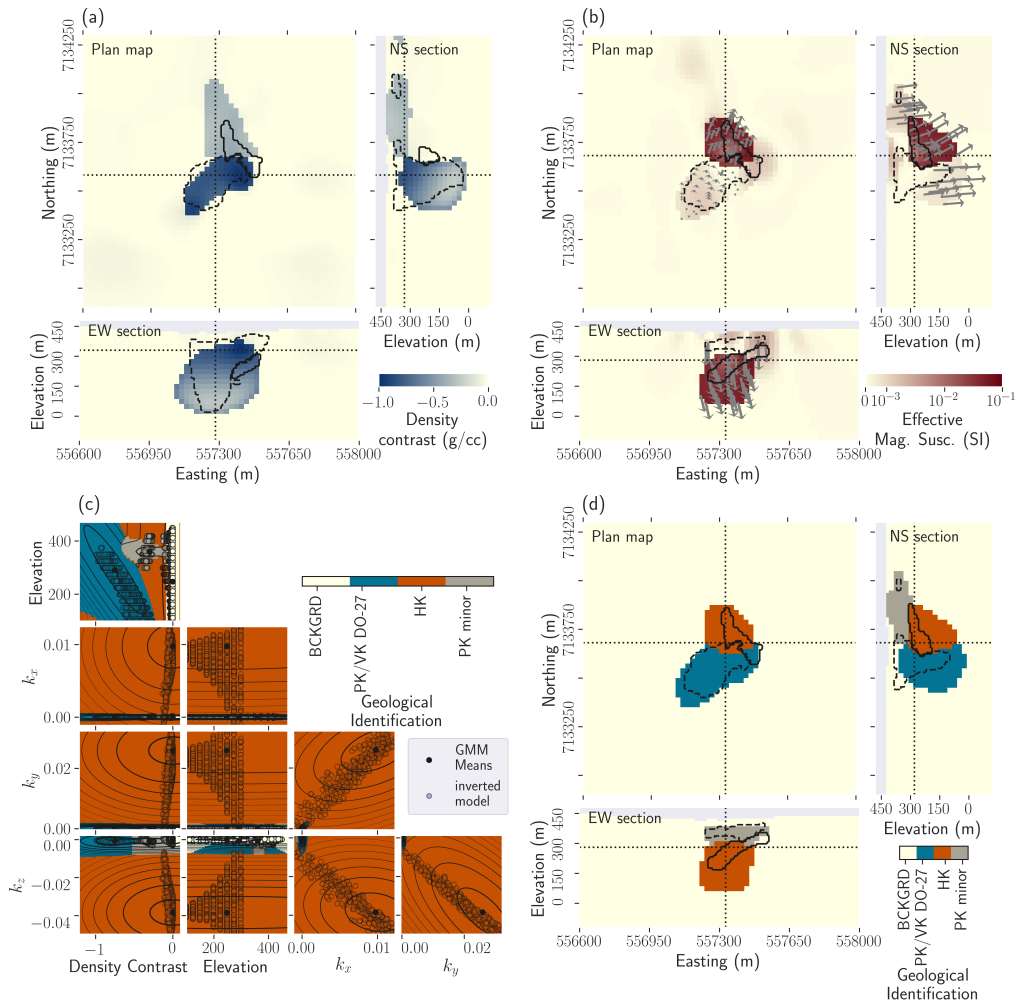


Figure 5.13: Results of the multi-physics PGI with an additional rock unit for near-surface PK-minor occurrences, and geological domains. (a) Plan map, east-west, and north-south cross-sections through the density contrast model; (b) Magnetic vector model. The grey arrows are the projections of the magnetization directions (unit vector) on the plane for the kimberlite units; (c) Presentation of the 5-dimensional GMM: visualization of all possible 2D projections. Comparison with the recovered model represented as the scatter plots of the four physical properties of the geophysical model and the elevation; (d) Resulting quasi-geology model from the multi-physics PGI with four rock units.

PK-minor units, whose locations match with known occurrences in drillholes. For the HK unit, I start to obtain some sense of the dip of that unit. Its near-surface outline is again well recovered, but its thickness appears overestimated.

The introduction of the new unit has changed how well petrophysical signatures are recovered. The density contrast of the HK unit now is closer to the null density contrast measured in samples, at an average of -0.03 g/cm^3 (compared to -0.12 g/cm^3 in the previous multi-physics inversion with three rock units). Similarly, the PK/VK-pipe unit now is very close to its measured magnetic amplitude at $8 \cdot 10^{-4} \text{ SI}$ (compared to $1.06 \cdot 10^{-3} \text{ SI}$ in the previous multi-physics inversion). The orientations of the magnetization are consistent with the values in the GMM: they align with the Earth's magnetic field for PK/VK-pipe and PK-minor and are along the remanence direction for the HK unit. The clustering of the magnetic petrophysical values of the HK unit is not as good as in previous inversions, but they still are within acceptable bounds as defined by its distribution.

The geophysical surveys are individually fit, along with the GMM petrophysical distribution. The scaled data misfit value of each survey is 0.99 for the ground gravity survey, 0.84 for the airborne gravity gradiometry survey, and 0.92 for the airborne magnetic survey (targets of unity). The normalized data misfit maps are presented in Figure 5.14. The maps associated with gravity data are random and consistent with the assigned noise levels (Figures 5.14b to 5.14d). The misfits of the airborne gravity gradiometry data (Figures 5.14c and 5.14d) appear to follow the flight path. The flight lines are also visible in the observed data (Figure 5.3c and 5.3d). For the magnetic data, even though the algorithm achieved the global

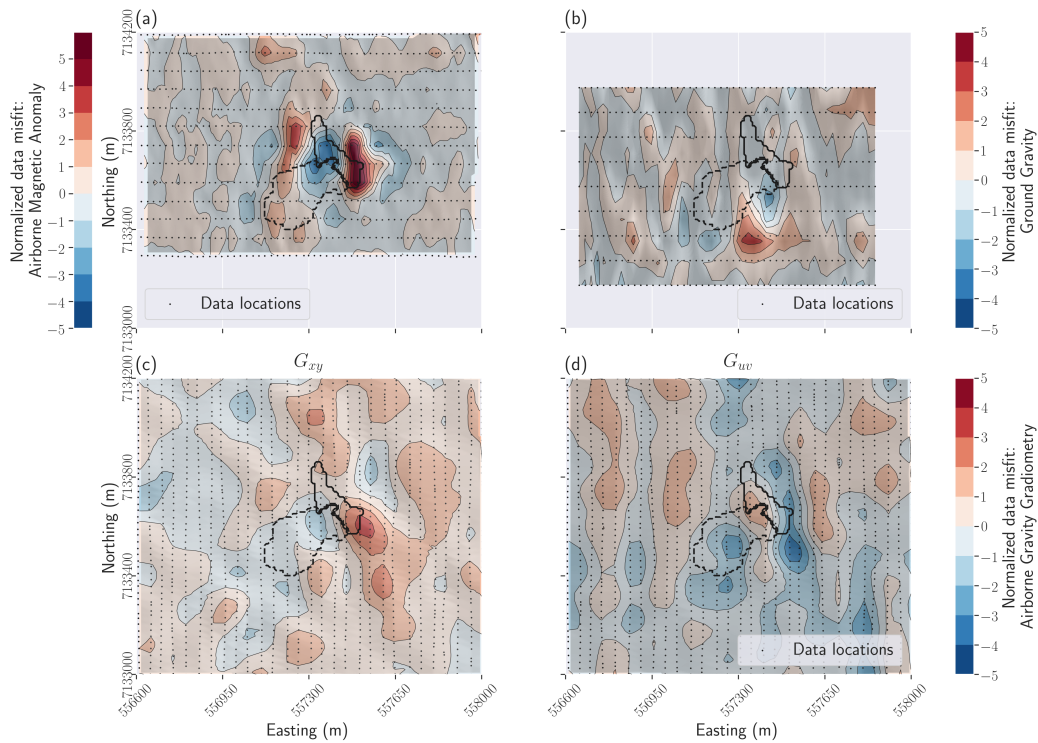


Figure 5.14: Normalized data misfits for all the datasets from the multi-physics PGI with geological domains and four rock units. (a) For the magnetic data; (b) For the gravity data; (c) and (d) For the gravity gradiometry data.

geophysical target misfit, there is a coherent residual signal in the misfit map (Figure 5.14a). The misfits are higher, up to 7 nT, just above the eastern extension of the HK body that I seem to not recover in the inversion (Figures 5.12b and 5.12d).

5.7 Discussion

The PGI framework has enabled me to jointly invert three types of geophysical data (airborne magnetic, ground gravity, and airborne gravity gradiometry) using five coupled parameters (density, elevation, and the three components of the

magnetic vector). This joint approach recovers a final quasi-geology model that maps all expected geological units (the background, PK/VK-pipe, HK, and PK-minor units) by reproducing their petrophysical characteristics in the inversion. This result is unobtainable by inverting datasets separately and then carrying out a post-inversion classification of the recovered physical properties.

For this study, a geologic model built from drillhole information is available to compare with my results. For DO-27, the PK unit is the diamondiferous kimberlite facies and so estimating its volume and shape is key for resource estimation. Although PK is indistinguishable from VK from the potential fields data, VK has a negligible volume in the geologic model compared to PK. Therefore, I can interpret the PK/VK-pipe unit as representing the diamondiferous PK unit. Reproducing the PK density signature, with its depth dependence, allows me to obtain an informed estimation of its shape and volume. The surface outline and bottom extension of the potentially diamondiferous unit are in good agreement with the geologic model, but the quasi-geology model is more rounded at depth. The estimated volume of the PK/VK-pipe is evaluated at $28 \cdot 10^6 \text{ m}^3$ and can be compared to $15.7 \cdot 10^6 \text{ m}^3$, obtained from the geologic model (see Harder et al. (2009) and Figure 5.12d). Most of the volume discrepancy is concentrated at depth, where the gravity surveys are less sensitive.

From a numerical perspective, the MVI problem with petrophysical information has been more challenging than the gravity inversions. This is due in part to the orders of magnitude difference between the various units, the challenge of inverting for logarithmically distributed effective susceptibilities, and the lack of

oriented samples to determine the magnetic characteristics of the HK unit. In principle, the use of MVI in spherical coordinates seems desirable, but the additional nonlinear transformations complicate an already challenging problem. Nevertheless, I still was able to recover a unit with the identified magnetic signature of HK. Realistically, however, the geology probably is more complicated than I have modelled. Assuming a single and relatively uniform HK unit is likely insufficient to explain the whole magnetic data, as shown by the data misfit map in Figure 5.14a. During the study, I tried to obtain various estimates of the orientation of the remanent field by using a sparse MVI code in spherical coordinates (Fournier & Oldenburg, 2019) or by calculating the best-fitting amplitude and angles for the available shape of HK in the geologic model. While the recovered inclinations appeared consistent across estimations with the value obtained in Devriese et al. (2017), the declinations spanned a wide range. Those challenges could be explored in a future case study. Although the inversion results seem to validate the current petrophysical estimates, the estimation of the density, magnetic susceptibility, and remanent magnetization orientation of the HK unit could be significantly improved by measuring new, oriented samples.

Finally, while I used local proportions to implement elementary geological expectations, a complete inclusion of all the drillhole information is yet to be done. It could help further refine the quasi-geology model, such as narrowing the PK/VK-pipe unit at depth or constraining the thickness of the HK unit. The inclusion and extrapolation of drillhole information within the PGI framework is part of my current research.

5.8 Conclusion

Inferences from inversions of single datasets, even when they are input into post-inversion classification algorithms, can be deficient. This limitation is a motivation to carry out joint inversions. The challenge is how to link the datasets together, in a practical sense, and how to include other relevant information. I adopt the PGI framework to use petrophysical measurements as the linkage and apply it to the field data acquired over the DO-27 kimberlite pipe. I have successfully jointly inverted airborne gradiometry, ground gravity, and airborne magnetic data, along with measured physical properties and geological information. My framework outputs both physical property models and a quasi-geology model. The results that include multiple physics, coupled with petrophysical and geological information, are shown to better resolve and distinguish the rock unit bodies compared to interpreting single-physics inversion results. The fact that I have been able to fit all the geophysical datasets while reproducing the petrophysical signatures, such as varying densities with depth and magnetization orientations, is a significant achievement. The quasi-geology model successfully recovers the location and main structural features of the PK/VK and HK kimberlite pipe units. A third near-surface kimberlite facies, with distinct petrophysical properties inferred from inversions, is also imaged. Working with a complex geologic model presents challenges, and the flexibility of the PGI framework offers multiple ways to tackle them. Refining the classification of rock units, testing for various petrophysical signatures, and defining local geological information to satisfy field observations

have been keys to recover a satisfying quasi-geology model. Nevertheless, further refinements of the PGI implementation could improve the estimate of the volumes and structures of the PK and HK units. Such refinements could include a more extensive integration of the drillhole information, and address the complexity of the magnetization signatures. Moreover, there are other geophysical datasets that can provide constraints on the electromagnetic properties of the rock units, and incorporating those can further reduce the discrepancies between the geophysical and geologic models. The DO-27 kimberlite pipe presents an ideal test site on which to test these procedures.

Chapter 6

Discussions and conclusion

6.1 Introduction

In chapters 3 and 4, I have defined my multi-physics Petrophysically and Geologically guided Inversion (PGI) framework as three interconnected optimization problems over the geophysical, petrophysical, and geological data. The graphical representation of the PGI framework is reproduced here in Figure 6.1. Each of these problems requires specifying sets of parameters that influence the recovered image of the subsurface. For the geophysical inversion (Figure 6.1, Process 1), strategies for the weighting of the geophysical objective function, with one or several geophysical data misfits, have been discussed in sections 3.4 and 4.4. For the petrophysical characterization (Figure 6.1, Process 2), section 3.3.2 introduced the concept of confidences in the prior parameters of the GMM. I have, through various examples (sections 3.5.1, 3.5.2, 3.5.3, 4.5.5), demonstrated the use of those confi-

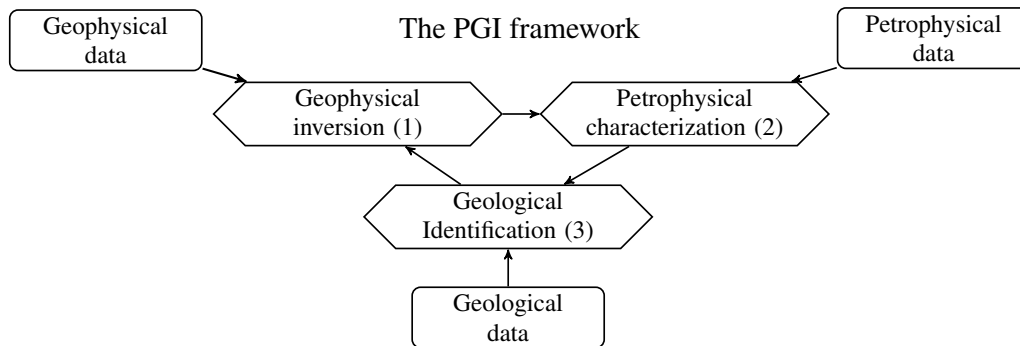


Figure 6.1: A graphical representation of the PGI framework. Each diamond is an optimization process that requires data (shown in rectangular boxes) as well as information provided by the other processes (reproduction of Figure 4.1).

dence parameters to include qualitative information into inversions. The analyses were, however, tied to specific values of the GMM’s parameters (means, covariance matrices and proportions) and their respective confidences. As for the geological identification (Figure 6.1, Process 3), I highlighted how defining local proportions for the GMM could help comply with *a priori* geologic information (sections 3.5.2 and 5.6.2). The building of the quasi-geology model lacks, however, the enforcement of structural prior information.

In this chapter, I develop some discussions to delineate the capabilities of the PGI approach and future developments. I first highlight situations where the PGI framework can be challenging to implement due to the configuration of physical properties. I then analyze the impacts of some of the new inversion parameters I introduced. To this end, I study the impact of: 1) the global proportions, whose true values can be hard to obtain for any area; 2) the confidence parameters, in the means and variances, that affect the characteristics of the GMM; and 3) the

mean and variance values, which characterize each cluster. I then highlight differences between the PGI framework and other existing approaches for including petrophysical and geological information in geophysical inversions. Finally, I conclude this chapter by proposing research directions to expand the framework's capabilities to include or enforce various types of geologic information.

6.2 Challenges due to consecutive clusters

In this section, I highlight some challenging situations for the PGI algorithm and how they can be addressed.

6.2.1 DC example

Setup

In this example, I revisit the DC 2D example shown in section 3.5.2. The setup is modified, so there are two resistive cylinders, with different resistivities (150 and 250 Ω -m, respectively), buried in a 100 Ω -m background (see Figure 6.2).

Result

I ran two PGIs with different levels of prior information. The results are shown in Figure 6.3.

For the first PGI (Figure 6.3a and 6.3b), I used the true means and variances for the GMM. No local geology information was given through local proportions; the proportion parameters of the GMM are constant everywhere (true global proportions). The result shows that, while the petrophysical distribution is well re-

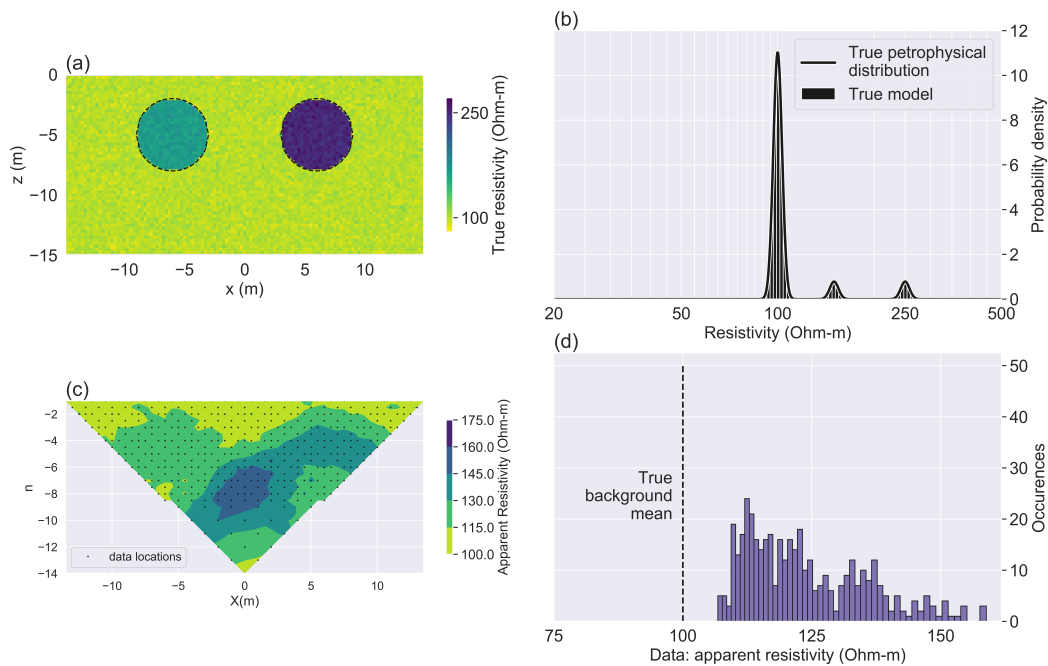


Figure 6.2: DC 2D survey over 2 buried resistive cylinders. (a) Underground model; (b) Petrophysical characteristics of the model; (c) Simulated DC data; (d) Histogram of the geophysical data.

produced, a halo is visible around the more resistive unit on the right (Figure 6.3a). This result is expected because, from the initial background value, the two cylinders have consecutive resistivity values (Figure 6.3b). A smooth inversion extending from a background resistivity of 100 Ω -m to 250 Ω -m will have values in between and thus around 150 Ω -m. The quasi-geology model identifies this transition zone around the most resistive cylinder as the rock unit of intermediary resistivity. Note that, in a different configuration (more noise, etc.), no cell may reach the cluster 250 Ω -m; in this case, the model would only show two cylinders with the same resistivity but different sizes. The same problem happens if both cylinders are more conductive than the background.

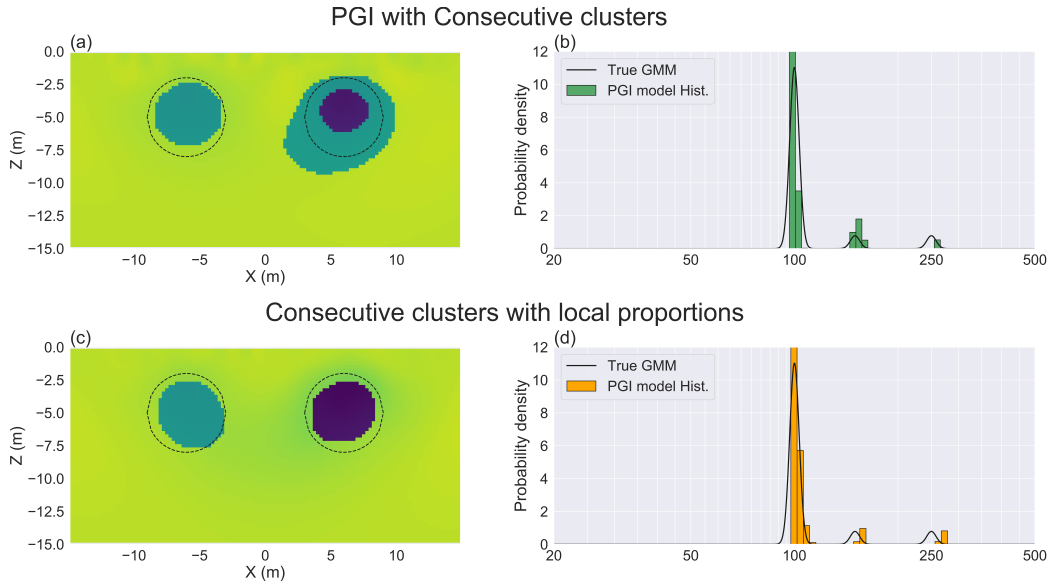


Figure 6.3: Results of the two PGIs for the DC 2D survey over 2 buried resistive cylinders. Panels (a) and (b) show the resulting model, and its distribution, from a PGI with full petrophysical information but no geology information, while panels (c) and (d) show the resulting model, and its distribution, from a PGI with full petrophysical information and geology information.

More *a priori* information is necessary to overcome this issue. For the second PGI (Figure 6.3c and 6.3d), I used the full petrophysical information (true means and variances) again, but I also added geology information that says that the rock unit of intermediary resistivity ($150 \Omega\text{-m}$) can only be encountered on the left of the model. I set this information through the use of local proportion parameters $\{\pi_{i,j}\}$ in the GMM. The proportion of the $150 \Omega\text{-m}$ cluster is set to zero on the right when $x > 0$ m. The result (Figure 6.3c) shows that the model is then recovered without a halo around the most resistive unit, while the petrophysical distribution is still reproduced (Figure 6.3d).

This problem of consecutive clusters in the GMM is also why, for the individual PGIs in section 4.5.3, I chose only to use two clusters (background and one kimberlite facies) to avoid the problem highlighted in Figure 6.3a.

6.2.2 Synthetic DO-27 example: joint inversion with three clusters and no geology or prior petrophysical information

The problem of consecutive clusters in the GMM can also be resolved by working with multiple physical properties. With a multidimensional petrophysical space, the model's cells now have more paths to travel to high-contrast values of a particular physical property, without necessarily having to “travel through” the less contrasting clusters (see Figure 4.2). This is one reason why, in section 4.5.4, the multi-physics inversion was capable of recovering well the two kimberlite facies at DO-27 from the synthetic data. However, the problem can still occur in a multidimensional space, particularly when no petrophysical information is known *a priori*. In section 4.5.5, I demonstrated that by constraining one cluster to resolve the gravity data and another to resolve the magnetic data, then a PGI with three units (background, PK/VK, HK) recovers insightful information about the two kimberlite facies from the geophysical datasets. However, in section 4.5.5, I also showed that, when no petrophysical information or qualitative information about the kimberlite facies is provided, both gravity and magnetic data can be reproduced by a single low density, high magnetic susceptibility kimberlite unit. I claimed that adding a third cluster would not help, as it just adds complexity to the model that is not supported by the data. Here, I demonstrate this claim to identify

signs in the inverted model that indicate there are too many clusters in the GMM.

In Figure 6.4, I show the result, using the synthetic data at DO-27 I presented in section 4.5, of the PGI algorithm with three clusters and no petrophysical information about the mean values. The confidences for the means of the two kimberlite clusters are all set to zero; the PGI is in charge of finding adequate values for the means of the two kimberlite units. There is no restriction about a kimberlite unit being more magnetic or less dense than the other. The mean of the background unit is fixed to zero for both physical properties. The global proportions and covariances matrices are the same ones used in section 4.5 and are held fixed. Holding the proportions fixed ensures that one cluster's proportion will not go to zero, bringing the PGI to a two units case (background and undefined kimberlite).

The result (Figure 6.4) shows the same phenomenon as in section 6.2.1. As both anomalous kimberlite facies are set free to explain either dataset and with no information on the petrophysical contrasts, the model displays a halo with one cluster regrouping the high-contrasting cells and one cluster regrouping the lesser-contrasting cells. Thus, when no other information is available, using a small number of clusters is recommended to avoid recovering halo-structures that are non-informative artifacts. For this specific example, the case with only two clusters (background and kimberlite) is enough to reproduce the geophysical datasets when no other information is provided (see Figure 4.9). For a successful PGI with three clusters and no petrophysical information on the means, additional information is required (such as specifying the role of each cluster as I did in section 4.5.5).

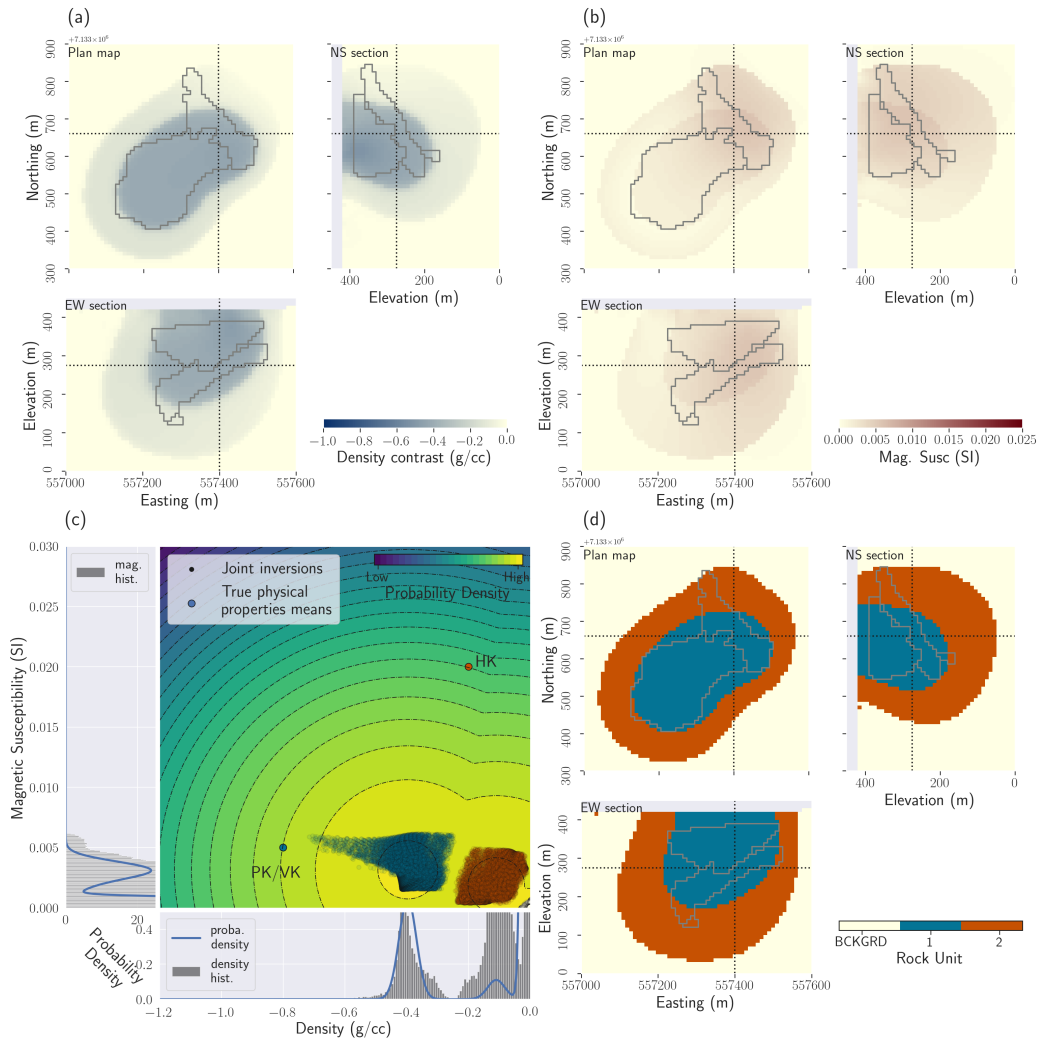


Figure 6.4: Result of the joint inversion of the synthetic data over DO-27 with PGI using the following characteristics: the number of clusters is set to 3, and no petrophysical or geological information is provided. The confidences for the means of the two kimberlite clusters are set to zero.

6.2.3 Summary

Using several clusters with closely related signatures can potentially result in the development of “onion-like” structures where clusters form halos around each other by categorizing each as a separate layer. For that reason, it is important to keep the number of clusters to a reasonably low number. If more knowledge is available, one can use more clusters. Additional information can be an expected zone of occurrence (such as what I did for the PK-minor unit in section 5.6.2) or the definition of a specific role for each cluster (such as in section 4.5.5 with one low density and one highly magnetic clusters).

6.3 Sensitivity analysis

The integration of the petrophysical characterization and geologic identification (Figure 6.1, Processes 2 and 3) with the geophysical inverse problem introduced new parameters that serve various purposes. In order to use these new tools, it is crucial to understand their effects on the recovered subsurface images.

I first demonstrate that the proportions of the GMM, when their values are set globally, have minimal impacts on the inversion results. To this end, I use the same DC example as in section 3.5.2.

I then investigate the effects of the confidence parameters $\{\kappa\}$ and $\{\nu\}$, in the means and variances of the GMM, respectively, such as defined in section 3.3.2. For that purpose, I use the DC example (section 3.5.2) and the Bookpurnong field example (section 3.5.3).

Finally, I highlight, through the DO-27 field case study (chapter 5), how vary-

ing the means and variances of the PK-minor unit modifies the inverted model and can help to explore the model space to find a result that complies with *a priori* geology information.

6.3.1 Impact of the proportions values set globally

The proportions $\{\pi_j, j = 1..c\}$ of the GMM encodes the relative occurrences of each unit. I have shown how varying their values locally, to zero or unity, allows me to encode geological information (section 3.5.2, 5.6.2). While it can be hard to estimate global (constant everywhere) values for the proportions before obtaining a reliable geological model, it appears that they do not significantly affect the inversion results as long as they are not set at zero or unity values or close. To illustrate this claim, I use the DC example with two cylinders, one conductive and one resistive, presented in 3.5.2. I ran several PGIs with various global proportions for each rock unit. The proportion of the background unit varies from $7 \cdot 10^{-4}$ to almost unity. The proportions of the cylindrical rock units are equal to each other and vary from $7 \cdot 10^{-7}$ to almost 0.5. The sum of proportions in each configuration sums to unity. Within each PGI, these proportions are held fixed. All the PGIs are provided with the true values for the means and variances of the GMM and held fixed. For these inversions, I also used the non-approximated smallness term, described in equation (3.10); this ensures that the minimum impact of the global proportions is not due to the least-squares approximation.

The results of these various PGIs are shown in Figure 6.5. Each panel is the result of one PGI with a particular set of proportions; the proportion values are

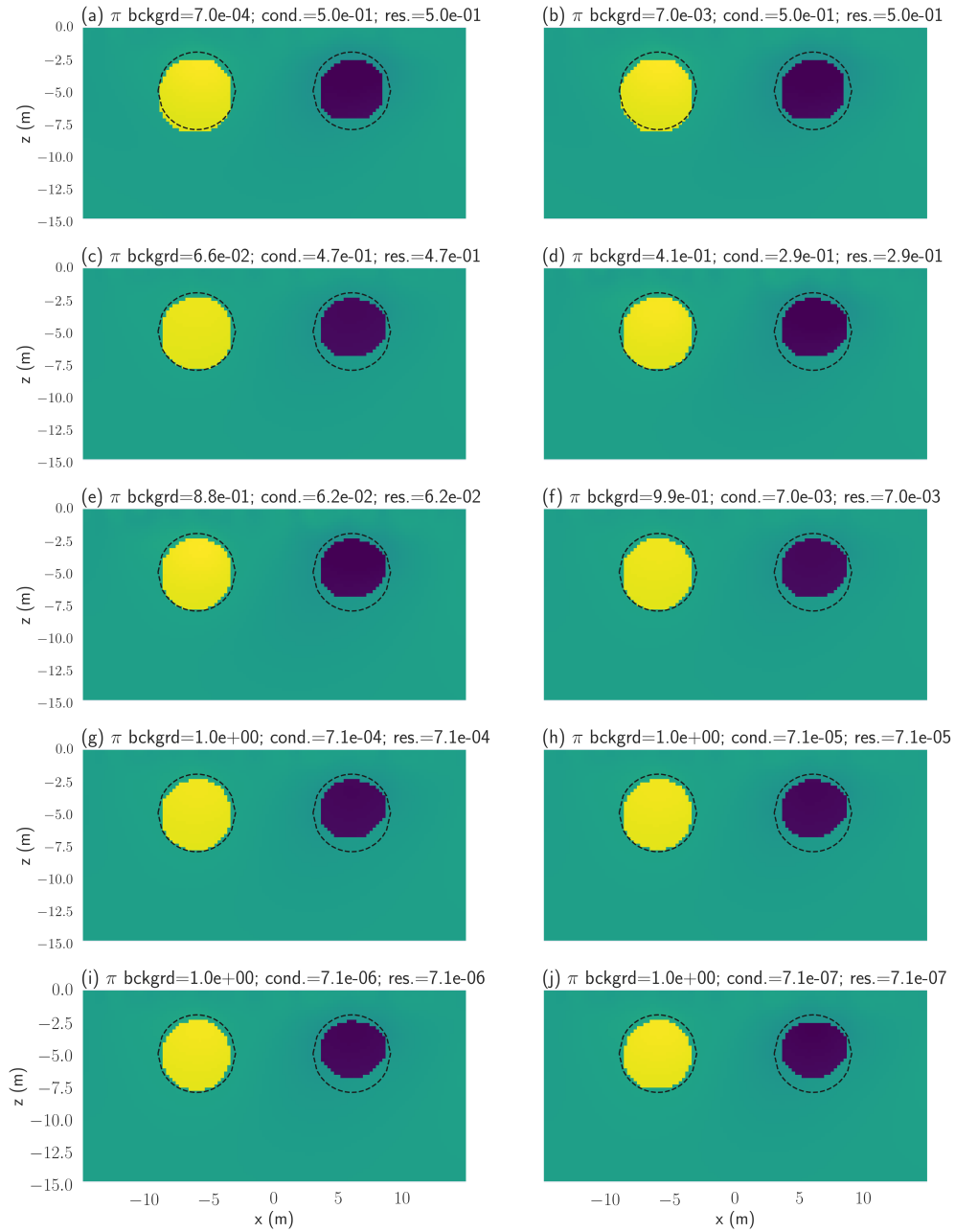


Figure 6.5: Results of the PGIS for the DC 2D survey over 2 buried cylinders for various combinations of proportions for the GMM, with full petrophysical information.

provided above each result. The volume of the cylinders is minimally affected by the proportions, with negligibly smaller cylinders as their proportion gets exponentially smaller. This highlights how the resistivity model recovered by PGI is not affected by the values of the global proportions, as long as they are not set to zero or unity.

6.3.2 Impact of the confidences in the means

When no or few petrophysical values are available for the various rock units, which is the majority of cases, I have designed a MAP estimate of the GMM's means based on the available samples and the inversion model at any iteration (section 3.3.2). Those MAP estimates are, schematically, an average between the prior means and the means observed in the inversion model. This average is weighted by the confidence parameters κ . A high value of κ indicates high confidence in the prior means used as input for the GMM; the impact of the current geophysical model in the estimation of the means is low. For values of κ close to zero, on the contrary, the estimation of the means is mainly controlled by the current geophysical model. I have previously shown, in this thesis, cases where the confidence parameters κ in the prior means are either zero (no prior mean value, sections 3.5.2, 3.5.3 and 4.5), unity (equal confidence in the prior and inversion means, section 3.5.1), infinite (total confidence in the prior means, the GMM's means are kept fixed, chapter 5 or sections 3.5.2 and 4.5), or a combination of these values depending on the rock units and physical properties (section 4.5.5).

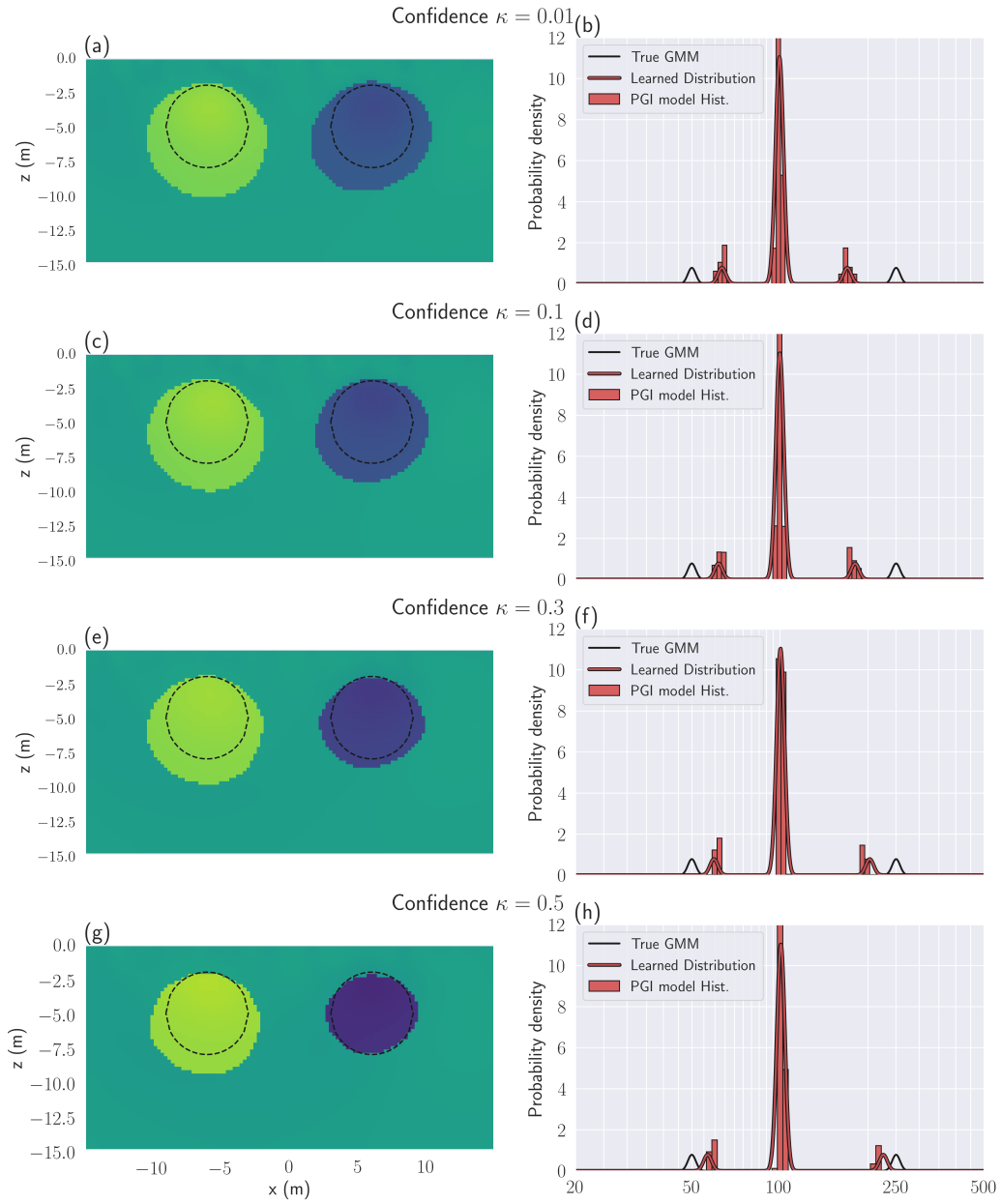


Figure 6.6: Results of the PGIs for the DC 2D survey over 2 buried cylinders for various confidences κ values in the prior means, from 0.01 to 0.5, for determining the means of the GMM.

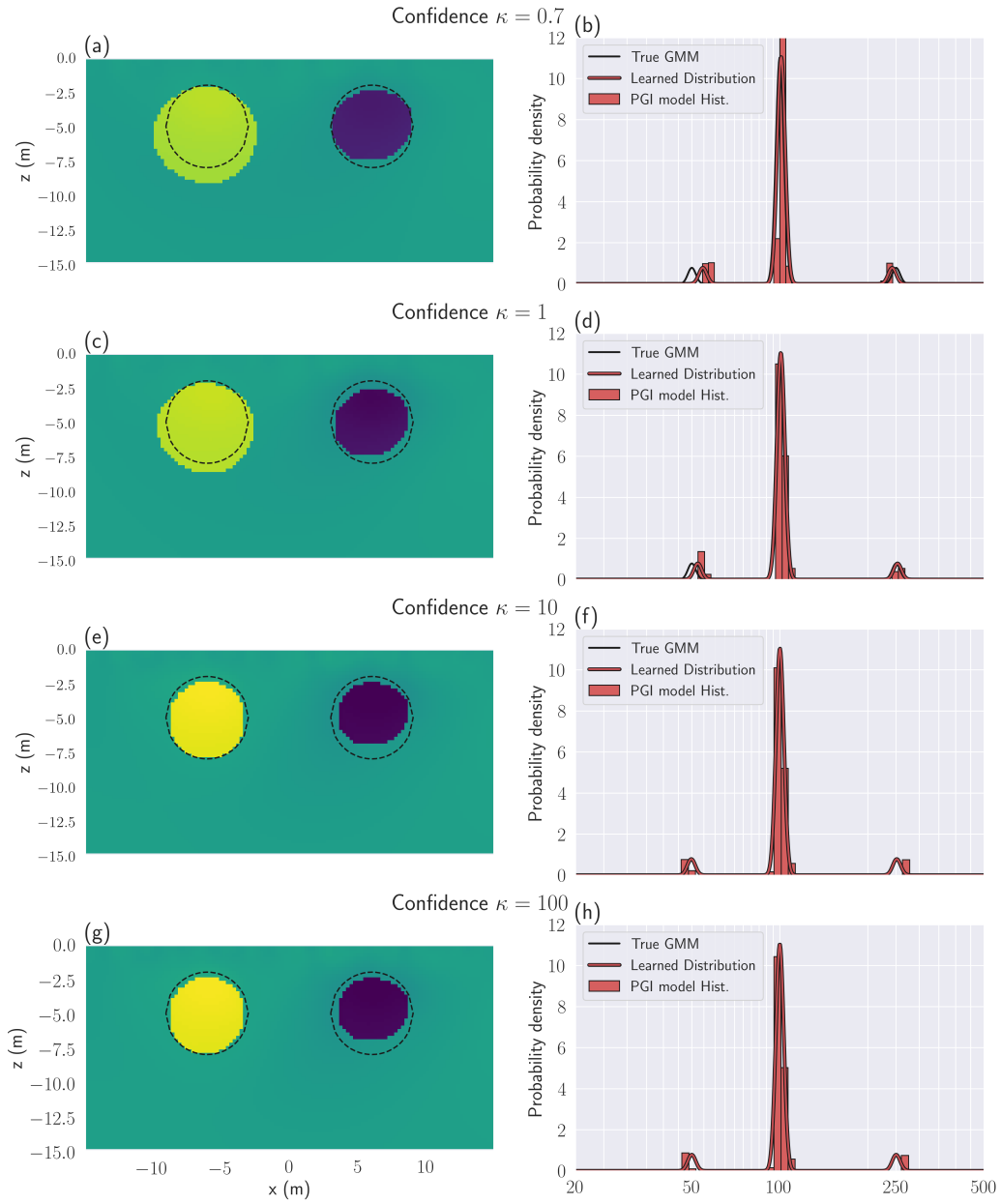


Figure 6.7: Results of the PGIs for the DC 2D survey over 2 buried cylinders for various confidences κ values in the prior means, from 0.7 to 100, for determining the means of the GMM.

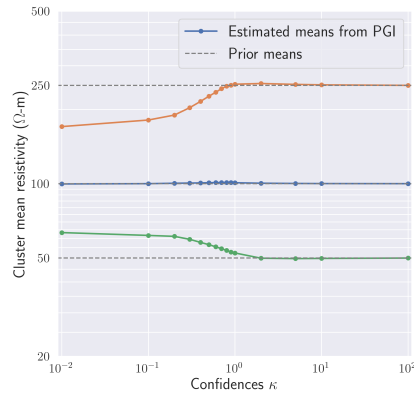


Figure 6.8: Evolution of the MAP estimates of the cluster means by PGI for the DC example with two cylinders, for various values of the confidences κ in the prior means. The prior means are the true means.

In this section, I use the DC example with two cylinders, presented in section 3.5.2, to illustrate how the inversion results, and the learned GMM's means, are impacted by various values of confidence κ . For each PGI, I use the same κ value for all three rock units (background, resistive and conductive cylinders). For the prior means, I used the true means of each rock unit. The variances and proportions of the GMM are held fixed.

The results are shown in Figure 6.6 for low κ confidences, and in Figure 6.7 for high κ confidences. The evolution of the MAP estimate of the means is summarized in Figure 6.8. With confidence values of 0.01, the result is similar to the model with zero confidence (shown in Figure 3.11). When the confidences in the prior means are unity or higher, this is sufficient to force the algorithm to recover the prior mean values. The range of confidences from 0.1 to 1 appears as the area of compromise between fixing the means or updating them solely based on the geophysical model.

6.3.3 Impact of the confidences in the variances

In section 3.5.3, I applied the PGI algorithm to a FDEM dataset for freshwater contamination. I showed that adding the constraint of recovering three units led to more consistent results when starting from different initial half-space models. In this example, little prior information was available. I chose to use three clusters to represent regions saturated with freshwater, saltwater and an intermediate zone, respectively. I made a reasonable guess for the prior variance values, set the confidences ν in those values to unity, and let the algorithm determine the mean values (κ confidences were set to zero).

Here, I use the Bookpurnong setup to analyze the importance of the assigned confidences $\{\nu\}$ in the prior variances. Starting from the resistive half-space of 100 Ω -m, I ran multiple PGIs with various values of ν (all the same for all three clusters). The recovered geophysical models and associated GMMs are shown in Figure 6.9 for low to moderate values of ν and in Figure 6.10 for moderate to high values of ν . Models recovered for other values of ν can be found in Appendix E. For low confidence ν values, the results are quite close to the Tikhonov smooth inversions shown in Figure 3.13. A threshold is noticeable at $\nu = 0.5$ in Figure 6.9, where the inversion moves away from the smooth inversion behaviour and closer to the result presented in section 3.5.3. In this specific example, for confidence values $\nu \geq 2$, some pocket-like structures appear in the South that seem to indicate that the clustering might be pushed too hard.

The effect on the estimation of the means is summarized in Figure 6.11a. The $\nu = 0.5$ and $\nu \geq 2$ threshold values mentioned earlier are seen in the plot with

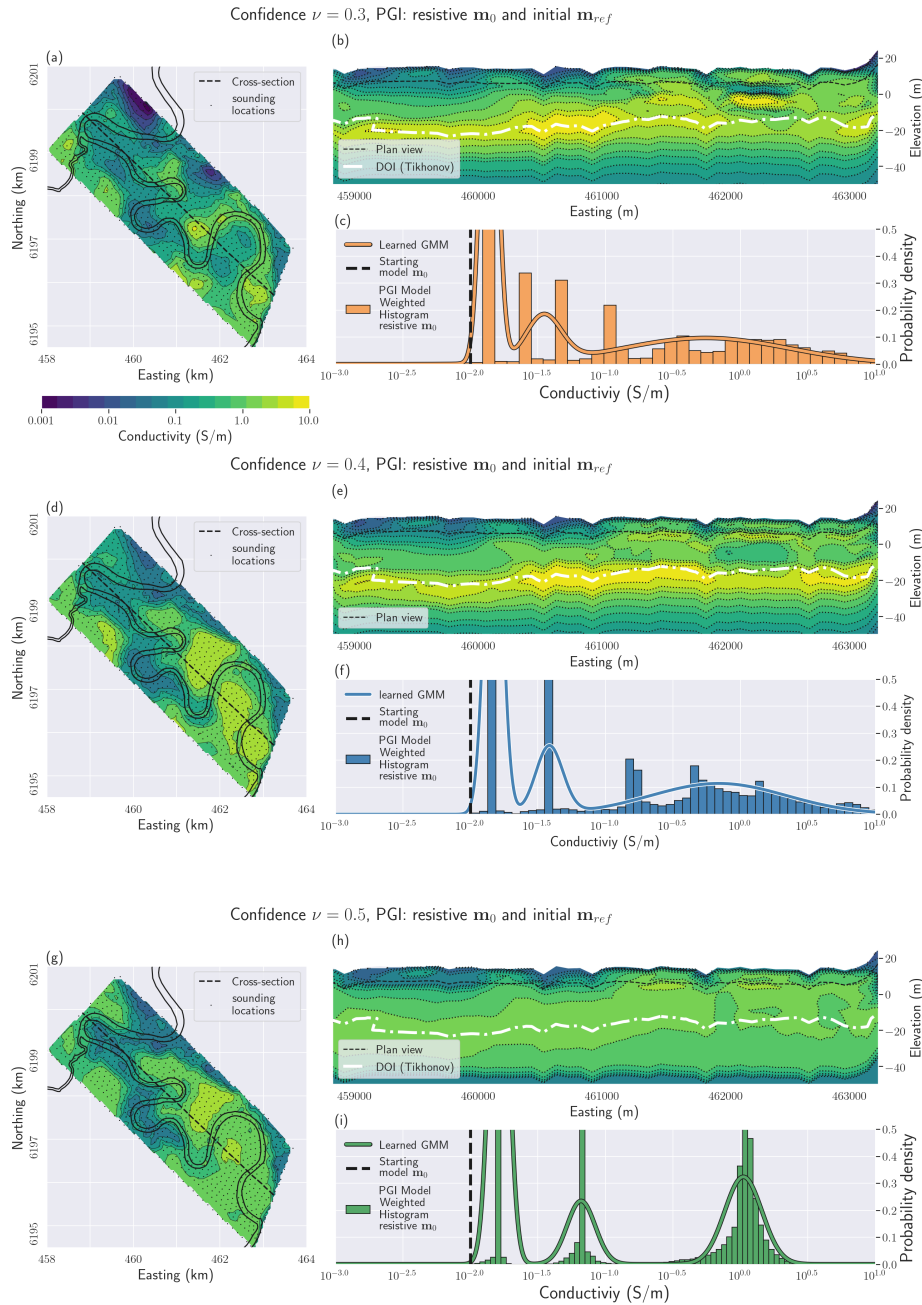


Figure 6.9: PGIs results on the Bookpurnong case study for various value of the confidence parameter ν in the prior variances. $\nu = 0.3$, $\nu = 0.4$, $\nu = 0.5$.

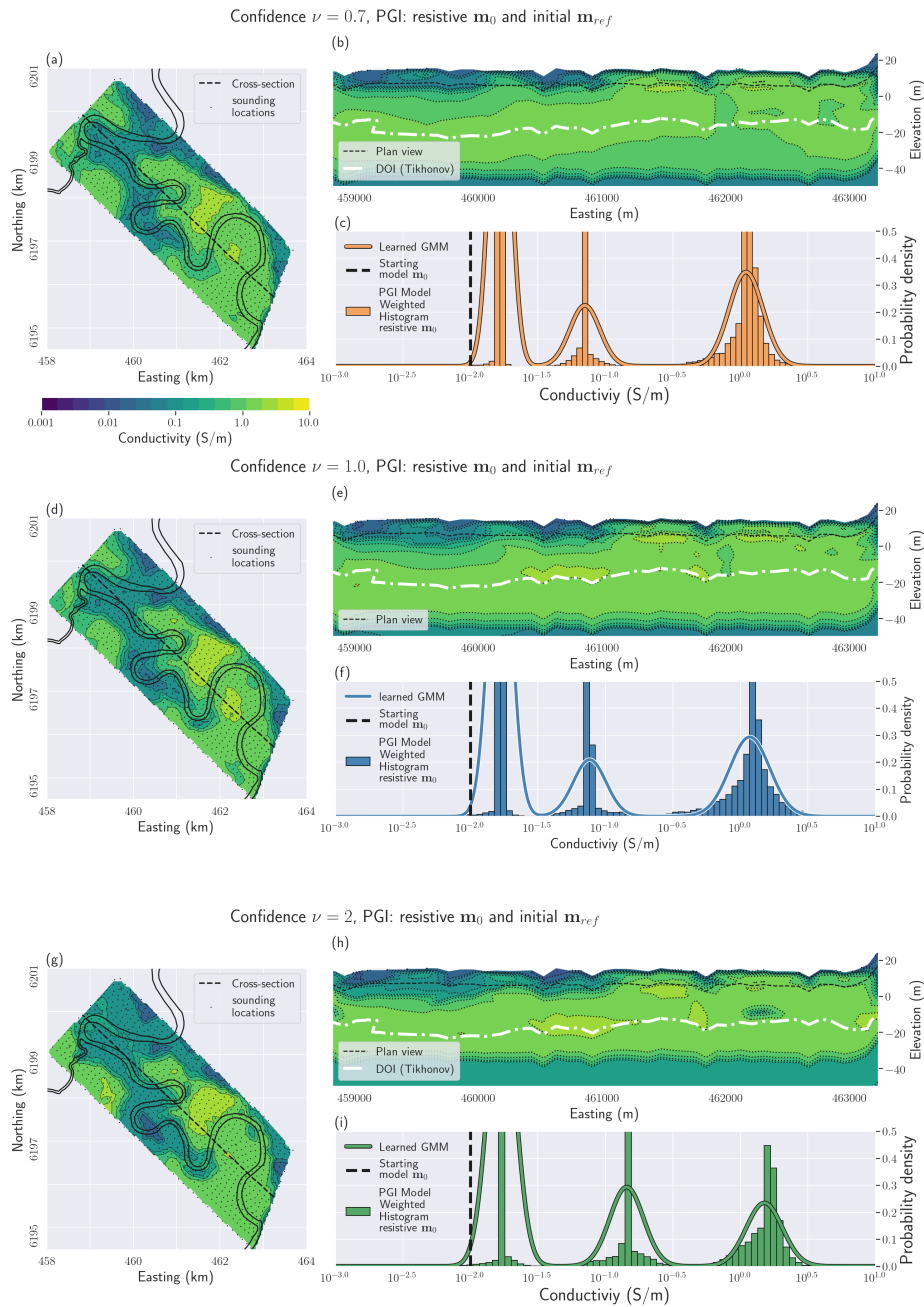


Figure 6.10: PGIs results on the Bookpurnong case study for various value of the confidence parameter ν in the prior variances. $\nu = 0.7$, $\nu = 1$, $\nu = 2$.

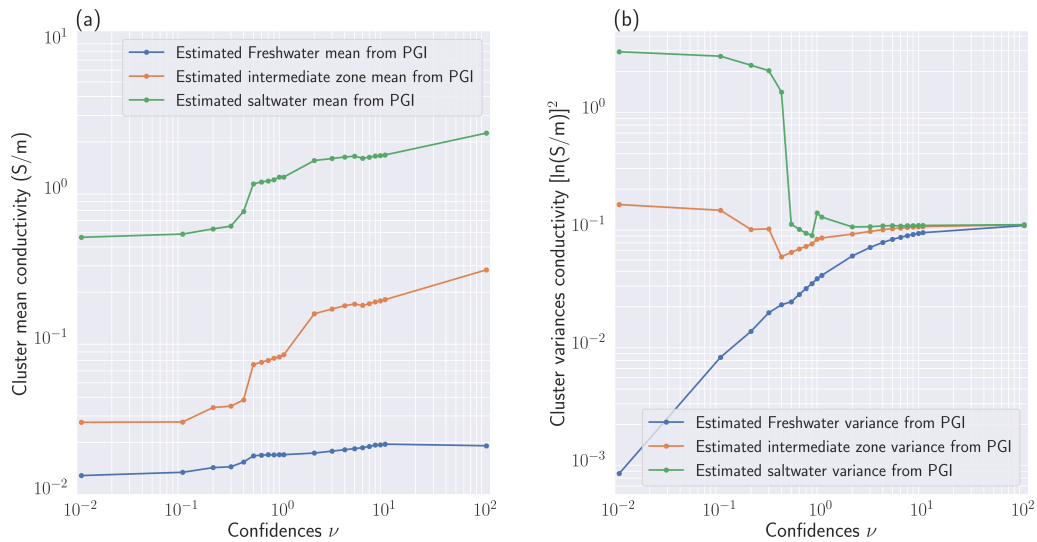


Figure 6.11: MAP estimates of the clusters' mean (panel (a)) and variance (panel (b)) from PGIs for the Bookpurnong case study for various values of the confidence parameter ν in the prior variances.

significant relative changes of the recovered means. However, while there are some variations, each cluster stays within the same order of magnitude across inversions, which is encouraging. Moreover, the range of electrical conductivities of each cluster is not overlapping with the others. The units stay well-defined, even when all inversions are considered.

The effect on the estimation of the variances is summarized in Figure 6.11b. Allowing too much freedom for the variances results in very high variance values, which hinders the clustering and classification aspects of the PGI approach. Fortunately, the inversion remains stable with low confidence results resembling the Tikhonov smooth inversions. The $\nu = 0.5$ threshold value is visible within the plot, with a sheer drop of the highest variance value.

Following that study, and as the covariance matrices play the role of noise levels for the petrophysics, values of ν below 0.5 are not recommended. This is because, for low values of ν , variances can become quite high, which hinders my goal of clustering the model's values. However, allowing some limited freedom on the variances to the algorithm can accommodate, as in the Bookpurnong example, some variations across clusters. In that example, it allowed me to accommodate a distribution with a low variance for the cluster representing the starting half-space and padding cells while allowing more variance for the two other units.

6.3.4 Impact of varying cluster characteristics

For the DO-27 case study (chapter 5), I had to add a cluster to the rock classification model to account for minor kimberlite occurrences at the near-surface. Suitable mean and covariance matrix parameters for the representation of that unit in the GMM had to be chosen. To this end, multiple gravity PGIs were run with various values for the mean density contrast, density variance and depth variance of that additional unit. The models recovered from those PGIs, and the associated GMMs, are available in appendix F.

I show in Figure 6.12 gravity PGIs for two combinations of parameters for the PK-minor unit. Figure 6.12a shows the combination of values I chose to keep for the multi-physics inversions (section 5.6). Figure 6.12b shows an example where the chosen characteristics did not reproduce the expected geological characteristics. In the latter, the PK-minor cluster is assumed to have a high density contrast (-0.5 g/cm^3) and a low density standard deviation (0.01 g/cm^3). This results in

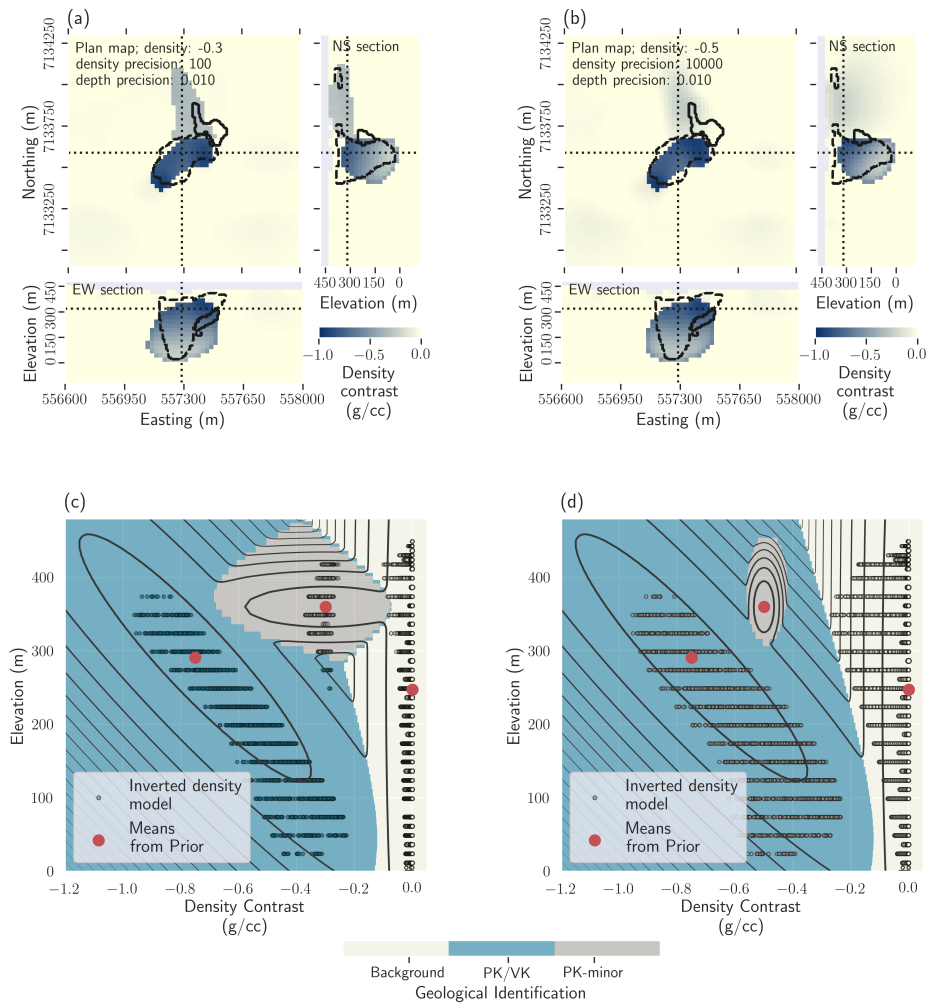


Figure 6.12: PGIs of the DO-27 gravity data for various values defining the PK-minor cluster. Panel (a) shows the density contrast model with the characteristics chosen for the multi-physics PGI in section 5.6.2 (see Table 5.1): density contrast of -0.3 g/cm^3 , density standard deviation of 0.1 g/cm^3 , and depth standard deviation of 10 m. Panel (c) represents the GMM corresponding to panel (a). Panel (b) shows another example with different values: density contrast of -0.5 g/cm^3 , density standard deviation of 0.01 g/cm^3 , and depth standard deviation of 10 m. Panel (d) represents the GMM corresponding to panel (b).

the PK-minor cluster not being “reached,” and the gravity anomaly at the expected locations of the PK-minor unit stays smooth and classified as background. Results for intermediate values of the three parameters of the cluster are shown in Appendix F. It highlights that the recovered model gradually varies with the choice of parameters. No drastic changes for small input variations are observed.

As demonstrated here, the PGI framework offers the possibility to easily test multiple hypotheses regarding the petrophysical characteristics of an otherwise undocumented rock unit. It would have been much more difficult to precisely formulate those hypotheses with the usual Tikhonov inversion framework.

6.4 Comparison with existing frameworks

I now compare the key components of the PGI framework with the approaches taken in recent literature. I first discuss how the framework introduced by Sun & Li (2015, 2016, 2017) can become a special case of PGI. In particular, I show how the petrophysical characterization process formalizes and generalizes their update of the means of the petrophysical distribution. I then discuss how the geological identification process is consistent with the framework introduced by Giraud et al. (2017). I also highlight how the PGI formulation differs from Giraud et al. (2017) and Giraud et al. (2019b), particularly in how the GMM representing the petrophysical and geological information is used in the objective function. I then highlight some of the key differences between the PGI framework and the work done by Grana & Della Rossa (2010), Grana et al. (2017), and Zhdanov & Lin (2017). Table 6.1 summarizes the main points of my comparison.

Table 6.1: Comparison table with other frameworks

Comparison with previous frameworks for inclusion of petrophysical and geological prior					
Characteristics	PGI framework	Sun & Li (2015, 2016, 2017)	Giraud et al. (2017, 2019b)	Grana & Della Rossa (2010); Grana et al. (2017)	Zhdanov & Lin (2017)
Compatible with a Bayesian formulation	Yes	No	No	Yes	Yes
Can handle multiple physical properties	Yes	Yes (Sun & Li, 2017)	Yes	Yes	No
Can be used with nonlinear physics	Yes	Yes	Yes	No	No
Update the petrophysical prior	All Θ parameters	Petrophysical means only (and without the volume weighting)	No	No	Increasing variances only
Add a term to the Tikhonov objective function	No	Yes	Yes	No	Yes
Include localized geology information	Yes	Yes (Rapstine et al., 2016)	Yes	Yes	No
Include spatial continuity of the geological labels	See section 6.5	No	No	Yes, with a HMM prior	No
Petrophysical target misfit	Yes	No	No	Not required	No
Compatibility of other approaches with the PGI framework	-	Is a special case of the current framework	Incompatible objective function	Stochastic version of PGI for linear problems and fixed prior	Also based on the Tikhonov approach, but uses a mapping instead of a prior
Open Source	Yes	No	No	No	No
Framework applied to	Gravity, Gravity Gradiometry, Magnetic, MVI, DC, FDEM, and MT	Gravity, Gravity Gradiometry, Magnetic, MVI, DC, IP, and seismic	Gravity and Magnetic	Seismic and rock physics inversion	Gravity and Gravity Gradiometry

6.4.1 Comparison with Sun and Li’s FCM guided inversion framework

In Sun & Li (2015, 2016, 2017), the authors proposed a framework for multi-physics geophysical inversions with petrophysical information by adding a Fuzzy C-Means (FCM) clustering term, with updatable cluster centres, to the objective function. Their work has become quite popular and been built upon by numerous authors (Capriotti & Li, 2017, 2018; Maag & Li, 2018; Rapstine et al., 2016; Singh & Sharma, 2018; Singh et al., 2018; Xu et al., 2019).

Sun & Li add the following term to the geophysical objective function (rewritten in the notation convention of this thesis):

$$\Phi_{\text{FCM}}(\mathbf{m}) = \underbrace{\sum_{i=1}^n \sum_{j=1}^c n_{ij}^{\rho} \|\mathbf{A}_k(\mathbf{m}_i - \boldsymbol{\mu}_j)\|_2^2}_{\text{FCM}} + \underbrace{\sum_{j=1}^c \lambda_j \|\boldsymbol{\mu}_j - \boldsymbol{\mu}_{\text{prior}}\|_2^2}_{\text{means update}}. \quad (6.1)$$

The matrices \mathbf{A} are norm-inducing matrices for Mahalanobis distances in a Gustafson-Kessel clustering algorithm (Babuka et al., 2002; Gustafson & Kessel, 1978). They play a similar role to the covariance matrices, but they do not include any weighting \mathbf{W} related to the physics. The FCM term in equation (6.1) sometimes replaces the smallness term in Sun & Li’s framework. However, when weighting is required, such as sensitivity or depth weighting for potential field data, a Tikhonov smallness term is added back in the objective function to include these weights. There are also included in the smoothness terms, as it is usual.

Their FCM term requires an additional exponent ρ for the petrophysical dis-

tribution, its fuzziness, applied to the responsibilities n_{ij} . Fuzziness is used in non-probability based clustering algorithms to get partial memberships to each cluster. In the PGI framework, this is taken care of at the E-step of the MAP-EM algorithm when computing the responsibilities (equation (3.16)). The fuzziness approach does not retain the probabilistic properties that allow me to define, for example, a stopping criterion (section 3.4.1). Nonetheless, there exists a variation of the EM algorithm that includes a fuzziness parameter (Ju & Liu, 2012).

The weights λ_j play a similar role as my κ confidences for updating the means, but there are differences. First, the λ_j weights are not normalized for the number of cells, the volume of the cells or the proportions of the units as done in PGI (see equations (3.18) to (3.26)). Second, these weights are defined as scalars for each unit. Thus, in their framework, it is not possible to vary the means of specific physical properties while fixing others, as I did in section 4.5. This allowed me to fix a cluster's magnetic susceptibility while varying its density contrast and vice versa.

Overall, their methodology appears as a special case of the PGI framework. I have redefined their update to the means of the petrophysical distribution in terms of a conjugate prior and generalized that concept to the other parameters of the distribution (see equations (3.15) to (3.26)). To reproduce their framework with the PGI approach, one must use the fuzziness variant of the EM algorithm, use only scalar confidence values for the means, fix all the proportions equal to $1/c$ and keep all the proportions and the variances equal to their priors. Keeping parameters equal to their prior corresponds to infinite confidences in the priors in

the PGI framework. More research is necessary to determine in which cases the inclusion of a fuzziness parameter could make a difference, or not, with a PGI approach. In my experience, this has not appeared to be a key factor in the model recovery so far.

6.4.2 Comparison with Giraud et al.'s frameworks

The framework developed by Giraud et al. (2017) focuses on the geological modelling done before the inversion. Inversions of gravity and magnetic data are used to reduce the uncertainties of geological modelling. They thus start with very strong geological and petrophysical priors, which cannot be adjusted during the inversion. This is contrary to what the PGI approach does with the conjugate prior updates. The PGI and Giraud et al. frameworks both represent the petrophysical information as a GMM, with the geology information included through the proportions. However, there are major differences in how the GMM is included in the inverse problem, and the formulations are incompatible. The main reason is due to how Giraud et al. incorporate petrophysical information inside their geophysical objective function. They add to the Tikhonov objective function a coupling term Φ_c . This term is defined as a sum of least-squares differences between the GMM probability density distribution, evaluated at the current density and magnetic susceptibility models, and a term \mathcal{P}^{\max} representing the likelihood of their prior knowledge, computed from the prior petrophysical and geological models.

Their term Φ_c takes the form, in the notation of this thesis:

$$\Phi_c(\mathbf{m}) = \sum_{i=1}^n \sum_{p=1}^2 (w_p(\mathcal{M}(\mathbf{m}_i|\Theta) - \mathcal{P}_i^{\max}))^2, \quad (6.2)$$

with:

$$w_p = \max_{j=1..c} (\Sigma_{pp})_j^{-\frac{1}{2}}, \quad (6.3)$$

where \mathcal{M} is a GMM distribution similar to the one defined in equation (4.3), and $(\Sigma_{pp})_j$ is the p diagonal term of the covariance matrix of rock unit j .

Thus, they mix the norm of a vector of probability values with log-probability terms (the Tikhonov objective function); this is incompatible with a Bayesian formulation as done in the PGI approach. Moreover, far from the expected petrophysical values, the gradient of that additional term vanishes and tends to zero. This means that, far from a solution, the coupling term no longer plays a significant role in the optimization. The usual behaviour of a least-squares problem is that the further the current model is from a solution, the bigger the gradients are, and the larger the updates to the model are.

Some of those issues are addressed in Giraud et al. (2019b). They modify their formulation of the coupling term to instead work with a least-squares misfit between the log-likelihood of the multidimensional GMM and a target log-likelihood (see equation (6.4)). This coupling term is still hard, if feasible, to represent meaningfully from a Bayesian perspective. It is also worth noting that putting the log-likelihood of the GMM within a least-squares misfit renders the term more akin to a quartic term (power 4) rather than a quadratic term (power 2).

$$\Phi_c(\mathbf{m}) = \sum_{i=1}^n (\log \mathcal{M}(\mathbf{m}_i|\Theta) - \log \max \mathcal{M}(\mathbf{m}_i|\Theta))^2. \quad (6.4)$$

Contrary to Giraud et al. (2017) (equation (6.3)) and Giraud et al. (2019b) (equation (6.4)), that include either the GMM or the GMM log-likelihood inside an additional least-squares term, the PGI formulation adopts a Bayesian formulation of the inverse problem by working directly with the GMM log-likelihood as a smallness, making the petrophysical misfit similar to the geophysical misfit.

6.4.3 Comparison with Grana et al.’s frameworks

The frameworks developed in Grana & Della Rossa (2010); Grana et al. (2017) and the PGI approach share the Bayesian formulation of the problem, where the GMM serves as prior. Grana et al. (2017) also adds a Hidden Markov Model (HMM) prior (Cappé et al., 2005) on the lithology classification to enforce geological continuity in the results. They both focus on linear 1D problems and adopted stochastic approaches to the resolution of the inverse problem. Grana et al. (2017), in particular, take advantage of the linearity to achieve an exact solution of an approximation of the posterior distribution, which allows them to efficiently sample from it with a MCMC algorithm and fully estimate the model distribution. It is computationally expensive but easily parallelizable. The PGI framework works for both linear and nonlinear problems. While my formulation is done in a Bayesian context, I have taken a deterministic approach so far for its resolution. Their prior is held fixed, contrary to my additional approach of learning the prior (section 3.3.2). Adding a prior that enforces the continuity of the geological units repre-

sents a potential improvement of the current PGI framework. I explore this idea in section 6.5.

6.4.4 Comparison with Zhdanov’s multinary framework

Also for linear problems, Zhdanov & Lin (2017) proposed a deterministic approach to find a global minimum to a gravity and gravity gradiometry inverse problem. To include prior petrophysical information, their approach is not based on modifying the regularization, but rather on transforming the physical property model into a superposition of error functions, which can be written in the following manner using the notation convention of this thesis:

$$\tilde{m}_i = \varepsilon m_i + \frac{1}{2} \sum_{j=1}^c \left(1 + \operatorname{erf} \left(\frac{m_i - \mu_j}{\sqrt{2\sigma}} \right) \right), \quad (6.5)$$

with ε “a small number to avoid singularities in the calculation of the derivatives of the quasimultinary densities” (Zhdanov & Lin, 2017). The derivative of each error function is a Gaussian distribution centred on the μ_j mean value.

There is, however, no closed-form inverse error function to convert the model back into density contrasts. Thus, they first compute a very accurate look-up table before using interpolation to recover density contrasts. Generalizing this approach as a coupling term for multi-physics inversion is not trivial, if feasible, since the error function is not generalizable to multidimensional spaces. Their only update to the petrophysical prior is to increase the variance σ when the geophysical misfit does not decrease enough, which relaxes the petrophysical constraint.

6.5 Future avenues of research: extensions of the framework to include geological rules and modelling

6.5.1 Introduction

In the previous chapters, I developed a framework to include petrophysical information using a GMM prior on the geophysical model. In this approach, the algorithm attributes a rock unit to each cell based on its petrophysical values, through a classifying variable \mathbf{z} that is used to update the reference model \mathbf{m}_{ref} and the smallness weights \mathbf{W}_s . So far, I have relied on the smoothness prior applied to the geophysical model to ensure the continuity of the geological units. However, it is possible to also include that prior knowledge, as well as more advanced information, into the prior $\mathcal{P}(\mathbf{z})$ of the geological identification process. Information such as dip orientations or other structural relationships can make the inversion result more realistic. The goal of this section is to introduce possible ways to include prior geological knowledge. In particular, I discuss methods that might allow me to take into consideration the values and classifications of the surrounding cells in the geological identification process, rather than working with each cell individually. For that purpose, I explore the notions of Markov Random Field (MRF) and image segmentation algorithms and discuss their applications to design and use a prior distribution on \mathbf{z} that includes geological information.

Image segmentation algorithms are classification algorithms that determine the class of a pixel, or cell, based on its current value and its neighbours. Image

segmentation algorithms have been widely used in the medical imaging community (Işın et al., 2016; Lee et al., 2005; Schmidt et al., 2005). There exist tens, if not hundreds, of image segmentation algorithms, based on PDEs, level sets, neural networks, etc. (Brox & Weickert, 2006; Lensink et al., 2019; Rother et al., 2004), just to cite a few. Considering the current formulation of the PGI framework, image segmentation algorithms based on Gaussian Mixture Markov Random Field (GMMRF) (Li, 2001), which relies on the concept of MRF (introduced below), appear to be the most appealing. The main principle behind a GMMRF is to consider local proportion parameters $\Pi = \{\pi_{ij}, i = 1..n, j = 1..c\}$. Priors $\mathcal{P}(\Pi)$ on these proportions are then designed to ensure the spatial continuity of the recovered geological units or enforce relationship rules between them. The classification of a cell no longer depends only upon the local physical properties and proportions, but it is also affected by the classification of the neighbouring cells. A similar idea has been explored by Grana et al. (2017) for 1D linear problems using a GMM with a HMM (Cappé et al., 2005), which is the simpler 1D case of a MRF, to enforce the continuity of the recovered lithological facies in a borehole log. MRFs are also part of a suite of tools that have been investigated in the recent literature for stochastic geological modelling (Wang et al., 2017).

An example of image segmentation using a GMMRF is shown in Figure 6.13. For this example, I implemented the prior on local proportions developed by Nguyen & Wu (2013), because of its computational speed and robustness. The parameters specific to this prior were set as in the original publication. The neighbours of each cell are defined as the cells within an isotropic 5×5 cells square

around it. Note that choosing anisotropic neighbouring areas (tilted and elongated) can present an opportunity for including structural information. Figure 6.13a presents the original picture to segment into different unsupervised categories. I first applied the MLE EM algorithm (no prior values, no relationship between adjacent cells) to fit a GMM with 24 units on the image. The resulting categories are shown in Figure 6.13b, each represented by its mean colour. The classification appears “noisy”, as small isolated groups of pixels are found to have a different classification than their surroundings; this is especially visible in more homogeneous areas such as the background, flag, or spacesuit. Finally, Figure 6.13c presents the classification obtained by fitting a GMMRF with 24 units, using the prior defined in Nguyen & Wu (2013), on the original image. The result is much smoother, as the GMMRF favours spatial continuity of categories. Small details can, however, be lost (like the facial features). Note, however, that this is an unsupervised approach, so there is no meaning enforced in the categories. If one wants, for example, a category to represent the whole spacesuit, then more *a priori* information needs to be provided.

I propose in this section a proof of concept for using GMMRF for including geologic information in geophysical inversions with the PGI framework. To this end, I implement one of the simplest priors to express relationships between adjacent cells: a generalization of the Ising model (Ising, 1925; Murphy, 2012), which I introduce below. I then apply this approach to the DC example, first used in section 3.5.2. The result is shown in Figure 6.15.



Figure 6.13: An example of image segmentation. Panel (a) shows the original image, astronaut and Space Shuttle Commander Eileen Collins (NASA Great Images database, 1998). Panel (b) is the image classified pixel-by-pixel by training a GMM with 24 clusters. Panel (c) is the image classified by a GMMRF with 24 clusters trained using the image segmentation algorithm presented in Nguyen & Wu (2013). Notice the smoothness of this classification compared to the pixel-by-pixel approach shown in panel (b).

6.5.2 Introduction to Markov random fields

Here, I briefly introduce the concept of graphs and MRF, on which GMMRF relies upon to build relationships between adjacent cells. Unlike \mathbf{m} , which is a continuous variable over the physical properties space, the membership \mathbf{z} is a categorical variable. Because of this different nature, I need a different type of approach to design and add prior information than what I have used so far, like smoothness.

A graph is composed of a set of nodes representing variables and edges which represent possible interactions. Because I do not set directions for the edges, this makes the graph undirected and constitutes a MRF. The mesh that is usually used in geophysical inversions can be easily seen as such a graph; each cell is a node containing the corresponding value of the geophysical model. Edges can be drawn

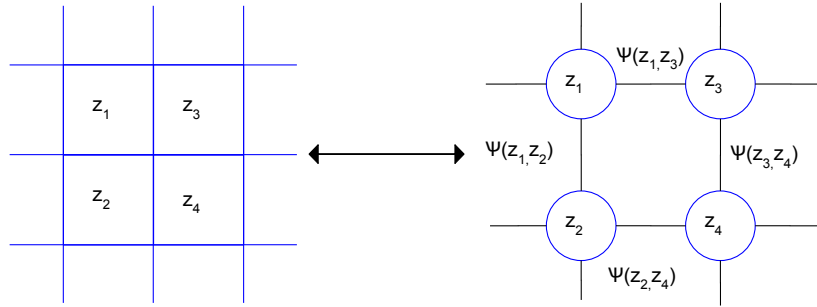


Figure 6.14: Mesh versus graph representation

between each cell to its neighbours (Figure 6.14). The corresponding graph is a 2D or 3D lattice. The functions ψ , which determine the relationships between neighbours, are called “pairwise potentials.”

The posterior probability of a vector \mathbf{z} is then proportional to a likelihood times a prior, such as defined by the Bayes’ theorem (section 2.2.3). The likelihood \mathcal{L} is the product, over the cells, of the probability of the category z_i at the cell i (for example based on the physical property values at this cell). The MRF prior $\mathcal{P}(\Pi)$ is the product of the pairwise potentials of all the neighbouring cells:

$$\mathcal{P}(\mathbf{z}|\mathbf{m}, \Theta) \propto \prod_i \mathcal{L}_{\{\mathbf{m}_i, \Theta\}}(z_i) \underbrace{\left(\prod_{j \in \partial_i} \psi(z_i, z_j) \right)}_{\mathcal{P}(\Pi_i)}, \quad (6.6)$$

where ∂_i is the set of neighbours for the cell i .

Below I present a simple approach to design the pairwise potentials ψ , a generalization of the Ising model, to serve as a proof of concept for the inclusion of geologic rules in the geological identification step of the PGI framework.

6.5.3 Proof of concept with the Ising model

The Ising model was developed in the early 20th century to describe magnets' behaviour (Ising, 1925). Each atom of a given magnet is represented as a node classified according to its spin, up ($z = 1$) or down ($z = -1$). In ferromagnets, neighbouring spins tend to be similar, while in anti-ferromagnets, they tend to be in opposite directions.

This can be modelled through a MRF as follows. On a lattice such as the one illustrated in figure 6.14, I define the following pairwise potentials between two connected nodes:

$$\psi(\mathbf{z}_i, \mathbf{z}_j) = \begin{pmatrix} e^{Tz_i=1, z_j=1} & e^{Tz_i=1, z_j=2} \\ e^{Tz_i=2, z_j=1} & e^{Tz_i=2, z_j=2} \end{pmatrix}. \quad (6.7)$$

The diagonal elements of the Ising matrix above determine the pairwise potentials ψ for the adjacent cells i and j when they have an identical classification ($z_i = z_j$). The off-diagonal elements represent the ψ pairwise potential for adjacent cells when they have different classifications ($z_i \neq z_j$). The parameters $\{T\}$ are “temperatures”, that control the coupling strength between cells i and j . In the original work on magnets, they are different depending on if the two nodes carry the same spin or not. A positive temperature increases the probability of a particular configuration in equation (6.6), while a negative temperature decreases it. A temperature of zero denotes the absence of a relationship; this is because the multiplicative factor in equation (6.6) is then simply unity ($\exp(0) = 1$). In the Ising

model (equation (6.7)), if $T_{z_i=z_j}$ is positive and $T_{z_i \neq z_j}$ is negative, then configurations of adjacent atoms with similar spins are favoured. If $T_{z_i=z_j}$ is negative and $T_{z_i \neq z_j}$ is positive, then the Ising model enforces adjacent atoms to have opposite spins. The most stable configurations are the ones with the highest probability, according to equation (6.6).

This approach is generalizable to a c -units classifier, one for each unit in the GMM. The pairwise potentials become:

$$\psi(\mathbf{z}_i, \mathbf{z}_j) = \begin{pmatrix} e^{Tz_i=1, z_j=1} & e^{Tz_i=1, z_j=2} & \dots & e^{Tz_i=1, z_j=c} \\ e^{Tz_i=2, z_j=1} & e^{Tz_i=2, z_j=2} & \dots & e^{Tz_i=2, z_j=c} \\ \vdots & \vdots & \ddots & \vdots \\ e^{Tz_i=c, z_j=1} & e^{Tz_i=c, z_j=2} & \dots & e^{Tz_i=c, z_j=c} \end{pmatrix}. \quad (6.8)$$

Optimization

The classic optimization approach to maximize the score function described in equation (6.6) is to adopt a coordinate descent approach. These algorithms visit each node randomly and either set it to its maximum likelihood, the algorithm is then known as Iterative Conditional Modes (ICM), or sample from the relative categorical probability distribution, this approach is then known as Gibbs Sampling (see for reference Murphy (2012)). To match with the deterministic work done so far, I adopt in the following example the ICM algorithm as the standard optimizer over the membership.

DC example

I apply the PGI framework with a GMMRF, using a c -units Ising model prior (equation (6.8)), to the DC example that I first presented in section 3.5.2. The true model is composed of two cylindrical units, one conductive and one resistive, embedded in a background of intermediate resistivity (reminded in Figure 6.15a). This example has been extensively covered throughout this thesis (sections 3.5.2, 6.2, 6.3.1), with accurate recovery of the true model (see Figure 6.15c). To demonstrate the impact an image segmentation approach can have, I use the c -units Ising model to include a geologic assumption that is not true: the background and the conductive rock units cannot be in contact. In addition, I use the c -units Ising model to enforce the geological continuity of rock units by favouring configurations where adjacent cells have a similar classification. The neighbourhood of each cell is defined as the twelve closest cells (see Figure 6.15d).

To enforce these geologic rules, I define the following pairwise potentials between the three geological units (background, conductive and resistive cylinders):

$$\psi(\mathbf{z}_i, \mathbf{z}_j) = \begin{pmatrix} e^1 & e^{-\infty} & e^0 \\ e^{-\infty} & e^1 & e^0 \\ e^0 & e^0 & e^1 \end{pmatrix}. \quad (6.9)$$

The geological continuity of rock units is favoured by setting a positive temperature for the diagonal elements. The background and the conductive cylinder, which correspond to units 1 and 2 in the matrix (equation (6.9)), are forbidden to

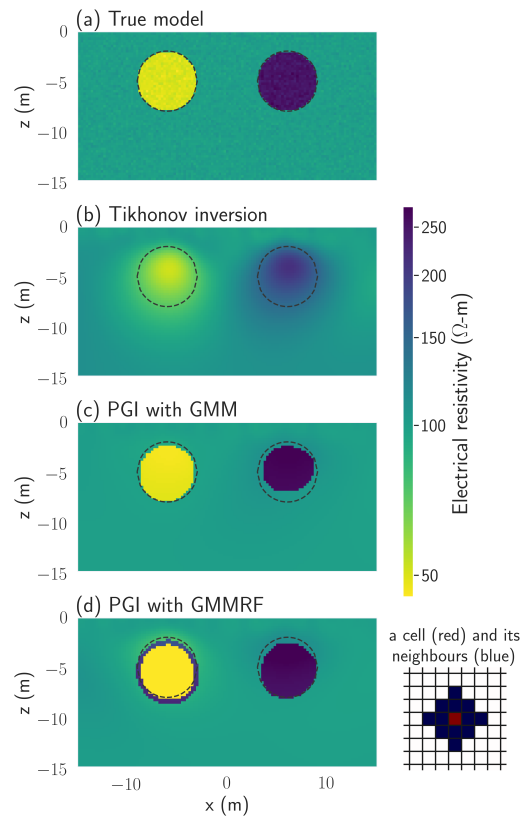


Figure 6.15: An example of an inversion using structural rules dictated by the c -units Ising model. The following rule is implemented: 'The conductive unit and background cannot touch'. (a) True resistivity model; (b) model recovered with a Tikhonov approach; (c) model recovered with PGI and no structural rule; (d) model recovered with PGI and a GMMRF to implement the structural rule; the plot on the right shows the defined neighbourhood of a cell.

be in contact by setting an infinite negative temperature in the off-diagonal elements; the probability of them being in contact is thus zero, according to equation (6.6). The resistive cylinder, the last line and column in the matrix, does not have this restriction.

The result of the PGI with the c -units Ising prior defined in equation (6.9) is shown in Figure 6.15d. The PGI was provided with the true petrophysical means and variances (see section 3.5.2). The impact of the c -units Ising prior is significant. In order to comply with the enforced geologic rules, the conductive rock unit is surrounded by the resistive rock unit; this avoids the background and conductive units to be in contact. Note that this is a very different situation from the halo presented in section 6.2, which was due to the consecutive values of resistivities of the cylindrical rock units compared to the background resistivity. Here, the model does not progressively go from background resistivity to high resistivity. Around the cylinder on the right, the values of the model directly go from background to highly resistive, and then to highly conductive.

While this example is not representative of a true situation, it is a proof of concept that geologic rules, such as stratigraphy, that are used to numerically build quantitative geological models (Calcagno et al., 2008; Jessell et al., 2014; Linde et al., 2015), might be integrated into geophysical inversions through the PGI framework with GMMRF to obtain more realistic geologic models that benefit from all fields of expertise.

6.6 Conclusion

The PGI framework is composed of three regularized optimization problems (Figure 6.1). Chapter 3 laid the mathematical foundation of the framework, with an emphasis on the inclusion and the learning of the petrophysical signatures (Process 2 in Figure 6.1). In chapter 4, I focused on the coupling of several geophysical surveys with various physical properties, thus extending the Process 1 in Figure 4.1. The third and last process, the geological identification, is still one where there is much room for advancement; the use of the proportions of the GMM shows promise. In section 3.5.2, I showed, with a direct-current resistivity example, the efficacy of the proportions when they are locally set to zero or unity. Proportions values of zero or unity are “constraining”, in the sense that they forbid local occurrences of certain units, rather than just favouring it. While intermediate values of the global proportions appear to have minimal impact on the inversions in our experiments (section 6.3.1), further studies are required to address the importance and the effects of intermediate (strictly between zero and unity) local proportions. The approach taken by Giraud et al. (2017) combines local proportions, computed from stochastic geological modelling before the inversions, with various warm-started initial geophysical models. In section 6.5, I introduced the concepts of GMMRF to include relationships between adjacent cells through local proportions in the GMM. The integration, extrapolation, and learning of geological information will be the key ingredient of future development. More types of geological information, such as dips, contacts or strikes, also need to be formalized within the

PGI framework approach. A major exploratory avenue that has yet to be tested is to link the PGI approach with the `GemPy` probabilistic geological modeller (de la Varga et al., 2019). This geological modeller formulates the geological modelling problem, starting from structural and location information, as an optimization on a posterior distribution. The similar formulations of the problems make the two approaches ideal candidates for bridging the gap between geophysical and geological modelling. Combining the PGI smallness term with approaches including prior structural information in the smoothness terms (Brown et al., 2012; Fournier & Oldenburg, 2019; Giraud et al., 2019a; Lelièvre & Oldenburg, 2009a; Yan et al., 2017) is also to be investigated.

The PGI algorithm offers considerable flexibility to include different types of information in a variety of ways. I have illustrated its capabilities throughout the thesis and, in particular, explored how changing some of the parameters affects the final result. I have highlighted situations that can be challenging for the framework and proposed ways to tackle them. I have also illustrated the major advantages of this framework over other approaches while stating the points of convergence or divergence (section 6.4). Finally, I have proposed exploratory ways to improve the framework (section 6.5).

Lastly, I comment upon how important the development of open-source software packages has been for my research. It has allowed me to benefit from the work carried out by others. The development of the MAP-EM algorithm has been facilitated by the MLE code available through the open-source `Scikit-Learn` project, a library of tools for machine-learning (Pedregosa et al., 2011). The suc-

cessful application of the methodology to various geophysical survey methods, such as potential fields, DC, MT or FDEM, has been made possible because of the interconnectivity of SIMPEG, an open-source package to carry out geophysical inversions (Cockett et al., 2015; Heagy et al., 2017; Kang et al., 2018; Oldenburg et al., 2019). It allows the implementation of the framework to be readily used with any type of geophysical surveys or discretization (such as Octree meshes) that are supported in the source code. To ensure reproducibility of the results in this paper, and to contribute to the development of the open-source community, I made the examples presented in this thesis available online (Astic, 2019, 2020), through the use of Jupyter Notebooks (Perez et al., 2015). This allows researchers to use my framework readily and contribute to the development of inversion codes that incorporate geophysical, geological and petrophysical data to yield meaningful solutions.

Bibliography

- Afnimar, P., Koketsu, K., & Nakagawa, K., 2002. Joint inversion of refraction and gravity data for the three-dimensional topography of a sediment–basement interface, *Geophysical Journal International*, **151**(1), 243–254. → page 11
- Andrieu, C., de Freitas, N., Doucet, A., & Jordan, M. I., 2003. An Introduction to MCMC for Machine Learning, *Machine Learning*, **50**(1), 5–43. → page 53
- Armijo, L., 1966. Minimization of functions having Lipschitz continuous first partial derivatives, *Pacific Journal of Mathematics*, **16**(1), 1–3. → page 52
- Ascher, U. & Greif, C., 2011. *A First Course in Numerical Methods*, Society for Industrial and Applied Mathematics, Philadelphia, PA. → pages 50, 52
- Astic, T., 2019. Open source software for petrophysically and geologically guided geophysical inversion, <https://doi.org/10.5281/zenodo.2564169>, Accessed: 2019-02-14. → pages vi, 84, 240
- Astic, T., 2020. Collection of scripts for forward modelling and joint inversion of potential fields data, <https://doi.org/10.5281/zenodo.3571471>, Accessed: 2020-01-31. → pages vii, 137, 240
- Astic, T. & Oldenburg, D. W., 2018. Petrophysically guided geophysical inversion using a dynamic Gaussian mixture model prior, in *SEG Technical Program Expanded Abstracts 2018*, pp. 2312–2316. → page vii
- Astic, T. & Oldenburg, D. W., 2019. A framework for petrophysically and geologically guided geophysical inversion using a dynamic Gaussian mixture model prior, *Geophysical Journal International*, **219**(3), 1989–2012. → page vi

- Astic, T., Fournier, D., & Oldenburg, D. W., 2020a. Joint inversion of potential fields data over the DO-27 kimberlite pipe using a Gaussian mixture model prior, *Interpretation*. → page vii
- Astic, T., Heagy, L. J., & Oldenburg, D. W., 2020b. Petrophysically and geologically guided multi-physics inversion using a dynamic Gaussian mixture model, *Geophysical Journal International*. → page vii
- Babuka, R., van der Veen, P. J., & Kaymak, U., 2002. Improved covariance estimation for Gustafson-Kessel clustering, in *2002 IEEE World Congress on Computational Intelligence. 2002 IEEE International Conference on Fuzzy Systems. FUZZ-IEEE'02. Proceedings (Cat. No.02CH37291)*, vol. 2, pp. 1081–1085 vol.2. → page 222
- Bijani, R., Lelièvre, P. G., Ponte-Neto, C. F., & Farquharson, C. G., 2017. Physical-property-, lithology- and surface-geometry-based joint inversion using pareto multi-objective global optimization, *Geophysical Journal International*, **209**(2), 730–748. → page 131
- Bosch, M., 2004. The optimization approach to lithological tomography: Combining seismic data and petrophysics for porosity prediction, *Geophysics*, **69**(5), 1272–1282. → page 12
- Bosch, M. & McGaughey, J., 2001. Joint inversion of gravity and magnetic data under lithologic constraints, *The Leading Edge*, **20**(8), 877–881. → pages 3, 7
- Bosch, M., Carvajal, C., Rodrigues, J., Torres, A., Aldana, M., & Sierra, J., 2009. Petrophysical seismic inversion conditioned to well-log data: Methods and application to a gas reservoir, *Geophysics*, **74**(2), O1–O15. → page 8
- Brown, V., Key, K., & Singh, S., 2012. Seismically regularized controlled-source electromagnetic inversion, *Geophysics*, **77**(1), E57–E65. → page 239
- Brox, T. & Weickert, J., 2006. Level set segmentation with multiple regions, *IEEE Transactions on Image Processing*, **15**(10), 3213–3218. → page 229
- Calcagno, P., Chilès, J., Courrioux, G., & Guillen, A., 2008. Geological modelling from field data and geological knowledge: Part i. modelling method coupling 3d potential-field interpolation and geological rules, *Physics of the Earth and Planetary Interiors*, **171**(1), 147 – 157, Recent Advances in

- Computational Geodynamics: Theory, Numerics and Applications. → page 237
- Cappé, O., Moulines, E., & Ryden, T., 2005. *Inference in Hidden Markov Models*, Springer-Verlag, Berlin, Heidelberg. → pages 9, 226, 229
- Capriotti, J. & Li, Y., 2017. Time-lapse gravity inversion for multiple reservoir parameters using fuzzy C-means clustering, in *SEG Technical Program Expanded Abstracts 2017*, pp. 5865–5869. → page 222
- Capriotti, J. & Li, Y., 2018. Guided fuzzy c-means clustering inversion of electrical potential due to an anisotropic-layered half-space, in *SEG Technical Program Expanded Abstracts 2018*, pp. 914–918. → page 222
- Carter-McAuslan, A., Lelièvre, P. G., & Farquharson, C. G., 2015. A study of fuzzy c-means coupling for joint inversion, using seismic tomography and gravity data test scenarios, *Geophysics*, **80**(1), W1–W15. → pages 66, 67
- Chen, J. & Hoversten, G. M., 2012. Joint inversion of marine seismic AVA and CSEM data using statistical rock-physics models and Markov random fields, *Geophysics*, **77**(1), R65–R80. → page 12
- Chen, J., Hoversten, G. M., Vasco, D., Rubin, Y., & Hou, Z., 2007. A Bayesian model for gas saturation estimation using marine seismic AVA and CSEM data, *Geophysics*, **72**(2), WA85–WA95. → page 11
- Cockett, R., Kang, S., Heagy, L. J., Pidlisecky, A., & Oldenburg, D. W., 2015. SimPEG: An open source framework for simulation and gradient based parameter estimation in geophysical applications, *Computers and Geosciences*, **85**, 142–154. → pages 136, 169, 240, 262
- Constable, S. C., Parker, R. L., & Constable, C. G., 1987. Occam's inversion: A practical algorithm for generating smooth models from electromagnetic sounding data, *Geophysics*, **52**(3), 289–300. → pages 3, 5
- de Figueiredo, L. P., Grana, D., Roisenberg, M., & Rodrigues, B. B., 2019a. Gaussian mixture Markov chain Monte Carlo method for linear seismic inversion, *Geophysics*, **84**(3), R463–R476. → page 53
- de Figueiredo, L. P., Grana, D., Roisenberg, M., & Rodrigues, B. B., 2019b. Multimodal Markov chain Monte Carlo method for nonlinear petrophysical seismic inversion, *Geophysics*, **84**(5), M1–M13. → page 53

- de la Varga, M., Schaaf, A., & Wellmann, F., 2019. GemPy 1.0: open-source stochastic geological modeling and inversion, *Geoscientific Model Development*, **12**(1), 1–32. → page 239
- De Stefano, M., Golfré Andreasi, F., Re, S., Virgilio, M., & Snyder, F. F., 2011. Multiple-domain, simultaneous joint inversion of geophysical data with application to subsalt imaging, *Geophysics*, **76**(3), R69–R80. → page 11
- Dempster, A. P., Laird, N. M., & Rubin, D. B., 1977. Maximum likelihood from incomplete data via the EM algorithm, *Journal of the Royal Statistical Society, series B*, **39**(1), 1–38. → pages 68, 69, 124, 148, 152, 165
- Devriese, S. G. R., Davis, K., & Oldenburg, D. W., 2017. Inversion of airborne geophysics over the DO-27/DO-18 kimberlites — Part 1: Potential fields, *Interpretation*, **5**(3), T299–T311. → pages xxx, 3, 137, 158, 163, 164, 168, 169, 170, 171, 173, 174, 177, 196
- Doetsch, J., Linde, N., Coscia, I., Greenhalgh, S. A., & Green, A. G., 2010. Zonation for 3D aquifer characterization based on joint inversions of multimethod crosshole geophysical data, *Geophysics*, **75**(6), G53–G64. → page 10
- Doyle, B. J., Kivi, K., & Smith, B. H. S., 1998. The Tli Kwi Cho (DO27 and DO18) diamondiferous kimberlite complex, Northwest Territories, in *Proceedings of the 7th International Kimberlite Conference*, pp. 194–204. → pages 162, 167
- Dyke, A. & Prest, V., 1987. Late Wisconsinan and Holocene History of the Laurentide Ice Sheet, *Géographie physique et Quaternaire*, **41**(2), 237–263. → page 162
- Eggleston, T., Brisebois, K., & Pell, J., 2014. Lac de Gras project Northwest Territories, Canada, Tech. Rep. NI 43-101, Peregrine Diamonds Ltd. → pages xxxii, 174, 176
- Enkin, R. J., Hamilton, T. S., & Morris, W. A., 2020. The Henkel Petrophysical Plot: Mineralogy and Lithology From Physical Properties, *Geochemistry, Geophysics, Geosystems*, **21**(1), e2019GC008818. → page 176

- Farquharson, C. G. & Oldenburg, D. W., 1993. Inversion of time-domain electromagnetic data for a horizontally layered Earth, *Geophysical Journal International*, **114**(3), 433–442. → page 52
- Farquharson, C. G. & Oldenburg, D. W., 2004. A comparison of automatic techniques for estimating the regularization parameter in non-linear inverse problems, *Geophysical Journal International*, **156**(3), 411–425. → pages 52, 79
- Field, M. & Smith, B. H. S., 1998. Textural and genetic classification schemes for kimberlite: a new perspective, in *Extended abstracts, 7th International Kimberlite Conference, Cape Town*, pp. 214–216. → page 162
- Fournier, D., 2015. *A cooperative magnetic inversion method with L_p -norm regularization*, Master's thesis, University of British Columbia. → page 82
- Fournier, D. & Oldenburg, D. W., 2019. Inversion using spatially variable mixed ℓ_p norms, *Geophysical Journal International*, **218**(1), 268–282. → pages 3, 110, 196, 239
- Fournier, D., Kang, S., McMillan, M. S., & Oldenburg, D. W., 2017. Inversion of airborne geophysics over the DO-27/DO-18 kimberlites — Part 2: Electromagnetics, *Interpretation*, **5**(3), T313–T325. → pages 3, 158, 164, 173
- Fournier, D., Heagy, L. J., & Oldenburg, D. W., 2020. Sparse magnetic vector inversion in spherical coordinates, *GEOPHYSICS*, **85**(3), J33–J49. → pages 111, 139
- Fullagar, P. K., Pears, G. A., & McMonnies, B., 2008. Constrained inversion of geologic surfaces—pushing the boundaries, *The Leading Edge*, **27**(1), 98–105. → pages 3, 7
- Gallardo, L. A. & Meju, M. A., 2003. Characterization of heterogeneous near-surface materials by joint 2D inversion of dc resistivity and seismic data, *Geophysical Research Letters*, **30**(13). → page 11
- Gallardo, L. A. & Meju, M. A., 2004. Joint two-dimensional DC resistivity and seismic travel time inversion with cross-gradients constraints, *Journal of Geophysical Research: Solid Earth*, **109**(B3). → page 132

- Gallardo, L. A. & Meju, M. A., 2011. Structure-coupled multiphysics imaging in geophysical sciences, *Reviews of Geophysics*, **49**(1). → page 11
- Giraud, J., Pakyuz-Charrier, E., Jessell, M., Lindsay, M., Martin, R., & Ogarko, V., 2017. Uncertainty reduction in joint inversion using geologically conditioned petrophysical constraints, *Geophysics*, **82**(6), 1–16. → pages 9, 12, 14, 60, 62, 114, 143, 220, 221, 224, 226, 238
- Giraud, J., Lindsay, M., Ogarko, V., Jessell, M., Martin, R., & Pakyuz-Charrier, E., 2019a. Integration of geoscientific uncertainty into geophysical inversion by means of local gradient regularization, *Solid Earth*, **10**(1), 193–210. → page 239
- Giraud, J., Ogarko, V., Lindsay, M., Pakyuz-Charrier, E., Jessell, M., & Martin, R., 2019b. Sensitivity of constrained joint inversions to geological and petrophysical input data uncertainties with posterior geological analysis, *Geophysical Journal International*, **218**(1), 666–688. → pages 9, 12, 60, 114, 131, 220, 221, 225, 226
- Giuseppe, M. G. D., Troiano, A., Troise, C., & Natale, G. D., 2014. k-Means clustering as tool for multivariate geophysical data analysis. An application to shallow fault zone imaging, *Journal of Applied Geophysics*, **101**, 108 – 115. → page 10
- Grana, D. & Della Rossa, E., 2010. Probabilistic petrophysical-properties estimation integrating statistical rock physics with seismic inversion, *Geophysics*, **75**(3), O21. → pages 8, 14, 60, 114, 115, 220, 221, 226
- Grana, D., Fjeldstad, T., & Omre, H., 2017. Bayesian Gaussian Mixture Linear Inversion for Geophysical Inverse Problems, *Mathematical Geosciences*, **49**(4), 493–515. → pages 9, 60, 220, 221, 226, 229
- Granek, J., 2011. *Computing geologically consistent models from geophysical data*, Master's thesis, University of British Columbia. → page 60
- Gustafson, D. & Kessel, W. C., 1978. Fuzzy clustering with a fuzzy covariance matrix, *1978 IEEE Conference on Decision and Control including the 17th Symposium on Adaptive Processes*, pp. 761–766. → page 222
- Haber, E., 2014. *Computational methods in geophysical electromagnetics*, vol. 1, SIAM. → page 50

- Haber, E. & Oldenburg, D., 1997. Joint inversion: a structural approach, *Inverse Problems*, **13**(1), 63. → page 11
- Haber, E. & Oldenburg, D., 2000. A GCV based method for nonlinear ill-posed problems, *Computational Geosciences*, **4**(1), 41–63. → page 52
- Hansen, P. C., 1998. *Rank-Deficient and Discrete Ill-Posed Problems*, Society for Industrial and Applied Mathematics. → page 51
- Hansen, P. C., 2000. The L-Curve and its Use in the Numerical Treatment of Inverse Problems, in *Computational Inverse Problems in Electrocardiology*, ed. P. Johnston, *Advances in Computational Bioengineering*, pp. 119–142, WIT Press. → pages 51, 131
- Hansen, P. C. & O’Leary, D. P., 1993. The Use of the L-Curve in the Regularization of Discrete Ill-Posed Problems, *SIAM Journal on Scientific Computing*, **14**(6), 1487–17, Copyright - Copyright] © 1993 Society for Industrial and Applied Mathematics; Last updated - 2012-06-29. → pages 51, 131
- Harder, M., Smith, B. S., Hetman, C., & Pell, J., 2009. The evolution of geological models for the DO-27 kimberlite, NWT, Canada: Implications for evaluation, *Lithos*, **112**, 61 – 72, Proceedings of the 9th International Kimberlite Conference. → pages 160, 162, 195
- Heagy, L. J., Cockett, R., Kang, S., Rosenkjaer, G. K., & Oldenburg, D. W., 2017. A framework for simulation and inversion in electromagnetics, *Computers & Geosciences*, **107**, 1–19. → pages 102, 136, 240, 262
- Hestenes, M. R. & Stiefel, E., 1952. Methods of conjugate gradients for solving linear systems, *Journal of Research of NIST*, **49**(6), 409–436. → page 51
- Holland, K., Jolly, I., McEwan, K., White, M., Berens, V., Souter, N., & Osmond, G., 2008. The 'Bookpurnong Experiment': will groundwater management and flooding improve the health of the floodplain vegetation?, in *2nd International Salinity Forum; 31 March - 3 April 2008*. → page 102
- Hoversten, G. M., Cassassuce, F., Gasperikova, E., Newman, G. A., Chen, J., Rubin, Y., Hou, Z., & Vasco, D., 2006. Direct reservoir parameter estimation using joint inversion of marine seismic AVA and CSEM data, *Geophysics*, **71**(3), C1–C13. → page 11

- Ising, E., 1925. Beitrag zur theorie des ferromagnetismus, *Zeitschrift für Physik*, **31**(1), 253–258. → pages 230, 233
- Işın, A., Direkoğlu, C., & Şah, M., 2016. Review of MRI-based Brain Tumor Image Segmentation Using Deep Learning Methods, *Procedia Computer Science*, **102**, 317 – 324, 12th International Conference on Application of Fuzzy Systems and Soft Computing, ICAFS 2016, 29-30 August 2016, Vienna, Austria. → page 229
- Jansen, J. & Witherly, K., 2004. The Tli Kwi Cho kimberlite complex, Northwest Territories, Canada: A geophysical case study, in *2004 SEG Annual Meeting*. → pages 3, 116, 136, 137, 164
- Jaynes, E. T., 2003. *Probability Theory: The Logic of Science*, Cambridge University Press. → page 27
- Jegen, M. D., Hobbs, R. W., Tarits, P., & Chave, A., 2009. Joint inversion of marine magnetotelluric and gravity data incorporating seismic constraints: Preliminary results of sub-basalt imaging off the Faroe Shelf, *Earth and Planetary Science Letters*, **282**(1-4), 47–55. → page 10
- Jessell, M., Aillères, L., Kemp, E. d., Lindsay, M., Wellmann, F., Hillier, M., Laurent, G., Carmichael, T., & Martin, R., 2014. Next Generation Three-Dimensional Geologic Modeling and Inversion, in *Building Exploration Capability for the 21st Century*, Society of Economic Geologists. → page 237
- Ju, Z. & Liu, H., 2012. Fuzzy Gaussian mixture models, *Pattern Recognition*, **45**(3), 1146–1158. → page 223
- Kadiyala, K. R. & Murthy, K. S. R., 1977. Estimation of Regression Equation with Cauchy Disturbances, *The Canadian Journal of Statistics / La Revue Canadienne de Statistique*, **5**(1), 111–120. → page 167
- Kamm, J., Lundin, I. A., Bastani, M., Sadeghi, M., & Pedersen, L. B., 2015. Joint inversion of gravity, magnetic, and petrophysical data — A case study from a gabbro intrusion in Boden, Sweden, *Geophysics*, **80**(5), B131–B152. → page 10
- Kang, S., Cockett, R., Heagy, L. J., & Oldenburg, D. W., 2015. Moving between dimensions in electromagnetic inversions, in *SEG Technical Program Expanded Abstracts 2015*, pp. 5000–5004. → pages 58, 265

- Kang, S., Fournier, D., & Oldenburg, D. W., 2017a. Inversion of airborne geophysics over the DO-27/DO-18 kimberlites — Part 3: Induced polarization, *Interpretation*, **5**(3), T327–T340. → pages 3, 10, 158, 164, 173
- Kang, S., Heagy, L. J., Cockett, R., & Oldenburg, D. W., 2017b. Exploring nonlinear inversions: A 1D magnetotelluric example, *The Leading Edge*, **36**(8), 696–699. → page 85
- Kang, S., Heagy, L. J., Cockett, R., & Oldenburg, D. W., 2018. SimPEG-EM1D: Gradient-Based 1D Inversion Software for Large-Scale Airborne Electromagnetic Data, in *2018 AGU Fall Meeting*, American Geophysical Union. → pages 102, 240
- Keating, P. & Sailhac, P., 2004. Use of the analytic signal to identify magnetic anomalies due to kimberlite pipes, *Geophysics*, **69**(1), 180–190. → page 164
- Kjarsgaard, B. & Levinson, A., 2002. Diamonds in Canada, *Gems & Gemology*, **38**, 208–238. → page 160
- Kjarsgaard, B. A., 2007. Kimberlite Pipe Models: Significance for Exploration, in *Proceedings of Exploration 07: Fifth Decennial International Conference on Mineral Exploration*, pp. 667–677. → page 162
- Koenigsberger, J. G., 1938. Natural residual magnetism of eruptive rocks, *Terrestrial Magnetism and Atmospheric Electricity*, **43**(3), 299–320. → page 175
- Latham, A. G., Harding, K. L., Lapointe, P., Morris, W. A., & Balch, S. J., 1989. On the lognormal distribution of oxides in igneous rocks, using magnetic susceptibility as a proxy for oxide mineral concentration, *Geophysical Journal International*, **96**(1), 179–184. → page 176
- Lee, C.-H., Schmidt, M., Murtha, A., Bistriz, A., Sander, J., & Greiner, R., 2005. Segmenting brain tumors with conditional random fields and support vector machines, in *Computer Vision for Biomedical Image Applications*, pp. 469–478, Springer Berlin Heidelberg, Berlin, Heidelberg. → page 229
- Lee, J. B., 2001. Falcon Gravity Gradiometer Technology, *Exploration Geophysics*, **32**(3-4), 247–250. → pages 164, 168

- Lelièvre, P. G. & Farquharson, C. G., 2016. Integrated Imaging for Mineral Exploration, in *Integrated Imaging of the Earth*, chap. 8, pp. 137–166, American Geophysical Union (AGU). → page 10
- Lelièvre, P. G. & Oldenburg, D. W., 2009a. A comprehensive study of including structural orientation information in geophysical inversions, *Geophysical Journal International*, **178**(2), 623–637. → page 239
- Lelièvre, P. G. & Oldenburg, D. W., 2009b. A 3D total magnetization inversion applicable when significant, complicated remanence is present, *Geophysics*, **74**(3), L21–L30. → pages 169, 171
- Lelièvre, P. G., Oldenburg, D. W., & Williams, N. C., 2009. Integrating geological and geophysical data through advanced constrained inversions, *Exploration Geophysics*, **40**(4), 334–341. → pages 8, 42, 55, 79, 129
- Lelièvre, P. G., Farquharson, C. G., & Hurich, C. A., 2012. Joint inversion of seismic traveltimes and gravity data on unstructured grids with application to mineral exploration, *Geophysics*, **77**(1), K1–K15. → pages 8, 12, 132, 133
- Lensink, K., Haber, E., & Peters, B., 2019. Fully hyperbolic convolutional neural networks. → page 229
- Li, S. Z., 2001. *Markov Random Field Modeling in Image Analysis*, Springer-Verlag, Berlin, Heidelberg. → page 229
- Li, Y. & Oldenburg, D. W., 1994. Inversion of 3-D DC resistivity data using an approximate inverse mapping, *Geophysical Journal International*, **116**(3), 527–537. → page 3
- Li, Y. & Oldenburg, D. W., 1996. 3-D inversion of magnetic data, *Geophysics*, **61**(2), 394–408. → pages 3, 111, 139, 166, 258
- Li, Y. & Oldenburg, D. W., 1998. 3-D inversion of gravity data, *Geophysics*, **63**(1), 109–119. → pages 3, 111, 139
- Li, Y. & Oldenburg, D. W., 1999. 3-D inversion of DC resistivity data using an L-curve criterion, in *SEG Technical Program Expanded Abstracts 1999*, pp. 251–254. → page 52
- Li, Y. & Oldenburg, D. W., 2000. Incorporating geological dip information into geophysical inversions, *Geophysics*, **65**(1), 148–157. → page 8

- Li, Y., Melo, A., Martinez, C., & Sun, J., 2019. Geology differentiation: A new frontier in quantitative geophysical interpretation in mineral exploration, *The Leading Edge*, **38**(1), 60–66. → pages 10, 56, 83, 109, 115, 118, 164
- Linde, N., Renard, P., Mukerji, T., & Caers, J., 2015. Geological realism in hydrogeological and geophysical inverse modeling: A review, *Advances in Water Resources*, **86**, 86 – 101. → pages 8, 237
- Lochbühler, T., Vrugt, J. A., Sadegh, M., & Linde, N., 2015. Summary statistics from training images as prior information in probabilistic inversion, *Geophysical Journal International*, **201**(1), 157–171. → page 8
- Maag, E. & Li, Y., 2018. Discrete-valued gravity inversion using the guided fuzzy c-means clustering technique, *Geophysics*, **83**(4), G59–G77. → page 222
- Macnae, J., 1995. Applications of geophysics for the detection and exploration of kimberlites and lamproites, *Journal of Geochemical Exploration*, **53**(1), 213 – 243, Diamond Exploration: Into the 21st Century. → page 164
- Martinez, C. & Li, Y., 2015. Lithologic characterization using airborne gravity gradient and aeromagnetic data for mineral exploration: A case study in the Quadrilátero Ferrífero, Brazil, *Interpretation*, **3**(2), SL1–SL13. → page 10
- McGillivray, P. R. & Oldenburg, D. W., 1990. Methods for calculating Fréchet derivatives and sensitivities for the non-linear inverse problem: a comparative study, *Geophysical Prospecting*, **38**(5), 499–524. → page 49
- McMillan, M. S., Schwarzbach, C., Haber, E., & Oldenburg, D. W., 2015. 3D parametric hybrid inversion of time-domain airborne electromagnetic data, *Geophysics*, **80**(6), K25–K36. → pages 3, 7
- Mehanee, S., Golubev, N., & Zhdanov, M. S., 2005. Weighted regularized inversion of magnetotelluric data, in *SEG Technical Program Expanded Abstracts 1998*, pp. 481–484. → pages 94, 111
- Meju, M. A. & Gallardo, L. A., 2016. Structural Coupling Approaches in Integrated Geophysical Imaging, in *Integrated Imaging of the Earth*, chap. 4, pp. 49–67, American Geophysical Union (AGU). → page 11

- Melo, A. T., Sun, J., & Li, Y., 2017. Geophysical inversions applied to 3D geology characterization of an iron oxide copper-gold deposit in Brazil, *Geophysics*, **82**(5), K1–K13. → page 10
- Moorkamp, M., Heincke, B., Jegen, M., Roberts, A. W., & Hobbs, R. W., 2011. A framework for 3-D joint inversion of MT, gravity and seismic refraction data, *Geophysical Journal International*, **184**(1), 477–493. → pages 11, 131
- Moorkamp, M., Heincke, B., Jegen, M., Hobbs, R. W., & Roberts, A. W., 2016a. Joint inversion in hydrocarbon exploration, in *Integrated Imaging of the Earth*, chap. 9, pp. 167–189, American Geophysical Union (AGU). → page 12
- Moorkamp, M., Lelièvre, P. G., Linde, N., & Khan, A., 2016b. *Integrated Imaging of the Earth: Theory and Applications*, American Geophysical Union (AGU). → pages 8, 10
- Mosegaard, K. & Tarantola, A., 1995. Monte Carlo sampling of solutions to inverse problems, *Journal of Geophysical Research: Solid Earth*, **100**(B7), 12431–12447. → page 53
- Murphy, K. P., 2012. *Machine Learning: A Probabilistic Perspective*, The MIT Press. → pages 26, 27, 36, 60, 152, 165, 230, 234
- Nguyen, T. M. & Wu, Q. M. J., 2013. Fast and Robust Spatially Constrained Gaussian Mixture Model for Image Segmentation, *Circuits and Systems for Video Technology, IEEE Transactions on*, **23**, 621–635. → pages xxxvii, 229, 230, 231
- Nocedal, J. & Wright, S. J., 2006. *Numerical Optimization*, Springer, New York, NY, USA, 2nd edn. → page 52
- Oldenburg, D. W. & Li, Y., 1999. Estimating depth of investigation in DC resistivity and IP surveys, *Geophysics*, **64**(2), 403–416. → pages xxii, 103, 107
- Oldenburg, D. W. & Li, Y., 2005. Inversion for Applied Geophysics: A Tutorial, in *Near-Surface Geophysics*, chap. 5, pp. 89–150, ed. Butler, D. K., Society of Exploration Geophysicists. → pages 2, 41, 79, 102, 129
- Oldenburg, D. W., Li, Y., & Ellis, R. G., 1997. Inversion of geophysical data over a copper gold porphyry deposit: A case history for Mt. Milligan, *Geophysics*, **62**(5), 1419–1431. → page 10

- Oldenburg, D. W., Heagy, L. J., Kang, S., & Cockett, R., 2019. 3D electromagnetic modelling and inversion: a case for open source, *Exploration Geophysics*, **0**(0), 1–13. → page 240
- Onizawa, S., Mikada, H., Watanabe, H., & Sakashita, S., 2002. A method for simultaneous velocity and density inversion and its application to exploration of subsurface structure beneath Izu-Oshima volcano, Japan, *Earth, Planets and Space*, **54**(8), 803–817. → pages 117, 158
- Paasche, H., 2016. Post-Inversion Integration of Disparate Tomographic Models by Model Structure Analyses, in *Integrated Imaging of the Earth*, chap. 5, pp. 69–91, American Geophysical Union (AGU). → page 10
- Paasche, H. & Tronicke, J., 2007. Cooperative inversion of 2D geophysical data sets: A zonal approach based on fuzzy c-means cluster analysis, *Geophysics*, **72**(3), A35–A39. → pages 8, 12
- Paasche, H., Tronicke, J., Holliger, K., Green, A. G., & Maurer, H., 2006. Integration of diverse physical-property models: Subsurface zonation and petrophysical parameter estimation based on fuzzy c -means cluster analyses, *Geophysics*, **71**(3), H33–H44. → page 10
- Parker, R. L., 1977. Understanding Inverse Theory, *Annual Review of Earth and Planetary Sciences*, **5**(1), 35–64. → pages 41, 48, 51, 76, 170
- Pawlowski, B., 1998. Gravity gradiometry in resource exploration, *The Leading Edge*, **17**(1), 51–52. → page 168
- Pearson, K., 1900. On the criterion that a given system of deviations from the probable in the case of a correlated system of variables is such that it can be reasonably supposed to have arisen from random sampling, *The London, Edinburgh, and Dublin Philosophical Magazine and Journal of Science*, **50**(302), 157–175. → pages 48, 123
- Pedregosa, F., Varoquaux, G., Gramfort, A., Michel, V., Thirion, B., Grisel, O., Blondel, M., Prettenhofer, P., Weiss, R., Dubourg, V., Vanderplas, J., Passos, A., Cournapeau, D., Brucher, M., Perrot, M., & Duchesnay, E., 2011. Scikit-learn: Machine Learning in Python, *Journal of Machine Learning Research*, **12**, 2825–2830. → pages 239, 267

- Perez, F., Berkeley, L., & Granger, B. E., 2015. Project Jupyter : Computational Narratives as the Engine of Collaborative Data Science, (April), 1–24. → pages 84, 240
- Portniaguine, O. & Zhdanov, M. S., 2002. 3-D magnetic inversion with data compression and image focusing, *Geophysics*, **67**(5), 1532–1541. → page 139
- Power, M. & Hildes., D., 2007. Geophysical strategies for kimberlite exploration in northern Canada, in *Proceedings of Exploration '07: Fifth Decennial International Conference on Mineral Exploration*, pp. 1025–1031. → page 164
- Raiffa, H. & Schlaifer, R., 1961. *Applied statistical decision theory*, Studies in managerial economics, Division of Research, Graduate School of Business Administration, Harvard University. → pages 28, 67
- Rapstine, T., Li, Y., & Sun, J., 2016. Integrating a spatial salt likelihood map and prior petrophysical data into a gravity gradiometry inversion through fuzzy c-means clustering, in *SEG Technical Program Expanded Abstracts 2016*, pp. 1622–1626. → pages 221, 222
- Rauen, A., Soffel, H. C., & Winter, H., 2000. Statistical analysis and origin of the magnetic susceptibility of drill cuttings from the 9.1-km-deep KTB drill hole, *Geophysical Journal International*, **142**(1), 83–94. → page 176
- Rother, C., Kolmogorov, V., & Blake, A., 2004. "GrabCut": Interactive Foreground Extraction Using Iterated Graph Cuts, in *ACM SIGGRAPH 2004 Papers*, SIGGRAPH '04, pp. 309–314, ACM, New York, NY, USA. → page 229
- Sambridge, M. & Mosegaard, K., 2002. Monte Carlo Methods in Geophysical Inverse Problems, *Reviews of Geophysics*, **40**(3), 3–1–3–29. → page 53
- Santos, E. & Bassrei, A., 2007. L- and Θ -curve approaches for the selection of regularization parameter in geophysical diffraction tomography, *Computers & Geosciences*, **33**(5), 618 – 629. → pages 51, 131
- Schmidt, M., Levner, I., Greiner, R., Murtha, A., & Bistritz, A., 2005. Segmenting brain tumors using alignment-based features, in *Fourth International Conference on Machine Learning and Applications (ICMLA'05)*, pp. 6 pp.–. → page 229

- Shamsipour, P., Marcotte, D., & Chouteau, M., 2012. 3D stochastic joint inversion of gravity and magnetic data, *Journal of Applied Geophysics*, **79**, 27 – 37. → page 12
- Singh, A. & Sharma, S., 2018. Identification of different geologic units using fuzzy constrained resistivity tomography, *Journal of Applied Geophysics*, **148**, 127 – 138. → page 222
- Singh, A., Sharma, S. P., Akca, İ., & Baranwal, V. C., 2018. Fuzzy constrained L_p -norm inversion of direct current resistivity data, *Geophysics*, **83**(1), E11–E24. → page 222
- Sosa, A., Velasco, A. A., Velazquez, L., Argaez, M., & Romero, R., 2013. Constrained optimization framework for joint inversion of geophysical data sets, *Geophysical Journal International*, **195**(3), 1745–1762. → page 131
- Sun, J. & Li, Y., 2015. Multidomain petrophysically constrained inversion and geology differentiation using guided fuzzy c-means clustering, *Geophysics*, **80**(4), ID1. → pages 8, 12, 14, 66, 67, 111, 112, 114, 115, 220, 221, 222
- Sun, J. & Li, Y., 2016. Joint inversion of multiple geophysical data using guided fuzzy c-means clustering, *Geophysics*, **81**(3), ID37–ID57. → pages 12, 14, 116, 131, 157, 220, 221, 222
- Sun, J. & Li, Y., 2017. Joint inversion of multiple geophysical and petrophysical data using generalized fuzzy clustering algorithms, *Geophysical Journal International*, **208**(2), 1201–1216. → pages 11, 12, 14, 116, 131, 220, 221, 222
- Sun, J. & Li, Y., 2018. Magnetization clustering inversion — Part 1: Building an automated numerical optimization algorithm, *Geophysics*, **83**(5), J61–J73. → page 111
- Tarantola, A., 2005. *Inverse Problem Theory and Methods for Model Parameter Estimation*, vol. 89, siam. → pages 3, 23, 43, 123
- Tikhonov, A. N. & Arsenin, V. Y., 1977. *Solutions of ill-posed problems*, V. H. Winston & Sons, Washington, D.C.: John Wiley & Sons, New York, Translated from the Russian, Preface by translation editor Fritz John, Scripta Series in Mathematics. → page 5

- Viezzoli, A., Christiansen, A. V., Auken, E., & Sørensen, K., 2008. Quasi-3D modeling of airborne TEM data by spatially constrained inversion, *Geophysics*, **73**(3), F105–F113. → page 102
- Viezzoli, A., Auken, E., & Munday, T., 2009. Spatially constrained inversion for quasi 3D modelling of airborne electromagnetic data – an application for environmental assessment in the Lower Murray Region of South Australia, *Exploration Geophysics*, **40**(2), 173–183. → pages 100, 109
- Viezzoli, A., Munday, T., Auken, E., & Christiansen, A. V., 2010. Accurate quasi 3D versus practical full 3D inversion of AEM data – the Bookpurnong case study, *Preview*, **2010**(149), 23–31. → pages 100, 109
- Wahba, G., 1990. Spline models for observational data, *Regional Conference Series in Applied Mathematics*, **59**. → page 51
- Wang, H., Wellmann, J. F., Li, Z., Wang, X., & Liang, R. Y., 2017. A segmentation approach for stochastic geological modeling using hidden markov random fields, *Mathematical Geosciences*, **49**(2), 145–177. → page 229
- Ward, S. H. & Hohmann, G. W., 1988. Electromagnetic Theory for Geophysical Applications, in *Electromagnetic Methods in Applied Geophysics*, chap. 4, pp. 130–311. → pages 84, 85, 100
- Williams, N. C., 2006. Applying UBC-GIF potential field inversions in greenfields or brownfields exploration, in *Proceedings of the Australian Earth Sciences Convention. ASEG/GSA.* → page 129
- Williams, N. C., 2008. *Geologically-constrained UBC-GIF gravity and magnetic inversions with examples from the Agnew-Wiluna greenstone belt, Western Australia*, Ph.D. thesis, University of British Columbia. → pages 8, 42, 79, 129
- Witherly, K., 2005. Report on VTEM test program over three kimberlites, Lac de Gras area, Northwest Territories, Canada, Technical report, Condor Consulting. → page 164
- Wu, X., 2017. Structure-, stratigraphy- and fault-guided regularization in geophysical inversion, *Geophysical Journal International*, **210**(1), 184–195. → page 8

- Xu, Z., Wan, L., Han, M., Zhdanov, M. S., & Mao, Y., 2019. Joint inversion of gravity gradiometry data by model-weighted clustering in logarithmic space, in *SEG Technical Program Expanded Abstracts 2019*, pp. 1779–1783. → page 222
- Yan, P., Kalscheuer, T., Hedin, P., & Garcia Juanatey, M. A., 2017. Two-dimensional magnetotelluric inversion using reflection seismic data as constraints and application in the COSC project, *Geophysical Research Letters*, **44**(8), 3554–3563. → page 239
- Yang, D., 2017. Airborne electromagnetic data inversion for floodplain salinization investigation at Bookpurnong, South Australia, https://figshare.com/articles/Airborne_electromagnetic_data_inversion_for_floodplain_salinization_investigation_at_Bookpurnong_South_Australia/5071573”, Accessed: 2019-02-01. → pages 100, 109
- Zhdanov, M. S. & Lin, W., 2017. Adaptive multinary inversion of gravity and gravity gradiometry data, *Geophysics*, **82**(6), G101–G114. → pages 8, 220, 221, 227

Appendix A

Working with nonlinear petrophysical relationships

While linear trends can be accounted through the covariance matrix to obtain elongated clusters, it is also possible to account for nonlinear relationships between physical properties in my framework (Figure A.1). This is achieved by composing the Gaussian function with the nonlinear relationship P_j between the physical properties of the particular rock unit j . For each rock unit j in the GMM in equation (3.8), this corresponds to using $\mathcal{N}(P_j(\mathbf{m}_i)|\boldsymbol{\mu}_j, \mathbf{W}_i^{-1}\boldsymbol{\Sigma}_j\mathbf{W}_i^{-1})$.

In this section, I present a joint inversion of two linear problems whose respective physical properties have nonlinear petrophysical relationships between each other. For simplicity, the physics of the two problems are the same and is based on the examples previously used in Li & Oldenburg (1996). The models are discretized on a 1D mesh defined on the interval $[0, 1]$ and divided into 100 cells.

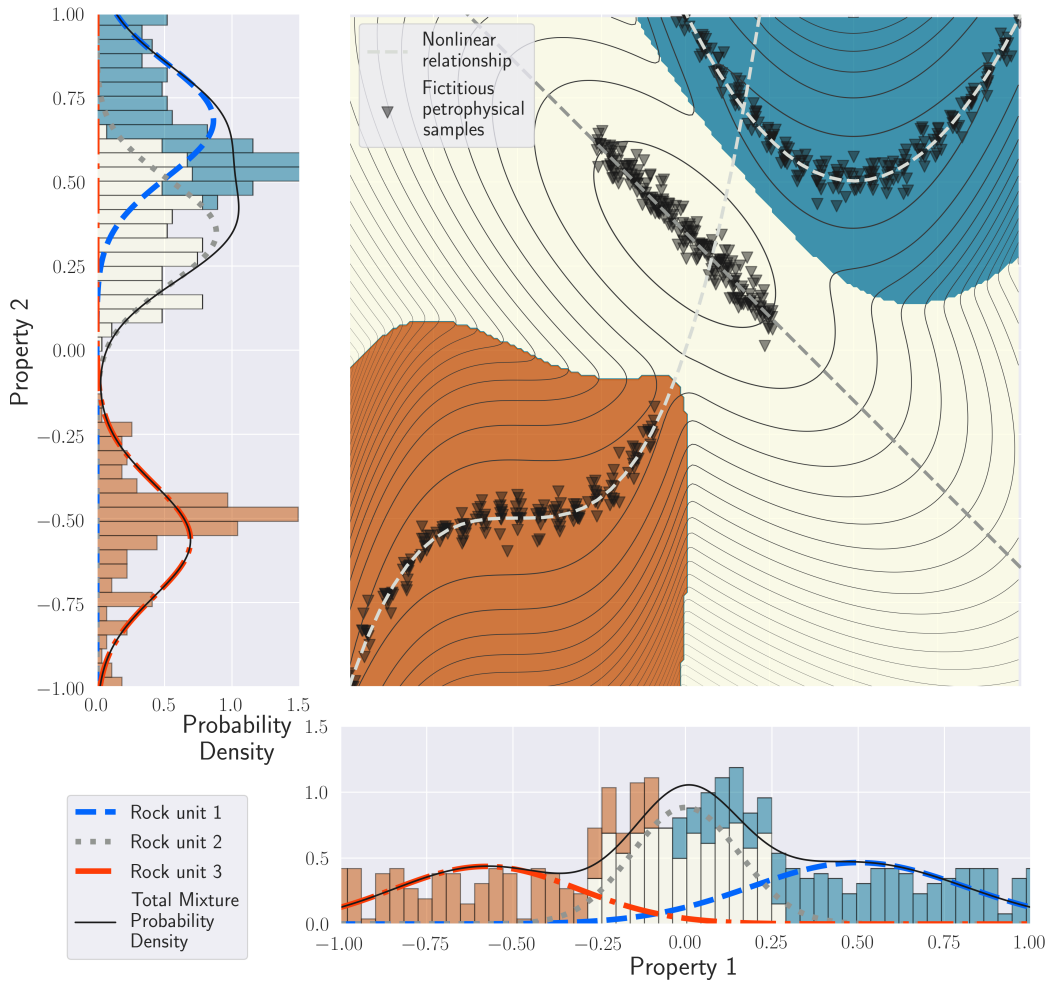


Figure A.1: GMM with various polynomial relationships: one linear (no addition required), one quadratic and one cubic. The 1D probability distribution for each physical property, and the respective histogram of each unit, are projected on the left and bottom panels.

Both datasets consist of 30 data points at various frequencies equally distributed from 1 to 59 evaluated according to:

$$d_j = \int_0^1 e^{-jx} \cos(2\pi jx) m(x) dx, \quad j = 1, 3, \dots, 59. \quad (\text{A.1})$$

Each model presents three distinct units. The background for both models is set to 0 while the two other units are linked through a quadratic and a cubic relationship respectively.

I inverted the two datasets using the multi-physics PGI framework, including *a priori* knowledge of the petrophysical distributions and relationships. The result can be seen in the first row of Figure A.2 (panels A.2a to A.2c). Note that the petrophysical relationships are well reproduced. This allows the recovery of details of the two models.

For comparison, I also jointly inverted the datasets but without the polynomial relationships (by merely fitting a Gaussian distribution to each unit). The result can be seen in the second row of Figure A.2 (panels A.2d to A.2f). While the overall structures are well recovered, I miss some details of the models. The background is not as flat as with the full information, the lower tip of the model of problem 2 is completely missed.

I also inverted both datasets individually using the classic Tikhonov inversion. The result is shown in the last row of Figure A.2 (panels A.2g to A.2i). The models are smoother, as expected. The background presents even more variations, but the overall structures are recovered. Same as for the joint inversion without the polynomial relationships, the details are missing.

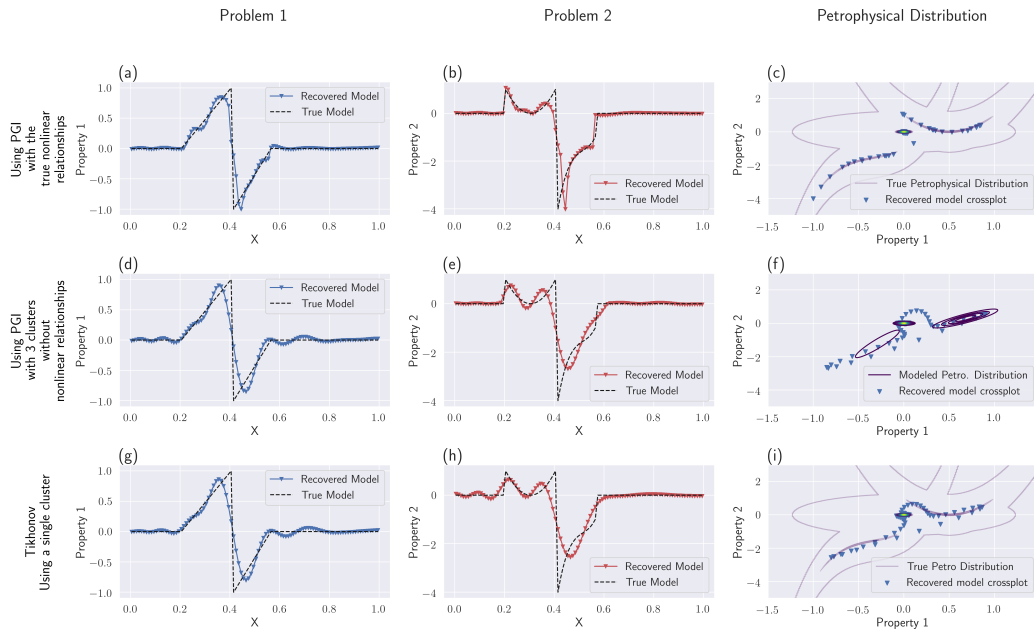


Figure A.2: Linear joint inversions with various types of physical properties relationships (no trend, quadratic, cubic). Panels (a) to (c) show the inversion result with PGI using the known nonlinear relationships. The first panel (a) shows the result for the first problem, (b) for the second problem. The panel (c) shows the cross-plot of the models over the contour of the GMM with nonlinear relationships. Panels (d) to (f) show the result with PGI without nonlinear relationships. In panel (f), I show the used GMM without nonlinear relationships. Panels (g) to (i) show the Tikhonov inversions results and their cross-plot.

Appendix B

Numerical implementation

B.1 Integration within SimPEG

The PGI framework is implemented as part of the open-source SIMPEG (Simulation and Parameter Estimation in Geophysics) project (Cockett et al., 2015; Heagy et al., 2017). SIMPEG is designed to be a modular, extensible framework for simulations and inversions of geophysical data. In particular, two features enabled me to focus my implementation efforts on the PGI framework, while using tools provided by the open-source community (such as the forward operators etc.):

1. the composability of objective functions in the data misfit and the regularization terms,
2. the use of `directives` which orchestrate updates to components of the inversion at each iteration.

The first point enables the implementation of joint inversions. In the code,

each misfit term is a Python object that has properties, such as the weights used to construct \mathbf{W}_d , and methods, including functions to evaluate the misfit given a model as well as derivatives for use in the optimization routines. To construct a joint inversion with gravity and magnetic data, I first define each misfit term independently and then sum them. I use operator-overloading in Python so that when I express the addition of two objective functions in code, the evaluation of this creates a `combo-objective` function. This is an object that has the same evaluation and derivative methods as the individual data misfits, and thus readily inter-operates with the rest of the simulation and inversion machinery in SIMPEG.

To the second point, `directives` are functions that are evaluated at the beginning or end of each iteration in the optimization. They are the mechanism I use to make updates to components of the inversion, including the data misfit scaling parameters (equation (4.23)) or smallness weights and reference model (equations (3.13) and (3.14)), as well as for evaluating the target misfits and stopping criteria for the inversion.

B.2 Pseudo-code for the implementation in SimPEG

Here, I provide a tutorial for the use of my implementation of the multi-physics PGI framework by other scientists. I outline the main components of the multi-physics PGI implementation using SIMPEG and other core tools in the Python ecosystem. As in the thesis, I consider the multi-physics inversion of gravity and

magnetic data.

I begin by creating a simulation `mesh` and defining mappings that translate the model vector, which contains all of the parameters I will invert for, to physical properties on the mesh to be used in each forward simulation. The inversion model is a single vector; for an inversion with multiple physical parameters, I stack them and use the `Wires` map to keep track of which indices in the vector correspond to each physical parameter.

```
import numpy as np
# construct a simulation mesh with discretize
import discretize
from SimPEG import maps

# model vector with size 2 * number of cells
initial_model = np.hstack([model_grav, model_mag])

# the Wires map selects the indices in the vector
# that correspond to the physical properties.
wires = maps.Wires(
    ("density", mesh.nC),
    ("susc", mesh.nC)
)
```

Note that mappings can be composed; for example if I wanted to invert for log-susceptibility rather than susceptibility, then I would compose the `wires.susc` mapping with an `ExpMap` instance. For examples, see Kang et al. (2015).

Next, I construct the forward simulations for both the gravity and magnetic data. The `survey` objects contain the locations of the receivers as well as parameters defining the source field for the magnetics simulation (magnitude, inclination, and declination).

```
from SimPEG.potential_fields import gravity
from SimPEG.potential_fields import magnetics

# construct the gravity simulation
grav_simulation = gravity.Simulation3DIntegral(
    mesh,
    map_density=wires.density,
    survey=grav_survey
)

# construct the magnetics simulation
mag_simulation = magnetics.Simulation3DIntegral(
    mesh,
    map_susc=wires.susceptibility,
    survey=mag_survey
)
```

With both gravity and magnetic simulations defined, I now have the ability to compute predicted data given a model. The next step is to construct the data misfit term as described in equation (2.62).

```
from SimPEG import data_misfit

# Construct the geophysical data misfits
phi_grav = data_misfit.L2DataMisfit(
    simulation=grav_simulation,
    data=grav_data
)
phi_mag = data_misfit.L2DataMisfit(
    simulation=mag_simulation,
    data=mag_data
)
# Combine to create the whole data misfit
phi_data = chi_grav * phi_grav + chi_mag * phi_mag
```

The `mag_data` and `grav_data` objects contain the observed data as well as user-specified uncertainties, and the scalar `chi`-values are initialized according to equation (4.25).

Next, I construct the GMM and regularization which consists the petrophysical smallness term described in equation (3.11) and smoothness terms for both the density and susceptibility. To construct the GMM, I use my implementation of

the `WeightedGaussianMixture` object, which inherits from and extends the `sklearn.mixture.GaussianMixture` object in Scikit-Learn (Pedregosa et al., 2011). The instantiated `gmm` object has methods for fitting a GMM on a model and computing membership as needed in steps 4 and 5 in Algorithm 1.

```
from SimPEG import regularization
from SimPEG.petrophysics import WeightedGaussianMixture

gmm = WeightedGaussianMixture(
    n_components=3, # number of rock units
    mesh=mesh,
    means_init=initial_means,
    covariances_init=initial_covariances,
)

pgi_smallness = regularization.Petrophysical(
    mesh=mesh,
    mref=initial_model,
    gmm_prior=gmm,
    wires_map=wires,
    cell_weights=sensitivity_weights
)
```

```

# smoothness terms are constructed using
# regularization.SmoothDeriv class
phi_m = (
    alpha_s * pgi_smallness +
    alpha_smooth_grav * smoothness_grav +
    alpha_smooth_mag * smoothness_mag
)

```

Having defined the components of the objective function, I now specify the optimization routine, in this case, an inexact Gauss-Newton with projections for bound constraints.

```

from SimPEG import optimization, inverse_problem

# Define the optimization routine and model bounds
opt = optimization.ProjectedListedGNC(
    lower_bound=lower_bound, upper_bound=upper_bound
)

# Inverse problem
inv_prob = inverse_problem.BaseInverseProblem(
    phi_d, phi_m, opt
)

```

Finally, I assemble the inversion using directives in SimPEG to orchestrate updates throughout the inversion. Directives have a `initialize` method

which is called at the beginning of the inversion and can be used to set initial values of parameters, for example to initialize β and the α -values, as well as an `end_iteration` method which is called after a model update (at the end of step 3 in Algorithm 1) and can be used to update parameters in the inversion. The updates in steps 4 through 7 in Algorithm 1 make use of the `directives` functionality.

```
from SimPEG import inversion, directives

# Inverse problem with directives
inv = inversion.BaseInversion(
    inv_prob,
    directives=[
        estimate_beta0,
        estimate_alphas,
        target_misfits,
        update_classification,
        update_regularization_weights,
        include_mref_in_smoothness, # optional
        update_geophysical_misfit_weights,
    ]
)

recovered_model = inv.run(initial_model)
```

Appendix C

**Additional models obtained by
individual PGIs for the DO-27
synthetic case study**

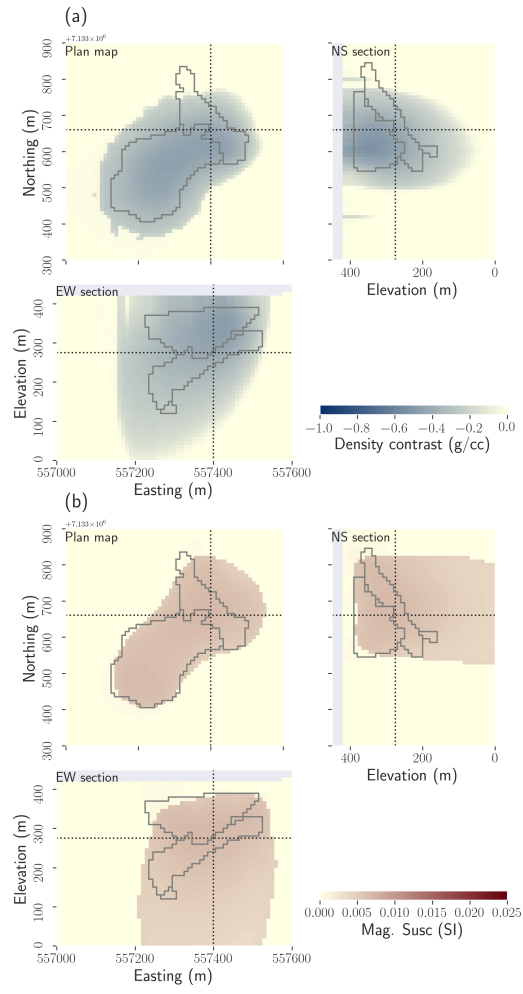


Figure C.1: (a) magnetic PGI using the magnetic signature of PK/VK. Note that the recovered volume is much larger than the volume of PK/VK recovered from the gravity inversion with this unit density contrast (Figure 4.6c); (b) gravity PGI using the density contrast signature of HK. Note again the larger volume compared to Figure 4.6d.

Appendix D

**Additional models obtained by
multi-physics PGIs with full
petrophysical information for the
DO-27 synthetic case study with
various initializations of the
geophysical data misfit scaling
parameters**

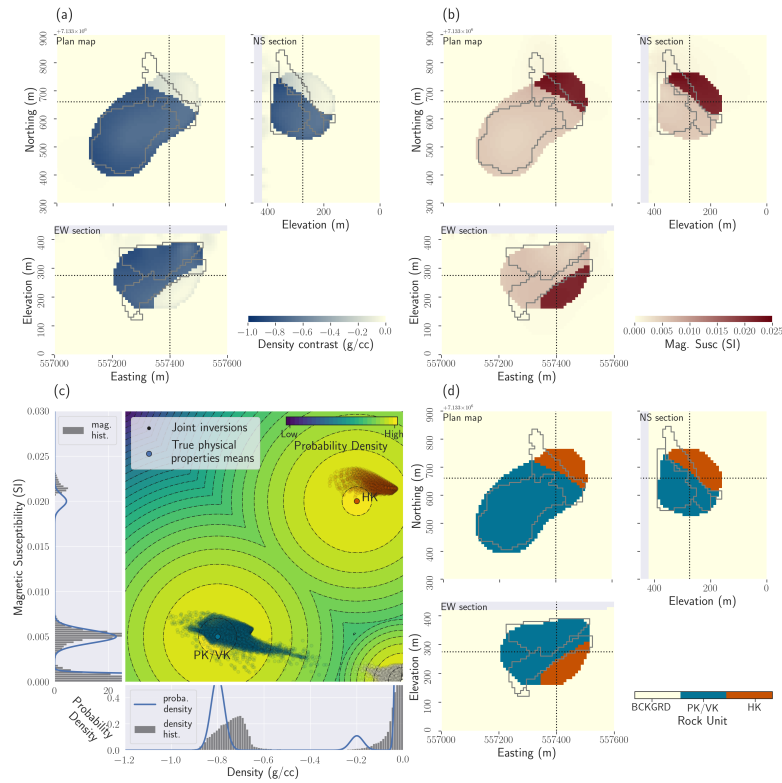


Figure D.1: Results of the multi-physics PGI with petrophysical information and initialized with $\chi_{0,grav} = 0.72$ and $\chi_{0,mag} = 0.28$. (a) Plan map, east-west, and north-south cross-sections through the recovered density contrast model; (b) Plan map, east-west, and north-south cross-sections through the magnetic susceptibility contrast model; (c) Cross-plot of the inverted models. The colour of the points has been determined by the clustering obtained from this framework joint inversion process. In the background the prior joint petrophysical distribution; (d) Plan map, east-west, and north-south cross-sections through the resulting quasi-geology model.

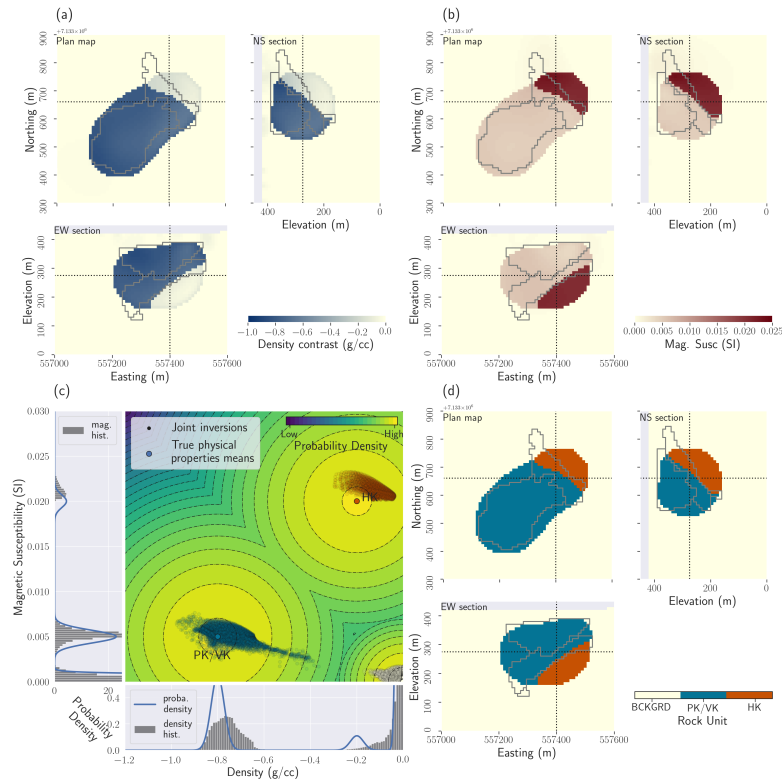


Figure D.2: Results of the multi-physics PGI with petrophysical information and initialized with $\chi_{0,\text{grav}} = 0.2$ and $\chi_{0,\text{mag}} = 0.8$. a) Plan map, east-west, and north-south cross-sections through the recovered density contrast model; b) Plan map, east-west, and north-south cross-sections through the magnetic susceptibility contrast model; c) Cross-plot of the inverted models. The colour of the points has been determined by the clustering obtained from this framework joint inversion process. In the background the prior joint petrophysical distribution; d) Plan map, east-west, and north-south cross-sections through the resulting quasi-geology model.

Appendix E

Bookpurnong: varying the confidence in the prior variances

To complete section 6.3.3, I present additional recovered models of the Bookpurnong area for various values of the confidences ν in the prior variances. In Figure E.1, low values of ν are used. In Figure E.2, high values of ν are used.

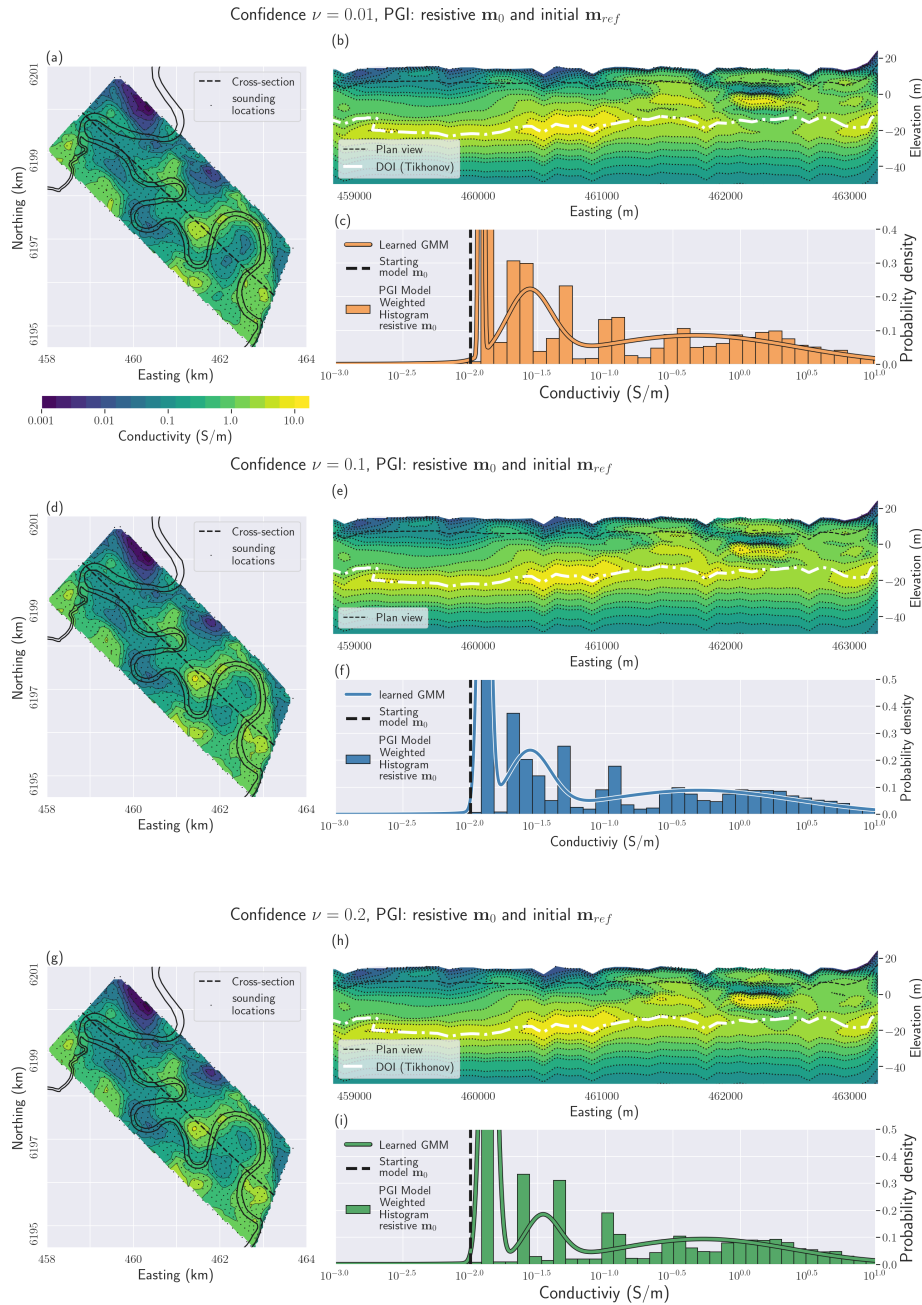


Figure E.1: PGIs results for the Bookpurnong case study using various values of the confidence parameter ν in the prior variances. $\nu = 0.01$, $\nu = 0.1$, $\nu = 0.2$.

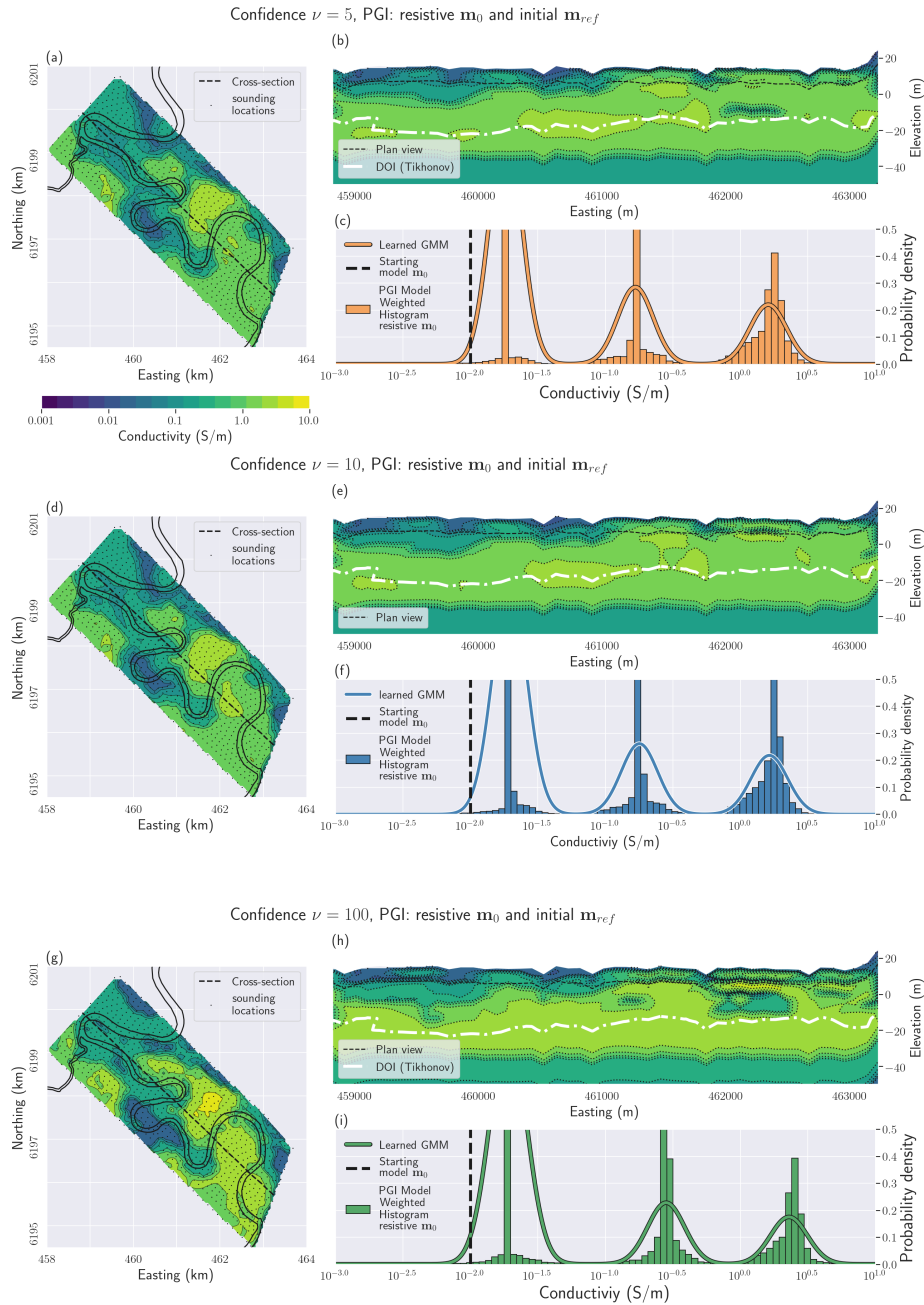


Figure E.2: PGIs results for the Bookpurnong case study for various values of the confidence parameter ν in the prior variances. $\nu = 5$, $\nu = 10$, $\nu = 100$.

Appendix F

DO-27: Choosing the characteristics of the PK-minor rock unit

Here I present the results, from gravity inversions, recovered with PGIs using various values of the PK-minor unit's characteristics for the DO-27 case study (chapter 5). Three parameters of the Gaussian distribution representing PK-minor were tested: the variance for the depth, the variance of the density contrast, and the mean of the density contrast. In each figure, one parameter is kept fixed while the two others vary along the row or column. One type of figure presents the density contrast models while the other presents the three clusters used in the GMMs for the respective inversions. Figures representing the models and those representing the GMMs share the same layout (number of rows by number of columns) to help the reader associate the models with their respective GMM. While the figures showing the GMMs present the three clusters together, the PK/VK and PK-minor

units are set to different spatial locations through the proportions of the GMMs. This actually defines two different GMMs for the North and South part of the area, respectively. I decided, however, to concatenate them in a single plot for clarity. This explains why some points of the PK-minor unit might appear misclassified (for example in Figure F.2); they are not misclassified, but the PK/VK cluster does not exist at those locations.

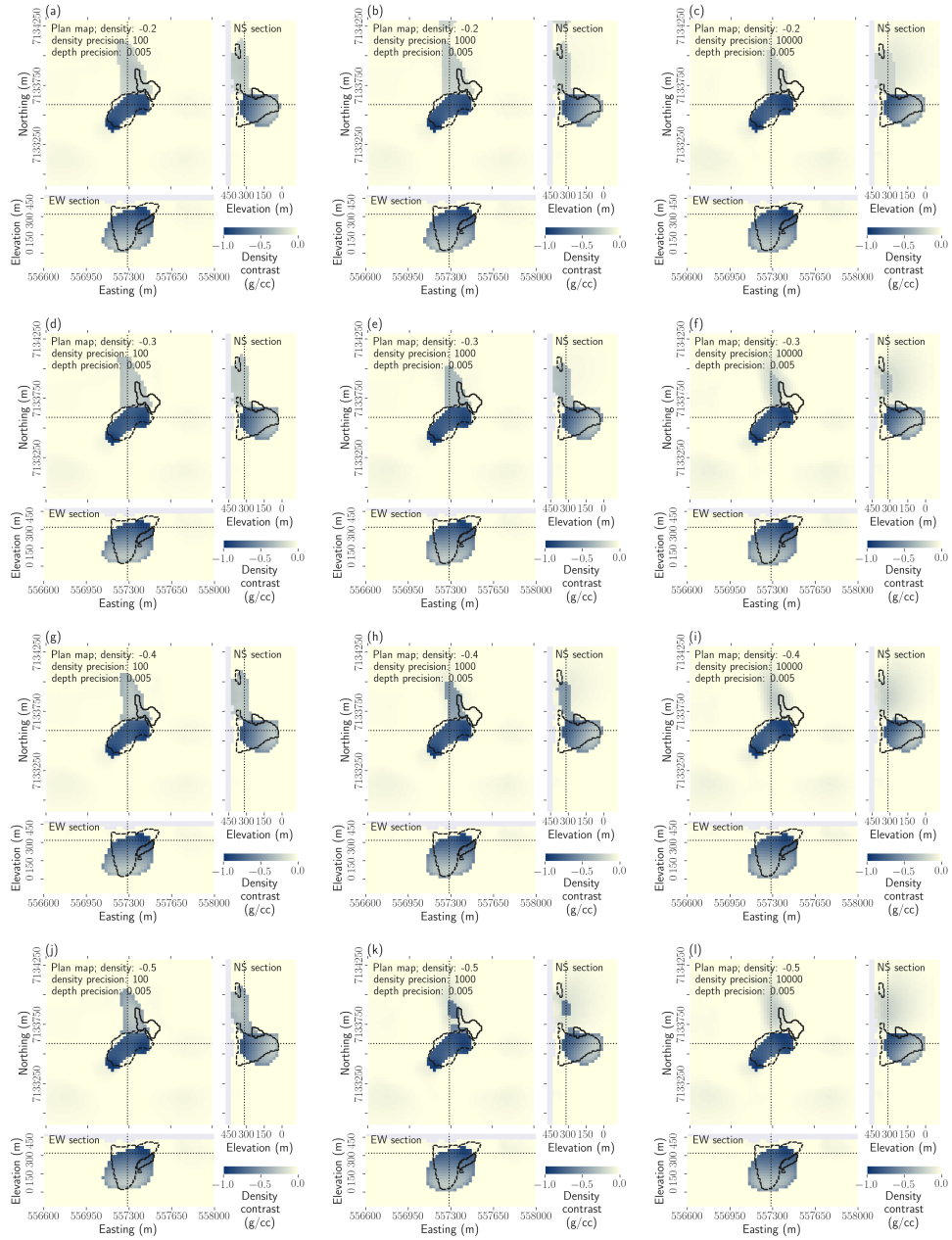


Figure F.1: Density contrast models recovered from PGIs for the DO-27 case study for various values of the mean and variance of the density contrast for the PK-minor unit. The depth variance is equal to 200 m^2 .

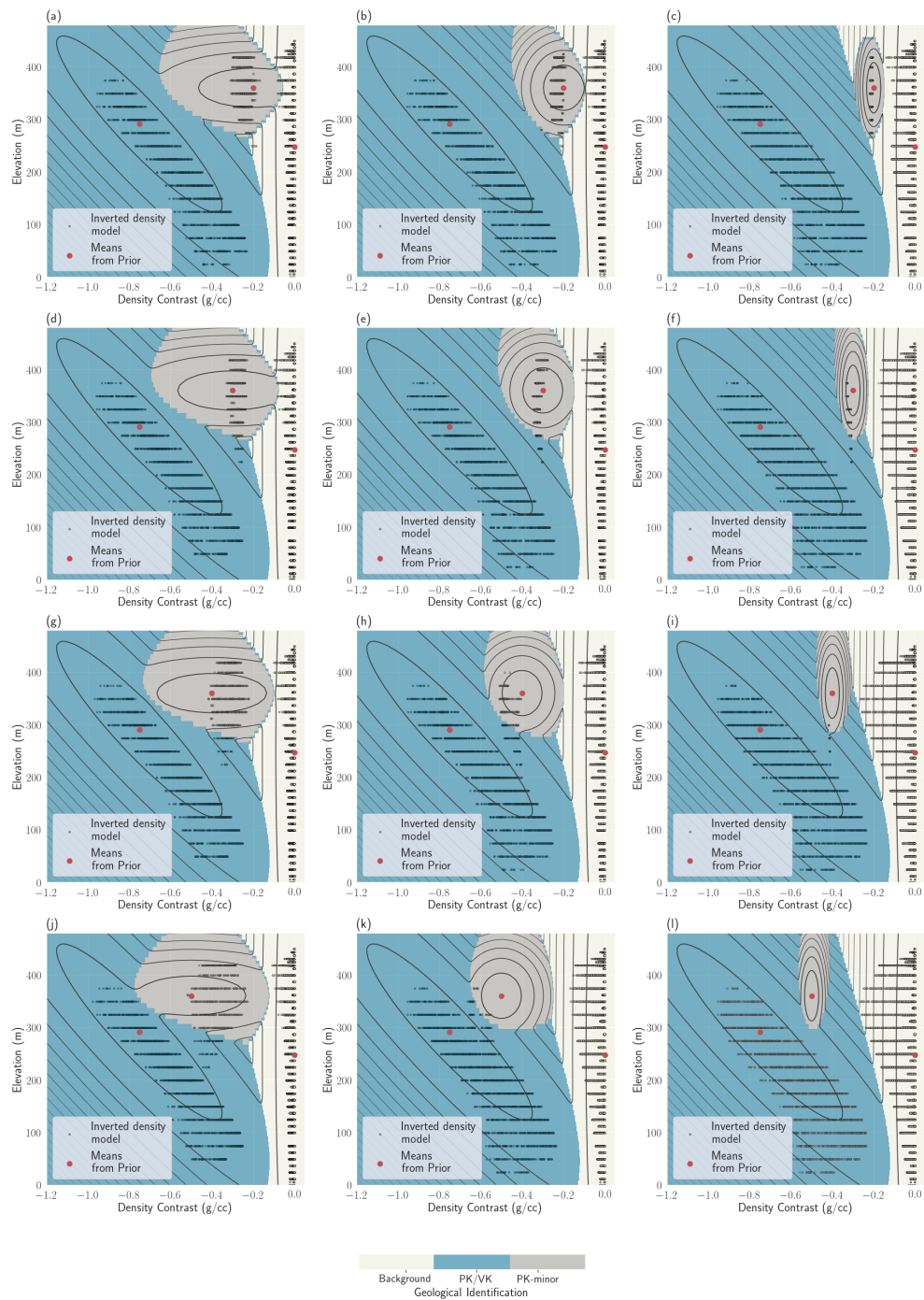


Figure F.2: GMMs used to recover the models presented in Figure F.1.

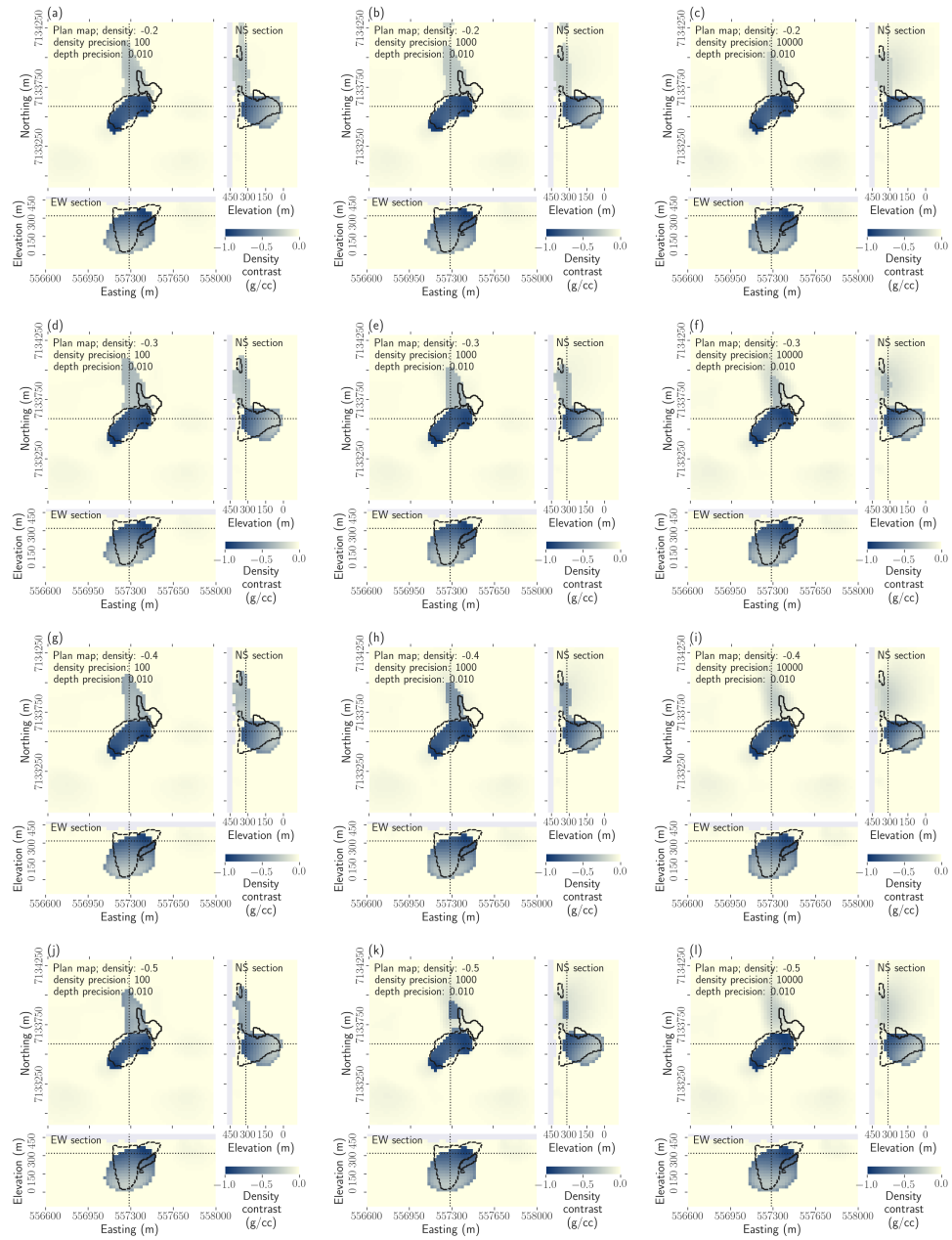


Figure F.3: Density contrast models recovered from PGIs for the DO-27 case study for various values of the mean and variance of the density contrast for the PK-minor unit. The depth variance is equal to 100 m^2 .

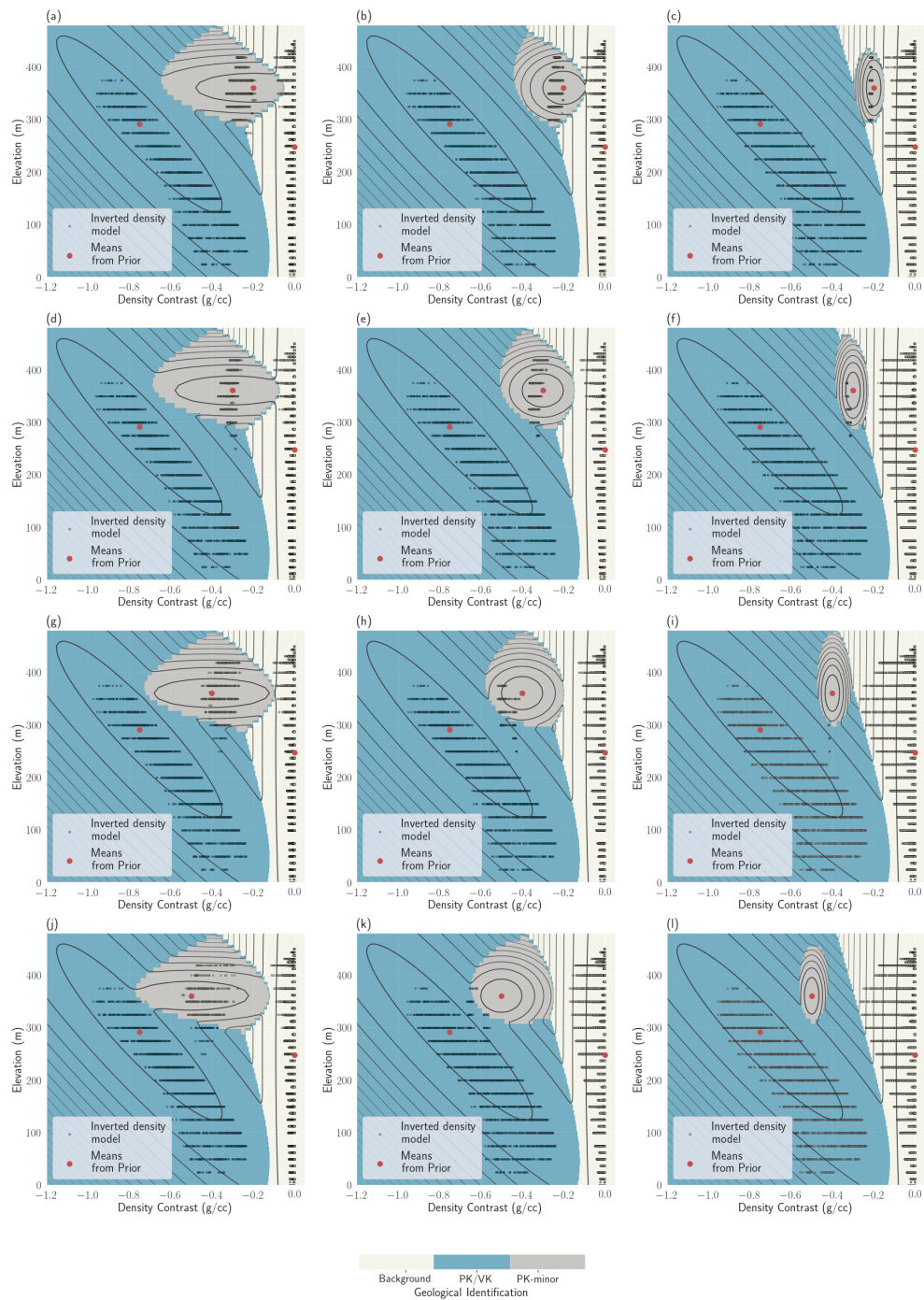


Figure F.4: GMMs used to recover the models presented in Figure F.3.

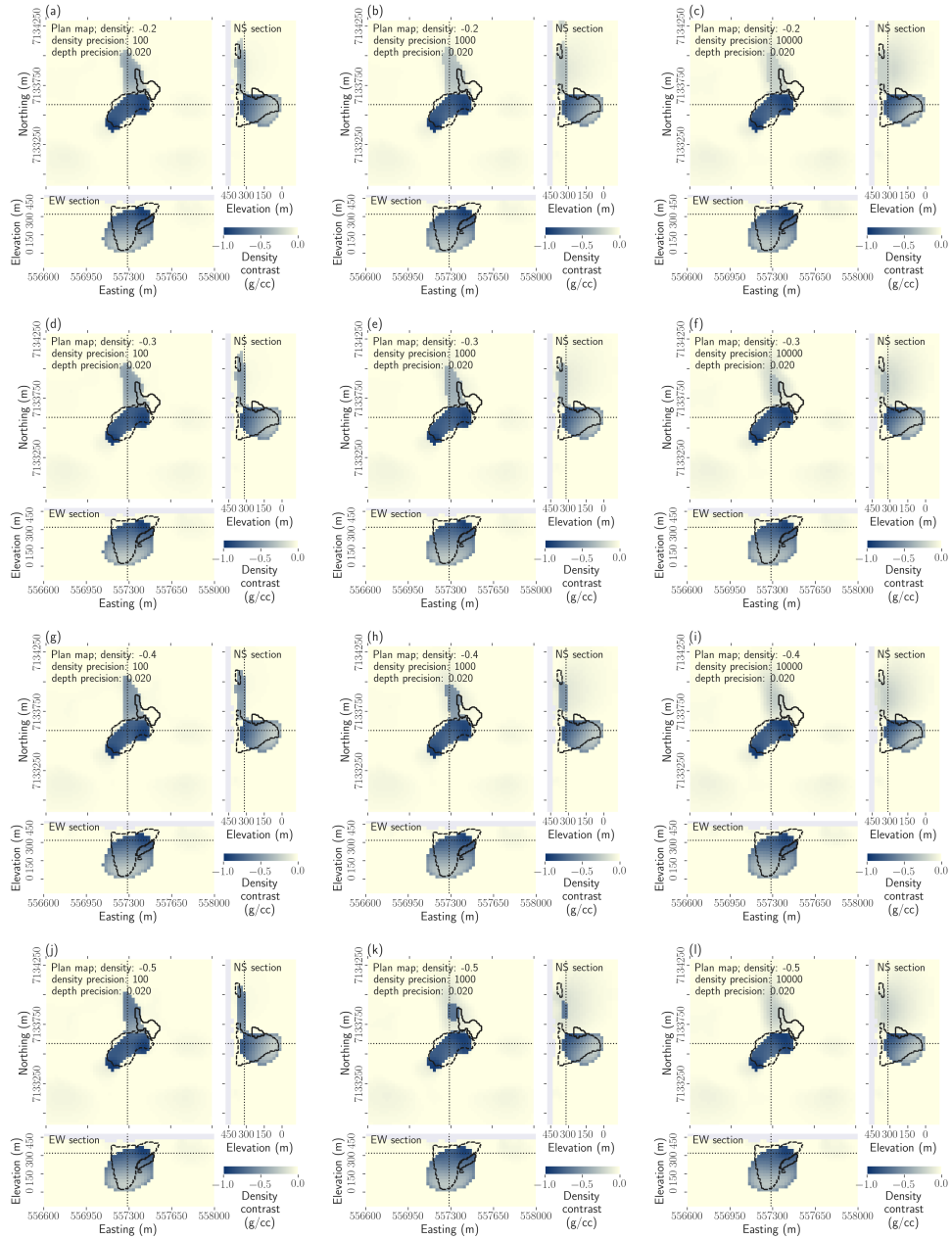


Figure F.5: Density contrast models recovered from PGIs for the DO-27 case study for various values of the mean and variance of the density contrast for the PK-minor unit. The depth variance is equal to 50 m^2 .

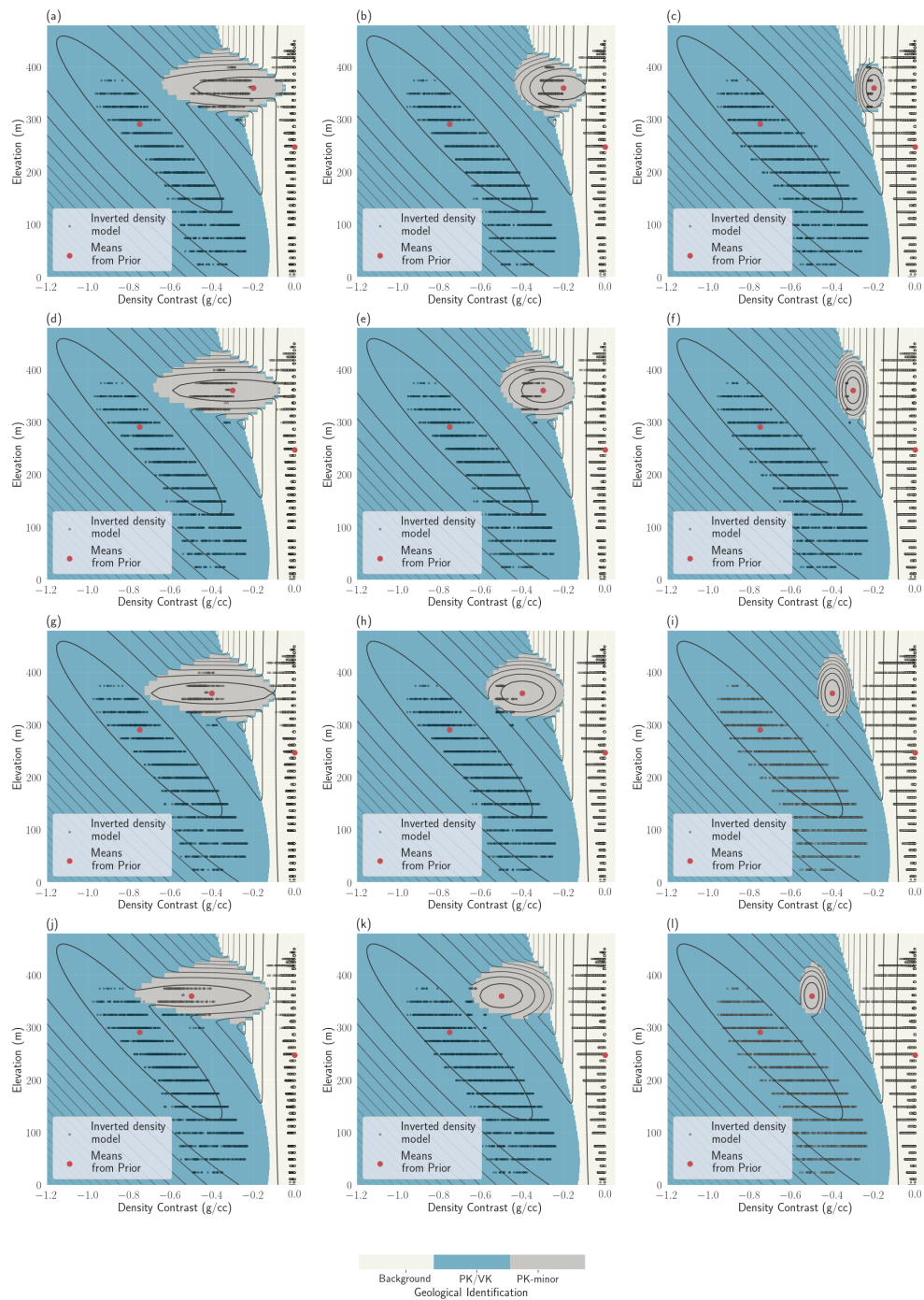


Figure F.6: GMMs used to recover the models presented in Figure F.5.

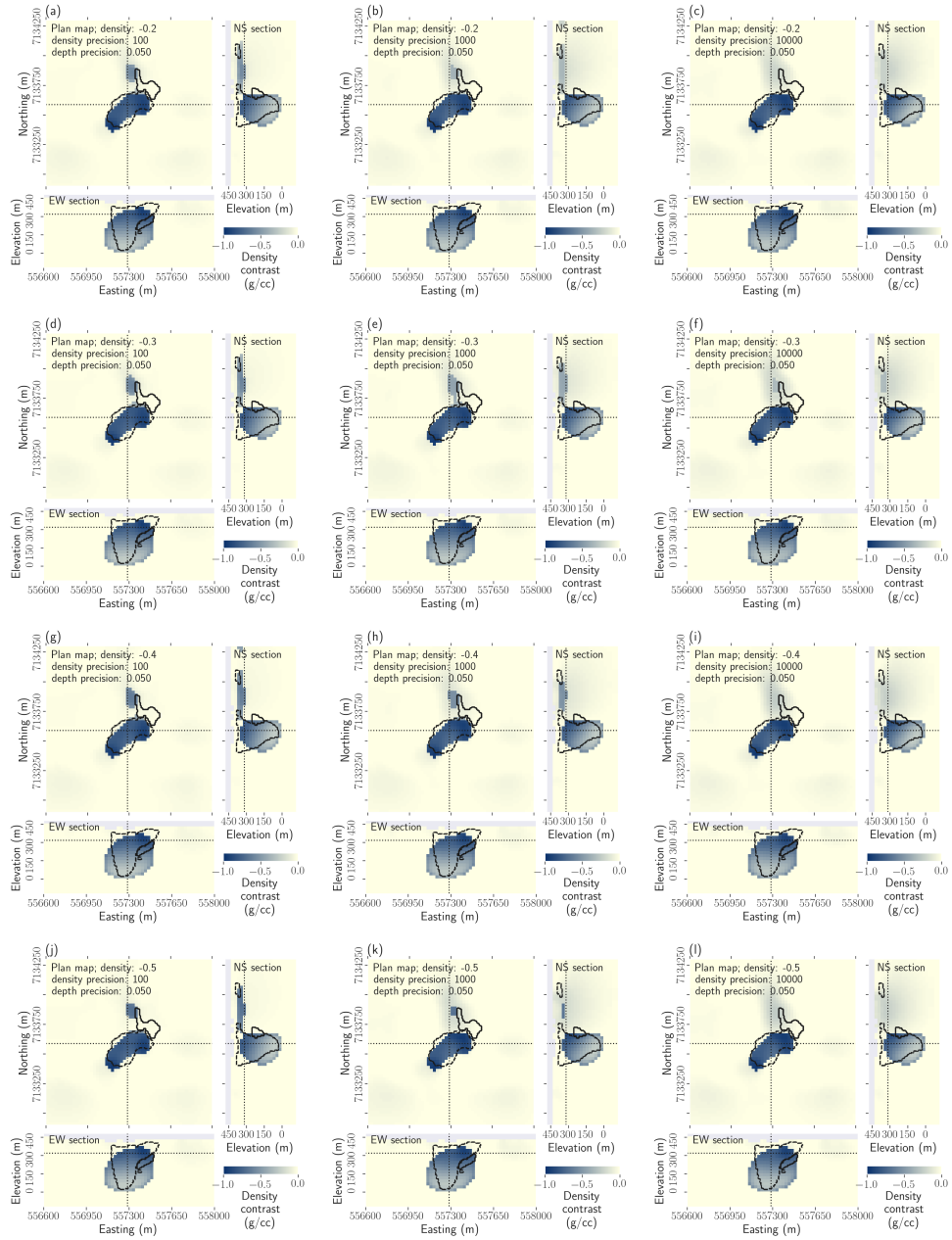


Figure F.7: Density contrast models recovered from PGIs for the DO-27 case study for various values of the mean and variance of the density contrast for the PK-minor unit. The depth variance is equal to 20 m^2 .

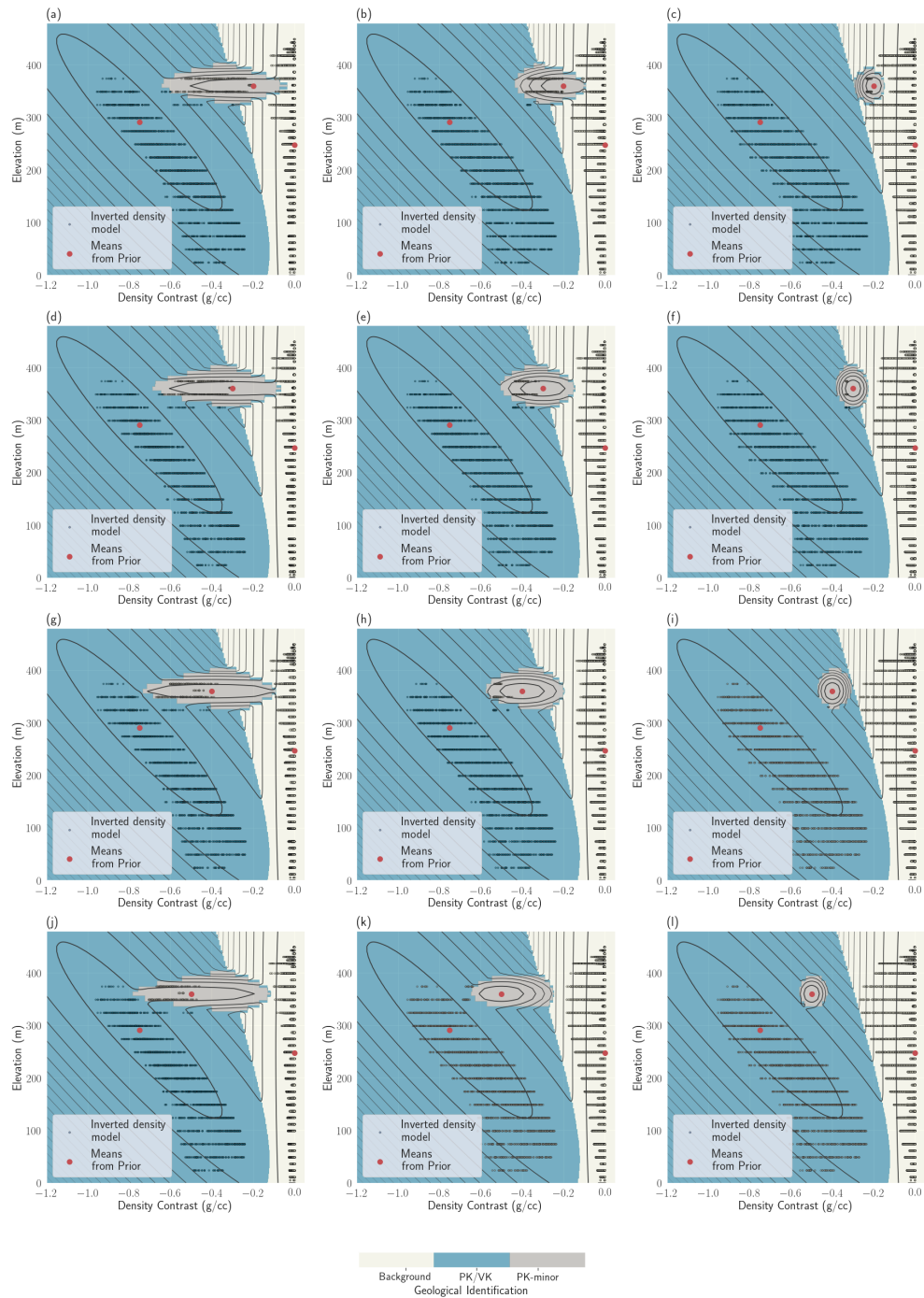


Figure F.8: GMMs used to recover the models presented in Figure F.7.

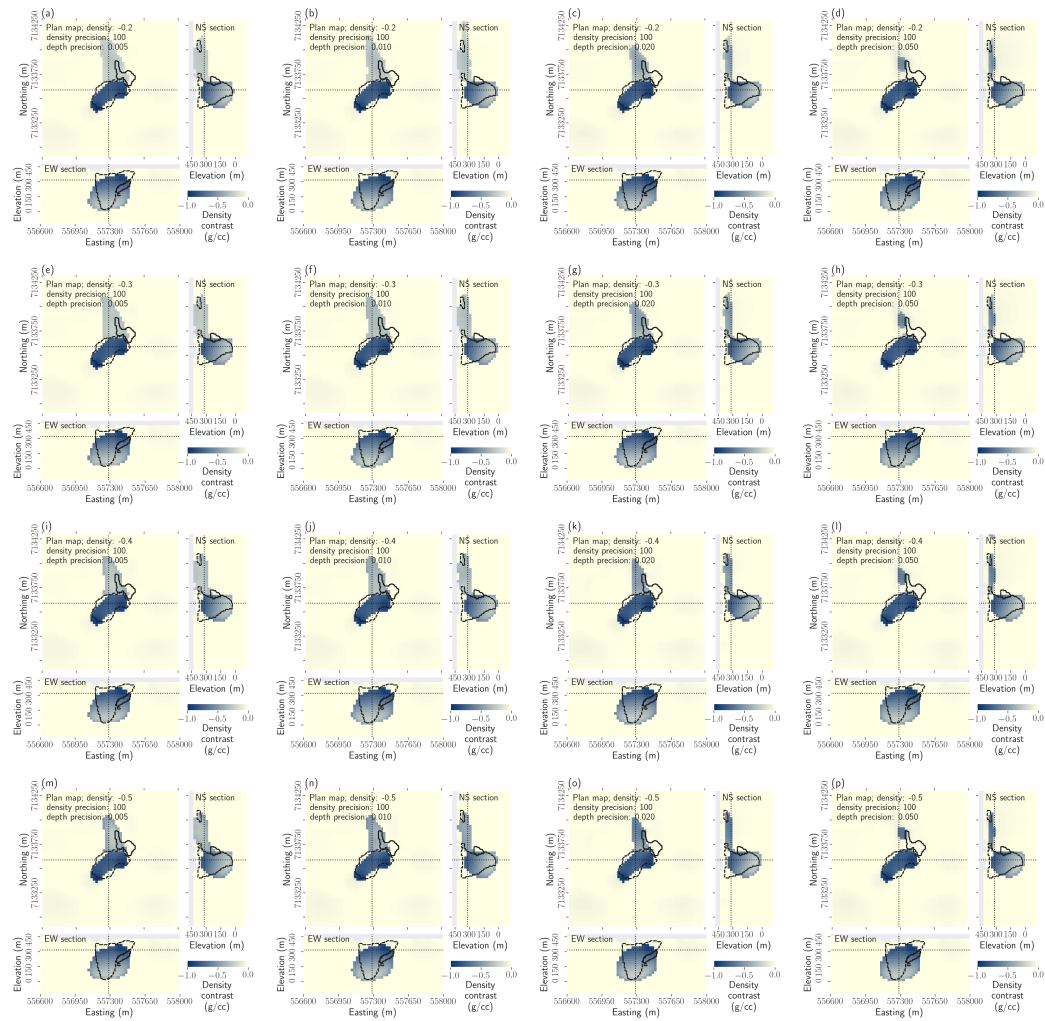


Figure F.9: Density contrast models recovered from PGIs for the DO-27 case study for various values of the mean density and variance of the depth for the PK-minor unit. The density variance is equal to $0.01 \text{ (g/cm}^3\text{)}^2$.

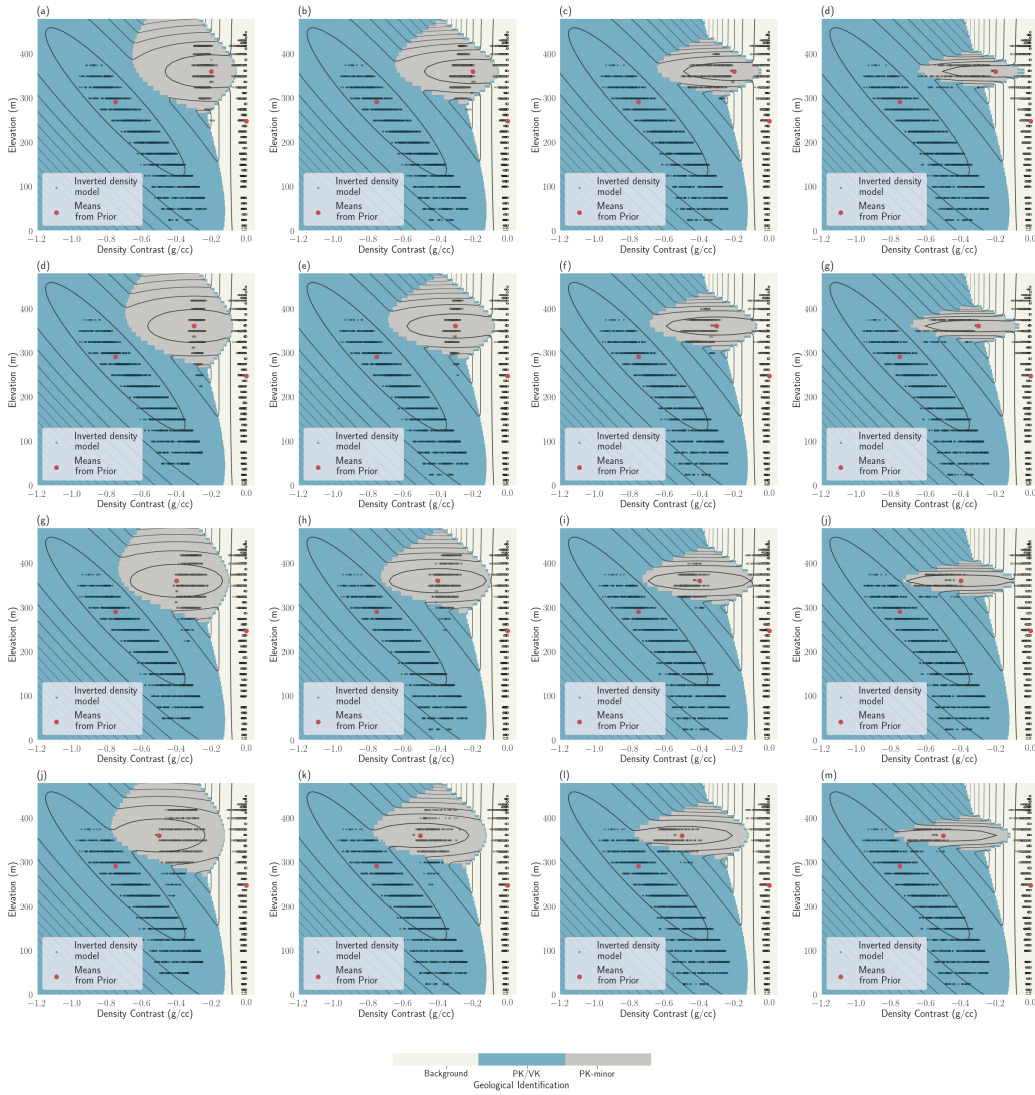


Figure F.10: GMMs used to recover the models presented in Figure F.9.



Figure F.11: Density contrast models recovered from PGIs for the DO-27 case study for various values of the mean density and variance of the depth for the PK-minor unit. The density variance is equal to $0.001 \text{ (g/cm}^3\text{)}^2$.

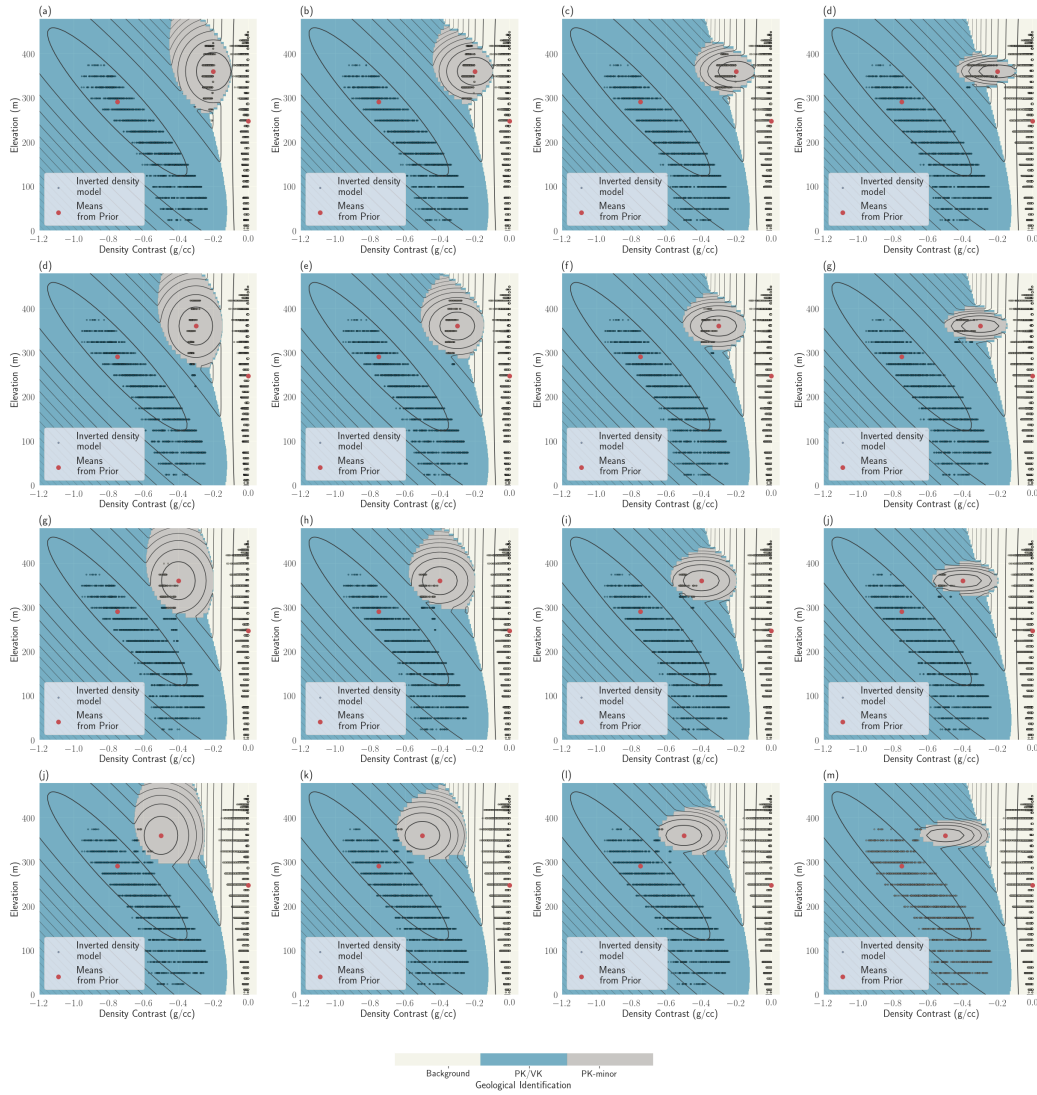


Figure F.12: GMMs used to recover the models presented in Figure F.11.



Figure F.13: Density contrast models recovered from PGIs for the DO-27 case study for various values of the the mean density and variance of the depth for the PK-minor unit. The density variance is equal to $0.0001 \text{ (g/cm}^3\text{)}^2$.

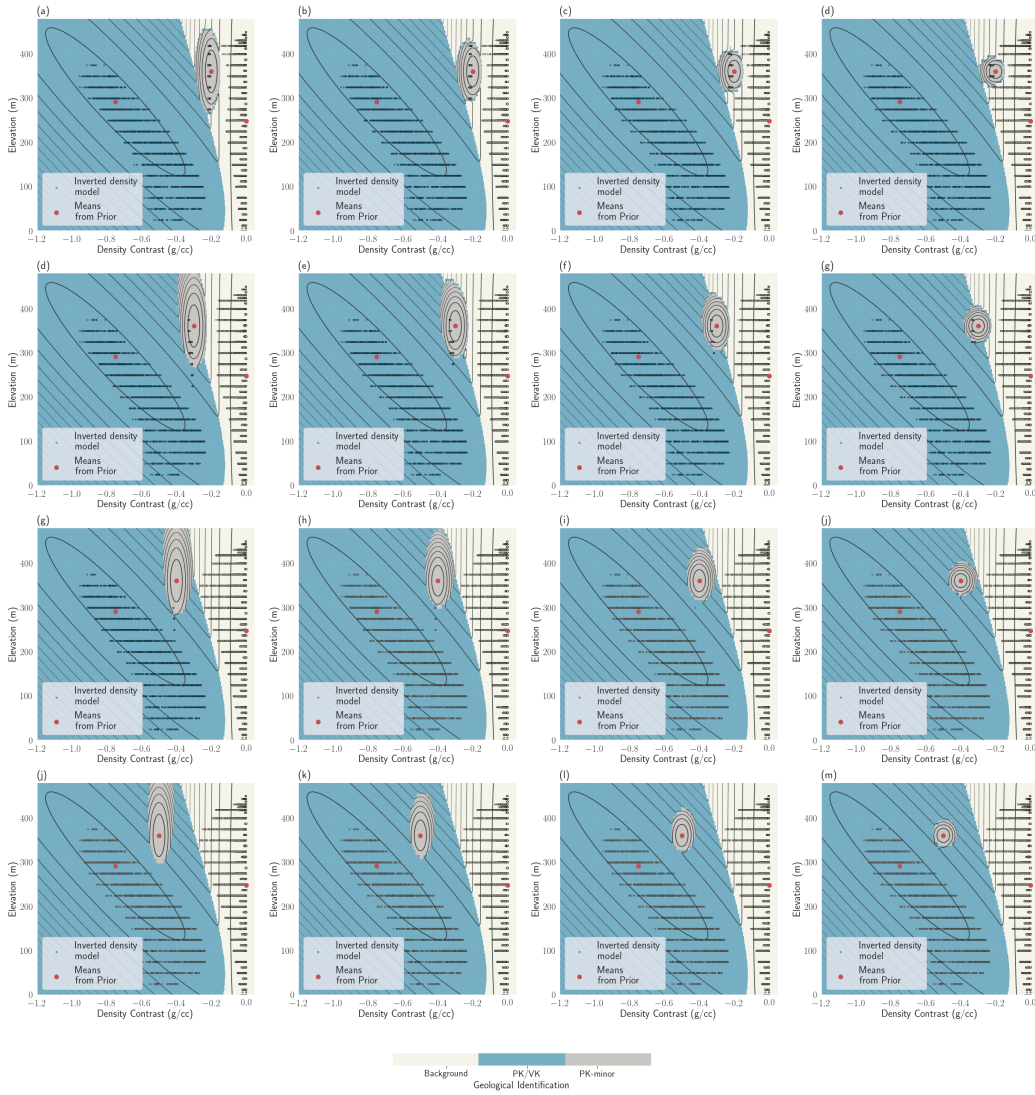


Figure F.14: GMMs used to recover the models presented in Figure F.13.

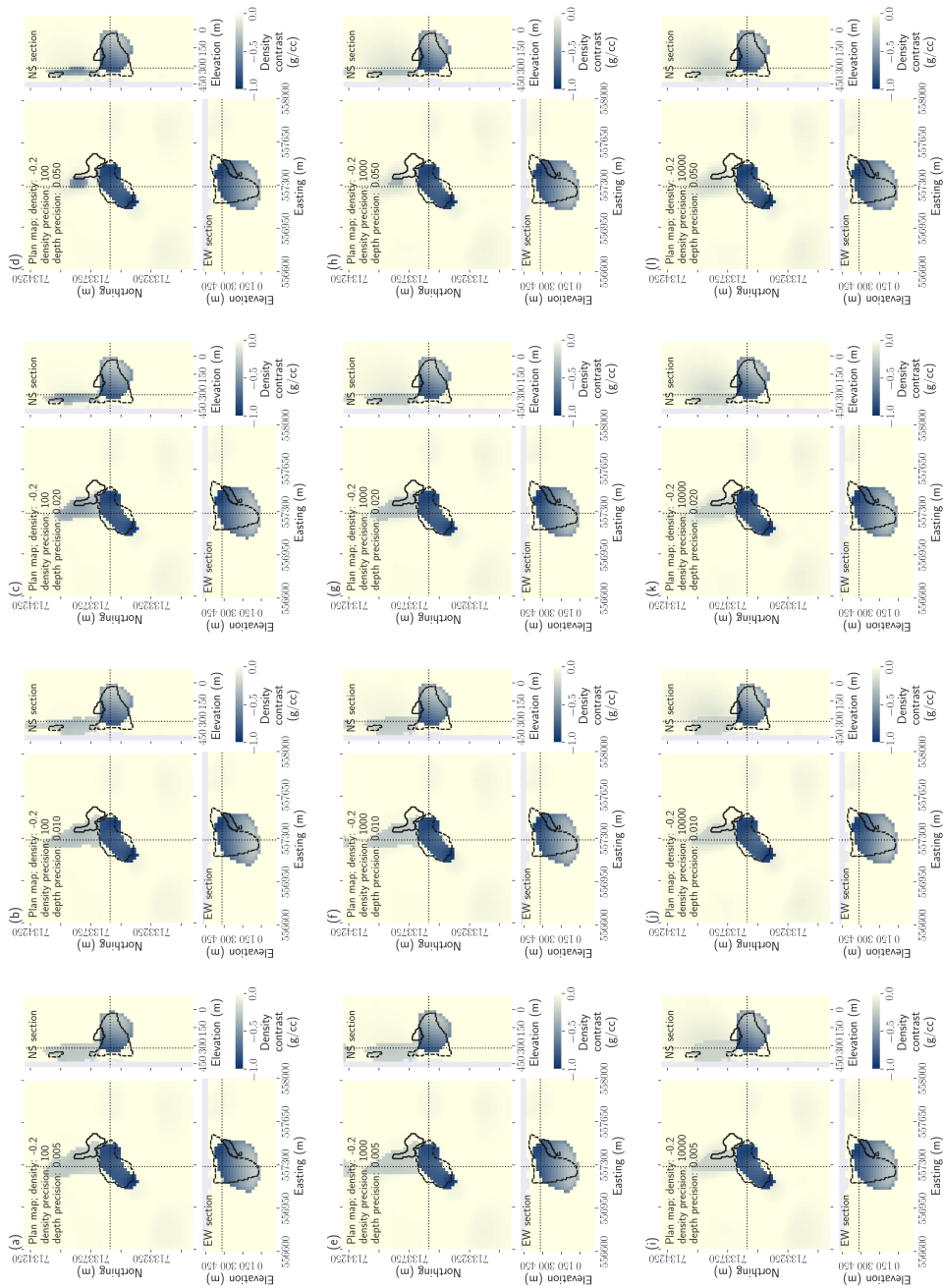


Figure F.15: Density contrast models recovered from PGIs for the DO-27 case study for various values of the variances of the densities and depth for the PK-minor unit. The density mean is equal to -0.2 g/cm^3 .

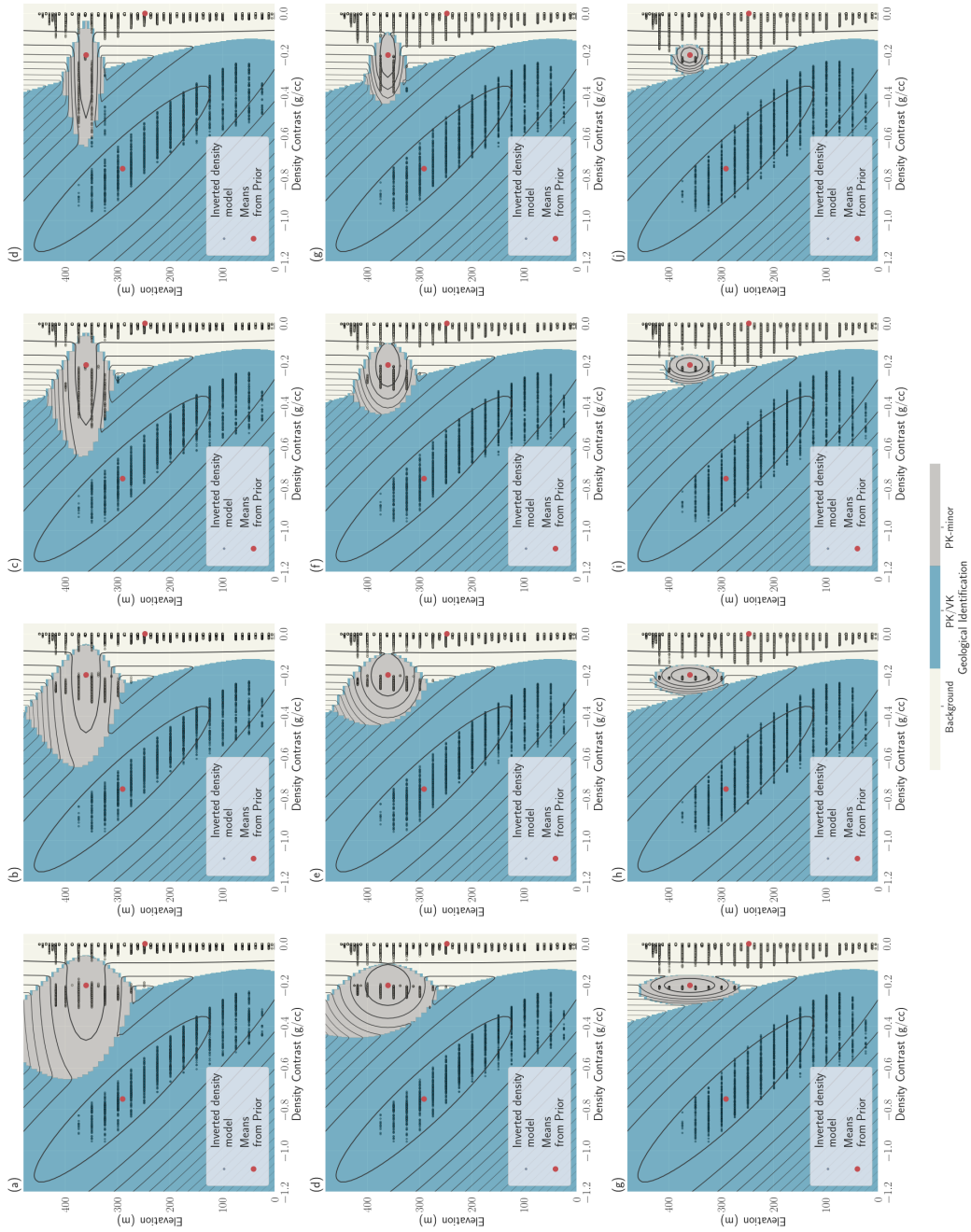


Figure F.16: GMMs used to recover the models presented in Figure F.15.

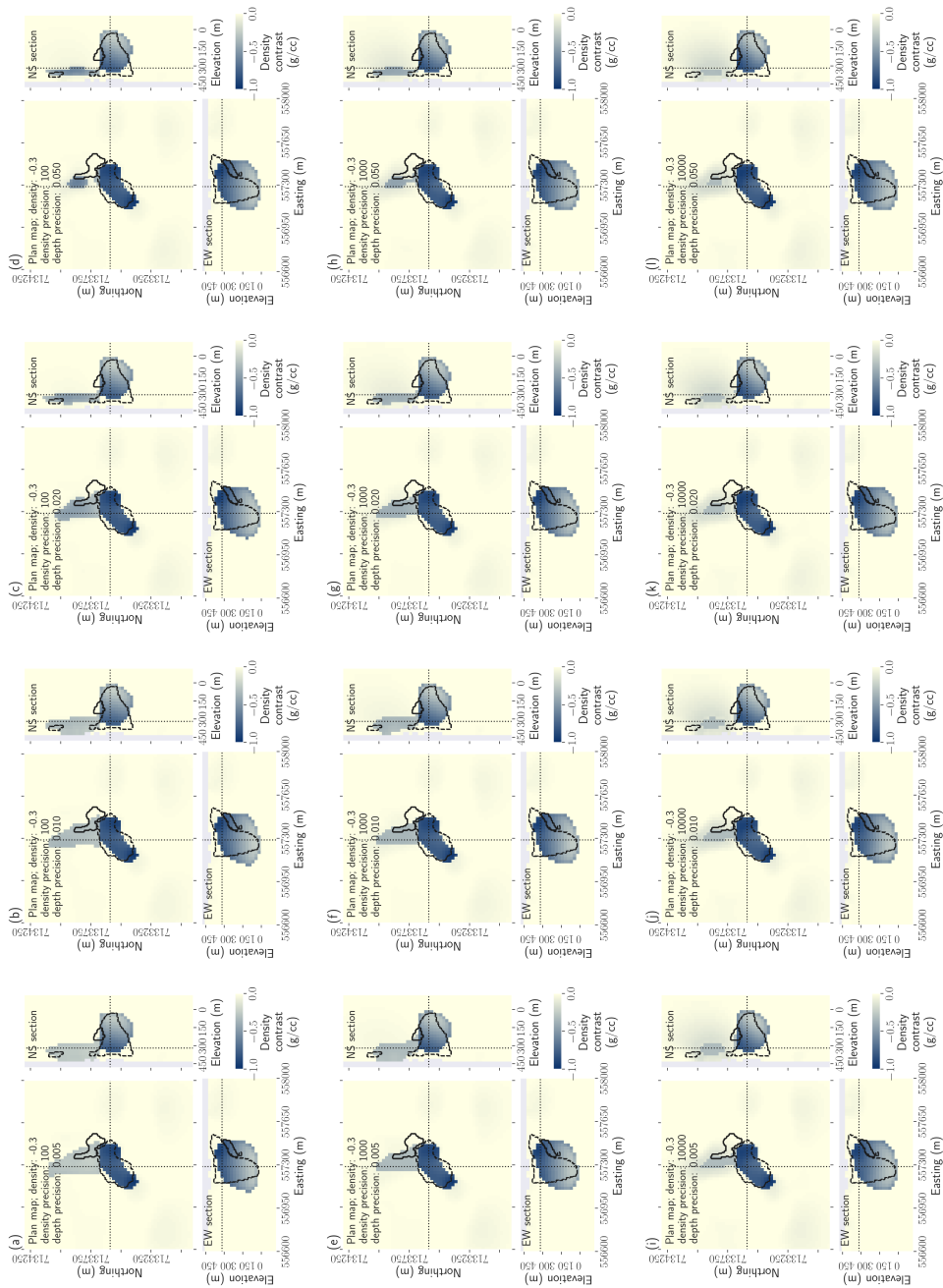


Figure F.17: Density contrast models recovered from PGIs for the DO-27 case study for various values of the variances of the density and depth for the PK-minor unit. The depth variance is equal to -0.3 g/cm^3 .

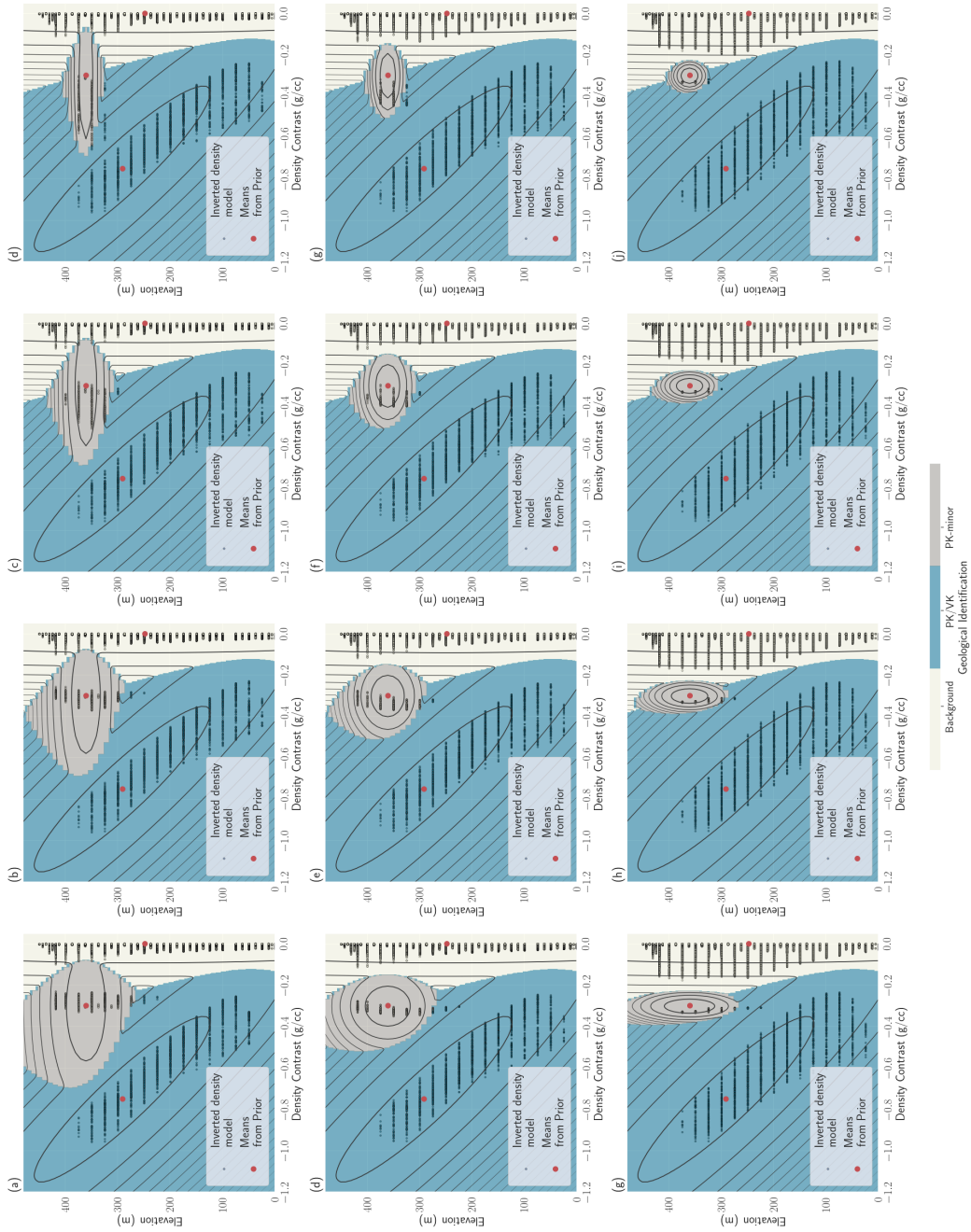


Figure F.18: GMMs used to recover the models presented in Figure F.17.

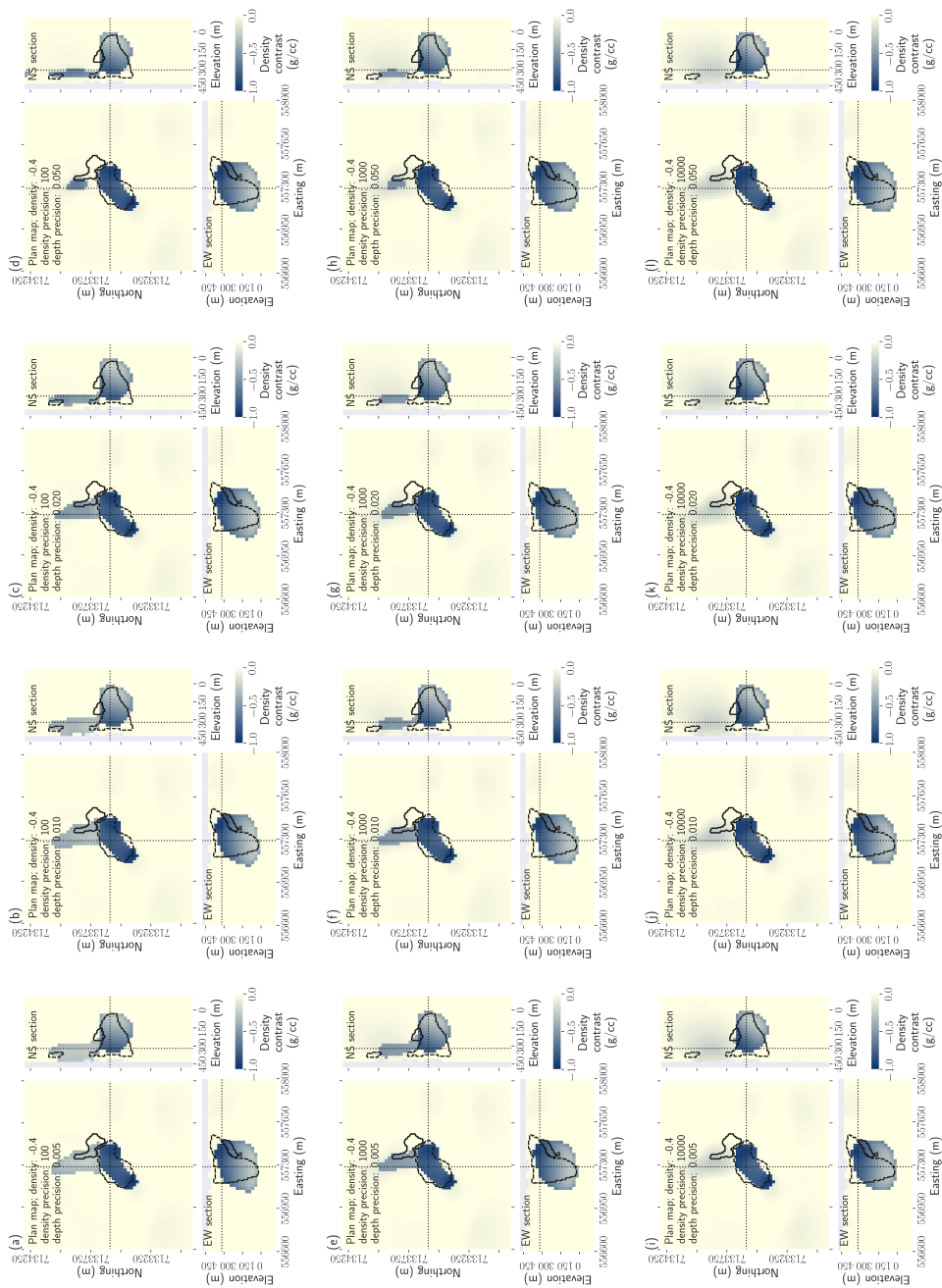


Figure F.19: Density contrast models recovered from PGIs for the DO-27 case study for various values of the variances of the density and depth for the PK-minor unit. The depth variance is equal to -0.4 g/cm^3 .

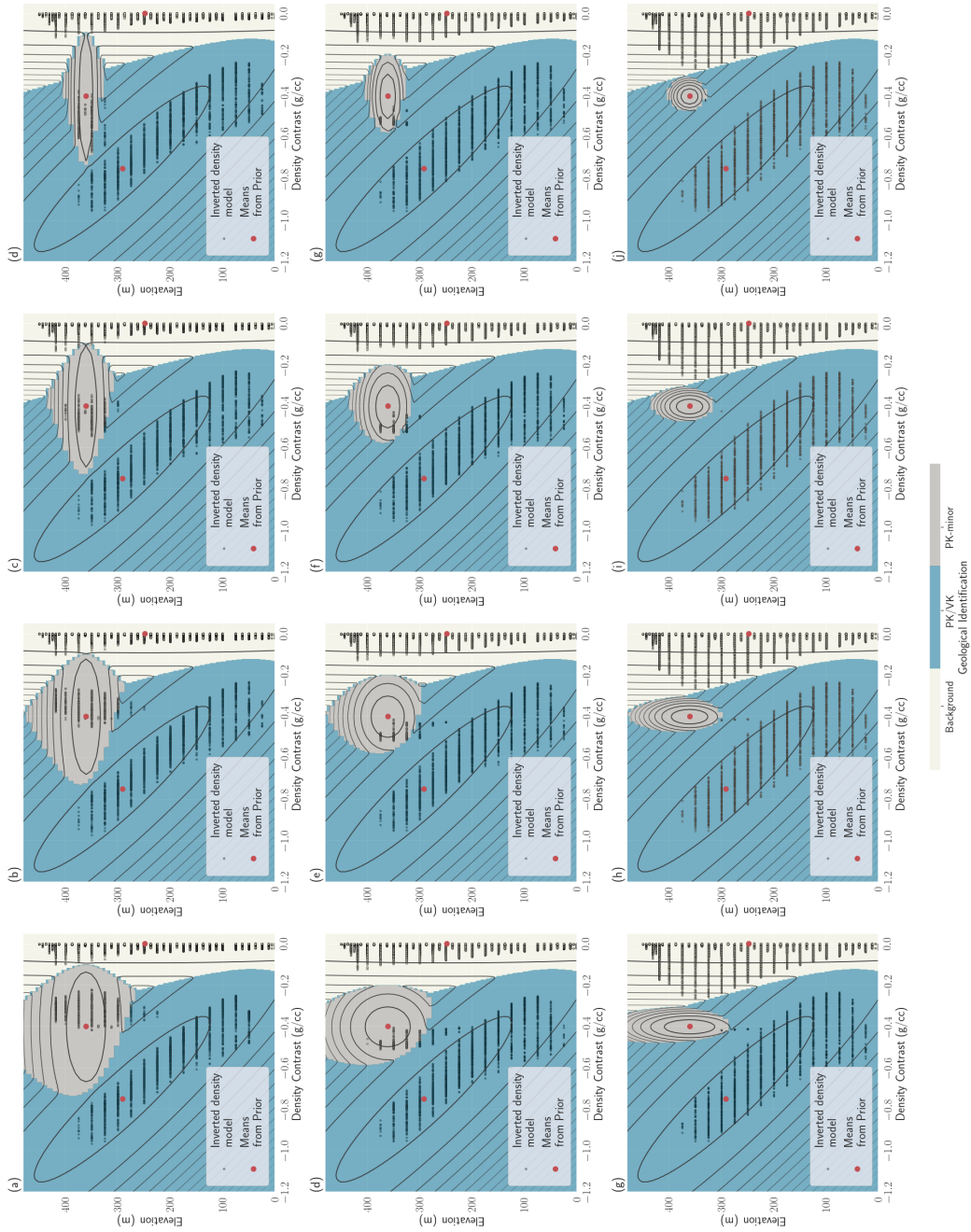


Figure F.20: GMMs used to recover the models presented in Figure F.19.

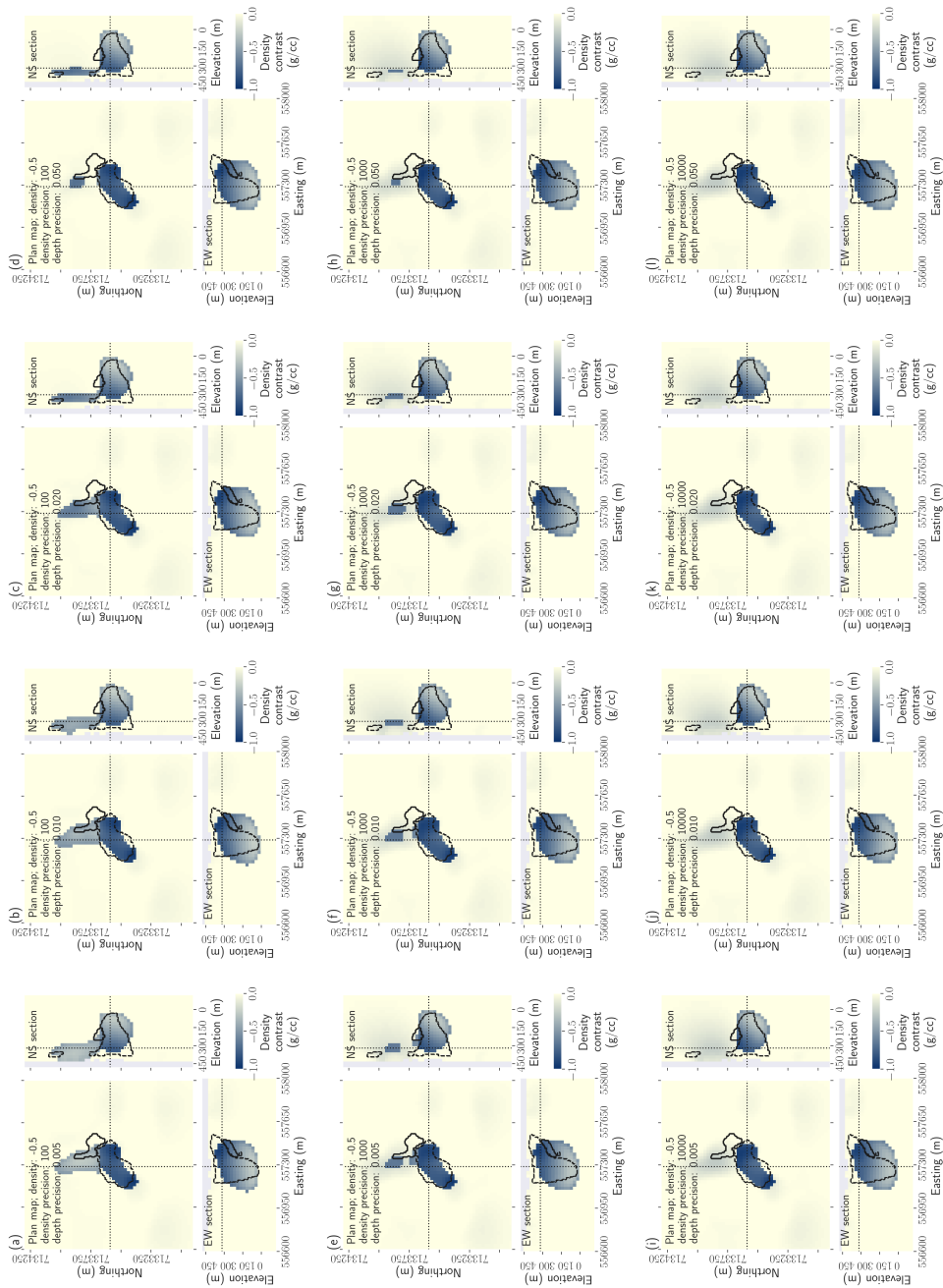


Figure F.21: Density contrast models recovered from PGIs for the DO-27 case study for various values of the variances of the density and depth for the PK-minor unit. The depth variance is equal to -0.5 g/cm^3 .

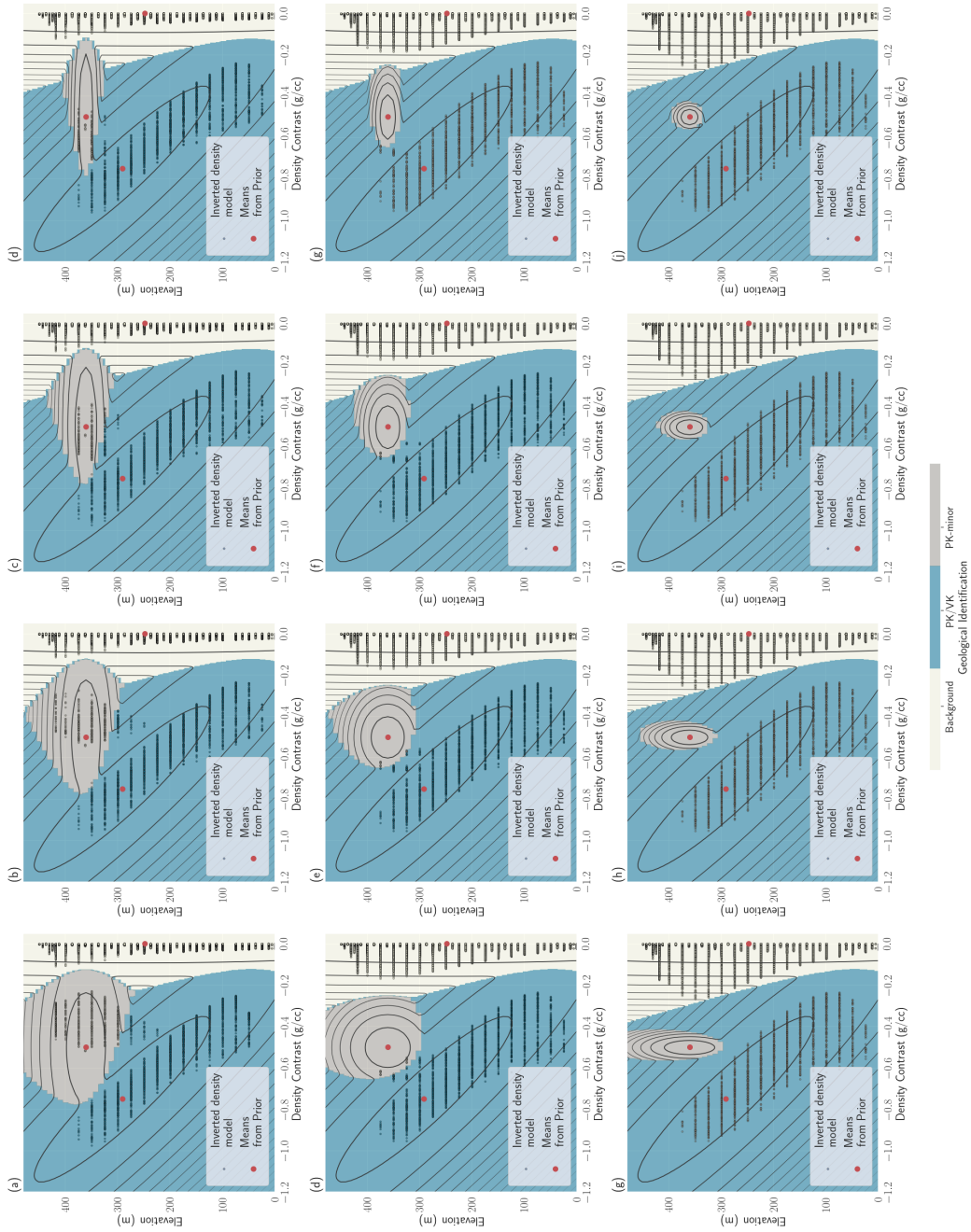


Figure F.22: GMMs used to recover the models presented in Figure F.21.